ISBN 978-82-326-3944-1 (printed version)
ISBN 978-82-326-3945-8 (electronic version)
ISSN 1503-8181

Doctoral theses at NTNU, 2019:173

Finn-Christian Wickmann Hanssen

Non-Linear Wave-Body Interaction in Severe Waves

NTNU
Norwegian University of
Science and Technology
Faculty of Engineering
Department of Marine Technology

NTNU
Norwegian University of
Science and Technology

Doctoral theses at NTNU, 2019:173

NTNU

NTNU
Norwegian University of
Science and Technology

Finn-Christian Wickmann Hanssen

Non-Linear Wave-Body Interaction in Severe Waves

Thesis for the degree of Philosophiae Doctor

Trondheim, June 2019

Norwegian University of Science and Technology
Faculty of Engineering
Department of Marine Technology

NTNU
Norwegian University of
Science and Technology

NTNU
Norwegian University of Science and Technology

Thesis for the degree of Philosophiae Doctor

Faculty of Engineering
Department of Marine Technology

ISBN 978-82-326-3944-1 (printed version)
ISBN 978-82-326-3945-8 (electronic version)
ISSN 1503-8181

Doctoral theses at NTNU, 2019:173

Printed by Skipnes Kommunikasjon as

Abstract

Offshore structures located in harsh environments may experience large wave loads and wave-induced responses. The present thesis documents a two-dimensional numerical investigation of interactions between fixed or floating structures and waves. Examined scenarios include large rigid-body motions and steep waves. The main objective of the research has been to develop an accurate and efficient fully non-linear potential-flow method for an incompressible liquid, and to use this in a systematic analysis to provide fundamental insight into wave-body interaction mechanisms beyond the capability of linear and weakly non-linear methods. Free-surface tension is neglected.

The numerical method uses the harmonic polynomial cell (HPC) method to solve the governing Laplace equation for the velocity potential and its time derivative. The HPC method is a field method where the entire fluid domain is discretized by overlapping cells, and the velocity potential in each cell is represented by harmonic polynomials up to fourth order. Here, the HPC method is proposed combined with novel features that include an immersed boundary method where markers track the time-evolution of the free surface, and using overlapping grids in a domain-decomposition strategy. By doing this, boundaries with arbitrary geometries are managed straightforwardly, and the numerical discretization can be refined locally without increasing the computational cost unnecessarily. Systematic studies are performed to validate the numerical method. It is shown that the solver is able to accurately propagate steep waves in deep and intermediate waters over a long time scale, and to deal with non-linear wave phenomena in shallow water including non-linear dispersion, solitary waves and a steep and eventually breaking focused wave. The method's ability to deal with local free-surface behavior close to a curved body is confirmed through studying a circular cylinder undergoing forced heave motions in still water. Wave loads on a fixed ship section in beam-sea incident waves show satisfactory agreement with published reference results.

A freely floating ship-section is studied in beam-sea waves with different wave heights. Wave-frequency motions and the mean wave drift force in sway are compared with experimental, numerical and theoretical reference results. Near heave and roll resonance, significant non-linear coupling effects are observed between the different modes of motion. In this wave-frequency range, mean wave drift forces larger than those predicted by second-order theory are observed. For higher wave frequencies, on the other hand, they are lower than from second-order theory. The latter is confirmed also when the body is restrained from moving. These

observations indicate that there are important non-linear effects, beyond the capability of second-order theory, that influence the mean wave drift force. This has relevance for mooring analysis of ship-shaped structures exposed to waves from the side. Contrary to claims made by other authors, the mean wave drift force is estimated most accurately from direct pressure integration. It is found that weakly non-linear methods based on conservation of fluid momentum, such as Maruo's formula, may be inaccurate and should be used with care in connection with fully non-linear wave-body interaction simulations. The results obtained from conservation of fluid momentum without any additional assumptions are consistent with direct pressure integration, other than when wave-frequency motions are large. It is demonstrated that the mean wave drift force is particularly sensitive to a non-linear term in the body-boundary condition when a separate boundary value problem is solved to estimate the time derivative of the velocity potential. Treating this term erroneously may dramatically increase the mean wave drift force near heave and roll resonance, while wave-frequency motions are insignificantly affected. It is questioned whether this may have contributed to other authors claiming that direct pressure integration is inaccurate in their work.

A domain-decomposition strategy to couple the developed potential-flow method with an existing Navier-Stokes solver based on laminar flow is proposed. Within this framework, viscous effects can be properly accounted for where they matter, while benefiting from the accuracy and efficiency of the potential-flow method elsewhere. The exchange of information between the two solvers is examined for a wave-propagation case. This serves as a guidance towards future work.

Preface

This thesis is submitted to the Norwegian University of Science and Technology (NTNU) for partial fulfilment of the requirements for the degree of philosophiae doctor (PhD).

This work has been carried out at the Centre for Autonomous Marine Operations and Systems (AMOS), Department of Marine Technology, NTNU, Trondheim, with Professor Marilena Greco as the main supervisor and with Professor Odd M. Faltinsen at the Department of Marine Technology, NTNU as co-supervisor.

This work was supported by the Research Council of Norway through the Centre of Excellence funding scheme, project number 223254-AMOS. The Norwegian Research Council is acknowledged as the main sponsor of AMOS.

Acknowledgements

Working towards this thesis has been the most rewarding experience, much thanks to the tireless support and enthusiasm shown by my main supervisor Prof. Marilena Greco. When in doubt, she has supported me with helpful advice and insight, but always allowed me to follow my own path. In times of frustration, she has provided invaluable perspective. I have always left our meetings feeling encouraged, for which I am deeply grateful. I also sincerely thank my co-supervisor prof. Odd M. Faltinsen for sharing from his unparalleled knowledge and experience during discussions. These discussions contributed significantly to form this work. I would also like to acknowledge the major influence he has had on me as a teacher of PhD courses in hydrodynamics.

I have benefited substantially from working with and learning from many dedicated and generous people during this study. I would like to thank Dr. Andrea Bardazzi and Prof. Claudio Lugni for great collaboration in studying nonlinear wave problems, both in Trondheim and during my visits to Rome. I am full of gratitude to Dr. Giuseppina Colicchio, who has spent countless hours helping me to adjust her Navier-Stokes solver. Prof. Yanlin Shao has been a continuous source of inspiration through sharing from his vast knowledge, discussing new ideas and in general showing interest in my work. I also thank the members of the EXWAVE joint industry project for letting me take part in their meetings.

The director of NTNU AMOS, Prof. Asgeir Sørensen, is acknowledged for creating a research environment where we are encouraged to be proud of our work and achievements. I also appreciate the assistance provided by the staff at NTNU AMOS and the Department of Marine Technology. In particular, Sigrid Bakken Wold has been most kind and helpful.

It has been a pleasure to work alongside all my fellow colleagues at the Department of Marine Technology. My office mate, Dr. Yugao Shen, who I have shared valuable discussions as well as quite a few hours playing ping-pong with, has meant a great deal to me. I appreciate the assistance from my friend Dr. Isar Ghamari in facilitating so that I could follow PhD courses in hydrodynamics before moving to Trondheim. Collaborating with Shaojun Ma and Mohd Atif Siddiqui has led to many inspiring discussions and new ideas. Taking PhD courses and preparing for exams together with Dr. Kjersti Bruserud has been a joy. It has been much fun sharing flats with Dr. Martin Storheim and Dr. Eirik Bøckmann during my stay in Trondheim.

My employer Moss Maritime is acknowledged for granting me a leave of absence in connection with the PhD.

I appreciate the support from my family and friends. A special thank-you goes to my lovely fiancée Silje Skår for the patience shown during these years. I could definitely not have finished this work without her love and support.

Finally, I would like to dedicate this work in the memory of my mother, who taught me the importance of pursuing the things one finds meaningful and takes joy from in life. Taking the leap to study for a PhD was definitely in the spirit of those words.

Nomenclature

General Rules

- Only the most central symbols are listed below
- Meaning of symbols are as a minimum given when first introduced
- The same symbol is sometimes used to describe different quantities
- Vector quantities are given with bold letters

Abbreviations

2D	Two-dimensional
3D	Three-dimensional
ASCII	American standard code for information interchange
BEM	Boundary element method
BGG	Background grid
BVP	Boundary value problem
CFL	Courant-Friedrichs-Lewy
CFM	Conservation of fluid momentum
CPU	Central processing unit
DD	Domain decomposition
DFSC	Dynamic free-surface condition
DP	Dynamic positioning
DPI	Direct pressure integration
FDM	Finite difference method
FEM	Finite element method
FPSO	Floating production, storage and offloading
FSBI	Free surface-body intersection
FVM	Finite volume method
GPU	Graphic processing unit
HPC	Harmonic polynomial cell

IBM	Immersed boundary method
IBOGM	Immersed boundary-overlapping grid method
KFSC	Kinematic free-surface condition
LS	Level set
MTF	Multi-transmitting formula
NS	Navier-Stokes
NWT	Numerical wave tank
OG	Overlapping grid
RK	Runge-Kutta
UK	United Kingdom
VOF	Volume of fluid

Subscripts

$b \rightarrow i$	Body-fixed to inertial
bf	Body-fixed
fs	Free surface
$i \rightarrow b$	Inertial to body-fixed
n	Time step number
ref	Reference value
t	Time derivative
wm	Wavemaker

Superscripts

l	Linear
n	Time step number
(n)	n^{th} order
q	Quadratic

Coordinate systems

Oxz	Earth-fixed inertial coordinate system
$ox_{bf}z_{bf}$	Body-fixed coordinate system
$o\overline{xz}$	Local cell coordinate system

Roman letters

A_{ij}	Added mass coefficient
B	Breadth of ship section
B_{ij}	Damping coefficient
c	Phase speed
$c_{i,j}$	Element of inverse of harmonic-polynomial matrix $\boldsymbol{D}$
C_{ij}	Stiffness coefficient
d	Draught of ship section
D	Cylinder diameter
E	Sum of potential and kinetic energy
f_j	Harmonic polynomial number j
g	Acceleration of gravity
h	Water depth
H	Wave height
H_b	Breaking-wave height
I_{yy}	Moment of inertia about y-axis
k	Wave number
KE	Kinetic energy
KG	Vertical center of gravity from keel
L_2	$\|L2\|$ norm
L_{beach}	Length of numerical beach
L_{tank}	Length of wave tank
M	Mass
M_y	External moment about y-axis
$M_{y,add}$	Additional external moment about y-axis
n_x	Number of grid nodes in x-direction
n_z	Number of grid nodes in z-direction
$p(x,z,t)$	Excess pressure $P(x,z,t)$–p_{atm}
$P(x,z,t)$	Total pressure
p_{atm}	Atmospheric pressure
PE	Potential energy
R	Cylinder radius
r_{wm}	Wavemaker ramp function
S_0	Mean submerged area
S_B	Body boundary

S_{seabed}	Seabed boundary
S_{SF}	Free-surface boundary
S_{wall}	Wall boundary
s_{wm}	Wavemaker motion
S_{WM}	Wavemaker boundary
t	Time
T	Wave period
T_{ramp}	Wavemaker ramp time
V	Fluid volume

Bold Roman letters

$\boldsymbol{A}$	Global coefficient matrix
$\boldsymbol{B}$	Damping matrix
$\boldsymbol{b}_{\varphi}$	Right-hand side vector, velocity potential
$\boldsymbol{b}_{\varphi_t}$	Right-hand side vector, time derivative of velocity potential
$\boldsymbol{C}$	Stiffness matrix
$\boldsymbol{D}$	Inverse of harmonic-polynomial matrix or rate-of-strain tensor
$\boldsymbol{F}(t)$	Fluid force vector
$\boldsymbol{F}_{add}$	Additional external force vector
$\boldsymbol{F}_{ext}$	Total external force vector
$\boldsymbol{g}$	Acceleration of gravity vector
$\boldsymbol{i}$	Unit vector in x-direction
$\boldsymbol{I}$	Rotational inertia matrix
$\boldsymbol{j}$	Unit vector in y-direction
$\boldsymbol{k}$	Unit vector in z-direction
$\boldsymbol{M}$	Mass matrix
$\boldsymbol{M}(t)$	Fluid moment vector
$\boldsymbol{M}_{ext}$	Total external moment vector
$\boldsymbol{n}$	Normal vector
$\boldsymbol{P}$	Coordinates of a point P
$\boldsymbol{P}_{fs}$	Coordinates of a general point on the free surface
$\boldsymbol{P}_m$	Coordinates of a free-surface marker
$\boldsymbol{r}$	Vector from origin of $ox_{bf}z_{bf}$ coordinate system to a point P
$\boldsymbol{R}$	Vector from origin of Oxz coordinate system to a point P
$\boldsymbol{R}_0$	Origin of $ox_{bf}z_{bf}$ coordinate system
$\boldsymbol{U}, \boldsymbol{v}, \boldsymbol{V}$	Velocity vector
$\boldsymbol{u}_b$	Velocity vector of a fixed point in $ox_{bf}z_{bf}$ coordinate system
$\boldsymbol{v}'$	Velocity vector relative to $ox_{bf}z_{bf}$ coordinate system

Greek Letters and Mathematical Symbols

α	Rotation angle about y-axis
γ	Measure of cell skewness
Δt	Time step
Δx	Grid spacing in x-direction
Δz	Grid spacing in z-direction
ζ	Free-surface elevation
ζ_a	Wave amplitude
ζ_c	Crest amplitude
ζ_R	Reflected-wave amplitude
ζ_T	Transmitted-wave amplitude
η_i	Motion in degree of freedom i
η_{ia}	Motion amplitude in degree of freedom i
$\theta_b(x)$	Envelope function, suppression of wave breaking
$\kappa(x)$	Spatial ramp function
λ	Wavelength
$\mathbf{\Lambda}$	Rotation matrix
μ	Dynamic viscosity
$\mu_b(x)$	Dissipative term, suppression of wave breaking
ν	Damping coefficient associated with numerical beach
ξ_B	Non-dimensional wave frequency
ρ	Mass density
φ	Velocity potential
$\boldsymbol{\varphi}$	Vector with velocity potential in grid nodes
φ_t	Eulerian time derivative of φ in inertial reference frame
$\boldsymbol{\varphi}_t$	Vector with time derivative of velocity potential in grid nodes
ϕ	Level-set function
Φ	Acceleration potential
ω	Angular frequency or angular wave frequency
$\boldsymbol{\omega}$	Angular velocity vector
Ω	Computational domain
$\partial\Omega_D$	Dirichlet boundary
$\partial\Omega_N$	Neumann boundary

Contents

Chapter 1

Introduction

1.1 Motivation

Floating offshore structures in harsh locations are exposed to large environmental loads from waves, wind and current. In the North Sea, for example, significant wave heights above $15\ m$, wind speeds above $40\ m/s$ and current speeds in the order of $1.5\ m/s$ may be seen (DNV GL, 2018). Examples of relevant floating offshore structures are given in Figure 1.1. Some of these floaters, such as semi-submersible drilling rigs and ship-shaped or circular floating production, storage and offloading (FPSO) units, have been used by the oil and gas industry for decades. More recently, other types of structures that have traditionally been deployed in sheltered locations, are for various reasons moved offshore. Examples of these include floating wind turbines and fish farms.

In order to withstand environmental loads and maintain their position, the offshore floaters are equipped with a station-keeping system that may consist of mooring lines, a dynamic positioning (DP) system or a combination of the two. In order to dimension these systems, it is important that the environmental loads are accurately estimated. The focus in the present work is on the wave action, i.e. the loading on and response of a structure due to waves, while disregarding wind and current loads. Depending on the type of structure, the nature of the wave loads may vary. For a ship-shaped structure, for instance, inviscid wave loads dominate. For a fish farm, on the other hand, the viscous drag loads on the net structure may govern the global behaviour of the structure. In severe sea states, the wave-induced loading on and response of a structure may display significant non-linear behaviour. There are several types of such non-linear effects, both local and global, that are important to take into account when designing an offshore structure. Examples of local non-linear effects, although they may have global consequences from a structural viewpoint, are violent wave impacts on the bow or deck structure of a ship (Faltinsen et al., 2004), or on the columns or deck box of a semi-submersible.

Slowly-varying wave drift loads represent non-linear global loads that are important to account for in the design of a station-keeping system. If the oscillation frequency of these loads coincides with the natural frequency of a moored

(a) Semi-submersible

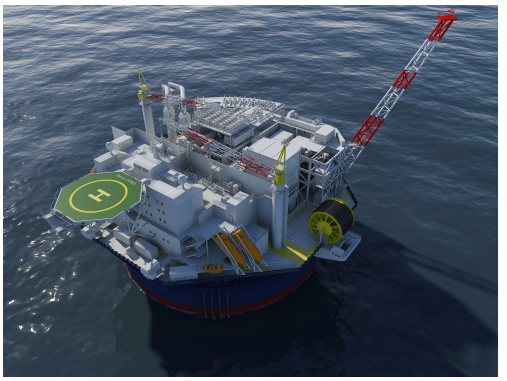

(b) Circular FPSO

(c) Ship-shaped FPSO

(d) Floating wind turbine

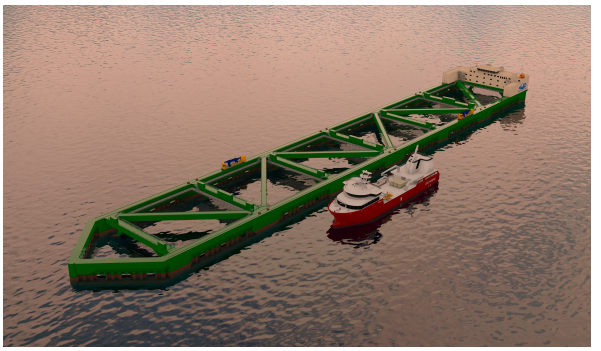

(e) Offshore fish farm

Figure 1.1: Examples of floating offshore structures taken from the following sources: a) www.seadrill.com, b) www.sevanssp.com, c) www.bp.com, d) www.equinor.com, e) www.nordlaks.no.

structure, they may induce large slowly-varying motions leading to significant mooring-line forces. Traditionally, slowly-varying wave drift loads are assumed weakly non-linear and are estimated from analysis based on potential-flow perturbation theory where terms up to 2^{nd} order are included, see e.g. Pinkster (1980) and Wichers (1988). Potential-flow theory does not account for viscous effects. However, viscous damping loads may be approximated by including additional linear or quadratic damping, while viscous loads on mooring lines may be approximated from Morison theory. The perturbation theory assumes that the wave height and body motions are small, and that non-linear wave drift loads can be estimated from truncated power series. By looking at the real scenario experienced by a floater in a storm sea state, such as depicted in Figure 1.2, or during model testing in a severe sea state such as in Figure 1.3, the general validity of the assumptions used within this approach is not obvious.

Figure 1.2: The Maersk Gryphon FPSO during a storm. Source: www.themariner.co.uk.

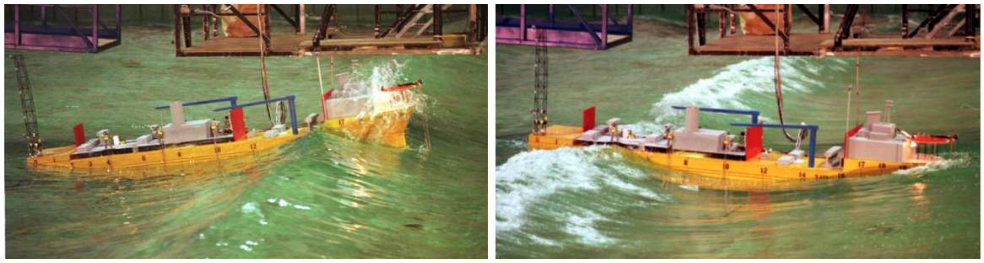

Figure 1.3: Model testing of a FPSO (courtesy of Sintef Ocean).

Several mooring line failures for both semi-submersibles and FPSOs in harsh weather have been reported over the last decade at the Norwegian Continental

Shelf (Kvitrud, 2014a,b) and in UK sector (Noble Denton Europe, 2006). In some of the incidents it is indicated that the failure mode was mooring-line *overload*, i.e. exceedance of the mooring line's strength capacity. While there are plausible reasons that could cause this, such as unintended response from a DP system leading the floater to drive off, there are also cases where the cause of mooring-line overload is less obvious. A possible explanation for mooring line failures in such cases is that the environmental loads and subsequent response were higher than the mooring system was dimensioned to withstand. It has been questioned by e.g. Stansberg et al. (2015) whether larger-than-anticipated wave loads contributed to some recent mooring line failures in the North Sea. Dev and Pinkster (1995) found that viscous effects may significantly increase the slowly-varying wave drift loads on a semi-submersible compared to those predicted by potential-flow theory. This observation was confirmed by Stansberg et al. (1998). Fonseca et al. (2016), Fonseca and Stansberg (2017b), Fonseca et al. (2017) performed systematic studies on the wave drift loads for a semi-submersible and a FPSO. Based on extensive model tests, they confirmed that wave drift loads may be significantly under-predicted by state-of-the-art computational tools in severe sea states. The increase in wave drift loads for the semi-submersible is mainly due to viscous effects, while for the FPSO also other non-linear effects may contribute. Similarly, Aksnes et al. (2015) found it necessary to increase the wave drift loads computed from potential-flow perturbation theory in order to achieve reasonable comparison with model tests. Non-linear mechanisms also influence the damping of slowly-varying motions (Fonseca and Stansberg, 2017a). Furthermore, there is experimental evidence that, when large waves and strong currents interact, wave drift loads are significantly influenced (Stansberg et al., 2013).

1.2 Objective

Although many of the scenarios described above are three-dimensional (3D) by nature, and may be influenced by viscous-flow effects, there are also mechanisms that can be systematically investigated in a two-dimensional (2D) inviscid framework. The aim of the present thesis is (1) to develop an accurate and efficient potential-flow solver to handle severe wave-body interactions within a 2D framework and (2) to provide fundamental insight into global non-linear effects beyond the capability of linear and weakly non-linear methods. This is achieved by investigating wave-body interaction problems involving steep waves and large rigid-body motions in a 2D numerical study. In particular, non-linear effects influencing the mean wave drift force on a ship section in beam-sea waves are investigated in detail. This has relevance for example for spread moored FPSOs that risk large waves from the side because the vessel's heading is restricted by the mooring system.

1.3 Previous Work

The boundary element method (BEM) has historically been the most widely used method for numerical solution of potential-flow problems involving wave-body

interactions. Under certain assumptions, the unknown linear velocity potential can be expressed in terms of singularities only over the mean wetted surface of the body in an analysis using the perturbation approach (Faltinsen, 1993). Thus, the method is attractive in that the number of unknowns is restricted. The most widely used commercial frequency-domain codes, such as Wamit by Wamit, Inc. and Hydrostar by Bureau Veritas, use BEM. If required, the 2^{nd}-order velocity potential can be solved for by in addition distributing singularities over the mean free surface. Commercially available partially non-linear BEM solvers include DNV GL Software's Wasim and ANSYS AQWA. Here, Froude-Krylov and hydrostatic loads evaluated at a body's instantaneous position are combined with linear scattering and radiation loads. Such method can be useful e.g. to estimate the hull-girder bending moment on a container ship in waves, as the water plane area typically varies with the relative wave elevation. A common feature of methods based on perturbation theory and partially non-linear methods is that they are only valid under certain assumptions. In terms of fully non-linear potential-flow methods, the majority of work exists in the field of research. A few notable works using BEM are mentioned in the following.

Vinje and Brevig (1981) and Dommermuth et al. (1988) performed numerical analysis of steep, overturning waves in finite water depth in 2D until the point where the overturning wave reattaches to the underlying surface, where potential-flow theory does not apply. Greco (2001) examined water-on-deck problems, typically relevant for FPSOs in large waves, using a BEM in 2D. You (2012) studied wave loads on and motions of moored ships in finite water depth in a fully non-linear numerical wave tank using a BEM in both 2D and 3D. Water entry of 2D bodies, accounting for non-viscous flow separation and hydroelastic effects, was investigated using BEM by Sun (2007). For a comprehensive overview of the historical development of potential-flow numerical wave tanks until the end of the twentieth century, reference is given to Kim et al. (1999).

Also other methods have been applied to study non-linear wave and wave-body interaction problems within the framework of potential-flow theory. A finite element method (FEM) was adopted by Wu and Eatock Taylor (1994) to solve the Laplace equation of the velocity potential for non-linear wave propagation in 2D, and for non-linear wave-body interaction in 2D by Eatock Taylor (1996). Yan and Ma (2007) investigated steep waves interacting with a floating body in 2D using FEM, and later extended their work to 3D (Ma and Yan, 2009). Bingham and Zhang (2007) investigated non-linear wave problems in 2D using finite difference methods (FDM) of different accuracy orders. A FDM was implemented in 3D by Engsig-Karup et al. (2009), showing good agreement with reference results for steep periodic waves and for waves propagating over a shoal. Ducrozet et al. (2010) performed an analysis involving diffraction of non-linear waves around a bottom-mounted, upright cylinder in 3D using a FDM.

More recently, the harmonic polynomial cell (HPC) method was proposed by Shao and Faltinsen (2012, 2014b) as an accurate and efficient numerical solver for the Laplace equation in potential-flow problems. Although the method is relatively new, it has been used by several authors for both linear and non-linear applications. The method was adopted by Liang et al. (2015) to study various problems in marine hydrodynamics, including coupling with a local solution to deal

with singular flows at sharp corners, in 2D. Zhu et al. (2017) used the HPC method in developing a 2D non-linear numerical wave tank, while Strand (2018) used the method to describe the flow inside a closed, flexible fish cage. Wang and Faltinsen (2018) used the HPC method with local grid refinement to study strongly non-linear phenomena, including overturning waves and water entry of a wedge, in 2D. Robaux and Benoit (2018) investigated the use of the HPC method combined with an immersed boundary method for 2D waves propagating over a submerged cylinder. The accuracy of the HPC method in various 2D implementations was investigated in depth by Ma et al. (2018). 3D applications of the HPC method are still limited, but Shao and Faltinsen (2014a) demonstrated its use for fully non-linear waves, investigating the wave run-up around upright bottom-mounted cylinders in 3D. Considering the HPC method as a measure to discretize a general field equation, Bardazzi et al. (2015) showed how a generalized version of the HPC method can be used to accurately solve the Poisson equation in a viscous-flow solver. The method's capabilities are therefore not restricted to potential flows, and further use in connection with viscous flows is currently investigated.

While potential-flow solvers are superior in propagating waves in an accurate and efficient manner, more computationally expensive Navier-Stokes (NS) solvers are required to properly deal with problems involving wave breaking, fragmentation phenomena and viscous effects. To benefit from the strengths of both classes of solvers, coupling between the two have received increased attention in the research community during the last years. A strong domain-decomposition (DD) between a non-linear BEM potential-flow solver and a level-set Navier-Stokes (LS-NS) solver to analyze a dam-breaking problem and subsequent wave impact on a vertical wall was proposed by Colicchio et al. (2006) in 2D, showing good agreement with experiments. Kristiansen and Faltinsen (2011) used a linearized potential-flow solver coupled with a NS solver to study the gap resonance phenomenon in 2D, where both solvers were based on the finite volume method (FVM). By doing so, they obtained free-surface elevations in the gap in good agreement with experiments. Near resonance, it is well-known that the free-surface elevation is significantly over-estimated by potential-flow theory due to lack of viscous damping. The gap-resonance problem in 2D was again considered by Fredriksen (2015), who also took into account forward-speed effects. In his work, the potential-flow solver was based on the HPC method. In Kristiansen et al. (2015), a similar method as in Kristiansen and Faltinsen (2011) was used in 3D to investigate the behaviour with an object inside the moonpool of a ship. With a HPC potential-flow solver weakly coupled with the open-source NS solver OpenFOAM, Siddiqui et al. (2018) showed good agreement between experiments and simulations for the fluid flow inside a damaged ship compartment with forced oscillatory heave motion in 2D. In this case the weak coupling scheme was applicable because there were no incident waves.

1.4 Present Work

1.4.1 Method and Analysis

The present research is carried out numerically and is mainly performed with potential-flow theory, in which the water is assumed to be incompressible, inviscid and irrotational (Faltinsen, 1993). Surface tension is neglected. The free surface is defined to be a single-valued function, so that overturning waves cannot be modelled. However, these are not considered of major importance for the global effects studied here. Since potential-flow theory is applied, viscous effects are neglected, although linear and quadratic damping can be included in order to approximate viscous damping loads. This can e.g. be relevant in the case of a ship with small bilge radius or with bilge keels, where flow separation from the bilge may result in considerable viscous roll damping.

The HPC method is used to solve the governing equation for the velocity potential and combined with a Runge-Kutta scheme for the time evolution of the solution. In order to model the generation of steep waves by a wavemaker as well as wave-body interactions accurately, solely using Cartesian grids with constant geometry, the HPC method is combined with an immersed boundary method (IBM) and with overlapping computational domains in a novel way. The latter means that a DD approach is adopted between potential-flow solutions obtained in different Cartesian grids using different reference frames. This is illustrated by Figure 1.4 a) for the case of a floating body in waves. In a restricted computational domain surrounding the body, the potential-flow solution is solved in a grid that moves and rotates with the body using a body-fixed coordinate system. The solution in this domain is coupled with the solution in a stationary background domain that includes the majority of the water region and where the governing equations are solved in an Earth-fixed inertial coordinate system. In this way, the grid spacing in the two domains can be chosen individually, so that local flow effects near the body can be accounted for in a computationally efficient manner. A similar type of DD is used to model the wave generation by a moving wavemaker. The resulting method has been systematically validated and verified. Several wave-propagation problems, involving various non-linear features, are first considered. A wave-radiation problem involving a heaving circular cylinder in still water is thereafter investigated, where non-linearity is partly due to the non-wall sided geometry of the structure through the waterline. Then, we consider a wave-diffraction problem where a ship section in beam-sea waves is restrained from moving. The non-linear features of this problem, which are also part of the physical investigation, arise from steep waves interacting with a fixed body. Finally, the same ship section is studied as freely floating in beam-sea waves. In this case, the non-linearities are both from the incident waves and from induced body motions, especially near resonance conditions.

The proposed DD strategy, based on overlapping grids, can also be applied for the coupling between the HPC potential-flow method and a Navier-Stokes solver. This is useful for investigating the relevance of viscous-flow effects in the wave-body interactions, and is illustrated in Figure 1.4 b). Here, a viscous-flow solution applies in a restricted domain surrounding the body, and is coupled with

the potential-flow solution in the background domain. When a strong coupling is performed with another solver that has different assumptions, solution variables and numerical features, the exchanged information must be made consistent with the receiving solver. This is a crucial challenge as reported by Colicchio et al. (2006). In this thesis, a DD strategy using the single-phase (water) LS-NS solver documented in Colicchio et al. (2011) is proposed, where the viscous problem is also solved on a stationary Cartesian grid using an Earth-fixed inertial reference frame. The LS technique is adopted to capture the free-surface deformation and the body motions in the NS solver.

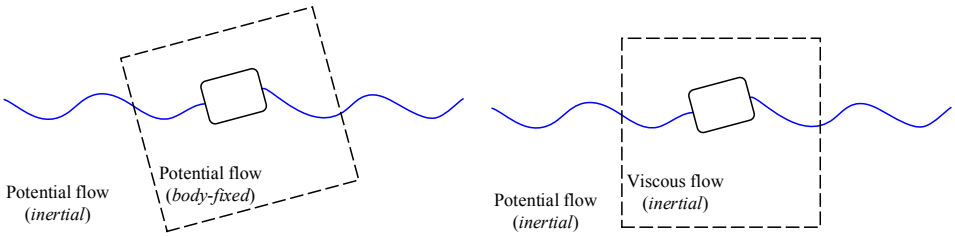

(a) Pure potential flow (b) Potential-viscous flow

Figure 1.4: Illustration of DD strategies to deal with wave-body interaction in the proposed numerical method.

It is emphasized that the pure potential-flow method is used for the physical investigations presented in this thesis. For the potential-viscous flow method, the details of the coupling strategy are introduced, and the exchange of information between the two solvers is examined for a simple wave-propagation case. The objective here is to outline a solution strategy to deal with viscous effects in an efficient manner as a basis for future work.

Whereas the present work is carried out strictly in 2D, the numerical method is developed with future 3D applications in mind. It is anticipated that both the immersed-boundary modelling and the overlapping between different computational domains can be extended to 3D.

1.4.2 Main Contributions

A complete list of the contributions of the present work is given towards the end of the thesis, among which the most important are summarized below. In relation to the numerical method, the following contributions are highlighted:

- A novel numerical solution method, combining the HPC method with an immersed boundary method and overlapping grids has been proposed. The method preserves the spatial accuracy of the HPC method while allowing for local refinement of the fluid flow in wave-propagation and wave-body interaction problems in a computationally efficient manner.
- A domain-decomposition strategy has been proposed to couple the potential-flow solver with a Navier-Stokes solver in order to account for localized viscous effects, where they matter, in an efficient manner. The cou-

pling is strong and the exchange of information between the solvers is handled through an overlapping zone that includes the free surface. A fully non-linear formulation is used everywhere.

From the systematic investigation of a 2D floating body in waves, the following main findings were made:

- Inconsistent handling of a non-linear term in the body-boundary condition for the time derivative of the velocity potential solved through an auxiliary hydrodynamic boundary value problem, strongly influences the mean wave drift force when wave-frequency motions are large. The wave-frequency motions were on the other hand insignificantly affected. This is important to be aware of when validating and verifying similar numerical methods.
- By adding quadratic roll damping near resonance, the reduced roll motions did not necessarily give a more linear behaviour. In particular, the relative decrease of the 1^{st} order sway force was stronger than that of the 2^{nd} order component. In general, strong coupling effects between the different modes of motion occurred near heave and roll resonance.
- The normalized mean wave drift force near heave and roll resonance was larger than unity, which is the maximum value predicted by 2^{nd} order theory. For higher wave frequencies, the mean wave drift force was significantly lower than predicted by 2^{nd} order theory, but in qualitative agreement with experiments. These observations were explained by non-linear effects.
- Contrary to statements made by other authors, the mean wave drift force for the 2D floating body in waves was most accurately estimated from the method of direct pressure integration. In this framework, the use of a consistent formulation for the boundary value problem of the time derivative of the velocity potential is essential. Moreover, it was seen that using weakly non-linear methods based on conservation of fluid momentum gave inaccurate estimates of the mean wave drift force. This is important to be aware of in connection with non-linear numerical simulations.

1.4.3 Outline of the Thesis

The thesis is built up of eight chapters organized in the following way:

Chapter 1 introduces the motivation and objective of the present study. An overview of some relevant previous works is given, and the present numerical solution strategy is outlined.

Chapter 2 gives the theoretical background related to body-fixed reference frames and potential-flow theory. The formulation of potential-flow problems in inertial and body-fixed reference frames is discussed.

Chapter 3 gives a brief introduction to the HPC method, and explains in detail the proposed numerical implementation. Techniques used to accelerate the computational speed, including suggestions for further improvement, are

discussed.

Chapter 4 provides validation and verification of the numerical method for various non-linear wave-propagation problems including steep and nearly breaking waves and shallow-water waves. A systematic investigation of the numerical accuracy and convergence properties is presented.

Chapter 5 presents numerical results for a heaving circular cylinder in initially still water, and for periodic waves interacting with a fixed ship section. These are considered as validation and verification studies for non-linear radiation and diffraction, respectively.

Chapter 6 presents an in-depth investigation of a freely floating ship section in beam-sea waves. Non-linear effects influencing the mean wave drift force are emphasized. Furthermore, different methods to estimate the mean wave drift force are investigated.

Chapter 7 proposes a domain-decomposition method to couple the potential-flow solver with an existing viscous-flow solver. The exchange of information between the two solvers is examined for a simple wave-propagation case.

Chapter 8 summarizes the present study and gives suggestions for further work.

1.4.4 List of Publications

As part of this thesis, the following papers have been published:

Conference Papers

- Hanssen, F.-C. W., Greco, M., and Shao, Y.-L. (2015). The Harmonic Polynomial Cell Method for Moving Bodies Immersed in a Cartesian Background Grid. *ASME 34th International Conference on Ocean, Offshore and Arctic Engineering*.
- Hanssen, F.-C. W., Greco, M., and Faltinsen, O. M. (2017). Wave-Body Interaction with Overlapping Structured Grids in the HPC Method. *The 32nd International Workshop on Water Waves and Floating Bodies*.
- Hanssen, F.-C. W., Colicchio G., and Greco, M. (2019). Severe Wave-Body Interactions: a Potential-Flow HPC Method and its Strong Domain-Decomposition Coupling with a Level-Set Navier-Stokes Solver. *The 34th International Workshop on Water Waves and Floating Bodies*.

Journal Papers

- Hanssen, F.-C., Bardazzi, A., Lugni, C., and Greco, M. (2017). Free-Surface Tracking in 2D with the Harmonic Polynomial Cell Method: Two Alternative Strategies. *International Journal for Numerical Methods in Engineering*. This

paper was awarded the Moan-Faltinsen Best Paper Award on Marine Hydrodynamics in 2017.

- Ma, S., Hanssen, F.-C. W., Siddiqui, M. A., Greco, M., and Faltinsen, O. M. (2017). Local and Global Properties of the Harmonic Polynomial Cell Method: In-Depth Analysis in Two Dimensions. *International Journal for Numerical Methods in Engineering*.

The following co-authored paper, where a modified version of the numerical solver developed in the present work is used, is considered as additional background:

- Tong, C., Shao, Y.-L., Hanssen, F.-C. W., Li, Y., Xie, B., and Lin, Z. (2019). Numerical Analysis on the Generation, Propagation and Interaction of Solitary Waves by a Harmonic Polynomial Cell Method. *Wave Motion*.

Chapter 2

Theoretical Framework

In the following, fundamental concepts used in the numerical implementation are introduced, starting with a dedicated explanation of the use of inertial and body-fixed reference frames. In particular, body-fixed reference frames are used to model the local potential flow near a moving wavemaker and rigid bodies. In this context, it is essential to be aware of how a body-fixed reference frame differs from an inertial reference frame. This is particularly important when working with physical laws, such as Newton's 2^{nd} law, that are originally formulated in the inertial reference frame. Finally, the governing equations of potential-flow theory are outlined.

2.1 A Note on Inertial and Non-Inertial Reference Frames

In this and the following chapter, the terms *inertial coordinate system* and *inertial reference frame* are frequently referred to. An inertial reference frame is a non-accelerating, non-rotating reference frame. We here take the Earth-fixed reference frame as an inertial reference frame, because the time scale of the problems dealt with throughout the present work is much smaller than that of the Earth's rotation (Faltinsen and Timokha, 2009). In contrast, a body-fixed reference frame is a *non-inertial*, accelerated reference frame.

2.2 Body-Fixed Reference Frames

A 2D body that is free to move in all degrees of freedom in waves is considered. As shown in Figure 2.1, an inertial Oxz coordinate system is defined with origin in the calm free surface, and a body-fixed $ox_{bf}z_{bf}$ coordinate system is defined with origin in the body's center of rotation. The center of rotation is here taken to coincide with the center of gravity[1]. Both the Oxz and $ox_{bf}z_{bf}$ coordinate systems are right-handed, Cartesian coordinate systems. The rotation of the $ox_{bf}z_{bf}$ coordinate system with respect to the Oxz coordinate system is denoted by the angle α, where α is positive for rotation in clockwise direction.

[1] As noted by Faltinsen and Timokha (2009), the rotational center is generally a time-dependent quantity.

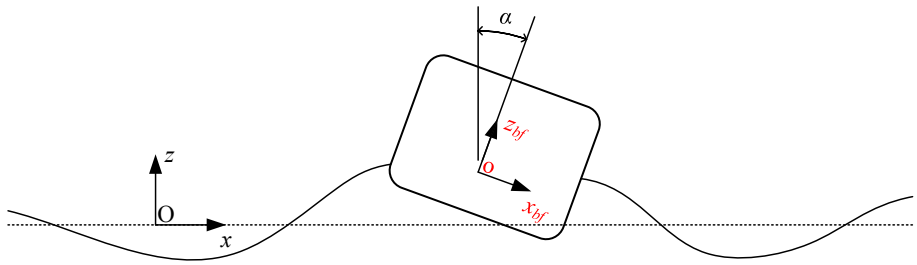

Figure 2.1: Definition of inertial Oxz and body-fixed $ox_{bf}z_{bf}$ coordinate systems.

A point $\boldsymbol{P} = (x_p, z_p)$ defined in the inertial Oxz coordinate system can be expressed in the body-fixed coordinate system by a two-step coordinate transformation consisting of

1. a coordinate displacement, where $\boldsymbol{P}$ is expressed in a coordinate system with origin coinciding with the $ox_{bf}z_{bf}$ system but with axes parallel to the Oxz system
2. a coordinate rotation, where the coordinates are projected onto the axes of the body-fixed coordinate system.

In order to illustrate the latter, a situation where the origins of the Oxz and $ox_{bf}z_{bf}$ systems coincide is considered. We define a rotation matrix

$$\boldsymbol{\Lambda}(\alpha) = \begin{pmatrix} cos\alpha & sin\alpha \\ -sin\alpha & cos\alpha \end{pmatrix}, \tag{2.1}$$

where α is a rotation given in radians and positive in clockwise direction. Then the point with coordinates $\boldsymbol{P} = (x_p, z_p)$ in the Oxz system has body-fixed coordinates $\boldsymbol{P}_{bf} = (x_{p,bf}, z_{p,bf})$ given by

$$\boldsymbol{P}_{bf} = \boldsymbol{\Lambda}_{i\to b} \cdot \boldsymbol{P}, \tag{2.2}$$

where $\boldsymbol{\Lambda}_{i\to b} = \boldsymbol{\Lambda}(-\alpha)$. A point $\boldsymbol{P}_{bf} = (x_{p,bf}, z_{p,bf})$ in the body-fixed coordinate system correspondingly has coordinates

$$\boldsymbol{P} = \boldsymbol{\Lambda}_{b\to i} \cdot \boldsymbol{P}_{bf} \tag{2.3}$$

in the inertial coordinate system, where $\boldsymbol{\Lambda}_{b\to i} = \boldsymbol{\Lambda}(\alpha)$.

When transforming the time derivative of a vector between inertial and non-inertial reference frames, one must also account for the time-rate of change of the unit vectors in the non-inertial coordinate system. Put in another way, because α generally is a time-dependent variable, so is $\boldsymbol{\Lambda}$:

$$\dot{\boldsymbol{P}} = \boldsymbol{\Lambda}_{b\to i} \cdot \dot{\boldsymbol{P}}_{bf} + \dot{\boldsymbol{\Lambda}}_{b\to i} \cdot \boldsymbol{P}_{bf}. \tag{2.4}$$

The overdot here means time derivative relative to the coordinate system that the quantity is defined in, i.e. $\dot{\boldsymbol{P}}$ and $\dot{\boldsymbol{P}}_{bf}$ are the time derivatives of $\boldsymbol{P}$ and $\boldsymbol{P}_{bf}$ in the inertial and body-fixed reference frames, respectively. In principle, the components of a time-derivative vector may be projected along the axes of a different

coordinate system than the reference frame in which the time derivative is taken. This is sometimes beneficial from a practical viewpoint when working with mixed reference frames. As an example, $\mathbf{\Lambda}_{b\to i} \cdot \dot{\boldsymbol{P}}_{bf}$ is a projection of $\dot{\boldsymbol{P}}_{bf}$ along the axes of the inertial coordinate system, but still a time derivative taken in the body-fixed reference frame.

2.2.1 Notation

Working with time derivatives of vectors in a mixture of inertial and body-fixed reference frames, as we will do in the following, it is instructional to define some general rules of notation. With $\boldsymbol{s}$ as an arbitrary vector, which can be defined in any coordinate system, we have that

- $d\boldsymbol{s}/dt$ is the time derivative of $\boldsymbol{s}$ in the inertial reference frame
- $\dot{\boldsymbol{s}}$ is the time derivative of $\boldsymbol{s}$ in the reference frame where it is defined
- a subscript bf explicitly means that the vector is projected along the axes of the body-fixed $ox_{bf}z_{bf}$ coordinate system.

It follows that if $\boldsymbol{s}$ is a vector defined in the body-fixed reference frame, $\ddot{\boldsymbol{s}}_{bf}$ is the double time derivative of $\boldsymbol{s}$ in the body-fixed reference frame, and with vector components projected along the unit axes of the $ox_{bf}z_{bf}$ coordinate system. We are in principle free to project this vector onto the axes of the inertial Oxz coordinate system, $\mathbf{\Lambda}_{b\to i} \cdot \ddot{\boldsymbol{s}}_{bf}$, but from (2.4) it is clear that the magnitude of this vector is not the same as the magnitude of the double time derivative of $\boldsymbol{s}$ in the inertial reference frame.

2.2.2 Kinematics

We now consider a point P on the surface of a moving, rigid body in Figure 2.2 defined by a position vector $\boldsymbol{r}$ relative to the origin of the body-fixed $ox_{bf}z_{bf}$ coordinate system. The corresponding position vector in the inertial Oxz coordinate system is

$$\boldsymbol{R} = \boldsymbol{R}_0 + \boldsymbol{r}, \tag{2.5}$$

where $\boldsymbol{R}_0$ is the position vector of the origin of the body-fixed coordinate system. We let the vectors $\boldsymbol{R}_0$ and $\boldsymbol{r}$ be defined in the body-fixed reference frame.

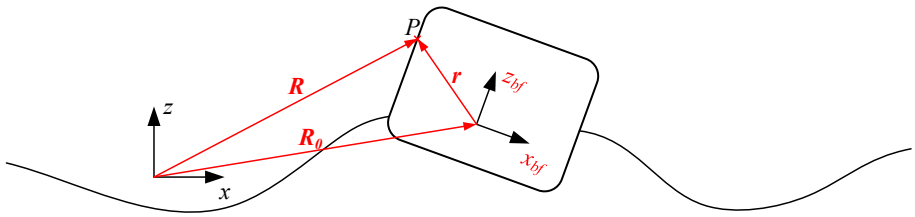

Figure 2.2: Definition of a point P in the inertial Oxz and body-fixed $ox_{bf}z_{bf}$ reference frames.

The velocity of the point P in the inertial reference frame is obtained by taking the time derivative of (2.5),

$$\frac{d\boldsymbol{R}}{dt} = \frac{d\boldsymbol{R}_0}{dt} + \frac{d\boldsymbol{r}}{dt} = \dot{\boldsymbol{R}}_0 + \dot{\boldsymbol{r}} + \boldsymbol{\omega} \times \boldsymbol{r}, \tag{2.6}$$

where $\dot{\boldsymbol{R}}_0$ and $\dot{\boldsymbol{r}}$ are the time derivatives of $\boldsymbol{R}_0$ and $\boldsymbol{r}$ in the body-fixed reference frame. $\boldsymbol{\omega}$ is the angular velocity vector, that in the present 2D framework is given as $\boldsymbol{\omega} = \dot{\alpha}\boldsymbol{j}$ with $\boldsymbol{j}$ the unit vector in y-direction. Obviously, the left- and right-hand sides of (2.6) must be projected along the unit axes of the same coordinate system in order for the relation to hold true. Note that (2.6) is only valid if the origin of the body-fixed coordinate system coincides with the body's center of rotation.

As explained by Faltinsen and Timokha (2009), the term $\boldsymbol{\omega} \times \boldsymbol{r}$ is due to the time-rate of change of axis unit vectors in the body-fixed coordinate system. This term is related to the expression defined in (2.4) through

$$\dot{\boldsymbol{\Lambda}}_{b\to i} \cdot \boldsymbol{s} = \boldsymbol{\Lambda}_{b\to i} \cdot (\boldsymbol{\omega} \times \boldsymbol{s}), \tag{2.7}$$

with $\boldsymbol{s}$ as an arbitrary vector. This relation is given by Shao (2010), who presents a comprehensive overview of the governing equations of rigid-body motions described in a body-fixed reference frame. It is also useful to note that, since $\boldsymbol{\omega} \times \boldsymbol{\omega} = \boldsymbol{0}$ in 2D, the angular velocity is independent of reference frame.

By taking the time derivative of (2.6), the acceleration of the point P in the inertial reference frame is found as

$$\frac{d^2\boldsymbol{R}}{dt^2} = \ddot{\boldsymbol{R}}_0 + \boldsymbol{\omega} \times \dot{\boldsymbol{R}}_0 + \ddot{\boldsymbol{r}} + \dot{\boldsymbol{\omega}} \times \boldsymbol{r} + 2\boldsymbol{\omega} \times \dot{\boldsymbol{r}} + \boldsymbol{\omega} \times (\boldsymbol{\omega} \times \boldsymbol{r}), \tag{2.8}$$

where $\dot{\boldsymbol{\omega}} = \ddot{\alpha}\boldsymbol{j}$ and all the individual time derivatives on the right-hand side are relative to the body-fixed reference frame.

If P is a fixed point on the body boundary, we have that $\dot{\boldsymbol{r}} = \ddot{\boldsymbol{r}} = \boldsymbol{0}$, so that (2.6) and (2.8) simplify to

$$\frac{d\boldsymbol{R}}{dt} = \dot{\boldsymbol{R}}_0 + \boldsymbol{\omega} \times \boldsymbol{r}, \tag{2.9}$$

$$\frac{d^2\boldsymbol{R}}{dt^2} = \ddot{\boldsymbol{R}}_0 + \boldsymbol{\omega} \times \dot{\boldsymbol{R}}_0 + \dot{\boldsymbol{\omega}} \times \boldsymbol{r} + \boldsymbol{\omega} \times (\boldsymbol{\omega} \times \boldsymbol{r}). \tag{2.10}$$

2.2.3 The Equations of Motions

The motions of a floating rigid body are governed by the body's equations of motion. The equation of translational motion follows from Newton's 2^{nd} law, which by definition is formulated in the inertial reference frame,

$$\boldsymbol{M} \cdot \frac{d^2\boldsymbol{R}_0}{dt^2} = \boldsymbol{F}_{ext}. \tag{2.11}$$

Here, $\boldsymbol{M}$ is the mass matrix with by the body's mass M along its diagonal as the only non-zero elements, $\boldsymbol{F}_{ext}$ is the external force vector, which is the sum of all loads acting on the body including its weight, and $d^2\boldsymbol{R}_0/dt^2$ is the acceleration of the center of gravity in the inertial reference frame.

Now we instead let the position of the body's center of gravity, which coincides with the origin of the body-fixed coordinate system, be defined in the body-fixed reference frame as $\boldsymbol{R}_{0,bf}$. By using (2.10), and noting that $\boldsymbol{r} = \boldsymbol{0}$, the equation of translational motion written in the body-fixed reference frame is

$$\boldsymbol{M} \cdot (\ddot{\boldsymbol{R}}_{0,bf} + \boldsymbol{\omega} \times \dot{\boldsymbol{R}}_{0,bf}) = \boldsymbol{F}_{ext,bf}. \tag{2.12}$$

$\dot{\boldsymbol{R}}_{0,bf}$ is here the body's translational velocity in the body-fixed reference frame, equal to the inertial-reference frame velocity projected along the axes of the body-fixed coordinate system. The body's translational acceleration in the body-fixed reference frame, $\ddot{\boldsymbol{R}}_{0,bf}$, is the time derivative of $\dot{\boldsymbol{R}}_{0,bf}$ estimated in the body-fixed reference frame. $\boldsymbol{F}_{ext,bf}$ is the external force vector projected along the axes of the body-fixed reference, i.e. $\boldsymbol{F}_{ext,bf} = \boldsymbol{\Lambda}_{i\to b} \cdot \boldsymbol{F}_{ext}$.

The equation of rotational motion follows from Euler's law of angular motion, which states that the change of angular momentum of a body in the inertial reference frame is equal to the external moments acting on it. Defining the rotational inertia matrix as $\boldsymbol{I}$ and the total external moment vector as $\boldsymbol{M}_{ext}$, this is written as

$$\boldsymbol{I} \cdot \dot{\boldsymbol{\omega}} + \boldsymbol{\omega} \times (\boldsymbol{I} \cdot \boldsymbol{\omega}) = \boldsymbol{M}_{ext}. \tag{2.13}$$

In 3D, the term $\boldsymbol{\omega} \times (\boldsymbol{I} \cdot \boldsymbol{\omega})$ means that the body has a time-varying inertia, representing a challenge in numerical simulations. It was shown by Shao (2010) that instead formulating the problem in the body-fixed reference frame, this time-dependence is avoided. In 2D, the inertia matrix is reduced to an inertia vector $\boldsymbol{I} = I_{yy}\boldsymbol{j}$, where I_{yy} is the body's moment of inertia about the y-axis. Furthermore, it was noted in Section 2.2.2 that $\boldsymbol{\omega} \times \boldsymbol{\omega} = \boldsymbol{0}$, and consequently the equation of rotational motion in 2D simplifies to

$$I_{yy}\dot{\boldsymbol{\omega}} = \boldsymbol{M}_{ext}. \tag{2.14}$$

Here, $\boldsymbol{M}_{ext} = M_y\boldsymbol{j}$ with M_y the total external moment on the body about the y-axis. (2.14) applies irrespective of reference frame.

2.2.4 Time Derivatives of Scalar Quantities

Thus far we have discussed how velocity and acceleration vectors in an inertial and a body-fixed reference frame are related. However, as explained by Faltinsen and Timokha (2009), care must also be taken for time derivatives of scalar quantities. We consider a general, time-dependent scalar quantity q and define D_{BO}/Dt as the time derivative performed following the rigid-body motions. D_{BO}/Dt therefore corresponds to a Lagrangian-type time derivative in the inertial reference frame and to an Eulerian time derivative in the body-fixed reference frame. The time derivative of q in a point fixed in the body-fixed coordinate system and with position vector $\boldsymbol{r}$ is then given as

$$\frac{D_{BO}q}{Dt} = \frac{\partial q}{\partial t} + (\dot{\boldsymbol{R}}_0 + \boldsymbol{\omega} \times \boldsymbol{r}) \cdot \nabla q, \tag{2.15}$$

where $\partial q/\partial t$ is the Eulerian time derivative of q, i.e. the time derivative of q in a fixed point in the inertial coordinate system. This relation plays a central role in

the implicit coupling of potential-flow variables between computational regions modelled in different reference frames in a domain decomposition, as well as in computing the fluid pressure in the body-fixed reference frame.

2.3 Potential-Flow Theory

The full theory of potential flow is outlined in e.g. the textbooks by Newman (1977) and Faltinsen (1993). Here we only repeat the most fundamental relations, before focusing in more detail on aspects that are relevant for the fully non-linear numerical implementation deployed in the present work.

2.3.1 Fundamentals

For an incompressible fluid, the continuity equation can be written as

$$\nabla \cdot \boldsymbol{V} = 0, \tag{2.16}$$

where $\boldsymbol{V}$ is the fluid velocity vector. If the fluid in addition is inviscid and irrotational, the velocity field can be described as the gradient of a velocity potential φ. In a 2D problem with principal axes x and z, we may thus write the fluid velocity vector as

$$\boldsymbol{V}(x,z,t) = \nabla\varphi(x,z,t). \tag{2.17}$$

Inserting (2.17) into (2.16) we get the Laplace equation for the velocity potential,

$$\nabla^2\varphi(x,z,t) = 0. \tag{2.18}$$

This equation is the governing equation to be solved in a potential-flow problem, and is valid in both an inertial and non-inertial reference frame.

2.3.2 Fluid Pressure

In the inertial reference frame, the total pressure $P(x,z,t)$ in any point in the fluid is given by the Bernoulli equation as

$$P(x,z,t) + \rho(\frac{\partial\varphi}{\partial t} + \frac{1}{2}|\nabla\varphi|^2 + gz) = C(t), \tag{2.19}$$

where g is the acceleration of gravity, ρ is the water density and z is the vertical coordinate in the inertial Oxz coordinate system and positive in upward direction. Throughout the present work, z is defined with origin in the still water line (as indicated in Figure 2.1). By setting the constant $C(t)$ equal to the atmospheric pressure p_{atm}, the excess pressure relative to the atmospheric pressure becomes

$$p(x,z,t) = P(x,z,t) - p_{atm} = -\rho(\frac{\partial\varphi}{\partial t} + \frac{1}{2}|\nabla\varphi|^2 + gz). \tag{2.20}$$

From (2.15) it follows that the fluid pressure evaluated in a body-fixed reference frame is

$$p(x_{bf},z_{bf},t) = -\rho(\frac{D_{BO}\varphi}{Dt} - \boldsymbol{u}_b \cdot \nabla\varphi + \frac{1}{2}|\nabla\varphi|^2 + gz) \tag{2.21}$$

with $\boldsymbol{u}_b = \dot{\boldsymbol{R}}_0 + \boldsymbol{\omega} \times \boldsymbol{r}$ and $\boldsymbol{r} = (x_{bf}, z_{bf})$. It is noted that z in the right-hand side of (2.21) is the vertical coordinate in the inertial reference frame.

2.3.3 Boundary Value Problem for φ

The Laplace equation (2.18) can be solved mathematically by specifying a set of appropriate conditions along the boundaries of the fluid domain. Formally, the boundary value problem (BVP) can be stated as

$$\begin{array}{lll} \nabla^2\varphi = 0 & \text{in} & \Omega \\ \varphi = \varphi_{\partial\Omega} & \text{on} & \partial\Omega_D \\ \frac{\partial\varphi}{\partial n} = \frac{\partial\varphi}{\partial n}_{\partial\Omega} & \text{on} & \partial\Omega_N \end{array} , \tag{2.22}$$

where $\varphi_{\partial\Omega}$ refers to specified values of φ on Dirichlet boundaries $\partial\Omega_D$ and $\partial\varphi/\partial n_{\partial\Omega}$ refers to specified values of the normal derivative of φ on Neumann boundaries $\partial\Omega_N$. Figure 2.3 illustrates the fluid domain Ω for the case of a floating body with Dirichlet boundaries consisting of the free surface S_{SF} and Neumann boundaries consisting of the body boundary S_B, the sea bed S_{Seabed}, the vertical side walls S_{Wall} and the wavemaker S_{WM}. The specific boundary conditions on each of these boundaries are outlined below.

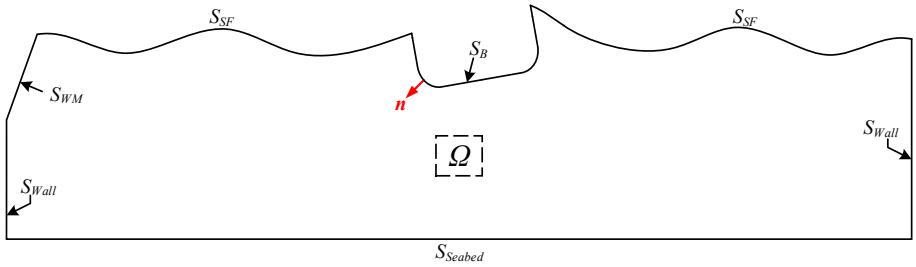

Figure 2.3: Fluid domain Ω for velocity-potential BVP bounded by the free surface S_{SF}, body boundary S_B, sea bed S_{Seabed}, vertical tank walls S_{Wall} and wavemaker S_{WM}. The normal vector $\boldsymbol{n}$ is positive pointing into Ω.

Free-Surface Boundary Conditions

Along S_{SF}, the dynamic free-surface condition (DFSC) follows from requiring the pressure to be equal to the atmospheric pressure [2], and the kinematic free-surface condition (KFSC) follows from requiring that a fluid particle on the free surface remains on the free surface. The free-surface elevation is denoted ζ, so that the coordinates of a point on the free surface are given by $(x, \zeta(x,t))$ in the inertial reference frame. Furthermore, we define the Lagrangian time derivative $\delta/\delta t = \partial/\partial t + \boldsymbol{v} \cdot \nabla$ to express the free-surface boundary conditions in the inertial

[2] Assuming that the effect of surface tension is negligible (Faltinsen and Timokha, 2009)

reference frame as

$$\begin{aligned} \frac{\delta\varphi}{\delta t} &= -\frac{1}{2}|\nabla\varphi|^2 - gz + \boldsymbol{v}\cdot\nabla\varphi - \nu(x,t)(\varphi-\varphi_{ref}) \\ \frac{\delta\zeta}{\delta t} &= \frac{\partial\varphi}{\partial z} + (\boldsymbol{v}-\nabla\varphi)\cdot\nabla\zeta - \nu(x,t)(\zeta-\zeta_{ref}) \end{aligned} \quad \text{on} \quad S_{SF}. \tag{2.23}$$

Choosing the velocity $\boldsymbol{v}$ as $\boldsymbol{v}=\boldsymbol{0}$ corresponds to an Eulerian description, $\boldsymbol{v}=\nabla\varphi$ corresponds to a fully Lagrangian description and $\boldsymbol{v}=(0,\partial\zeta/\partial t)$ corresponds to a semi-Lagrangian description.

Similarly, the free-surface conditions may be formulated in the body-fixed reference frame as

$$\begin{aligned} \frac{\delta'\varphi}{\delta' t} &= -\frac{1}{2}|\nabla\varphi|^2 - gz + (\boldsymbol{u}_b+\boldsymbol{v}')\cdot\nabla\varphi - \nu(x,t)(\varphi-\varphi_{ref}) \\ \frac{\delta'\zeta}{\delta' t} &= (\frac{\partial\varphi}{\partial z} - \boldsymbol{u}_b\cdot\boldsymbol{k}) + (\boldsymbol{u}_b+\boldsymbol{v}'-\nabla\varphi)\cdot\nabla\zeta - \nu(x,t)(\zeta-\zeta_{ref}) \end{aligned} \quad \text{on} \quad S_{SF}, \tag{2.24}$$

where $\delta'/\delta' t$ is defined as $D_{BO}/Dt + \boldsymbol{v}'\cdot\nabla$ with D_{BO}/Dt defined in (2.15), $\boldsymbol{u}_b$ is defined in connection with (2.21) and $\boldsymbol{v}'$ is a velocity relative to the body-fixed coordinate system. In particular, choosing $\boldsymbol{v}'=\boldsymbol{0}$ leads to an Eulerian formulation for a fixed point in the body-fixed coordinate system, while $\boldsymbol{v}'=(0,\delta'\zeta/\delta' t)$ leads to a semi-Lagrangian formulation in the body-fixed reference frame. $(\partial\varphi/\partial z - \boldsymbol{u}_b\cdot\boldsymbol{k})$ is a fluid velocity relative to the moving body-fixed reference frame in the same direction as $\boldsymbol{k}$, where $\boldsymbol{k}$ is the unit vector in z-direction. (2.24) can in principle be specified with ζ and vectors projected along the axes of either the inertial or body-fixed coordinate system. In practice, however, it is natural to use the latter formulation as will be done in (3.15) in Section 3.2.1.

In a fully Lagrangian description, the formulation in the inertial reference frame in (2.23) is generally more practical than a body-fixed formulation. A further discussion of the latter is thus omitted.

$\nu(x,t)$ in (2.23) and (2.24) is a damping coefficient associated with dissipation zones towards the ends of the domain, and is therefore zero elsewhere. φ_{ref} and ζ_{ref} are reference values for the velocity potential and wave elevation, respectively. These will be discussed later.

The DFSC and KFSC are used in a time-marching scheme to update respectively the position of, and velocity potential on, the free surface. The latter is imposed as a Dirichlet condition in the BVP for φ.

Neumann Boundary Conditions

Along Neumann boundaries, the following impermeability condition is set for the normal velocity $\partial\varphi/\partial n$:

$$\nabla\varphi\cdot\boldsymbol{n} = \boldsymbol{U}\cdot\boldsymbol{n} \quad \text{on} \quad \{S_B, S_{Seabed}, S_{Wall}, S_{WM}\}. \tag{2.25}$$

Here, $\boldsymbol{n}$ is the normal vector defined in Figure 2.3. The velocity of the boundary $\boldsymbol{U}$ is zero along S_{Seabed} and S_{Wall}. The boundary condition in (2.25) applies in both the inertial and body-fixed reference frames, with vectors and the gradient operator decomposed along the same unit axes.

2.3.4 Boundary Value Problem for Time Derivative of φ

In order to evaluate the fluid pressure from the Bernoulli equation, the term $\partial\varphi/\partial t$ in (2.20), or equivalently $D_{BO}\varphi/Dt$ in (2.21), must be obtained. The most straightforward way to do this is through a finite difference method. Although this strictly speaking is a numerical technique, it is instructive to discuss it in the present theoretical context. If we consider two consecutive time instances t and $t + \Delta t$, a 1^{st} order backward finite-difference estimate for the time derivative of φ in the inertial reference frame is

$$\frac{\partial\varphi}{\partial t} \approx \frac{\varphi(x, z, t + \Delta t) - \varphi(x, z, t)}{\Delta t}, \tag{2.26}$$

or in the body-fixed reference frame,

$$\frac{D_{BO}\varphi}{Dt} \approx \frac{\varphi(x_{bf}, z_{bf}, t + \Delta t) - \varphi(x_{bf}, z_{bf}, t)}{\Delta t}. \tag{2.27}$$

Higher-order backward finite-difference schemes can be constructed by using information from numerous consecutive time instances. However, as shown by Hanssen et al. (2015), such finite-difference schemes may produce spurious temporal oscillations in the fluid pressure and hence in the fluid loads on a body. In an immersed boundary method, these spurious oscillations are in particular related to grid nodes going in and out of the fluid domain due to rigid-body motions or free-surface deformations.

Alternatively, an auxiliary BVP can be formulated for the time derivative of φ. This method is adopted by e.g. Tanizawa (1995), Greco (2001), Koo and Kim (2004) and Sun (2007), to name a few, and is usually considered more accurate than the finite-difference approach. Moreover, it generally removes the risk of spurious pressure oscillations. The basis of the method lies in recognizing that the partial time derivative of the velocity potential, $\partial\varphi/\partial t \equiv \varphi_t$, satisfies a Laplace equation similar to (2.18), i.e.

$$\nabla^2\varphi_t(x, z, t) = 0. \tag{2.28}$$

By imposing appropriate Dirichlet and Neumann conditions, a BVP similar to (2.22) may thus be solved to obtain the φ_t field in the fluid. Furthermore, it is demonstrated by Greco (2001) that also $D_{BO}\varphi/Dt$ satisfies the Laplace equation and can be obtained from such auxiliary BVP. This means that the equation (2.28) can conveniently be solved for φ_t in the Earth-fixed inertial reference frame and for $D_{BO}\varphi/Dt$ in the body-fixed reference frame.

The appropriate boundary conditions for the BVP to be solved for the time derivative of φ are described in the following. Although elaborated more later on, it is noted that in the domain-decomposition method used in the present work, the choice of time derivative of φ solved for differs depending on reference frame.

Free-Surface Boundary Conditions

From Section 2.3.3 we have that the partial time derivative can be expressed as $\partial/\partial t = \delta/\delta t - \boldsymbol{v} \cdot \nabla$. Combining this with the DFSC in (2.23), the free-surface

boundary condition for φ_t becomes

$$\frac{\partial \varphi}{\partial t} = -\frac{1}{2}|\nabla\varphi|^2 - gz - \nu(x,t)(\varphi - \varphi_{ref}) \quad \text{on} \quad S_{SF}. \tag{2.29}$$

In the body-fixed reference frame, the equivalent boundary condition is

$$\frac{D_{BO}\varphi}{Dt} = -\frac{1}{2}|\nabla\varphi|^2 - gz + \boldsymbol{u}_b \cdot \nabla\varphi - \nu(x,t)(\varphi - \varphi_{ref}) \quad \text{on} \quad S_{SF}. \tag{2.30}$$

Neumann Boundary Conditions in the Inertial Reference Frame

To obtain the appropriate Neumann boundary conditions in the inertial reference frame, we take the Eulerian time derivative of (2.25):

$$\frac{\partial \nabla\varphi}{\partial t} \cdot \boldsymbol{n} + \nabla\varphi \cdot \frac{\partial \boldsymbol{n}}{\partial t} = \frac{\partial \boldsymbol{U}}{\partial t} \cdot \boldsymbol{n} + \boldsymbol{U} \cdot \frac{\partial \boldsymbol{n}}{\partial t}. \tag{2.31}$$

Since the boundaries S_B and S_{WM} in Figure 2.3 are handled in body-fixed reference frames, (2.31) is only relevant for the stationary boundaries S_{Seabed} and S_{Wall}. Here, both $\boldsymbol{U}$ and $\partial\boldsymbol{n}/\partial t$ are zero, so that the boundary condition reduces to

$$\nabla\varphi_t \cdot \boldsymbol{n} = 0 \quad \text{on} \quad \{S_{Seabed}, S_{Wall}\}. \tag{2.32}$$

In (2.32) we have used that $\partial(\nabla\varphi)/\partial t = \nabla(\partial\varphi/\partial t)$.

Neumann Boundary Conditions in Body-Fixed Reference Frames

We consider two types of body-fixed reference frames; one is the reference frame that follows the motion of the wavemaker, and the other is the reference frame that follows the motion of a rigid body. Figure 2.4 shows the two body-fixed coordinate systems with origin in the pivot point of the wavemaker and in the body's center of gravity, respectively. For sake of convenience, we hereafter refer to both the wavemaker and the rigid body simply as *body*, since their boundary conditions are similar.

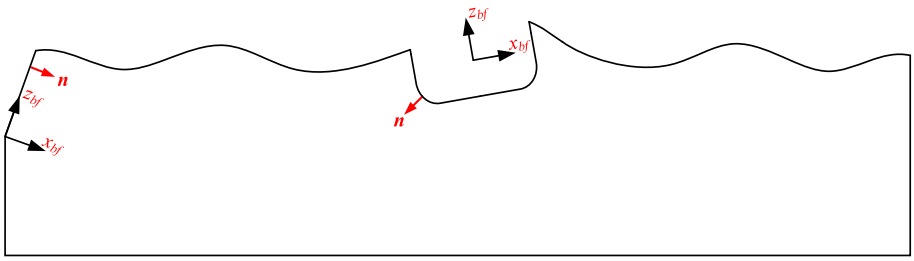

Figure 2.4: Body-fixed coordinate systems on body boundary S_B and wavemaker S_{WM}. The normal vector $\boldsymbol{n}$ is positive pointing into the fluid.

The velocity $\boldsymbol{U}$ in a point on the body is given as $\dot{\boldsymbol{R}}_0 + \boldsymbol{\omega} \times \boldsymbol{r}$, where $\boldsymbol{r}$ is a vector from the origin of the body-fixed coordinate system to the point. We now take the

time derivative following the motion of the body, D_{BO}/Dt, of (2.25) written in the body-fixed reference frame:

$$\frac{D_{BO}\nabla\varphi}{Dt}\cdot\boldsymbol{n}+\nabla\varphi\cdot\frac{D_{BO}\boldsymbol{n}}{Dt}=\frac{D_{BO}\boldsymbol{U}}{Dt}\cdot\boldsymbol{n}+\boldsymbol{U}\cdot\frac{D_{BO}\boldsymbol{n}}{Dt}. \tag{2.33}$$

The normal vector $\boldsymbol{n}$ is constant in the body-fixed reference frame, and (2.33) can thus be written out as

$$\frac{D_{BO}\nabla\varphi}{Dt}\cdot\boldsymbol{n}=\frac{D_{BO}(\dot{\boldsymbol{R}}_0+\boldsymbol{\omega}\times\boldsymbol{r})}{Dt}\cdot\boldsymbol{n}. \tag{2.34}$$

It was explained in Section 2.2.2 that $\boldsymbol{\omega}\times$ terms are related to the time-rate of change of unit vectors in the body-fixed coordinate system seen by an observer in the inertial reference frame. For an observer in the body-fixed reference frame, however, these unit vectors are constant. Thus, $\boldsymbol{\omega}\times$ terms do not apply for the left-hand side of (2.34). The final version of (2.34), that is imposed as Neumann condition in the body-fixed reference frame along S_B and S_{WM}, thus reads

$$\nabla\frac{D_{BO}\varphi}{Dt}\cdot\boldsymbol{n}=(\ddot{\boldsymbol{R}}_0+\dot{\boldsymbol{\omega}}\times\boldsymbol{r})\cdot\boldsymbol{n}\quad\text{on}\quad\{S_B,S_{WM}\}. \tag{2.35}$$

The change of operators from $D_{BO}(\nabla\varphi)/Dt$ to $\nabla(D_{BO}\varphi/Dt)$ is discussed in Appendix A.

Several different formulations of the body-boundary condition used in the BVP for the time derivative of φ can be found in the literature, see e.g. the comprehensive comparison done by Bandyk and Beck (2011). As it will be shown in Chapter 6, the way in which this boundary condition is imposed may in particular have a significant effect on mean wave drift loads when $\boldsymbol{\omega}$ is large.

2.4 Summary

Key aspects for body-fixed reference frames have been introduced, with particular focus on time derivatives of vector and scalar quantities. A brief introduction to potential-flow theory was given, before formally stating the boundary value problems to be solved for the velocity potential φ, as well as for the time derivative of φ. The latter is required in order to evaluate the fluid pressure.

The theoretical framework introduced here is used as basis for the numerical implementation described in the next chapter.

Chapter 3

Numerical Implementation

In the previous chapter, theoretical aspects related to the use of inertial and body-fixed reference frames and the formulation of the hydrodynamic boundary value problems (BVP) of potential-flow theory were stated. We now proceed to use these in the implementation of a fully non-linear numerical wave tank (NWT) in 2D.

The harmonic polynomial cell (HPC) method, that is used as a solver for the potential-flow BVPs, is first introduced. It is shown how the HPC method is implemented together with two modelling concepts, namely treating moving boundaries as immersed boundaries, and using overlapping grids in a domain-decomposition strategy. These two represent novel applications of the HPC method, making it versatile in dealing with arbitrary boundary geometries and refining the numerical solution locally without deforming the computational grid. The objective of introducing these concepts is to obtain a numerical method that is accurate yet efficient. The computational efficiency of any numerical method is a major factor affecting its practical relevance, and is thus addressed in a dedicated section. Suggestions for future enhancement of the computational efficiency are given.

3.1 The Harmonic Polynomial Cell Method

The harmonic polynomial cell (HPC) method was proposed by Shao and Faltinsen (2012, 2014b) as an accurate and efficient numerical method for the Laplace equation in potential-flow problems. We here use their formulation, denoted as the *classical* formulation, in 2D. This is explained in the following.

3.1.1 The Classical Formulation of the HPC Method in 2D

In contrast with the more traditional boundary element method (BEM), where only boundaries are discretized, the HPC method is a field method where the entire computational domain is discretized. The domain is divided into overlapping, quadrilateral cells as shown in Figure 3.1, where also an arbitrary located global Oxz coordinate system, that can be either inertial or non-inertial, is indicated. Each cell is made up of eight nodes along its boundaries, where the global

horizontal and vertical indices of a node are denoted (i, k). Each cell has a local cell-fixed coordinate system $o\overline{x}\overline{z}$ with origin in the interior node, which is a boundary node in any of the eight overlapping cells. We here consider that the axes of the $o\overline{x}\overline{z}$ and Oxz systems are parallel, i.e. we operate with a Cartesian grid.

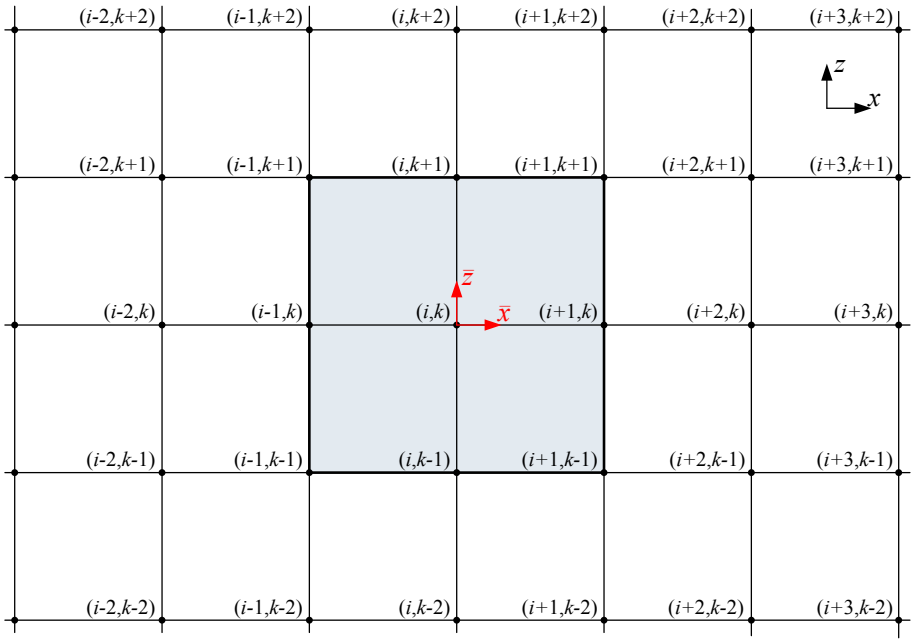

Figure 3.1: HPC grid consisting of nodes with global indices (i, k) and overlapping cells. Each cell has a local cell-fixed coordinate system $o\overline{x}\overline{z}$. Oxz is an arbitrary global coordinate system.

Figure 3.2 shows a square, quadrilateral cell, where the boundary nodes are given local indices $1 - 8$. The interior node has local node index 9, and its global position is given as $\boldsymbol{P}_9 = (x_9, z_9)$. For any point P within the cell with global coordinates $\boldsymbol{P} = (x_P, z_P)$, the local coordinates $\overline{\boldsymbol{P}} = (\overline{x}_P, \overline{z}_P)$ in the cell-fixed coordinate system are given as $\overline{\boldsymbol{P}} = \boldsymbol{P} - \boldsymbol{P}_9$.

Everywhere inside a cell, the velocity potential is represented as a linear combination of the velocity potentials in the boundary nodes, $\varphi_i, i = 1, ..., 8$,

$$\varphi\left(\overline{x}, \overline{z}\right) = \sum_{i=1}^{8} \left[\sum_{j=1}^{8} c_{j,i} f_j\left(\overline{x}, \overline{z}\right) \right] \varphi_i. \tag{3.1}$$

The fluid velocity vector is given as the gradient of (3.1),

$$\nabla\varphi\left(\overline{x}, \overline{z}\right) = \sum_{i=1}^{8} \left[\sum_{j=1}^{8} c_{j,i} \nabla f_j\left(\overline{x}, \overline{z}\right) \right] \varphi_i. \tag{3.2}$$

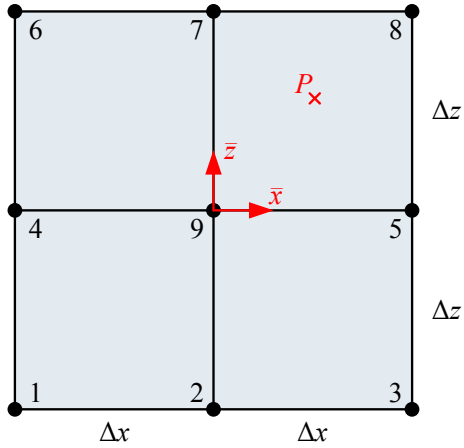

Figure 3.2: A square, quadrilateral cell with grid spacing Δx and Δz in x and z direction, respectively. The eight boundary nodes have local indices $1-8$, and a local cell-fixed coordinate system $o\overline{x}\overline{z}$ is defined with origin in the interior node with local index 9.

Here, $f_j(\overline{x},\overline{z})$ is either the real or imaginary part of the complex n^{th} order harmonic polynomial $(\overline{x}+i\overline{z})^n$ with $i=\sqrt{-1}$. $c_{j,i}$ is an element of the inverse of the matrix $\boldsymbol{D}$ with elements $d_{i,j}=f_j(\overline{x}_i,\overline{z}_i)$, where $(\overline{x}_i,\overline{z}_i)$ are the coordinates of the i^{th} boundary node. Because the harmonic polynomials satisfy the Laplace equation (2.18), so does automatically the velocity potential expressed through (3.1).

The same set of harmonic polynomials as used by Shao and Faltinsen (2012) are chosen. These are listed in Table 3.1, representing the complete set of harmonic polynomials up to 3^{rd} order, and an incomplete set up to 4^{th} order. Because of this, we can expect the expression (3.1) to have between 3^{rd} and 4^{th} order spatial accuracy. The expected spatial accuracy of the fluid velocity $\nabla\varphi$ in (3.2) is one order lower than that of φ. The choice of harmonic polynomials to be included is investigated by Ma et al. (2018), where it is concluded that the present set is the best choice for an eight-node cell.

Table 3.1: List of harmonic polynomials $f_j(\overline{x},\overline{z})$ defined by the real and imaginary parts of $(\overline{x}+i\overline{z})^n$.

n	Real part	Imaginary part
0	$f_1(\overline{x},\overline{z})=1$	
1	$f_2(\overline{x},\overline{z})=\overline{x}$	$f_3(\overline{x},\overline{z})=\overline{z}$
2	$f_4(\overline{x},\overline{z})=\overline{x}^2-\overline{z}^2$	$f_5(\overline{x},\overline{z})=\overline{x}\overline{z}$
3	$f_6(\overline{x},\overline{z})=\overline{x}^3-3\overline{x}\overline{z}^2$	$f_7(\overline{x},\overline{z})=3\overline{x}^2\overline{z}-\overline{z}^3$
4	$f_8(\overline{x},\overline{z})=\overline{x}^4-6\overline{x}^2\overline{z}^2+\overline{z}^4$	

It is clear from Table 3.1 that in the origin of the local cell-fixed coordinate system, where $(\overline{x},\overline{z})=(0,0)$, all the polynomials other than f_1 are zero. Applying

(3.1), the velocity potential in the interior cell node is thus expressed as

$$\varphi_9 = \varphi\left(\overline{x}_9, \overline{z}_9\right) = \sum_{i=1}^{8} c_{1,i}\varphi_i. \tag{3.3}$$

The expression in (3.3) can be regarded as a connectivity equation that ensures communication between the overlapping cells in the grid.

For the BVP of the Eulerian time derivative of φ described in Section 2.3.4, we take the time derivative of (3.1), (3.2) and (3.3). By noting that the harmonic polynomials $f_j(\overline{x}, \overline{z})$ are independent of time, the corresponding time derivatives in the inertial reference frame are

$$\varphi_t\left(\overline{x}, \overline{z}\right) = \sum_{i=1}^{8} \left[\sum_{j=1}^{8} c_{j,i} f_j\left(\overline{x}, \overline{z}\right)\right] \varphi_{t,i}, \tag{3.4}$$

$$\nabla\varphi_t\left(\overline{x}, \overline{z}\right) = \sum_{i=1}^{8} \left[\sum_{j=1}^{8} c_{j,i} \nabla f_j\left(\overline{x}, \overline{z}\right)\right] \varphi_{t,i} \tag{3.5}$$

and

$$\varphi_{t,9} = \varphi_t\left(\overline{x}_9, \overline{z}_9\right) = \sum_{i=1}^{8} c_{1,i}\varphi_{t,i}. \tag{3.6}$$

$\varphi_{t,i}$ is here the Eulerian time derivative of the velocity potential in the i^{th} boundary node.

3.1.2 Formulation in a Body-Fixed Reference Frame

Figure 3.3 shows a HPC grid with quadrilateral, square cells defined in a body-fixed $ox_{bf}z_{bf}$ coordinate system that is generally not aligned with the inertial Oxz coordinate system. If we now consider an arbitrary point P with body-fixed coordinates $\boldsymbol{P}_{bf} = (x_{p,bf}, z_{p,bf})$ within the highlighted cell, its coordinates in the cell-fixed $o\overline{xz}$ system are given as $\overline{\boldsymbol{P}} = \boldsymbol{P}_{bf} - \boldsymbol{P}_{9,bf}$ with $\boldsymbol{P}_{9,bf} = (x_{9,bf}, z_{9,bf})$ the coordinates of the interior cell node in the body-fixed coordinate system. This relation implies that $o\overline{xz}$ and $ox_{bf}z_{bf}$ are parallel coordinate systems.

It follows that (3.1) for the velocity potential, (3.2) for the fluid velocity vector and the connectivity equation (3.3) apply directly in the body-fixed reference frame. Some special considerations necessary for taking the time derivatives of these expressions are discussed next.

Time Derivative of φ in a Body-Fixed Reference Frame

The time derivative D_{BO}/Dt of a scalar quantity estimated in a point fixed in the body-fixed reference frame follows from (2.15). Applying this on both sides of (3.1), written for a cell defined in, and moving with, the body-fixed coordinate system, gives

$$\frac{D_{BO}\varphi(\overline{x}, \overline{z})}{Dt} = \sum_{i=1}^{8} \left[\sum_{j=1}^{8} c_{j,i} f_j\left(\overline{x}, \overline{z}\right)\right] \frac{D_{BO}\varphi_i}{Dt}, \tag{3.7}$$

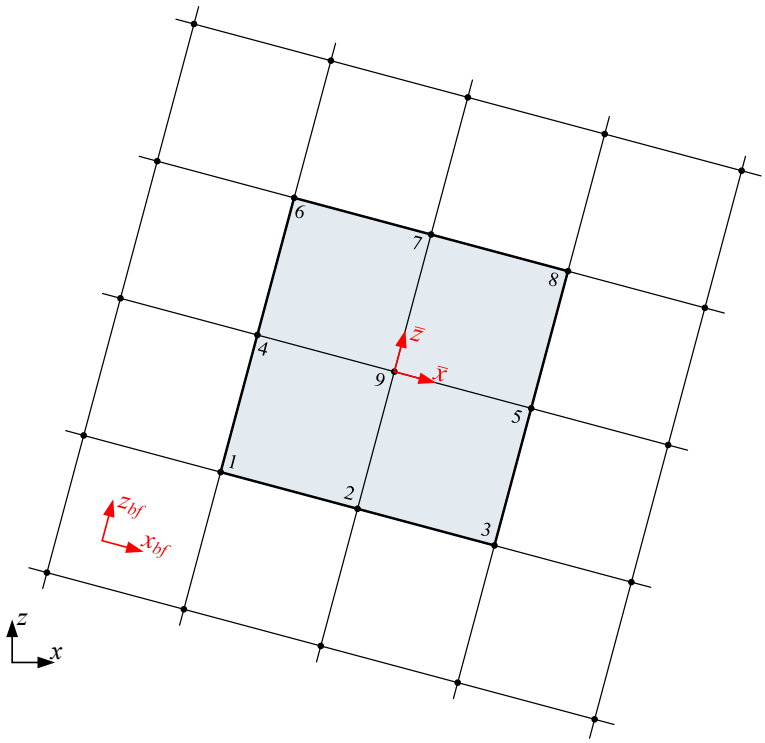

Figure 3.3: HPC grid in a body-fixed reference frame. Three coordinate systems are shown; an inertial Oxz system, a body-fixed $ox_{bf}z_{bf}$ system and a cell-fixed $o\overline{x}\overline{z}$ system. The cell-fixed coordinate system follows the motion of the cell's internal node, as well as the cell's rotation.

where $D_{BO}\varphi_i/Dt$ is the time derivative of the velocity potential in the i^{th} boundary node of the cell. It is noted that $D_{BO}f_j/Dt$ is zero, since $(\overline{x},\overline{z})$ is a fixed point in the body-fixed coordinate system.

The time derivative of the fluid velocity vector (3.2) can be evaluated as

$$\frac{D_{BO}\nabla\varphi(\overline{x},\overline{z})}{Dt} = \nabla\frac{D_{BO}\varphi(\overline{x},\overline{z})}{Dt} = \sum_{i=1}^{8}\left[\sum_{j=1}^{8} c_{j,i}\nabla f_j\left(\overline{x},\overline{z}\right)\right]\frac{D_{BO}\varphi_i}{Dt}, \tag{3.8}$$

which is further elaborated in Appendix A.

It follows from (3.7) that the time derivative of the connectivity equation (3.3) in the body-fixed reference frame is

$$\frac{D_{BO}\varphi_9}{Dt} = \frac{D_{BO}\varphi(\overline{x}_9,\overline{z}_9)}{Dt} = \sum_{i=1}^{8} c_{1,i}\frac{D_{BO}\varphi_i}{Dt}. \tag{3.9}$$

Equations (3.7), (3.8) and (3.9) are sufficient to enforce boundary conditions and continuity of the solution through the domain in a pure body-fixed formulation. However, in coupling the solution between domains, where the solution is

defined in a mixture of inertial and body-fixed reference frames, it is necessary to relate the time derivative in a fixed point in the body-fixed reference frame and the corresponding Eulerian time derivative in the inertial reference frame. This is done through

$$\begin{aligned}\frac{D_{BO}\varphi(\overline{x},\overline{z})}{Dt} =& \sum_{i=1}^{8}\left[\sum_{j=1}^{8} c_{j,i} f_j\left(\overline{x},\overline{z}\right)\right]\varphi_{t,i} + \\ & \boldsymbol{u}_b \cdot \sum_{i=1}^{8}\left[\sum_{j=1}^{8} c_{j,i}\nabla f_j\left(\overline{x},\overline{z}\right)\right]\varphi_i,\end{aligned} \tag{3.10}$$

where $\boldsymbol{u}_b$ is the rigid-body velocity of the point due to the motion of the body-fixed coordinate system. Similarly, the Eulerian time derivative in the inertial reference frame is expressed as

$$\begin{aligned}\frac{\partial\varphi(\overline{x},\overline{z})}{\partial t} =& \sum_{i=1}^{8}\left[\sum_{j=1}^{8} c_{j,i} f_j\left(\overline{x},\overline{z}\right)\right]\frac{D_{BO}\varphi_i}{Dt} - \\ & \boldsymbol{u}_b \cdot \sum_{i=1}^{8}\left[\sum_{j=1}^{8} c_{j,i}\nabla f_j\left(\overline{x},\overline{z}\right)\right]\varphi_i.\end{aligned} \tag{3.11}$$

Equations (3.10) and (3.11) are both required in a two-way coupling.

3.1.3 Algebraic Equation System

The hydrodynamic BVP of the velocity potential in Section 2.3.3 is established by using (3.1) and (3.2) to enforce the boundary conditions and (3.3) to enforce continuity through the fluid domain. This results in a global, algebraic equation system in the form

$$\boldsymbol{A}\cdot\boldsymbol{\varphi} = \boldsymbol{b}_{\varphi}. \tag{3.12}$$

Here, $\boldsymbol{A}$ is a global coefficient matrix, $\boldsymbol{\varphi}$ is a vector that contains the velocity potential of all grid nodes in the computational domain and $\boldsymbol{b}_{\varphi}$ is a vector with boundary conditions. $\boldsymbol{A}$ is generally sparse with nine or less non-zero entries in each row distributed along the main diagonal. Rows with some off-diagonal entries may occur when different computational regions are coupled within a DD approach. The matrix is however still essentially diagonally dominated.

Similarly, equations (3.4) - (3.6) for $\partial\varphi/\partial t$, and equations (3.7) - (3.9) for $D_{BO}\varphi/Dt$, are used to establish an algebraic equation system for the BVP of the time derivative of the velocity potential constituted in Section 2.3.4 in the form

$$\boldsymbol{A}\cdot\boldsymbol{\varphi}_t = \boldsymbol{b}_{\varphi_t}. \tag{3.13}$$

Here, $\boldsymbol{b}_{\varphi_t}$ is a vector that contains the fixed-point time derivative of the velocity potential in all grid nodes in the computational domain. For a node defined in the inertial reference frame, the corresponding vector entry is the Eulerian time

derivative ($\partial\varphi/\partial t$), and for a node defined in a body-fixed reference frame, it is the time derivative following the motion of the body ($D_{BO}\varphi/Dt$). As explained in Section 2.3.2, this difference is important to be aware of when evaluating the pressure from the Bernoulli equation, defined in the inertial reference frame in expression (2.20) and in the body-fixed reference frame in (2.21).

The coefficient matrix $\boldsymbol{A}$ in (3.13) is the same as in (3.12), which means that the computational effort in establishing (3.13) is restricted to populating the appropriate boundary-condition vector $\boldsymbol{b}_{\varphi_t}$.

3.2 Potential-Flow Solver based on the HPC Method

Wave-propagation and wave-body interaction problems involve boundaries that vary with time. These boundaries may have complex shapes and represent a challenge with respect to modelling, accuracy and computational efficiency of a numerical solution. The main goal here is to develop a method that enables modelling of arbitrary geometries while preserving numerical accuracy and efficiency within the framework of the HPC method.

Previous numerical implementations of the HPC method for non-linear wave problems by e.g. Shao and Faltinsen (2012, 2014a) apply surface-fitted grids, where the grid is stretched in vertical direction to conform with the deformation of the free surface. In wave-body interaction problems, where a body with arbitrary geometry may undergo large motions, it remains a challenge to deform the grid in a rational manner. It is foreseen that algorithms required to deform the grid increase the overall computational cost. Moreover, it means that the matrices $\boldsymbol{D}$ defined in Section 3.1.1 have to be built and inverted every time a cell is deformed. The cost of doing this for a single cell is small, but if the number of deforming cells is large, the total computational cost is still significant. Ma et al. (2018) showed that using cells with a high degree of distortion, either in terms of stretching or skewness, in the HPC method is penalized by a significant loss in numerical accuracy. Figure 3.4 illustrates the numerical error of φ and the components of $\nabla\varphi$ inside a single HPC cell subject to boundary conditions from an analytical solution that depends on both x and z. One finds that the highest accuracy is generally achieved when the cell is square or close to square, and that the accuracy in the HPC method is more sensitive to the cell geometry than e.g. the finite difference method (FDM). For further details regarding the analytical solution and an extended discussion of the HPC method's accuracy, reference is made to Ma et al. (2018). Experience made throughout the present work confirms that the risk of numerical instabilities developing in a time-integration scheme increases when the HPC cells are stretched.

To avoid the challenges related to boundary-fitted grids, and to be able to use grids with favourable cell shapes, we propose an immersed boundary method (IBM) to account for free-surface deformations and body motions. Combining the HPC method with an IBM was first attempted by Hanssen et al. (2015) to study the flow around a fixed and moving circular cylinder in uniform flow. The IBM used here is an enhanced version of that.

In certain fluid regions, it is necessary to refine the computational domain due

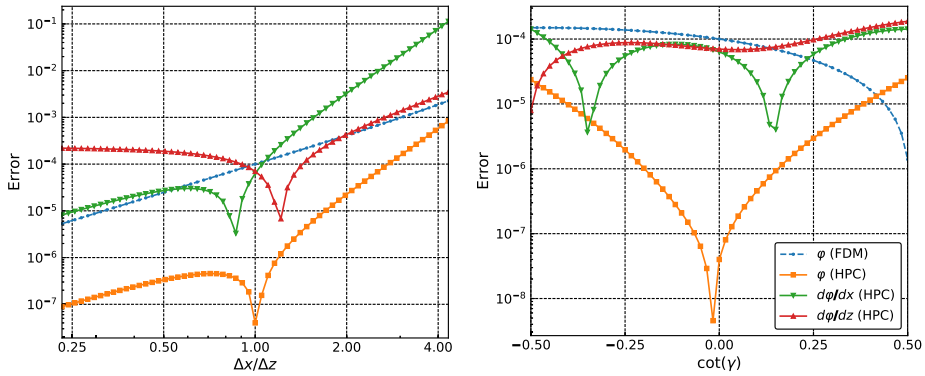

(a) Cell stretching

(b) Cell skewness

Figure 3.4: Numerical errors of φ and the components of $\nabla\varphi$ relative to an analytical solution in the center of a single cell documented by Ma et al. (2018). The errors are plotted as functions of the stretching, measured as the ratio between the horizontal and vertical grid spacing, and the skewness, measured by the angle γ between the vertical coordinate axis and the lateral cell boundaries. The results from a standard FDM are included for reference.

to e.g. large body motions or free-surface deformations, curvature in the body geometry or large changes of the velocity vectors. In order to allow for such local refinement, without compromising the square-like shape of grid cells and without increasing the number of total grid cells unnecessarily, the idea of overlapping grids is adopted. This, along with the use of the IBM, is considered a novel application of the HPC method. The body-fixed grids are used to model a physical wavemaker and to model fixed or moving rigid bodies in the NWT. The governing equations in these regions are implemented in body-fixed reference frames. In doing this, the geometries of the body-fixed grids are constant in their respective body-fixed coordinate systems. These grids overlap with a fixed background grid that is defined in an inertial, Earth-fixed coordinate system. As it will be explained, due to the fact that the HPC method is formulated as an interpolation method with smoothly varying coefficients, the exchange of information between the different domains becomes natural.

Hereafter, we refer to the method combining the IBM with overlapping grids as an *IBOGM* (immersed boundary-overlapping grid method). A principal sketch of the computational domain for a general scenario with a flap-type wavemaker to generate propagating waves and a floating body in the tank is shown in Figure 3.5.

Since the free surface and rigid bodies are modelled as immersed boundaries, the instantaneous computational domain at any time is a subset of the total grid, with the remaining part of the grid denoted as *inactive*. The inactive region includes the parts of the background grid that are well inside any of the overlapping, body-fixed grids. The main steps of the IBOGM can be summarized as follows:

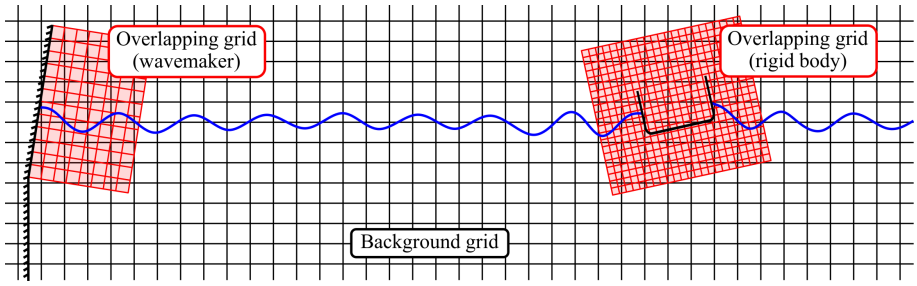

Figure 3.5: Principal sketch of computational domain used in the IBOGM consisting of a background grid and overlapping grids that move with the motion of the wavemaker and of a generic floating body, respectively.

1. At the start of a simulation, the background grid and the overlapping grids are generated in their respective coordinate systems, where the grids are structured and Cartesian.
2. The local HPC matrices $\boldsymbol{D}$ are computed for all cells in all grids and stored in memory. Since the grids remain constant in the coordinate systems where they are defined, these local matrices never need to be re-calculated.
3. The cells that belong to the instantaneous computational domain are identified.
4. The hydrodynamic BVPs are established and solved for φ and its time derivative in the instantaneous computational domain.
5. The solution is evolved forward in time.

Steps 1-2 are part of initialization and only performed once, while steps 3-5 are repeated until the end of the simulation.

In the following sections, the implementation of the hydrodynamic BVPs of φ and its time derivative outlined in Sections 2.3.3 and 2.3.4 is described in more detail. The modelling of a free surface and a body boundary are discussed separately, before the coupling between different computational domains, i.e. overlapping grids, is explained. The time-integration schemes used for the temporal evolution of the solution, the numerical damping zones for dissipation of waves and the smoothing techniques for the free surface are described.

3.2.1 Modelling of a Free Surface

The free surface is described by a set of discrete, evenly distributed massless markers. The markers' position and corresponding velocity potential are updated by time integrating the KFSC and DFSC introduced in Section 2.3.3. The position of a specific marker in the inertial and in a body-fixed reference frame is denoted $\boldsymbol{P}_m = (x_{P_m}, z_{P_m})$ and $\boldsymbol{P}_{m,bf} = (x_{P_m,bf}, z_{P_m,bf})$, respectively. The motion of the markers is either semi-Lagrangian, fully Lagrangian or a hybrid between the two.

Semi-Lagrangian Description for Free-Surface Markers

In a semi-Lagrangian time-evolution scheme, each solution domain has its own set of free-surface markers as illustrated in Figure 3.6. These are distributed so that their coordinates in the x or x_{bf}-direction coincide with the x or x_{bf} coordinate of the vertical grid lines[1], depending if they belong to the background grid or to an overlapping grid. This means that the markers' velocity component in the x-direction (or x_{bf}-direction) is set to zero. Hence, in the background grid, the DFSC and KFSC are defined in the inertial reference frame as

$$\begin{aligned}
\frac{\delta \varphi_{P_m}}{\delta t} &= -\frac{1}{2}|\nabla\varphi|^2 - gz + \frac{\delta z_{P_m}}{\delta t}\frac{\partial \varphi}{\partial z} - \nu(x,t)(\varphi - \varphi_{ref}) \\
\frac{\delta x_{P_m}}{\delta t} &= 0 \\
\frac{\delta z_{P_m}}{\delta t} &= \frac{\partial \varphi}{\partial z} - \frac{\partial \varphi}{\partial x}\frac{\partial \zeta}{\partial x} - \nu(x,t)(\zeta - \zeta_{ref}).
\end{aligned} \tag{3.14}$$

In contrast with the expression given in Section 2.3.3, the KFSC here also includes the horizontal velocity component of the marker, that is zero in the semi-Lagrangian description. This allows us to express the time evolution of the free surface marker's position in vectorial form, $\delta \boldsymbol{P}_m/\delta t = (\delta x_{P_m}/\delta t, \delta z_{P_m}/\delta t)$, which is convenient later in Section 3.2.10. All right-hand side terms of (3.14), previously explained in Section 2.3.3, are evaluated at the instantaneous position $\boldsymbol{P}_m$ of the marker. The free-surface slope $\partial\zeta/\partial x$ is evaluated from a 4^{th} order finite-difference scheme, or from a 3^{rd} order B-spline representation of the free-surface elevation.

In an overlapping grid, a marker's velocity relative to the body-fixed reference frame is defined as $\delta' \boldsymbol{P}_{m,bf}/\delta' t = (\delta' x_{P_m,bf}/\delta' t, \delta' z_{P_m,bf}/\delta' t)$. The DFSC and KFSC are then written as

$$\begin{aligned}
\frac{\delta' \varphi_{P_m}}{\delta' t} &= -\frac{1}{2}|\nabla_{bf}\varphi|^2 - gz + \boldsymbol{u}_{b,bf}\cdot\nabla_{bf}\varphi + \frac{\delta' z_{P_m,bf}}{\delta' t}\frac{\partial \varphi}{\partial z_{bf}} \\
&\quad - \nu(x,t)(\varphi - \varphi_{ref}) \\
\frac{\delta' x_{P_m,bf}}{\delta' t} &= 0 \\
\frac{\delta' z_{P_m,bf}}{\delta' t} &= (\frac{\partial \varphi}{\partial z_{bf}} - u_{b,z_{bf}}) + (u_{b,x_{bf}} - \frac{\partial \varphi}{\partial x_{bf}})\frac{\partial \zeta_{bf}}{\partial x_{bf}} - \nu(x,t)(\zeta - \zeta_{ref}).
\end{aligned} \tag{3.15}$$

The subscript bf is here used to explicitly state that variables and spatial derivatives are estimated along the axes of the body-fixed coordinate system. $\boldsymbol{u}_{b,bf}$ is the fixed-point velocity in $\boldsymbol{P}_m$ due to the motion of the body-fixed reference frame.

One should note that the terms associated with numerical damping zones, $\nu(x,t)(\varphi - \varphi_{ref})$ and $\nu(x,t)(\zeta - \zeta_{ref})$, as well as z in the DFSC, refer to the inertial coordinate system. This is because these terms are naturally defined in the inertial reference frame. Even though we here work in the body-fixed reference frame,

[1]The term *vertical grid line* in a body-fixed reference frame means a grid line parallel with the z_{bf} axis

the equivalent coordinates in the inertial coordinate system are known at all times from the relations defined in Section 2.2.

One important difference is emphasized between the semi-Lagrangian formulation in an inertial and in a body-fixed reference frame: In an inertial reference frame, the markers are forced to only move in the inertial z-direction. In a body-fixed reference frame, on the other hand, the markers are forced to move in the body-fixed z_{bf}-direction. The motion of a marker defined in a body-fixed reference frame is thus generally not parallel with the motion of a marker defined in the inertial reference frame.

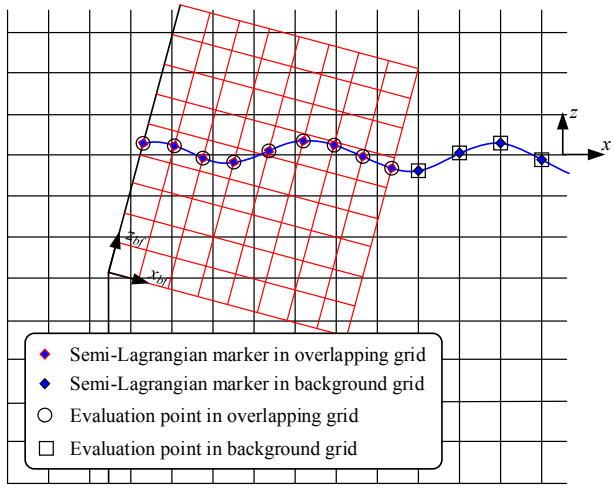

Figure 3.6: Semi-Lagrangian description of free-surface markers in an overlapping grid moving with the wavemaker and in the stationary background grid. The points where (3.14) and (3.15) are evaluated, i.e. the evaluation points, coincide with the position of the markers in the semi-Lagrangian description.

Fully Lagrangian Description for Free-Surface Markers

When the fully Lagrangian description is adopted, a single set of free-surface markers is used as shown in Figure 3.7. The markers do not belong to any specific grid, and are allowed to cross from an overlapping grid to the background grid and vice versa, with their evolution followed in the inertial reference frame. To prevent the markers from clustering together, we require them to be evenly distributed in the inertial x-direction. This is achieved by a re-initialization of the markers at every time step of a simulation. Moreover, an even spacing between the markers is convenient when using spatial filters to smooth the free surface. This is discussed later in Section 3.2.7. The temporal evolution of the free-surface markers is described in the inertial reference frame with DFSC and KFSC given as

$$\begin{aligned} \frac{D\varphi}{Dt} &= \frac{1}{2}|\nabla\varphi|^2 - gz - \nu(x,t)(\varphi - \varphi_{ref}) \\ \frac{D\boldsymbol{P}_m}{Dt} &= \nabla\varphi - \nu(x,t)(\zeta - \zeta_{ref})\boldsymbol{k}, \end{aligned} \tag{3.16}$$

where $\boldsymbol{k}$ is the unit vector in z-direction. Evaluating the gradient of φ at the exact marker position, with continuously changing horizontal coordinate, is found to easily cause numerical instabilities in the time evolution of the free surface. The way to overcome this is to estimate $\nabla\varphi$ in (3.16) through interpolation from the values of the fluid velocity at the intersection points between the free surface and vertical grid lines in either the background grid or in a body-fixed grid. The algorithm for doing this can be summarized as follows:

1. Represent the free-surface elevation with a 3^{rd} order B-spline.
2. Estimate $\nabla\varphi$ at the points where the free surface intersects vertical grid lines from (3.2).
3. Represent the components of $\nabla\varphi$ with 3^{rd} order B-splines and reconstruct $\nabla\varphi$ at the exact marker positions.

The fact that B-splines are used to represent the free-surface properties implies that the free surface must be a single-valued function. If a marker is inside one of the overlapping grids, the gradient of φ is taken in this grid, along the unit axes of the corresponding body-fixed coordinate system, and transformed to the inertial reference frame by means of a rotation matrix. Otherwise, the gradient is taken in the background grid along the unit axes of the inertial coordinate system.

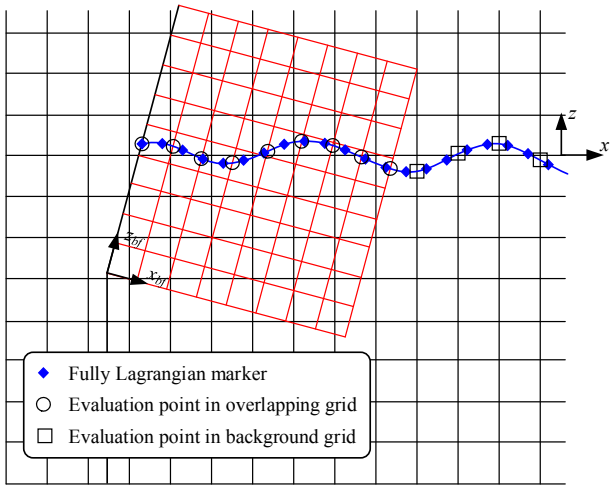

Figure 3.7: Fully Lagrangian description of free-surface markers. The points where (3.16) is evaluated in the overlapping grid and in the stationary background grid are indicated.

Hybrid Description for Free-Surface Markers

An advantage of adopting the semi-Lagrangian description for the motion of free-surface markers is that it is found less prone to develop numerical instabilities during time evolution of waves than the fully Lagrangian description. A drawback of using the semi-Lagrangian description in the IBOGM is that, with separate sets of markers in an overlapping grids and in the background grid, special

attention must be given to ensure the smoothness of the free surface across the intersection between grids. It also means that, depending on the instantaneous position of the overlapping grid, free-surface markers in the background grid may be activated or deactivated from one time instant to another. This requires some additional book-keeping in the numerical implementation. The fully Lagrangian description is attractive in the sense that it offers one continuous description of the free surface on either side of a surface-piercing body. Moreover, this description is generally required when dealing with non wall-sided bodies, because the free-surface markers at the wave-body intersections cannot separate from the body. Hence, the horizontal motion of these markers should not be subject to the restrictions involved in a semi-Lagrangian description.

As a compromise between the advantageous properties of the semi-Lagrangian and fully Lagrangian descriptions, the methods can be combined in a hybrid description. That is, close to moving boundaries, the description is fully Lagrangian, and is gradually transitioned to a semi-Lagrangian description away from the boundary. A single set of continuous markers are distributed on either side of a surface-piercing body, and the velocity of a single marker is given in the inertial reference frame with components

$$\begin{aligned} \frac{\delta x_{P_m}}{\delta t} &= \kappa(x)\frac{\partial \varphi}{\partial x} \\ \frac{\delta z_{P_m}}{\delta t} &= \frac{\partial \varphi}{\partial z} - (\kappa(x)-1)\frac{\partial \varphi}{\partial x}\frac{\partial \zeta}{\partial x} - \nu(x,t)(\zeta - \zeta_{ref}). \end{aligned} \tag{3.17}$$

$\kappa(x)$ is here a spatial ramp function. At x positions where $\kappa(x) = 1$, the description is fully Lagrangian, and at x positions where $\kappa(x) = 0$, the description is semi-Lagrangian. The scenario is illustrated in Figure 3.8.

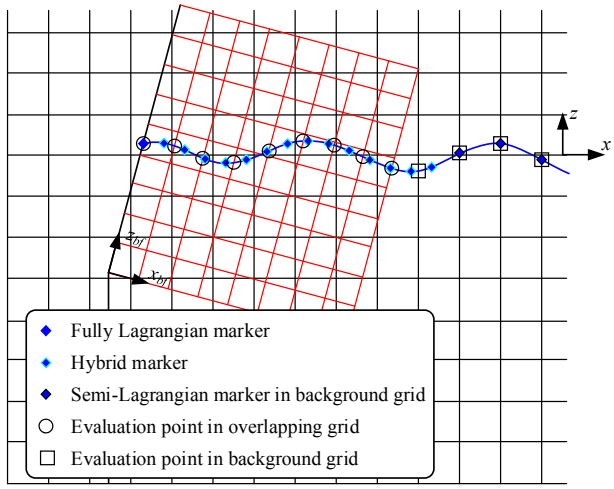

Figure 3.8: Hybrid between semi-Lagrangian and fully Lagrangian description of free-surface markers. The points where (3.17) is evaluated in the overlapping grid and in the stationary background grid are indicated.

An alternative version of (3.17) is to let $\kappa(x)$ be so that $\delta x_{P_m}/\delta t$ decays linearly from the value it has at the intersection points between the free surface and body boundary towards zero at the outer edge of the overlapping grid. This particular strategy is used in Chapter 5 to study a heaving circular cylinder.

Imposing Dirichlet Conditions on the Free Surface

The treatment of the free surface as an immersed boundary in a structured grid, tracked by markers, is explained hereafter. We consider a general scenario with fully Lagrangian markers in Figure 3.9. The approach is similar both if the grid represents the background grid or an overlapping grid. Three types of cells can be seen in the figure:

- *Active cells*: All cells that are part of the instantaneous computational domain.
- *Inactive cells*: All cells that are not part of the instantaneous computational domain.
- *Free-surface cells*: Subset of active cells where Dirichlet conditions for the free surface are imposed.

The upper nodes in the free-surface cells are denoted as free-surface ghost nodes. In interior fluid nodes, i.e. the internal nodes in all the active cells, the HPC connectivity equation (3.3) is enforced.

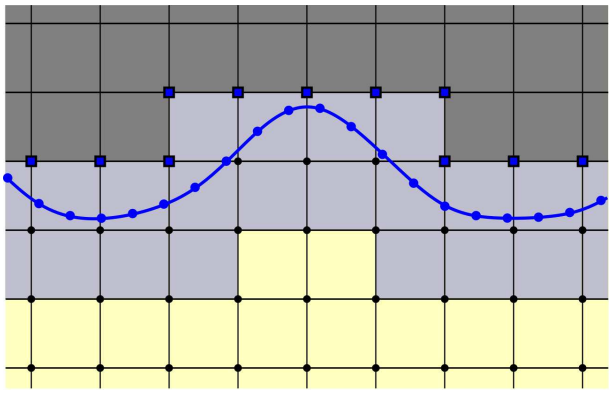

Figure 3.9: Free surface tracked by fully Lagrangian markers immersed in a structured grid defined either in an inertial or body-fixed coordinate system. Yellow and dark-grey cells indicate the active and inactive parts of the instantaneous computational domain. The grey-blue cells are cells used to impose Dirichlet conditions for the free surface, with free-surface ghost nodes (blue squares with black border) in the upper part. The black nodes below the free surface are internal fluid nodes where the connectivity equation (3.3) is enforced.

The steps necessary to identify the instantaneous computational domain in connection with a free surface are illustrated in Figure 3.10, starting from the configuration of the free surface (a), that is given by the position of the free-surface

markers. The free-surface elevation is then interpolated at the positions of vertical grid lines by fitting a B-spline through the markers (b). This step is omitted if the markers are semi-Lagrangian, since in this case they always move along the vertical grid lines. Along each vertical grid line, the first node above the free surface is identified (c). This is taken as a ghost node, and the cell where the node has local node index 7 (with reference to Figure 3.2) is a free-surface cell. If the grid line coincides with a vertical wall, or if the node to the left or right is not part of the instantaneous computational domain, the cell where the node has local index 6 or 8 is selected instead. All cells up to and including the free-surface cell are active, and the cells above the free-surface cell are inactive. The interior nodes in all active cells are identified as nodes where the HPC connectivity equation (3.3) is enforced. The final step (d) consists in a check of the free-surface cells, to detect any inactive nodes above the free surface (such as *Node 1* in *Cell 1* and *Node 2* in *Cell 2*). These nodes are set as ghost nodes to complete the equation system.

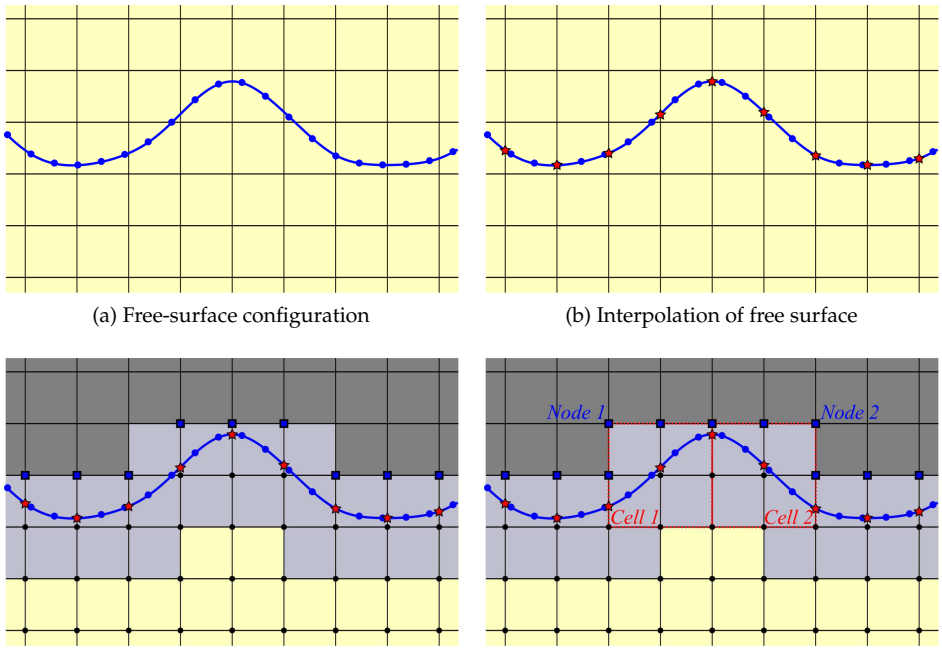

(a) Free-surface configuration

(b) Interpolation of free surface

(c) Identification of cell and node types

(d) Additional free-surface ghost nodes

Figure 3.10: Procedure for identification of cell and node types near the free surface in a time-varying computational domain. *Node 1* and *Node 2* are additional ghost nodes associated with *Cell 1* and *Cell 2*, respectively.

It is found beneficial from a stability viewpoint to evaluate the free-surface conditions represented by (3.14) - (3.17) at the intersection points between the free surface and vertical grid lines identified by red stars in Figure 3.10 (b). It is found equally important that the Dirichlet conditions for the velocity potential and its time derivative in the hydrodynamic BVPs are imposed at the same intersection

points. If we denote the coordinates of one of these points as $\boldsymbol{P}_{fs} = (x_{fs}, z_{fs})$, and the corresponding values of the velocity potential and its Eulerian time derivative as respectively φ_{fs} and $\varphi_{t,fs}$, the imposed boundary conditions are

$$\sum_{i=1}^{8} \left[\sum_{j=1}^{8} c_{j,i} f_j \left(\overline{x}_{fs}, \overline{z}_{fs} \right) \right] \varphi_i = \varphi_{fs} \tag{3.18}$$

and

$$\sum_{i=1}^{8} \left[\sum_{j=1}^{8} c_{j,i} f_j \left(\overline{x}_{fs}, \overline{z}_{fs} \right) \right] \varphi_{t,i} = \varphi_{t,fs}. \tag{3.19}$$

φ_{fs} is obtained by B-spline interpolation through the actual free-surface markers in the same way as for the free-surface elevation. Once the BVP of φ has been solved, $\varphi_{t,fs}$ can be evaluated from (2.29). The expressions (3.18) and (3.19) are evaluated in each of the free-surface cells defined in connection with Figure 3.10, where $(\overline{x}_{fs}, \overline{z}_{fs})$ are the corresponding coordinates in the cell-fixed coordinate system. The point $(\overline{x}_{fs}, \overline{z}_{fs})$ is generally taken as the intersection between the free surface and the vertical grid line through the ghost node. When two ghost nodes are located along the same vertical grid line, such as the situation arising due to the additional ghost nodes *Node 1* and *Node 2* in Figure 3.10 (d), the boundary condition for the same intersection point is thus set twice. However, since the boundary condition is imposed in two different cells, the resulting matrix system never becomes singular. The number of resulting free-surface Dirichlet conditions in the global matrix system, expressed in terms of equations (3.18) and (3.19), is equal to the number of free-surface ghost nodes. It is emphasized that these boundary conditions apply at the exact location of the free surface, and not at the positions of the ghost nodes. The values of φ and φ_t at the ghost nodes are considered unknown and found from the solution of the corresponding BVPs.

If the boundary condition for the time derivative of φ is instead enforced in an overlapping grid, the Eulerian time derivative in (3.19) must be exchanged with the time derivative D_{BO}/Dt of φ_{fs} following the motion of the overlapping grid evaluated from (2.30).

3.2.2 Modelling of a Body Boundary

The boundary of a surface-piercing body is modelled as an immersed boundary in an overlapping, body-fixed grid following the motion of the body. This means that, relative to the overlapping grid, the configuration of the body remains constant in time. The geometry of the body is described by a set of discrete points, and the normal vector is defined outwards. The configuration of the grid with a free surface and a portion of the body boundary is illustrated in Figure 3.11, where the nodes and cell types associated with the free surface have already been defined in Figure 3.9. The only difference is that here the free surface conditions must be enforced also at the wave-body intersection points, i.e. not only at the free-surface points intersected by vertical grid lines.

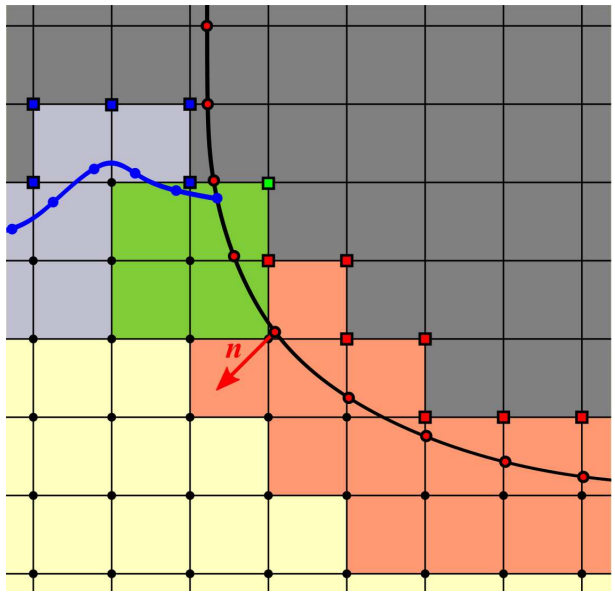

Figure 3.11: Free surface and body boundary immersed in a body-fixed grid. The body geometry is described by a set of discrete points with outwards surface normal vector $\boldsymbol{n}$. In addition to the node and cell types defined in Figure 3.9, the red-shaded cells, associated with ghost nodes (red squares with black border) inside the body, are used to enforce Neumann boundary conditions on the body boundary. The green-shaded cell is associated with the double node (green square with black border), used to enforce the boundary conditions for the free surface and body boundary simultaneously for the wave-body intersection point.

In order to account for the body as an immersed boundary, ghost nodes are identified inside the body. Since the configuration remains constant in the body-fixed reference frame, the possible ghost nodes need only to be identified once during initialization of the simulation. The procedure for doing this is illustrated in Figure 3.12, where a portion of the body, with the geometry described by a few discrete points, is immersed in the body-fixed grid (a). Only the points that are used to impose the body-boundary condition are here shown. A higher density of points is in practice used to describe the body geometry accurately. All grid nodes inside the body surface are identified, and those with at least one of their eight surrounding nodes outside the body, are labelled as ghost nodes (b). The interior nodes that are not ghost nodes constitute a grid region always inactive, i.e. never part of the instantaneous computational domain. Finally, appropriate cells for the ghost nodes are identified. These cells can never contain any inactive grid nodes, which means that there are only a few valid options for each ghost node. The cells are here generally taken as the cells where the vector pointing from the particular ghost node to the cell center is closest to being parallel with the normal vector in the body-boundary point nearest the ghost node. This strategy is found to select cells to be associated with ghost nodes in a logical manner for

the body geometries studied here. However, it is anticipated that other strategies for selecting the prioritized order of the possible cells that can be associated with the ghost nodes may be equally good. A reasonable choice of ghost cells is found to be characterized by that the ghost cells, if possible, overlap with surrounding ghost cells, and have the majority of the cell area located outside of the body.

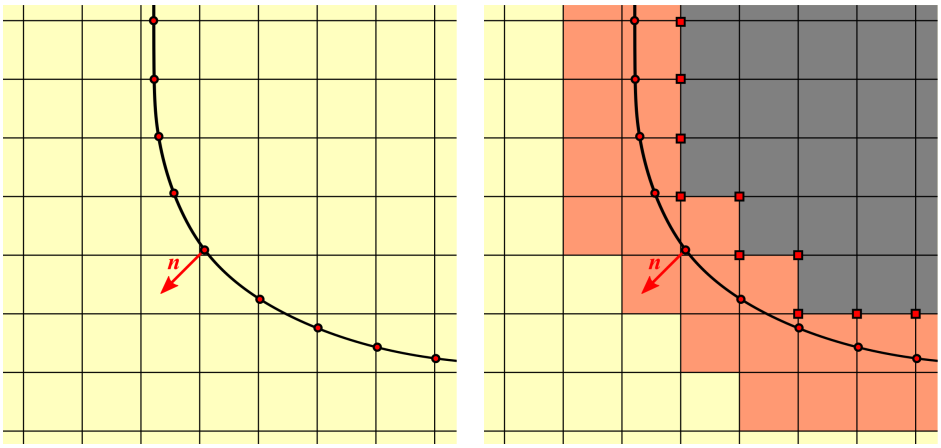

(a) Initial configuration (b) Ghost nodes and associated cells

Figure 3.12: Procedure for identification of ghost nodes and associated cells. $\boldsymbol{n}$ is an outwards normal vector that is constant in the body-fixed coordinate system following the motion of the body.

We now consider the scenario when a time-varying free surface is introduced. Starting from Figure 3.12 (b), the stepwise procedure for identification of nodes and cells is illustrated in Figure 3.13. The steps related to the free surface away from the body boundary have already been discussed in Figure 3.10, and are only dealt with briefly. Figure 3.13 (a) shows the body boundary, including ghost nodes and associated cells, together with the free surface that is tracked by fully Lagrangian markers. The points where the free-surface boundary conditions are enforced are first identified (b). In addition to the intersection with vertical grid lines, the intersection points between the free surface and body boundary are added. The appropriate free-surface cells and ghost nodes are identified (c), together with the cells used to enforce both the Neumann conditions on the body boundary and the free-surface Dirichlet conditions simultaneously in the wave-body intersection points. The simultaneous enforcement of the two conditions is achieved through a double-node technique, with details discussed later in the text. The double node is in the figure indicated with a green square with black border. In general, the double node is taken as the first body-boundary ghost node that is above the free-surface intersection point. The cells used to enforce the double-node boundary conditions (green-shaded), are as a general rule taken as the cells where the relevant double node is in one of the upper corners. That means, depending on if the wave-body intersection point is to the right or to the left of the

node, the cell where the double node has either local node index 6 or 8 is selected. In this way, the cell associated with the double node is so that it maximizes the cell area inside the physical domain (i.e. below the free surface and outside of the body). All nodes above the double node are set as inactive in the instantaneous computational domain. In the final step (d), additional free-surface ghost nodes are added if this is required. That is, if any of the active cells associated with the free surface include inactive nodes above the free surface, these are added as free-surface ghost nodes in the same way as explained in Figure 3.10 (d).

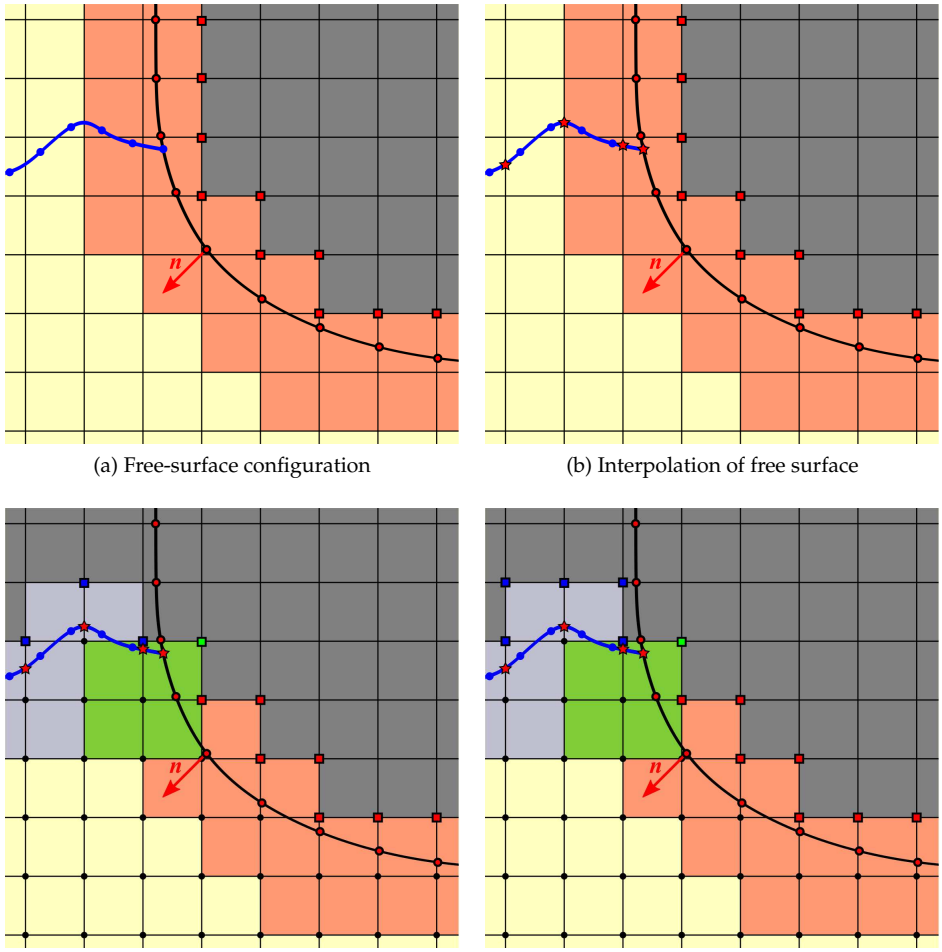

(a) Free-surface configuration

(b) Interpolation of free surface

(c) Identification of cell and node types

(d) Additional free-surface ghost nodes

Figure 3.13: Procedure for identification of cell and node types relative to instantaneous free surface and body boundary in a body-fixed grid.

Having determined the instantaneous ghost nodes inside the body and associated cells, we can enforce Neumann conditions on the body boundary. The

number of body-boundary conditions is equal to the number of instantaneous body-boundary ghost nodes plus the number of double nodes. As a general rule, the boundary condition is enforced at the body-boundary point closest to the center of the associated cell and that is below the free surface. Special care is taken to ensure that the same point is not used twice in the same cell, which would lead to a singular matrix system. We denote the coordinates of a point on the body boundary where boundary conditions are imposed as $\boldsymbol{P}_{b,bf} = (x_{b,bf}, z_{b,bf})$. The subscript bf is here used because the boundary condition is always imposed in a body-fixed reference frame. For the velocity potential, the Neumann condition is given by (3.2) as

$$\sum_{i=1}^{8}\left[\sum_{j=1}^{8} c_{j,i}\nabla_{bf} f_j\left(\overline{x}_b, \overline{z}_b\right)\cdot \boldsymbol{n}_{bf}\right]\varphi_i = (\dot{\boldsymbol{R}}_{0,bf} + \boldsymbol{\omega}\times \boldsymbol{r}_{bf})\cdot \boldsymbol{n}_{bf}, \tag{3.20}$$

where ∇_{bf} is the gradient operator along the axes of the body-fixed coordinate system, $\dot{\boldsymbol{R}}_{0,bf}$ is the velocity of the body in the center of gravity, $\boldsymbol{\omega}$ is the body's angular velocity vector, $\boldsymbol{r}_{bf}$ is a vector from the body's center of gravity to $\boldsymbol{P}_{b,bf}$ and $\boldsymbol{n}_{bf}$ is the body's normal vector in $\boldsymbol{P}_{b,bf}$. It is noted that, since the origin of the body-fixed coordinate system is defined in the body's center of gravity, we here have that $\boldsymbol{r}_{bf} = \boldsymbol{P}_{b,bf}$.

For the BVP of the time derivative of φ, the Neumann body-boundary condition is given by (3.8) as

$$\sum_{i=1}^{8}\left[\sum_{j=1}^{8} c_{j,i}\nabla_{bf} f_j\left(\overline{x}_b, \overline{z}_b\right)\cdot \boldsymbol{n}_{bf}\right]\frac{D_{BO}\varphi_i}{Dt} = (\ddot{\boldsymbol{R}}_{0,bf} + \dot{\boldsymbol{\omega}}\times \boldsymbol{r}_{bf})\cdot \boldsymbol{n}_{bf}. \tag{3.21}$$

The right-hand side of this equation follows from (2.35) in Section 2.3.4, where $\ddot{\boldsymbol{R}}_{0,bf}$ and $\dot{\boldsymbol{\omega}}$ are the time derivatives of $\dot{\boldsymbol{R}}_{0,bf}$ and $\boldsymbol{\omega}$, respectively, estimated in the body-fixed reference frame as previously explained.

It is emphasized that (3.20) and (3.21) are free-surface and body-boundary conditions for $D_{BO}\varphi/Dt$, which is the variable solved for in the overlapping body-fixed grid. Unless the body motion is zero, this differs from the Eulerian time derivative $\partial\varphi/\partial t$. The relation between D_{BO}/Dt and $\partial/\partial t$ was stated in (2.15).

Double-Node Technique for Wave-Body Intersection Points

In a free surface-body intersection point, hereafter referred to as a *FSBI* point, it is desirable to satisfy both the free-surface Dirichlet condition and the body-boundary Neumann condition simultaneously. However, because the number of equations in the global matrix system is equal to the number of nodes in the instantaneous computational domain, this is generally not possible if we want to avoid the solution of an overdetermined equation system. In order to overcome this challenge, a double-node technique is adopted. Figure 3.14 shows the details of a cell that contains the FSBI on one side of the body. The coordinates of the point in the body-fixed coordinate system and in the cell-fixed coordinate system are $\boldsymbol{P}_{FSBI,bf}$ and $\overline{\boldsymbol{P}}_{FSBI}$, respectively.

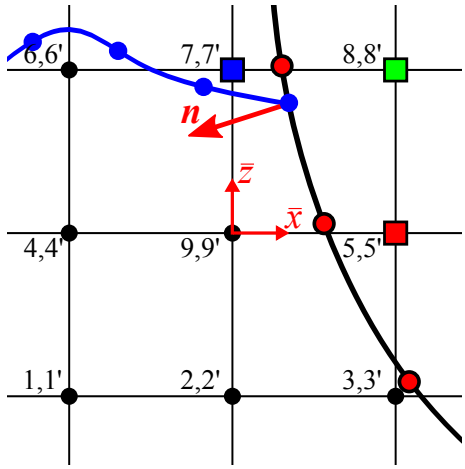

Figure 3.14: Double node and associated cell for simultaneous fulfilment of free-surface Dirichlet condition and body-boundary Neumann condition in FSBI point. The double node, indicated as a green square with black border, here has local node index 8.

The double-node technique consists of introducing fictitious nodes that replicate the boundary nodes in the original cell with local node indices $1-8$. The fictitious nodes have local node indices $1'-8'$. Using Figure 3.14 as an example, the node with local index 8 is a double node. In general, we denote the index of the double node as k, and enforce the free-surface Dirichlet condition (3.18)

$$\sum_{i=1}^{8}\left[\sum_{j=1}^{8} c_{j,i} f_j\left(\overline{x}_{FSBI}, \overline{z}_{FSBI}\right)\right] \varphi_i = \varphi_{FSBI}. \tag{3.22}$$

φ_{FSBI} is the velocity potential in the marker at the FSBI. In addition, for the fictitious node with local index k', we enforce the body-boundary Neumann condition (3.20),

$$\sum_{i=1}^{8}\left[\sum_{j=1}^{8} c_{j,i} \nabla_{bf} f_j\left(\overline{x}_{FSBI}, \overline{z}_{FSBI}\right) \cdot \boldsymbol{n}_{bf}\right] \varphi_i = \left(\dot{\boldsymbol{R}}_{0,bf} + \boldsymbol{\omega} \times \boldsymbol{r}_{bf}\right) \cdot \boldsymbol{n}_{bf}. \tag{3.23}$$

Here, $\left(\dot{\boldsymbol{R}}_{0,bf} + \boldsymbol{\omega} \times \boldsymbol{r}_{bf}\right) \cdot \boldsymbol{n}_{bf}$ is the normal velocity of the body in the same point. For the remaining fictitious nodes, we set $\varphi_{i'} = \varphi_i, \{i = 1, ..., 8, i \neq k\}$. As a consequence, for each FSBI point, eight rows and columns are added to the global matrix system. This increase is insignificant compared to the total number of nodes in the computational domain and has negligible influence on the computational efficiency.

For the BVP of the time derivative of φ, the corresponding Dirichlet and Neu-

mann boundary conditions are given by equations (3.19) and (3.21) as

$$\sum_{i=1}^{8}\left[\sum_{j=1}^{8} c_{j,i} f_j\left(\overline{x}_{FSBI}, \overline{z}_{FSBI}\right)\right] \frac{D_{BO}\varphi_i}{Dt} = \frac{D_{BO}\varphi_{FSBI}}{Dt} \tag{3.24}$$

and

$$\sum_{i=1}^{8}\left[\sum_{j=1}^{8} c_{j,i} \nabla_{bf} f_j\left(\overline{x}_{FSBI}, \overline{z}_{FSBI}\right) \cdot \boldsymbol{n}_{bf}\right] \frac{D_{BO}\varphi_i}{Dt} = \left(\ddot{\boldsymbol{R}}_{0,bf} + \dot{\boldsymbol{\omega}} \times \boldsymbol{r}_{bf}\right) \cdot \boldsymbol{n}_{bf}, \tag{3.25}$$

where $D_{BO}\varphi_{FSBI}/Dt$ is the time derivative of the velocity potential on the free surface and $(\ddot{\boldsymbol{R}}_{0,bf} + \dot{\boldsymbol{\omega}} \times \boldsymbol{r}_{bf}) \cdot \boldsymbol{n}_{bf}$ is the normal acceleration of the body in the FSBI point, both estimated in the body-fixed reference frame. For the remaining fictitious nodes, we set $D_{BO}\varphi_{i'}/Dt = D_{BO}\varphi_i/Dt, \{i = 1, ..., 8, i \neq k\}$.

It is pointed out that, for the cases examined in this thesis, the results applying the double-node technique are in close agreement with the results obtained only applying the free-surface Dirichlet condition in the FSBI points. This holds true also when the local solution close to the FSBI points is examined. Although further investigation is needed to properly understand this observation, a possible explanation is that the Dirichlet condition for the free surface is a stricter condition than the Neumann condition for the body boundary. It is also noted that, in the present implementation, the double-node technique is only applied for a floating body. At the wavemaker-free surface intersection point only the free-surface Dirichlet condition is enforced.

The FSBI points are revisited in Section 3.2.8, where special care is taken to prevent that free-surface markers separate from rigid boundaries.

3.2.3 General Comments concerning Immersed Boundaries

Some general remarks are appropriate regarding the use of immersed boundaries and Cartesian grids.

As illustrated by Figure 3.5, large portions of the grids are at any time outside the physical domain. We have previously referred to the nodes and cells in these parts of the grids as inactive. They do not influence the computational time required to solve the hydrodynamic BVPs at a given time instant. However, depending on the position of moving boundaries, inactive nodes and cells may become active and vice versa. Hence, the dimension and topology of the global matrix system generally vary with time. This has an adverse influence on the computational efficiency, since the global coefficient matrix must be reconstructed.

In connection with immersed boundaries, we have introduced ghost nodes above the free surface and inside the body. This means that the computational domain, where a solution exists, extends beyond the physical domain. The solution outside the fluid domain has no physical meaning, and no properties should be evaluated here. However, in a numerical interpretation, it has an important meaning: the solution in ghost nodes, obtained from solving the hydrodynamic

BVPs, attains the values required to fulfil conditions enforced on physical boundaries. The solution in ghost nodes is in this sense analogue with the concept of analytical continuation used by Faltinsen and Timokha (2009).

Lastly, it is emphasized that the number of boundary conditions we can impose on a boundary is governed by the number of ghost nodes. The number of ghost nodes do not depend on the number of discrete points or markers used to describe the boundary, but on the cell size in the grid. One should therefore take into consideration the minimum relevant wavelength and the local geometry of the body when deciding upon the cell size in different grids.

3.2.4 Coupling of Solutions in Different Domains

We have discussed the implementation of boundary conditions in the inertial background grid and the overlapping body-fixed grids separately. We now show how the solutions in the individual grids are implicitly coupled, resulting in a single global matrix system for the entire computational domain. The coupling strategy between an overlapping grid and the background grid is identical irrespective if the overlapping grid is fixed to a wavemaker or to a body. It is noted that the scenario where several body-fixed grids overlap with each other is disregarded in the present work. However, the method can be extended to cover this scenario without major modifications. To illustrate the coupling strategy, we use the overlapping grid following the motion of a flap-type wavemaker and the background grid as shown by a sketch in Figure 3.15.

In Figure 3.15 (a), the nodes indicated by red circles with black borders are coupling nodes in the overlapping grid. In these, φ and its time derivative are defined by local HPC-expressions in the background grid. Similarly, for the coupling nodes in the background grid (b), φ and its time derivative are expressed by local HPC-expressions in the overlapping grid. The coupling of the velocity potential is first considered. For the coupling nodes, we impose the following condition:

$$\varphi_{G_1} = \sum_{i=1}^{8} \left[\sum_{j=1}^{8} c_{j,i} f_j \left(\overline{x}, \overline{z} \right) \right] \varphi_i \Big|_{G_2} . \tag{3.26}$$

Here, G_1 is the grid with the coupling node, and G_2 is the grid to which the solution is coupled. The right-hand side can in principle be evaluated from any cell in G_2 that encloses the coupling node, and at the same time is part of the instantaneous computational domain. We here select the cell with center closest to the position of the coupling node, because the accuracy of the solution inside a cell is higher in this region as shown by Ma et al. (2018). $(\overline{x}, \overline{z})$ are the coordinates of the coupling node in the cell-fixed coordinate system of the selected G_2-cell. In relation with Figure 3.15, it is noted that in practice the coupling nodes in the background grid are taken some distance inside the contour of the overlapping grid. This is in order to prevent that the G_2-cell used to evaluate the right-hand side of (3.26) contains a node where the solution is coupled with G_1, and vice versa. Such scenario would represent a recursive condition that might influence the accuracy and stability of the numerical solution.

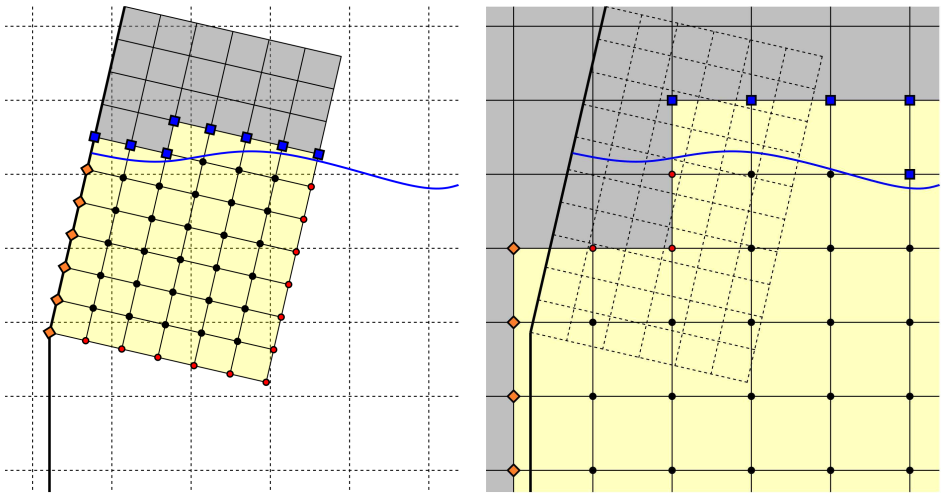

(a) Wavemaker-fixed grid highlighted (b) Background grid highlighted

Figure 3.15: Coupling scheme between grid regions. Features of the body-fixed grid following the motion of a flap-type wavemaker and the inertial background grid are highlighted in (a) and (b), respectively. The yellow and grey-shaded areas mark, respectively, active and inactive cells in both grids. The following node types are shown: Free-surface ghost nodes (blue squares with black borders), nodes used in connection with Neumann conditions on rigid boundaries (orange diamonds with black borders), interior nodes where the connectivity equation (3.3) is enforced (black filled circles) and nodes where coupling conditions are enforced (red circles with black borders).

For the time derivative of φ, we must take into consideration that the solution variable in the background grid is the Eulerian time derivative φ_t, while the solution variable in the overlapping grid is the time derivative $D_{BO}\varphi/Dt$. Using (2.15) in Section 2.2.4, the equation imposed for the coupling node in the overlapping grid (og) is

$$\begin{aligned}\left.\frac{D_{BO}\varphi}{Dt}\right|_{og} &= \sum_{i=1}^{8}\left[\sum_{j=1}^{8} c_{j,i} f_j\left(\overline{x},\overline{z}\right)\right]\left.\frac{\partial\varphi_i}{\partial t}\right|_{bgg} \\ &+\boldsymbol{u}_b\cdot\sum_{i=1}^{8}\left[\sum_{j=1}^{8} c_{j,i}\nabla f_j\left(\overline{x},\overline{z}\right)\right]\left.\varphi_i\right|_{bgg}.\end{aligned} \tag{3.27}$$

$D_{BO}\varphi/Dt|_{og}$ is the time derivative of φ in the coupling node in the overlapping grid, taken in the body-fixed reference frame. The right-hand side is evaluated from the appropriate cell in the background grid (bgg), which is the same as used in connection with (3.26). $\boldsymbol{u}_b$ is the velocity of the coupling node due to the motion of the overlapping grid.

For the coupling nodes in the background grid, the corresponding coupling equation is

$$\begin{aligned}\left.\frac{\partial\varphi}{\partial t}\right|_{bgg} &= \sum_{i=1}^{8}\left[\sum_{j=1}^{8} c_{j,i} f_j\left(\overline{x},\overline{z}\right)\right]\left.\frac{D_{BO}\varphi_i}{Dt}\right|_{og} \\ &-\boldsymbol{u}_b\cdot\sum_{i=1}^{8}\left[\sum_{j=1}^{8} c_{j,i}\nabla f_j\left(\overline{x},\overline{z}\right)\right]\left.\varphi_i\right|_{og},\end{aligned} \tag{3.28}$$

where $\partial\varphi/\partial t|_{bgg}$ is the Eulerian time derivative of φ in the coupling node in the background grid. The right-hand side is here evaluated from the appropriate cell in the overlapping grid.

General Comments concerning Coupling between Domains

It can be said that the coupling between different grid regions is natural in the HPC method, because the solution field inside each cell is given as a combination of smoothly varying coefficients. We can thus express the solution in any point, in any grid, as a function of already defined functions. This is highlighted as an advantage of the HPC method compared to other field methods, such as e.g. the FDM, because it allows us to couple the solution in arbitrary points without any significant loss of accuracy. Moreover, the coupling strategy outlined above is beneficial in the sense that it allows us to operate with Cartesian grids in the respective domains. As shown by Ma et al. (2018), this is strongly recommended with respect to numerical accuracy inside a cell in the HPC method. The use of overlapping grids can thus be considered a mean to refine a solution locally while using Cartesian grids throughout, without increasing the total number of unknowns (nodes) unnecessarily. Although not pursued in the present work, it is fully possible to add several levels of overlapping grids inside each other to locally enhance the refinement further. This is analogue to using so-called octree grids as was done by Ma et al. (2018).

A major strength of the coupling strategy adopted in the present work, is that the solution for the time derivative of φ in the different grids represents the time derivative relative to the grid-fixed reference frame. As a consequence, the body-boundary condition in the BVP of the time derivative of φ in the overlapping grids is simplified, and the difference in reference frame is instead accounted for in the coupling between different grids in a straightforward manner by (3.27) and (3.28).

3.2.5 Algebraic Equation System

The boundary conditions (3.18) - (3.25), the equations (3.26) - (3.28) enforcing the coupling between different grids, and the connectivity equations (3.3), (3.6) and (3.9), constitute the global algebraic equation systems for φ and its time derivative. As explained in Section 3.1.3, these two equation systems share the same coefficient matrix $\boldsymbol{A}$. An example of this coefficient matrix for a case with a moving wavemaker and with a rigid body in the middle of the tank is shown in Figure 3.16. The majority of non-zero entries in $\boldsymbol{A}$ originate from the connectivity

equations and are located along the matrix diagonal. Due to the multiple grids, there are also non-zero off-diagonal entries associated with communication between the grids. The number of rows with such entries is however small compared with the number of entries from the connectivity equations, and the matrix equation can be solved efficiently with the use of iterative solvers for sparse matrix systems. In the present work, the sparse iterative solvers included in the *SciPy* Python library are used. More specifically, it is found that using the *splu* decomposition of $\boldsymbol{A}$ as a pre-conditioner, together with the *gmres* or *bicgstab* solver with a tolerance of $0.5 \cdot 10^{-8}$, provides stable and efficient solutions of the global matrix equations.

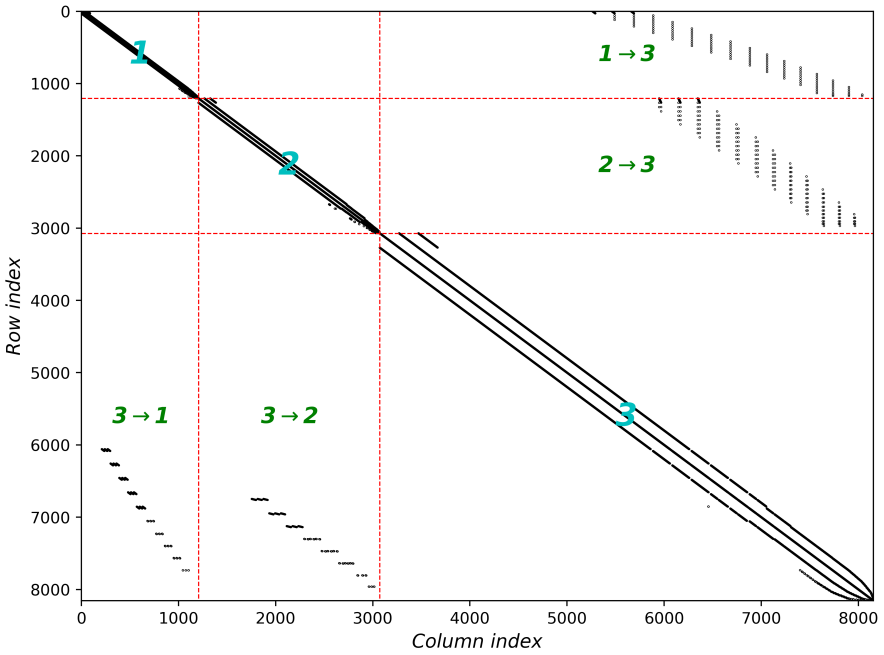

Figure 3.16: Example of global coefficient matrix in the IBOGM with a rigid body in the NWT. The wavemaker-fixed grid, the body-fixed grid and the background grid are for brevity denoted as 1, 2 and 3, respectively. $1 \rightarrow 3$ and $3 \rightarrow 1$ indicate coupling terms between the wavemaker-fixed grid and the background grid and vice versa, and $2 \rightarrow 3$ and $3 \rightarrow 2$ indicate coupling terms between the body-fixed grid and the background grid and vice versa.

It has already been highlighted that the nodes and cells that are part of the instantaneous computational domain represent a subset of the complete grids, which extend beyond the physical domain, in the IBOGM. Moreover, the meaning of any particular node and cell may vary with time. For instance, due to the moving free surface, a node that was a fluid node at the previous time step may become a free-surface ghost node at the present time instant. As a consequence, the dimension and topology of $\boldsymbol{A}$ is not constant. This is a matter of practical

importance when we build and solve the global matrix equations for φ and its time derivative, because the inactive nodes in the instantaneous computational domain would result in empty rows in the global matrix system. The iterative matrix solvers used here do not allow for this, and therefore a mapping between the global node indices and the node indices in the matrix system must be maintained. As we build $\boldsymbol{A}$, we number the nodes in a continuous order from 1 to Q. Q is here the number of active nodes, which is less than or equal to the total number of nodes N. After solving the global matrix equations, the solution in each active node is related back to its global node index. This book-keeping is managed by an array illustrated in Figure 3.17 that, at any time, links the global node indices $n = 1, ..., N$ to the node indices $q = 1, ..., Q$ of the active nodes in the matrix system.

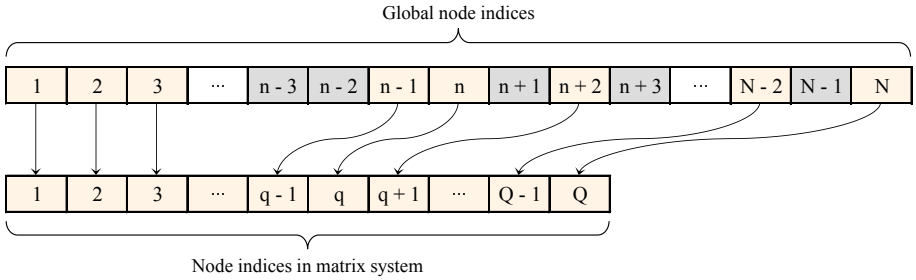

Figure 3.17: Example of mapping between global node indices $n = 1, ..., N$ and node indices $q = 1, ..., Q$ in the matrix system at any time instant, where $Q \leq N$.

3.2.6 Integration of Fluid Pressure

When the BVPs of φ and its time derivative have been solved, the pressure loads are calculated in the body-fixed coordinate system. The fluid pressure p is evaluated from the body-fixed formulation of the Bernoulli equation (2.21) in Section 2.3.2. A tangential coordinate s is defined, running along the body boundary in anti-clockwise direction, so that the instantaneous wetted body surface is given by $s_0 \leq s \leq s_1$. The body surface is here defined by the contour through all the discrete points used to describe it. As discussed in Section 3.2.2, the points where body-boundary conditions are enforced represent a subset of these. Furthermore, the body-fixed coordinates of the body surface are given as $\boldsymbol{P}_{b,bf}(s) = (x_{b,bf}(s), z_{b,bf}(s))$, where the components are parametrized by s using 3^{rd} order B-splines. The resulting fluid forces and moments are obtained by integrating the pressure over the wetted body surface in s-direction,

$$\boldsymbol{F}_{bf}(t) = -\int_{s_0}^{s_1} p(s,t)\boldsymbol{n}_{bf}(s)ds, \tag{3.29}$$

$$\boldsymbol{M}(t) = -\int_{s_0}^{s_1} p(s,t)(\boldsymbol{P}_{b,bf}(s) \times \boldsymbol{n}_{bf}(s))ds. \tag{3.30}$$

A negative sign appears in front of the integrals because the normal vector $\boldsymbol{n}_{bf}$ is defined outwards. Since we operate in 2D, the moment vector $\boldsymbol{M}$ is equal to $M_y\boldsymbol{j}$ with $\boldsymbol{j}$ the unit vector in y direction and M_y the moment about the y axis, equal in all reference frames. The force vector can be represented in the inertial coordinate system by using the rotation matrix, i.e., $\boldsymbol{F} = \boldsymbol{\Lambda}_{b\rightarrow i} \cdot \boldsymbol{F}_{bf}$. An arbitrary number of points can be used in the numerical integrations performed in (3.29) and (3.30). Typically we select the number of points sufficient to ensure numerical convergence, yet not so high that the computational efficiency is reduced unnecessarily. Since the Bernoulli equation must be evaluated in each of the points used in the integration, an excessive number of points may lead to a notable increase in computational time.

3.2.7 Smoothing of Free Surface

In a non-linear simulation, small disturbances of the free surface may over time grow and lead to non-physical behaviour and numerical instability. As shown by Hanssen et al. (2018), even when no smoothing of the free surface is performed with the semi-Lagrangian description, it takes a significant amount of wave periods for such instabilities to develop. However, instabilities at the free surface develop quicker the higher the wave steepness. The disturbance mechanism was in this case identified as sawtooth-instability, a phenomenon first discovered by Longuet-Higgins and Cokelet (1976). With the fully Lagrangian description of the free surface, it is found that disturbances occur earlier and grow quicker when no smoothing is performed. This is the case even for waves with low steepness.

In order to prevent instabilities from developing, two types of smoothing techniques are used in the present work. When the semi-Lagrangian description is adopted, the free-surface elevation and the velocity potential at the free surface are smoothed with a 12^{th} order Savitsky-Golay filter (Savitzky and Golay, 1964). It is in many cases sufficient to only perform the filtering every several time steps. However, since the additional computational effort is insignificant, and since the accuracy is not found to be reduced, the filtering is here performed after every complete time step. With the fully Lagrangian or hybrid description, the 3^{rd} order five-point filter used by Sun (2007) is applied to the free-surface elevation and velocity potential on the free surface after every complete time step. This provides a stronger smoothing than the higher-order Savitsky-Golay filter, which is found strictly necessary to ensure numerical stability in this case. In addition, the free-surface markers are redistributed with even spacing in horizontal direction. This is necessary because otherwise, with the fully Lagrangian description, the markers may over time cluster together. Also, both the mentioned filters require the markers to be evenly spaced. This can strictly speaking be circumvented by re-sampling the free surface at evenly distributed points. Studies here indicate that such re-sampling may lead to reduced accuracy of the solution, and should be performed with caution.

Whether the Savitsky-Golay or the five-point filter is applied, the free-surface elevation is always left unchanged in the intersection points between the free surface and the wavemaker or a body.

3.2.8 Special Treatment at Free Surface-Body Intersection Points

At FSBI points, either on the wavemaker, the fixed vertical tank wall on the opposite side of the wavemaker or a body surface, special care is taken to ensure that free-surface markers do not separate from the boundary. For the wavemaker and the opposite tank wall, which are plane boundaries, the separation between the marker on the boundary and the boundary itself is always several orders of magnitude smaller than the marker's motion in tangential direction. The separation can in this case be considered a consequence of numerical inaccuracy, and is avoided by simply modifying the coordinate of the marker normal to the boundary.

For the FSBI points on a body of arbitrary shape, separation may occur due to the curvature of the body. To avoid this, the KFSC for the markers at the FSBI is reformulated so that it is expressed in the curvilinear coordinate s running along the surface of the body, as introduced in Section 3.2.6. These markers always follow the fully Lagrangian description, i.e. the KFSC is given by (3.16) in the inertial reference frame. The velocity of the marker relative to the body-fixed reference frame is given as $\nabla\varphi - \boldsymbol{u}_b$, where $\boldsymbol{u}_b$ is the velocity of the body surface in the marker location. Since the Neumann condition along the body surface enforces the water and body normal velocities to be equal, this relative-velocity vector is tangential to the body surface in the FSBI points. With reference to Figure 3.18, the velocities of the markers are formulated as

$$\frac{Ds}{Dt} = |\nabla\varphi - \boldsymbol{u}_b| \cdot sgn, \tag{3.31}$$

where, remembering that s is positive when moving in anti-clockwise direction with respect to a generic point inside the body, sgn is the component in the body-fixed z_{bf} direction of a sign function defined as $-sign(\nabla\varphi - \boldsymbol{u}_b)$ if the FSBI is on the left side of the body and as $sign(\nabla\varphi - \boldsymbol{u}_b)$ on the right side of the body. The physical argument behind this is that the magnitude of the velocity vector is given by the KFSC, but in reality the trajectory of the marker will be along the body surface rather than tangential to the surface in the FSBI point. It is emphasized that s is a coordinate defined along the surface of the body, so that (3.31) represents a body-fixed formulation. By evolving the position of the marker in the coordinate s rather than in Cartesian coordinates, we ensure that the marker never separates from the body surface. The Cartesian coordinates of the marker are obtained in a straightforward manner since the functional relationship between s and (x_{bf}, z_{bf}) is known.

In some cases, such as when a cylinder is forced to oscillated with high frequency in heave, small angles may occur between the free surface and the body boundary at the FSBI. This is undesirable, since it can easily lead to numerical instabilities. Therefore, at any time instant of the simulation the angles between the free surface and the body boundary in the FSBI points are estimated from the free-surface slope and the curvature of the body surface. When this angle becomes less than 5°, a jet-cutting scheme is used to prevent numerical instability from developing. This is illustrated for a general scenario in Figure 3.19 and consists of the following steps:

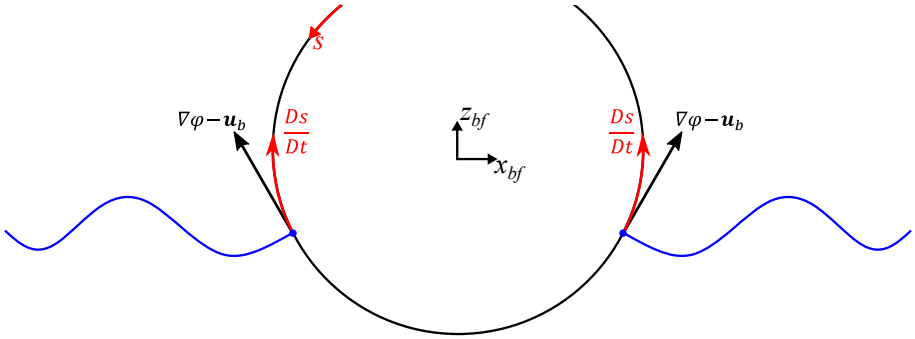

Figure 3.18: Reformulation of motion of free-surface markers on FSBI in terms of the curvilinear coordinate s.

1. The marker at the FSBI (position 1) is removed.
2. The marker next to the removed marker (position 2) is projected normally onto the body surface (position 1′). This new position of the marker identifies the new FSBI.
3. A new marker is introduced (position 2′) to keep the total number of markers unchanged, before the markers are redistributed so that they become evenly spaced.

The jet-cutting scheme is invoked both if the exterior or interior angle between the body and the free surface becomes less than $5°$. The scenario in Figure 3.19 illustrates a small exterior angle. If on the other hand the interior angle is small, the jet-cutting scheme prevents a thin run-up along the body to develop.

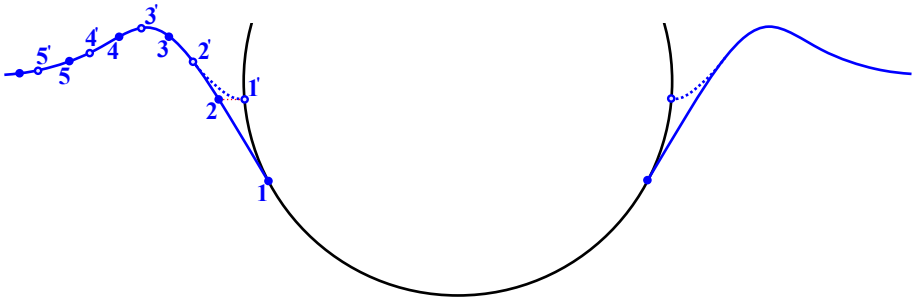

Figure 3.19: Illustration of jet-cutting scheme with small exterior angle. The markers prior to jet cutting are numbered $1, 2, \ldots$ and shown with blue filled circles, while the markers after jet cutting are numbered $1', 2', \ldots$ and shown with white circles with blue borders.

The cases where jet cutting is performed involve strong local non-linear behaviour, and because the potential-flow solution may become nearly singular, they are close to the capability limit of a potential-flow solver. Although the scheme proposed here is found to be effective in preventing numerical instabil-

ity, one should carefully assess the accuracy of the solution when jet-cutting is invoked. More details around the use of jet-cutting schemes can be found in works dealing with water-entry problems, see e.g. Sun (2007).

3.2.9 Wave Generation and Absorption

There are two main approaches that can be followed to generate waves in a non-linear NWT. One is to impose the surface elevation and fluid velocity from an analytical solution at a fixed control surface, such as done by e.g. Tanizawa et al. (1999). The other method, which is adopted here, is to generate waves by a moving wavemaker. We denote this as a *physical wavemaker*, since it is analogue to the way waves are generated in a physical wave tank. The main advantage of deploying a physical wavemaker instead of a fixed control surface is that the waves are not restricted to follow any specific wave theory. Although accurate non-linear theories exist for periodic waves, generation of non-linear irregular waves is more complicated unless linear theory is applied. A second advantage of applying a physical wavemaker is that the increase of fluid mass in the tank, that can be observed with a fixed control surface, is avoided. Such mass increase is shown by Shao (2010) to be a 2^{nd} order effect related to the Stokes drift, that is a Lagrangian property of the fluid particles. It is to be noted that this mass increase can be avoided also in the case of a fixed control surface by modifying the velocity boundary condition.

It was noted by Faltinsen and Zhao (1991) that the impulsive start of a piston-type wavemaker, with the horizontal velocity given as a step function, causes oscillatory behaviour of the free surface close to the wavemaker. This may lead to instabilities in a numerical solution that are highly undesirable. In order to avoid such instabilities, a ramp function is here applied. Denoting the displacement of a piston-type wavemaker or the angular motion of a flap-type wavemaker as $s_{wm}(t)$, the motion signal with a ramp function is given as $s_{wm}(t) \cdot r_{wm}(t)$. Here, $r_{wm}(t)$ is a ramp function defined as

$$r_{wm}(t) = \begin{cases} \frac{1}{2}\left[1 - \cos\frac{\pi t}{T_{ramp}}\right] & t \leq T_{ramp} \\ 1 & t > T_{ramp} \end{cases}, \tag{3.32}$$

where T_{ramp} is the time duration of the ramp function typically taken as $3-5$ periods of the generated, incident wave. When computing the velocity and acceleration of the wavemaker, it is important to remember to take into account the time derivative of the ramp function.

In order to prevent that waves are reflected from the tank wall opposite of the wavemaker and back into the tank, a numerical damping zone (beach) is implemented in the fluid region next to this wall. When there is a body in the tank, a numerical beach is also located next to the wavemaker. This is in order to prevent waves reflected from the body to reach the wavemaker and be reflected back into the tank, modifying the prescribed incident-wave conditions. Without such beach, long-time simulations without influence from back-reflected waves would require an accordingly long NWT. This may substantially increase the computational cost of the numerical solution. The numerical beaches add damping terms with a fictitious linear damping coefficient $\nu(x,t)$ in the DFSC and KFSC described

in Section 3.2.1, with the purpose to dissipate wave energy. The theory behind, and the performance of, the numerical damping zones are described in detail in Appendix B.

An attractive alternative to the downwave numerical beach is to deploy a non-reflective boundary. This means substituting the tank wall opposite of the wavemaker with a control surface where the Neumann boundary condition for the velocity potential is replaced by a boundary condition consistent with a propagating wave. Promising results were shown by Zhang (2009) applying a multi-transmitting formula (MTF) to model a non-reflective boundary. The MTF combines information of the phase speed of the wave as well as the velocity potential in the fluid at previous time steps to extrapolate the velocity potential at the tank wall, and is relatively straightforward to implement. Applying such non-reflective boundary condition, the NWT can be shortened by the distance otherwise required by the numerical beach, and thereby improves the computational efficiency. A significant effort has been made in the present work to implement the MTF as an alternative to the numerical beach opposite of the wavemaker. The attempts were however not successful, as it leads to a steady drift in the wave elevation near the tank wall. In hindsight, this may be due to the fact that waves were generated by a fixed control surface in this case. As mentioned, this may lead to an increase in fluid mass, analogue to a steady current in the tank. In the way the MTF was implemented, consistent with the strategy documented by Zhang (2009), no correction was made to account for this. A future investigation, combining the MTF with incident waves generated by a physical wavemaker, would indicate if this was the case. Further examination of this method is considered an interesting research topic with the objective to improve numerical efficiency in non-linear simulations.

3.2.10 Time Evolution of Solution

A 4^{th} order Runge-Kutta method (RK4) is used to evolve the free surface and the motion of a floating body forward in time. For a general variable y with time derivative given in the form $\dot{y} = \dot{y}(y, t)$, the evolution from the known state $y_n = y(t_n)$ at time $t_n = n\Delta t$ to the unknown state at $t_{n+1} = t_n + \Delta t$ is given as

$$y_{n+1} = y_n + \frac{\Delta t}{6}(k_{1,y} + 2k_{2,y} + 2k_{3,y} + k_{4,y}), \tag{3.33}$$

where Δt is the time step, taken as constant in the present work. The coefficients $k_{i,y}, i = 1, ..., 4$ are given as

$$\begin{aligned} k_{1,y} &= \dot{y}(y_n, t_n), \\ k_{2,y} &= \dot{y}(y_n + 0.5\Delta t k_{1,y}, t_n + 0.5\Delta t), \\ k_{3,y} &= \dot{y}(y_n + 0.5\Delta t k_{2,y}, t_n + 0.5\Delta t), \\ k_{4,y} &= \dot{y}(y_n + \Delta t k_{3,y}, t_n + \Delta t). \end{aligned} \tag{3.34}$$

As a consequence, for each complete RK4 time step, four BVPs must be established and solved for φ. If a floating body is involved, four BVPs must also be solved for

the time derivative of φ. If the body on the other hand is fixed or undergoes forced motions, the equations of motion are not coupled with the fluid dynamic problem. In these cases, to estimate the fluid pressure and integrated loads on the body, it is sufficient to solve the BVP of the time derivative of φ at the physical time instants i.e. at the end of the complete RK4 time step.

Free Surface

The free surface position and the velocity potential on it are tracked in time following the motion of the free-surface markers. In particular, the KFSC and DFSC, described in Section 3.2.1, provide directly the time derivatives for the position $\boldsymbol{P}_m = (x_{P_m}, z_{P_m})$ and velocity potential φ_m of each marker. Estimating these derivatives at each time a BVP for φ is solved gives the RK4 coefficients $k_{i,\boldsymbol{P}_m}$ and k_{i,φ_m} in (3.34) to evolve respectively $\boldsymbol{P}_m$ and φ_m in time through (3.33).

Floating Body

When a floating body is present in the NWT, its equations of motion discussed in Section 2.2.3 must be coupled with the fluid dynamic problem. Since the wave-body interaction problem here is solved in the body-fixed grid following the motion of the body, it is natural to also formulate the equations of motion in the body-fixed reference frame. The origin of the body-fixed coordinate system is located in the body's center of gravity, $\boldsymbol{R}_{0,bf}$. Equations (2.12) and (2.14) give the translation and angular accelerations $\ddot{\boldsymbol{R}}_{0,bf}$ and $\ddot{\alpha}$ as follows:

$$\begin{aligned} \ddot{\boldsymbol{R}}_{0,bf} =& \boldsymbol{M}^{-1} \cdot \boldsymbol{F}_{bf,ext} - \boldsymbol{\omega} \times \dot{\boldsymbol{R}}_{0,bf}, \\ \ddot{\alpha} =& I_{yy}^{-1} M_{y,ext}. \end{aligned} \tag{3.35}$$

Here, $\boldsymbol{M}$ is the body mass matrix, I_{yy} is the inertia about the y-axis, $\dot{\boldsymbol{R}}_{0,bf}$ is the translational body velocity in the body-fixed reference frame, $\boldsymbol{\omega}$ is the angular velocity vector, $\boldsymbol{F}_{bf,ext}$ is the external force vector and $M_{y,ext}$ is the external moment about the y_{bf}-axis. $\boldsymbol{F}_{bf,ext}$ consists of the integrated fluid forces $\boldsymbol{F}_{bf}$ defined in (3.29), the vertical gravity force, and possibly additional external forces $\boldsymbol{F}_{bf,add}$:

$$\boldsymbol{F}_{bf,ext} = \boldsymbol{F}_{bf} - \boldsymbol{\Lambda}_{i\to b} \cdot (Mg\boldsymbol{k}) + \boldsymbol{F}_{bf,add}. \tag{3.36}$$

Here, M is the body mass, g is the acceleration of gravity and $\boldsymbol{k}$ is the unit vector in z direction in the inertial coordinate system. $M_{y,ext}$ consists of the integrated fluid moment M_y given by (3.30) and possibly an additional external moment $M_{y,add}$:

$$M_{y,ext} = M_y + M_{y,add}. \tag{3.37}$$

The additional force vector $\boldsymbol{F}_{bf,add}$ and additional moment $M_{y,add}$ typically contain contributions from external linear and quadratic damping and from external restoring effects.

Evaluating (3.35) at each stage of the RK4 scheme gives the coefficients $\boldsymbol{k}_{i,\dot{\boldsymbol{R}}_{0,bf}}$ and $k_{i,\dot{\alpha}}$ in (3.34) used to evolve the translational and angular velocity respectively

of, and about, the body's center of gravity forward in time in the body-fixed reference frame through (3.33). The translational velocity in the inertial reference frame is obtained from

$$\dot{\boldsymbol{R}}_0 = \boldsymbol{\Lambda}_{b\to i} \cdot \dot{\boldsymbol{R}}_{0,bf}. \tag{3.38}$$

Evaluating (3.38) at appropriate time instants gives the RK4 coefficients $\boldsymbol{k}_{i,\boldsymbol{R}_0}$ in (3.34) used to evolve the position of the body center of gravity forward in time in the inertial reference frame through (3.33). The reason for doing this in the inertial reference frame is because the position of the center of gravity is constant in the body-fixed reference frame. The coefficients $k_{i,\alpha}$ to evolve the body angular motion forward in time are independent of reference frame in 2D. It is noted that the velocity and motion of the body must be evolved in time simultaneously.

3.2.11 Iterative Solution for the Time Derivative of φ

The fluid forces (3.29) and moment (3.30) used to evolve the velocity and position of the body in time, are obtained from evaluating the fluid pressure over the instantaneous wetted body surface. The fluid pressure is defined by the Bernoulli equation discussed in Section 2.3.2, where the time derivative of φ is found from solving an auxiliary BVP with body-boundary condition defined in (3.21). Since the body's translational and angular accelerations are involved in the latter, a problem occurs for a floating body, namely that the body acceleration appears on both sides of the equation of motion. It is possible to overcome such difficulty by e.g. using a mode decomposition method such as described by Koo and Kim (2004), where additional BVPs must be solved for each mode.

In the present work, we instead apply an iterative method that is illustrated in Figure 3.20. The iteration is performed at the end of every complete RK4 time step, where the acceleration used in the body-boundary condition at time $t_{n+1} = t_n + \Delta t$ is initially estimated with a 1^{st} order backward finite difference method. The BVP of the time derivative of φ is solved, and the fluid pressure is evaluated and integrated over the wetted body surface. The body's acceleration is then computed from the equations of motion. A new acceleration is estimated as the average between the acceleration used in the body-boundary condition and that obtained from the equations of motion, and the absolute error between this new acceleration and the one used in the body-boundary condition is computed. If the absolute error in any degree of freedom is larger than a specified tolerance, the body-boundary condition is updated with the new acceleration and the procedure is repeated until the error is below the specified tolerance. For the wave-body interaction problem considered in Chapter 6, the tolerance is typically taken as 10^{-3}, with dimension corresponding to the acceleration term. The reason for using an absolute error rather than a relative one is that the relative error can be slow to converge when the accelerations are close to zero. The tolerance is generally set to a level that gives converged results, meaning that further reducing the tolerance leads to insignificant changes in motion time series. The iterative procedure is efficient, because there are no changes to the coefficient matrix $\boldsymbol{A}$ or its preconditioner matrix, and only the elements in the right-hand side vector $\boldsymbol{b}_{\varphi_t}$ in (3.13) related to the body-boundary condition have to be updated. As a result, ob-

taining an updated solution for the time derivative of φ at each iteration is fast. The number of iterations required for each RK4 time step to satisfy the convergence criterion described above is typically found to be in the order of five. This provides an improved estimate of the body's acceleration at t_{n+1}, and the body motion can be evolved to the next time step $t_{n+1} + \Delta t$.

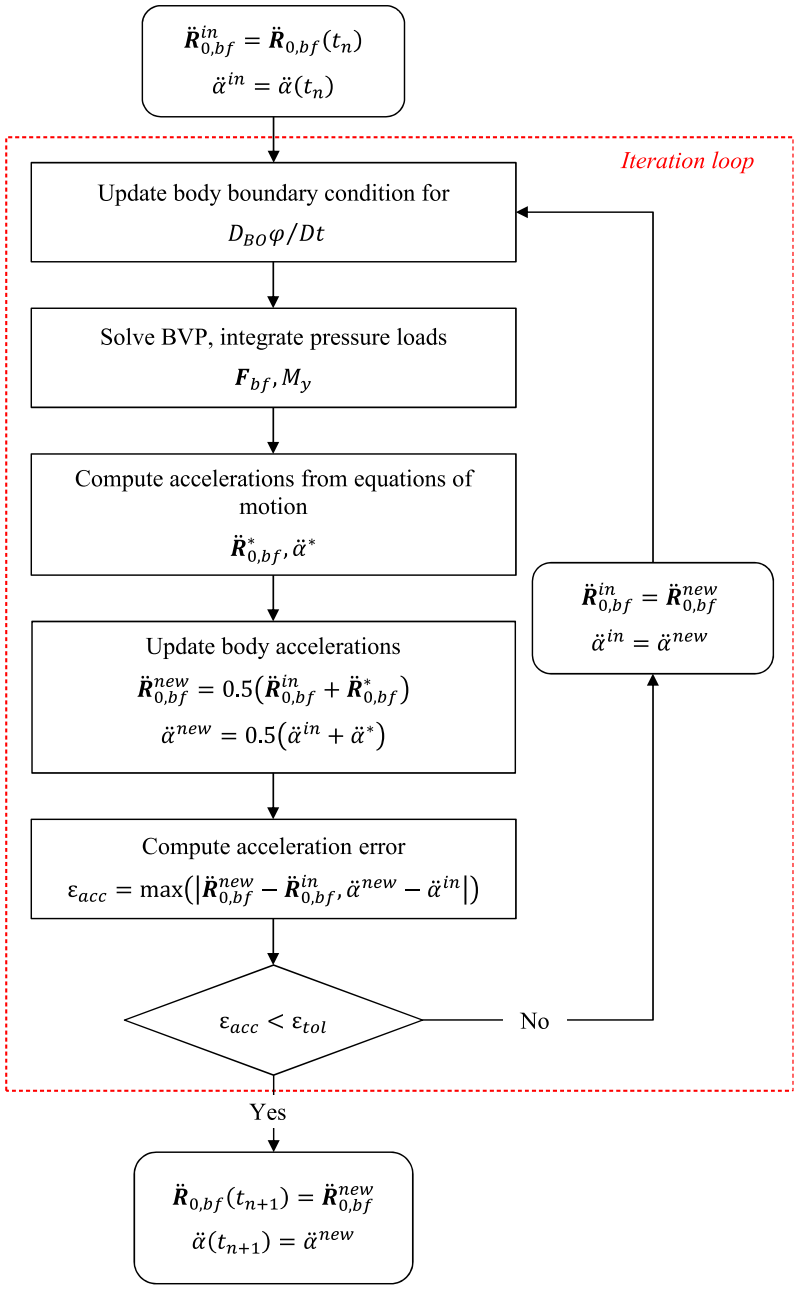

Figure 3.20: Iteration loop for time derivative of φ performed at the end of every complete RK4 time step.

3.3 Efficiency of Potential-Flow Solver

The performance of the IBOGM, that is implemented in the programming language Python 2.7, is now considered for a general case with waves generated with a moving wavemaker, and with a freely floating body in the middle of the NWT. Figure 3.21 shows the relative time used for main tasks in the present numerical implementation, i.e. the cumulative time used to perform each task relative to the total time of the simulation. This is used as basis to explain useful techniques developed in the present work, as well as to point out areas where there is room for further improvement. The discussion is intended as a guidance for future implementations of the specific numerical framework outlined in the present thesis, as well as for other methods sharing common features.

The first thing that stands out is that establishing the matrix equation for φ accounts for more than 20% of the total computational (CPU) time. The majority of this time is used to generate the global coefficient matrix $\boldsymbol{A}$, which is time consuming due to the continuously changing computational domain. In fact, the time used for this task was initially even higher. However, by recognizing that the majority of $\boldsymbol{A}$ consists of the connectivity equation (3.3) imposed for interior cell nodes, the efficiency was improved by initially generating a reservoir coefficient matrix where all interior nodes are given the continuity equation. Thus, at any given time, the relevant parts of this matrix is copied into the correct locations in $\boldsymbol{A}$. Another aspect that has improved computational efficiency is related to the identification of cells used to evaluate free-surface properties and fluid velocities in the coupling between grids. Instead of searching in a vast region of the grid, the search area is restricted to the cells where the properties were evaluated at the previous time step extended two cells in all directions. Generally it can be said that if the non-stationary boundaries move more than approximately one cell in any direction over one time step, the simulation is likely to eventually become unstable. A general technique that is found useful when searching for a point or cell in the grid, is to first search along one of the coordinate axes to identify a subset of possible cells, and thereafter search along the second coordinate axis among this subset. This reduces the effort significantly compared to searching along both axes simultaneously.

Furthermore, it is seen that generating the right-hand side vector for the global matrix equation of the time derivative of φ amounts to a little more than 10% of the CPU time. One of the reasons for this is that the fluid velocity must be evaluated in the locations where the solution in different domains are coupled. Since the coordinates of these points vary with time, the local HPC expressions cannot be pre-computed, and the cumulative time spent for these operations is considerable.

The time used by the iterative matrix solvers, including generation of preconditioner matrices, is more than 25% of the total time, while evaluating and integrating the fluid pressure over the wetted body surface amounts for a little less than 10% of the time. It should here be noted that the relative computational effort associated with this, as well as the effort required to update the right-hand side and solve for the time derivative of φ, are significantly reduced if the iterative solution algorithm discussed in Section 3.2.11 is not invoked.

The remaining tasks included in the group denoted *other* include e.g. the time

used to write data to files during the simulation, transforming grid coordinates between different coordinate systems and more.

A Python-specific advise is to use, as far as possible, functions included in the libraries *NumPy* and *SciPy*. The efficiency of these libraries is generally found to be better than attempting to write the functions explicitly, especially in connection with vector and matrix operations.

It is emphasized that the distribution of CPU time between tasks discussed in Figure 3.21 represents a typical case for a wave-body interaction problem. The relative distribution between tasks may obviously vary depending on e.g. the number of unknowns in the different solution domains and the amount of post-processing performed after each time step.

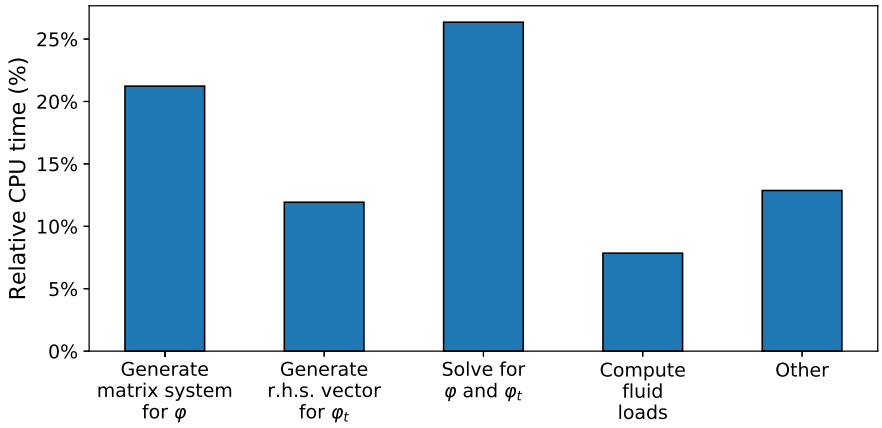

Figure 3.21: Relative CPU time for main tasks in a simulation using the IBOGM with a freely floating body in the middle of the NWT.

3.3.1 Suggestions for Further Improvement of Computational Efficiency

During the development and implementation of a novel method, such as the IBOGM method here, it is natural that aspects that could have improved the computational efficiency are discovered in retrospect. Although some techniques to enhance the efficiency have already been discussed, there is still room for significant improvement in the present implementation. It is noted that all suggestions given here relate to the specific implementation in Python. Although some suggestions are of general nature, it should be kept in mind that the efficiency of specific operations may differ for other programming languages. It is also noted that the code is not parallelized to run on several processors.

Two main experiences are made throughout the work:

1. For-loops, and especially nested for-loops, are expensive, and their use should be limited as much as possible.

2. Everything that *can* be pre-computed, *should* be pre-computed.

While the use of for-loops is difficult to avoid, there are ways to minimize the use of them. For instance, it is generally much more efficient to populate a matrix by using vector products than using for-loops. A good example of this in connection with the HPC method can be seen in e.g. (3.18), where the double-summation in the present work is replaced by the product between a matrix containing all the $c_{j,i}$ entries and a vector containing all f_j entries. It is believed that in particular the time spent generating the global coefficient matrix in the present implementation, which involves a for-loop over all grid nodes that are not interior fluid nodes, can still be reduced by writing as many functions as possible as vector functions instead of scalar functions.

While many quantities are precomputed, such as the local HPC expressions for each cell and the aforementioned reservoir coefficient matrix, enhancements are possible. The key in this respect is to look for anything that is constant or only partially changes with time. It should e.g. be possible to reduce the CPU time involved in evaluating and integrating the fluid pressure over a body, since the locations in which the pressure is computed are constant with respect to the body-fixed grid.

Finally, the numerical solution algorithms used to solve the global matrix equations for φ and its time derivative can be examined. Although the iterative, sparse solvers used here are believed to be efficient, other solvers can be investigated. This is also linked to developments in computational technology. For instance, graphic processing units (GPU) have during the last years shown to be very efficient in the amount of vector operations they can perform per time unit. The efficiency gains that can be achieved through multi-processing have not been investigated in the present work, since it has been a goal to develop a method feasible without the use of a computer cluster. However, most modern computers these days have several cores, and additional enhancement of the computational efficiency is certainly available through better utilizing this fact.

3.4 Summary

A numerical implementation to study wave-propagation and wave-body interaction problems in 2D has been proposed. The harmonic polynomial cell (HPC) method, that is an accurate and efficient field method, is used to solve the hydrodynamic boundary value problems (BVP) within the framework of potential flow. It was shown that the formulation of the BVP for the velocity potential in the HPC method is similar in a body-fixed and in an inertial reference frame. However, the fixed-point time derivative of the velocity potential in a body-fixed reference frame differs from that in an inertial reference. This has consequences for the BVP of the time derivative of the velocity potential. The free surface and the boundary of a rigid body were accounted for using an immersed boundary method (IBM). This allows arbitrary body shapes to be modelled in a more efficient manner than applying a body-fitted grid. Studies have shown that the accuracy in the HPC method is superior when the grid cells are square or close to square, and the IBM ensures that this condition always can be fulfilled.

To refined the numerical solution locally in a straightforward manner without excessively increasing the number of cells, using square cells, the idea of domain-decomposition (DD) was introduced. In the domains that need additional refinement, here defined as near a moving wavemaker and near a rigid body, the hydrodynamic problem is formulated in body-fixed reference frames. The grids in these regions overlap with a stationary background grid, where the hydrodynamic problem is formulated in an Earth-fixed inertial reference frame. The simultaneous application of the IBM and the domain-decomposition method is denoted as an immersed boundary-overlapping grid method (IBOGM). Although the individual modelling concepts in the IBOGM are not new, the combination of these with the HPC method represents an original contribution in the present work.

The details of how to model a free surface, a rigid body and the exchange of information between different computational domains have been outlined. It was explained how the fluid pressure is integrated over the instantaneous wetted surface of a rigid body to obtained pressure loads. Issues influencing the stability of the numerical solution, and means to ensure this in connection with the free-surface evolution and wave-body intersections, were discussed. For a freely floating body, the body motion and the fluid dynamic problem are coupled. An iterative scheme to handle this in time has been presented.

The numerical efficiency of any numerical method is of significant practical interest. Therefore, this aspect was investigated for the IBOGM using a typical wave-body interaction problem as example. The investigation includes an assessment of the distribution of time used between different computational tasks, along with experiences made during the present work, as well as suggestions for further improvement.

In the next chapter, the numerical method described here is used to examine several cases of wave propagation with different types of non-linear features. These include steep waves in deep water, shallow-water waves, solitary waves and a focused wave.

Chapter 4

Wave Propagation Studies

Using the numerical potential-flow framework introduced in Chapter 3, wave-propagation problems characterised by different sources of non-linearity are examined. With the objective of verifying and validating the method's ability to propagate non-linear waves accurately, periodic waves with various steepness, generated by a moving piston- or flap-type wavemaker, or with initial free-surface properties specified, are considered. Three special shallow-water scenarios are examined: long periodic waves, solitary waves and focused waves. The accuracy of the numerical solution is compared to theoretical, experimental or numerical reference results.

The semi-Lagrangian free-surface description outlined in Section 3.2.1 is used throughout the chapter, since there are no rigid bodies with curved geometries involved. All cases except the one in Section 4.3 are documented in Hanssen et al. (2018), where the numerical method here used to model the free surface was compared with an alternative strategy using overlapping, free-surface fitted grids, also within the framework of the HPC method.

4.1 Propagation of Periodic Waves over a Long Time Scale

Propagation of periodic waves in a wave tank with periodic boundary conditions and finite water depth is considered. By applying periodic boundary conditions, an infinitely long wave tank is approximated numerically by modelling the hydrodynamic problem in a computational domain with length equal to the wavelength λ of the propagating waves illustrated in Figure 4.1. This assumes that the waves are stationary, so that λ does not change with time.

The wave propagation is initialized by specifying the values of the wave elevation ζ and free-surface potential φ_{fs} from the higher-order solution given by Rienecker and Fenton (1981) at $t = 0$. This builds on Dean's stream function theory, and represents steadily progressing periodic waves in a potential flow over a flat seabed as a finite Fourier series. The number of Fourier components required to give a converged representation depends on the non-linear features of the wave. In the present work we include the first 20 Fourier components. For $t > 0$, the free surface is evolved in time applying the RK4 scheme described in Section 3.2.10.

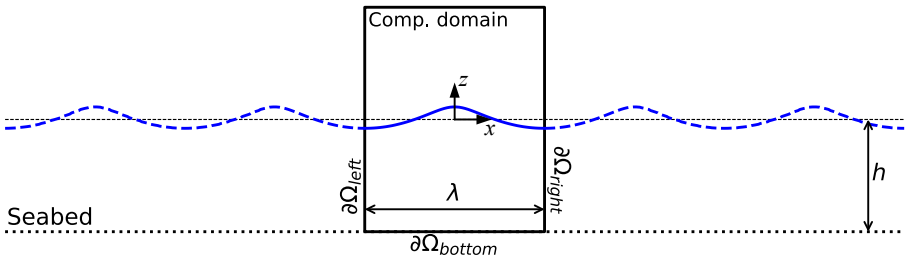

Figure 4.1: Illustration of periodic waves propagating in an infinitely long wave tank modelled by a restricted computational domain with periodic boundary conditions along the boundaries $\partial\Omega_{left}$ and $\partial\Omega_{right}$. The Oxz coordinate system has horizontal origin in the middle of the computational domain with vertical origin in the still waterline.

The free surface is tracked by following markers with the semi-Lagrangian description given in Section 3.2.1. With reference to Figure 4.1, the entire computational domain is denoted Ω. The free surface is treated as an immersed boundary in a structured grid, so that the computational domain at any time consists of an active part Ω_a and an inactive part Ω_i. The conditions enforced for the velocity potential along the boundaries of the active part of the computational domain are as follows:

$$\begin{array}{lll} \varphi = \varphi_{\partial\Omega_{right}} & \text{on} & \partial\Omega_{left} \subseteq \Omega_a \\ \varphi = \varphi_{\partial\Omega_{left}} & \text{on} & \partial\Omega_{right} \subseteq \Omega_a \\ \varphi = \varphi_{fs} & \text{on} & \partial\Omega_{fs} \subseteq \Omega_a \\ \frac{\partial\varphi}{\partial z} = 0 & \text{on} & \partial\Omega_{bottom} \end{array} . \tag{4.1}$$

$\partial\Omega_{fs}$ is here the free surface at its instantaneous position. Since the wave propagation is initialized from a specified theoretical steady-state solution, the method's ability to propagate waves over a long distance, without possible inaccuracies due to wave generation by a moving wavemaker, can be investigated. The theoretical solution by Rienecker and Fenton (1981) is in the following considered as an analytical solution, and is used to evaluate the error of the numerical solution. At any given time t, the numerical error of ζ and φ_{fs} is estimated from the $|L_2|$ norm. The $|L_2|$ norm of a generic variable χ, that can be either the free-surface elevation or the free-surface potential, is defined as

$$|L_{2,\chi}(t)| = \left(\frac{\sum_{i=1}^{N_m} |\chi_{num}(x_i,t) - \chi_{ana}(x_i,t)|^2}{\sum_{i=1}^{N_m} |\chi_{ana}(x_i,t)|^2} \right)^{1/2} . \tag{4.2}$$

Here, χ_{num} and χ_{ana} are numerical and analytical values of χ, respectively, evaluated at the horizontal position x_i of the N_m free-surface markers. The conservation of fluid volume $\epsilon_V(t)$ is estimated from the expression

$$\epsilon_V(t) = \frac{1}{V_0} \int_{L_x} \zeta(x,t) dx, \tag{4.3}$$

where L_x is the length of the computational domain and $V_0 = L_x h$ with h the water depth. We also estimate the energy per unit length of Ω, $E(t) = PE(t) + KE(t)$, associated with the free-surface process. $PE(t)$ and $KE(t)$ are defined as

$$PE(t) = \frac{1}{L_x} \int_{L_x} g[\zeta(x,t) - \overline{\zeta}(t)]dx \tag{4.4}$$

and

$$KE(t) = \frac{1}{2L_x} \int_{L_x} |\nabla \varphi_{fs}(x,t)|^2 dx, \tag{4.5}$$

where g is the acceleration of gravity and $\overline{\zeta}(t)$ is the mean wave elevation. The integrals in (4.3), (4.4) and (4.5) are evaluated using numerical integration.

The length of Ω and the water depth are set to $L_x = \lambda = 10\ m$ and $h = 5\ m$, respectively. The height of the computational domain is $2h$, and since there are no wavemaker or rigid bodies in the tank, no overlapping grids are present. The discretization of the computational domain is characterized by the number of grid nodes per wavelength in x and z-direction denoted as n_x and n_z, respectively. Only grids with square cells are considered, so that $n_x = n_z$. Four evenly spaced values of the wave steepness $k\zeta_a$ in the range 0.1 to 0.4, where k is the wave number, are analyzed. For each wave steepness, the convergence of the numerical solution is assessed by performing analysis for four values of $n_x = n_z$ in the range $15 - 90$. $k\zeta_a = 0.1$ represents a wave with moderate non-linearity, while the wave with $k\zeta_a = 0.4$ is rather steep and close to the kinematic breaking-criterion given by Mei et al. (2005). This states that a wave breaks when the horizontal wave particle velocity in the crest exceeds the phase speed of the wave. Using a Stokes representation to approximate the wave, the maximum wave height H before a wave breaks in finite water depth is estimated as

$$\left(\frac{H}{\lambda}\right)_{max} = 0.14 \tanh(kh). \tag{4.6}$$

For the present case with $h = 0.5\lambda$, this means $(k\zeta_a)_{max} \approx 0.438$. In other words, the waves with $k\zeta_a = 0.4$ are close to the limit of the waves that can be modelled with the present numerical potential-flow method in terms of wave steepness. The wave period, estimated from the analytical solution, decreases from $T = 2.52\ s$ for $k\zeta_a = 0.1$ to $T = 2.34\ s$ for $k\zeta_a = 0.4$. The time step is set to a fixed value of $\Delta t = 0.01\ s$, giving approximately 250 time steps per wave period T. This time step represents a temporal refinement that may lead to inefficient simulations, and that may be unnecessary, in cases with larger computational domain. It is chosen here based on the sensitivity analysis performed by Hanssen et al. (2018), so that the spatial convergence can be studied with confidence that the results are temporally converged.

The time evolution of the parameters $|L_{2,\zeta}|$, $|L_{2,\varphi_{fs}}|$, ϵ_V and E are shown in Figures 4.2 - 4.5 for the four values of $k\zeta_a$. The results denoted as *Analytical* are obtained by applying (4.3), (4.4) and (4.5) directly to the analytical solution. For $0.1 \leq k\zeta_a \leq 0.3$, the errors of ζ and φ_{fs} measured by their respective $|L_2|$ norms decrease with decreasing grid size. The increase with time can likely be denoted

to a small phase error, which is confirmed by the careful analysis performed for a similar case by Ma et al. (2018). The oscillatory behaviour seen for ϵ_V and E is caused by the fact that the leftmost free-surface marker in the computational domain, that is identical to the rightmost marker in the domain, was omitted in the numerical integrations. This is confirmed by similar oscillations in the analytical results. For $k\zeta_a \leq 0.3$, the most refined grids for each wave steepness give ϵ_V and E values that are visually converged to the analytical solution.

For $k\zeta_a = 0.4$, it can be observed that $|L_{2,\zeta}|$ is lower for $n_x = n_z = 60$ than for $n_x = n_z = 75$. Although the difference is small when we consider the logarithmic scale in the plots, this is indeed unexpected. The observation is possibly connected with the immersed-boundary modelling of the free surface, since the accuracy of the numerical solution in the HPC method generally varies with the location within each cell. Numerical instabilities start to grow after $t/T \approx 30$ for the three highest values of $n_x = n_z$ for $k\zeta_a = 0.4$. Hanssen et al. (2018) found that these instabilities were of sawtooth-type and developed close to the wave crest. The instabilities were kept at a moderate level for a long time when a 12^{th} order Savitsky-Golay filter was used to smooth the free surface after every time step. This filter is also used in the results presented here. Without smoothing the free surface, the instabilities grow rapidly after their onset and the simulations break down shortly after.

It is difficult to interpret the convergence rate with respect to the grid spacing from Figures 4.2 - 4.5. $|L_{2,\zeta}|$ and $|L_{2,\varphi_{fs}}|$ are therefore plotted as a function of grid spacing for two different time instants in Figure 4.6 together with exponential curves fitted through the $|L_2|$ norms for each separate wave steepness. The exponents of the curve fits, which estimate the convergence rate, are listed in Table 4.1. Except for with $k\zeta_a = 0.2$, both $|L_{2,\zeta}|$ and $|L_{2,\varphi_{fs}}|$ have more than 3^{rd} order convergence in the grid spacing at $t/T = 0.1$. This corresponds well with the fact that the HPC method has between 3^{rd} and 4^{th} order spatial accuracy. At $t/T = 10$, the convergence rate is on average slightly reduced. One reason may be that temporal errors are more influential at $t/T = 10$ than at $t/T = 0.1$, since the latter time instant is closer to the start of the simulation. The results for $k\zeta_a = 0.2$ differ from the other values of $k\zeta_a$ in that the convergence rates generally are lower, especially for $|L_{2,\zeta}|$ at $t/T = 10$. The reason for this is not fully understood, but may possibly be due to the immersed-boundary modelling. More specifically, it is possible that this wave steepness gives a particularly favourable or unfavourable configuration of the free surface relative to the cells for different grid spacings. One should nevertheless bear in mind that the errors for $k\zeta_a = 0.2$ can be considered moderate.

In general it is found that the magnitudes of the errors increase with wave steepness. This is in accordance with expectations, since waves with high steepness generally are more computationally challenging to model than waves with low steepness. However, it should be noted that the convergence rates do not decrease systematically with increasing wave steepness. This indicates that the higher-order spatial accuracy of the HPC method is preserved also in wave-propagation problems where the waves have significant non-linear features.

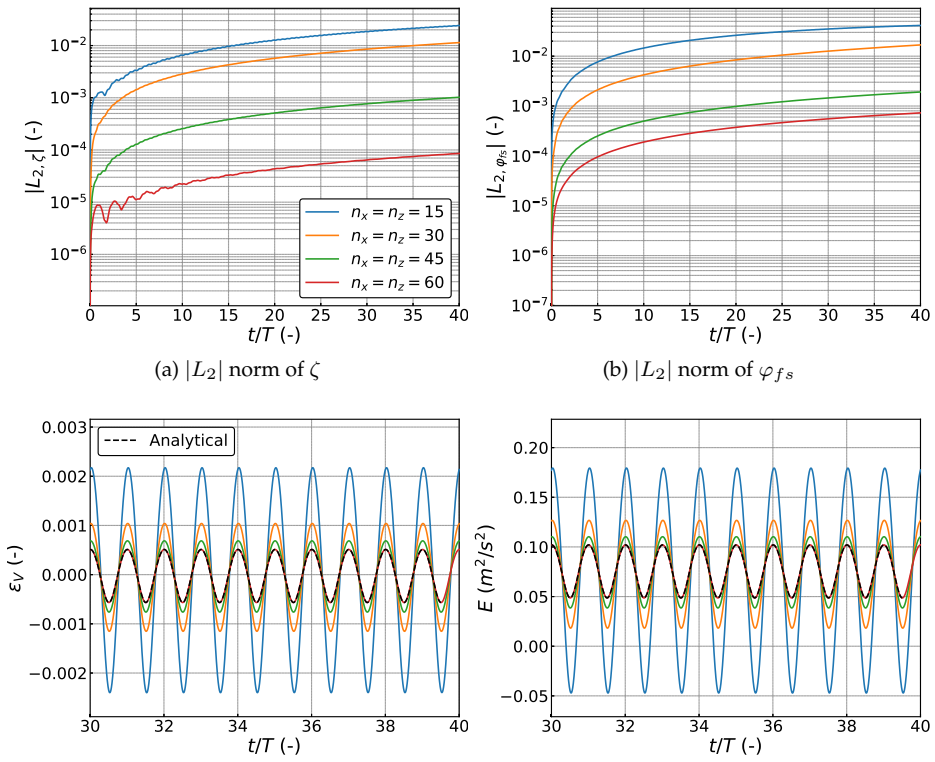

(a) $|L_2|$ norm of ζ

(b) $|L_2|$ norm of φ_{fs}

(c) Conservation of fluid volume

(d) Conservation of fluid energy

Figure 4.2: Time traces of $|L_{2,\zeta}|$, $|L_{2,\varphi_{fs}}|$, ϵ_V and E for a wave with steepness $k\zeta_a = 0.1$ propagating in a wave tank with periodic boundary conditions.

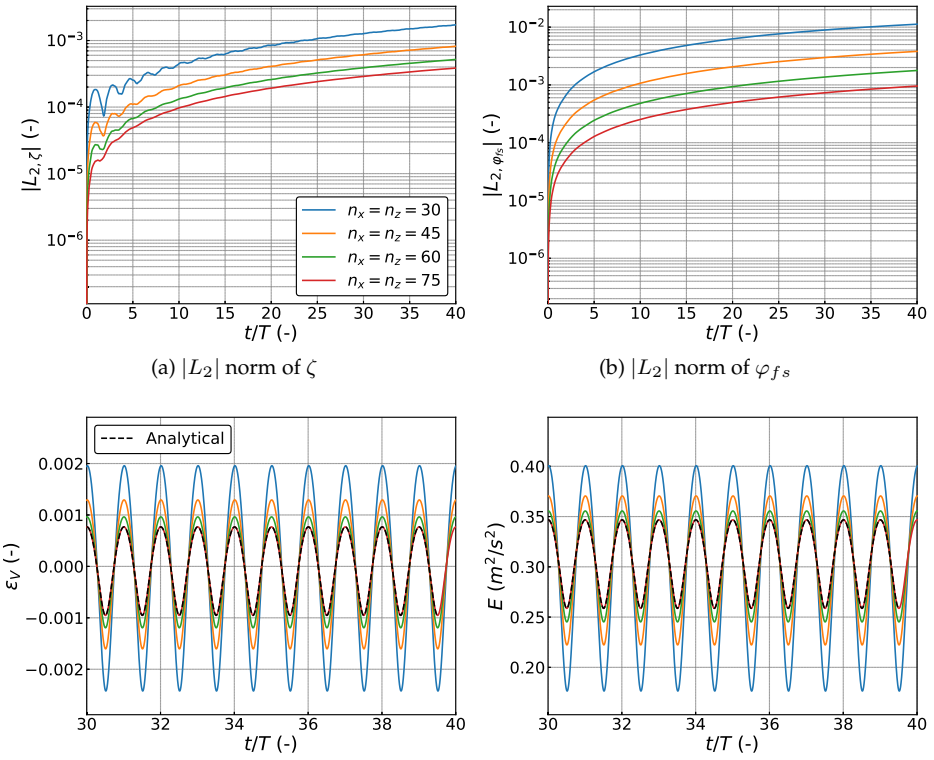

(a) $|L_2|$ norm of ζ

(b) $|L_2|$ norm of φ_{fs}

(c) Conservation of fluid volume

(d) Conservation of fluid energy

Figure 4.3: Time traces of $|L_{2,\zeta}|$, $|L_{2,\varphi_{fs}}|$, ϵ_V and E for a wave with steepness $k\zeta_a = 0.2$ propagating in a wave tank with periodic boundary conditions.

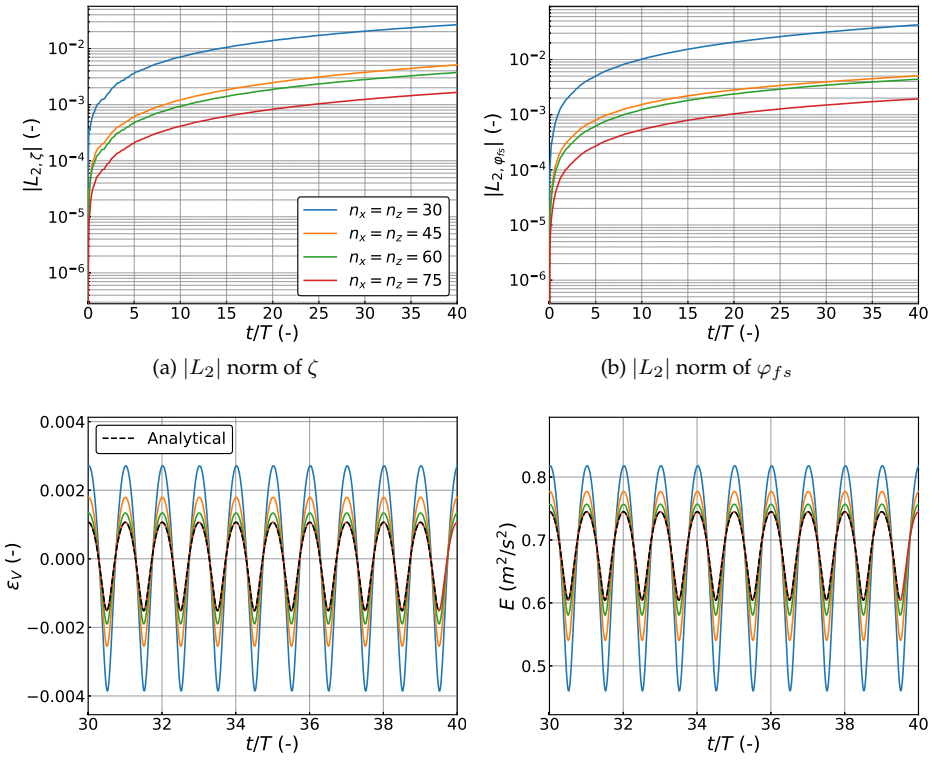

(a) $|L_2|$ norm of ζ

(b) $|L_2|$ norm of φ_{fs}

(c) Conservation of fluid volume

(d) Conservation of fluid energy

Figure 4.4: Time traces of $|L_{2,\zeta}|$, $|L_{2,\varphi_{fs}}|$, ϵ_V and E for a wave with steepness $k\zeta_a = 0.3$ propagating in a wave tank with periodic boundary conditions.

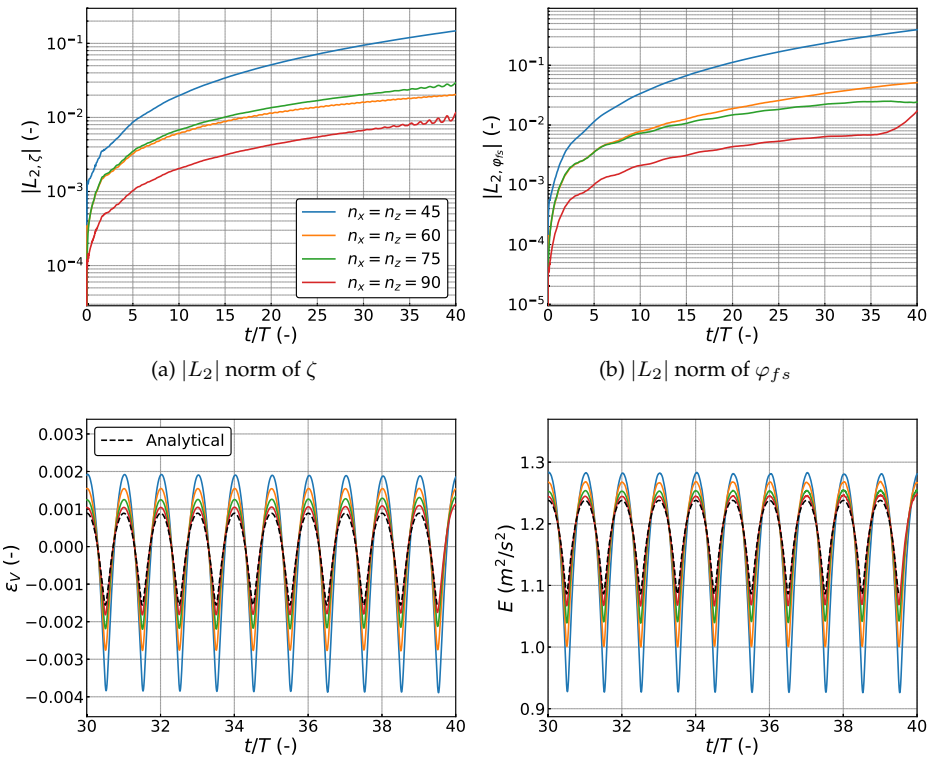

(a) $|L_2|$ norm of ζ

(b) $|L_2|$ norm of φ_{fs}

(c) Conservation of fluid volume

(d) Conservation of fluid energy

Figure 4.5: Time traces of $|L_{2,\zeta}|$, $|L_{2,\varphi_{fs}}|$, ϵ_V and E for a wave with steepness $k\zeta_a = 0.4$ propagating in a wave tank with periodic boundary conditions.

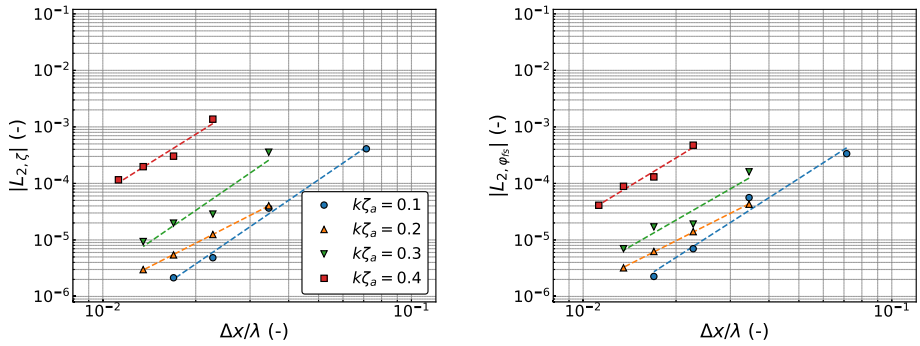

(a) $|L_2|$ norm of ζ at $t/T = 0.1$

(b) $|L_2|$ norm of φ_{fs} at $t/T = 0.1$

(c) $|L_2|$ norm of ζ at $t/T = 10$

(d) $|L_2|$ norm of φ_{fs} at $t/T = 10$

Figure 4.6: $|L_{2,\zeta}|$ and $|L_{2,\varphi_{fs}}|$ plotted as function of grid spacing Δx for a wave propagating in a wave tank with periodic boundary conditions for time instants $t/T = 0.1$ and $t/T = 10$, where T is the wave period. The dashed lines show exponential curve fits.

Table 4.1: Exponent in curve fits in Figure 4.6.

$k\zeta_a$	$t/T = 0.1$		$t/T = 10$	
	$\lvert L_{2,\zeta}\rvert$	$\lvert L_{2,\varphi_{fs}}\rvert$	$\lvert L_{2,\zeta}\rvert$	$\lvert L_{2,\varphi_{fs}}\rvert$
0.1	3.74	3.51	3.78	3.08
0.2	2.79	2.76	1.64	2.74
0.3	3.75	3.14	2.88	2.98
0.4	3.42	3.32	2.84	3.58

In order to better understand the nature of the numerical errors discussed above, the wave elevation is plotted against the analytical solution at $t/T = 20$ for $k\zeta_a = 0.1$ and $k\zeta_a = 0.4$ in Figure 4.7. While, for the finest grid, the numerical and analytical solutions are visually similar for both $k\zeta_a$ values, there is a visible difference for $k\zeta_a = 0.4$ with the coarsest grid. The phase error is more pronounced

than the amplitude error, and is likely due to a dispersion error that occurs when the fluid particle velocities close to the free surface are not estimated with sufficient accuracy. Because $k\zeta_a = 0.4$ represents a wave with significant non-linear properties, accurate estimation of particle velocities requires a denser grid than for the wave with $k\zeta_a = 0.1$.

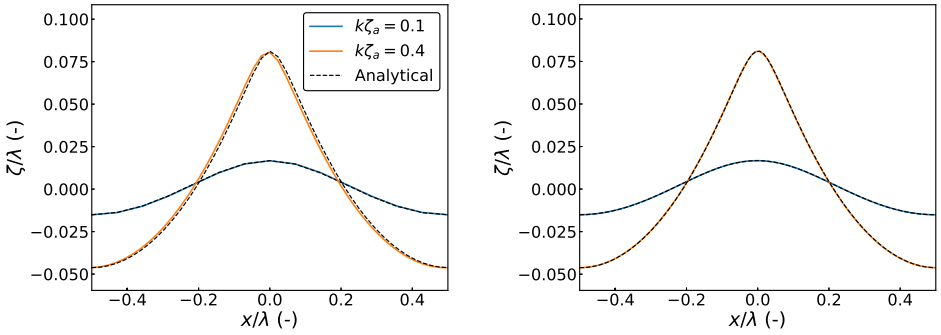

(a) Coarsest grid

(b) Finest grid

Figure 4.7: Wave elevation for waves with $k\zeta_a = 0.1$ and $k\zeta_a = 0.4$ propagating in a wave tank with periodic boundary conditions at the time instant $t/T = 20$ for the coarsest and finest grids used for each wave. The x position and wave elevation ζ are both normalized against the wavelength λ.

The studies here performed for periodic waves in an infinite wave tank show that the HPC method combined with an immersed-boundary modelling of the free surface is able to propagate waves with both low and high steepness accurately over a long time. The spatial convergence properties of the HPC method are found to be well maintained by the free-surface modelling. As one would expect, the grid spacing required to obtain a certain accuracy decreases with increasing wave steepness. In general, it is found that around 30 grid points per wavelength are sufficient to give accurate simulations for waves with steepness up to approximately $k\zeta_a = 0.3$.

4.2 Wave Generation with a Flap-Type Wavemaker for Periodic Waves in Deep Water

Lugni (1999) performed experiments with periodic deep-water waves in a long wave tank with water depth h equal to $3.6\ m$. Waves with steepness $k\zeta_a = \{0.10, 0.15, 0.20\}$ were generated by a flap-type wavemaker hinged at half the water depth. We here perform numerical analyses with waves generated by imposing the angular flap motions shown in Figure 4.8, that coincide with the flap motions used in the experiments.

The wave tank used in the numerical analysis is depicted in Figure 4.9. The water depth and the hinge point of the flap-type wavemaker are set equal to those in the experiments. The length of the tank is restricted to $25\ m$ and with a numerical

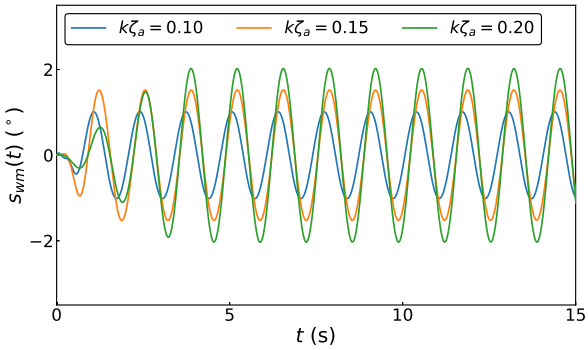

Figure 4.8: First part of time histories for angular flap-wavemaker motion s_{wm} used in experiments by Lugni (1999) to generate periodic deep-water waves with steepness $k\zeta_a = \{0.10, 0.15, 0.20\}$.

beach with damping coefficient $\nu_{max} = 2.0\ s^{-1}$ modelled at opposite side of the wavemaker. The length of the beach is taken as approximately three times the incident wavelength $\lambda \approx 2.8\ m$. Both the stationary background grid and the body-fixed grid following the motion of the wavemaker are uniform with grid spacing $\Delta x = \Delta z = 0.1\ m$, giving approximately 28 grid points per wavelength. This is consistence with the recommendations given towards the end of Section 4.1. The time step is set to $\Delta t = 0.033\ s$, i.e. approximately 40 time steps per wave period.

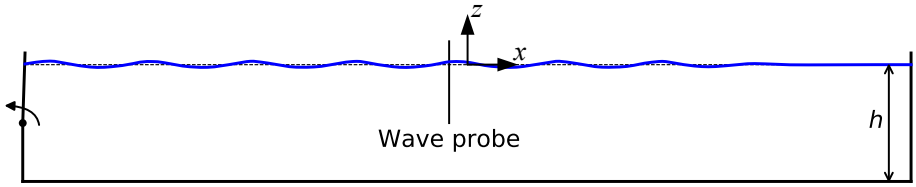

Figure 4.9: Sketch of wave tank with water depth h used in numerical analysis to propagate deep-water periodic waves. The wave elevation is recorded in a wave probe located at $(x - x_{wm}) = 12\ m$, where x_{wm} is the position of the flap-type wavemaker at rest. The global Oxz coordinate system is located in the middle of the computational domain with origin in the still waterline. The x and z-axes are not in scale 1:1.

The wave elevations in the wave probe located $12\ m$ from the wavemaker are compared with the results recorded during the experiments in Figure 4.10. In particular for $k\zeta_a = 0.10$ and $k\zeta_a = 0.20$, the results from the present analysis are in close agreement with the experiments. This includes both the transient phase, characterized by an amplified leading wave crest, and the steady-state behaviour thereafter. For reasons that are unknown, the crests are slightly higher and the troughs slightly shallower in the numerical results compared with the experiments in the steady-state part of the time series for $k\zeta_a = 0.15$. The error in

the crest and trough magnitudes are approximately similar, so that the two signals differ mainly by their mean values.

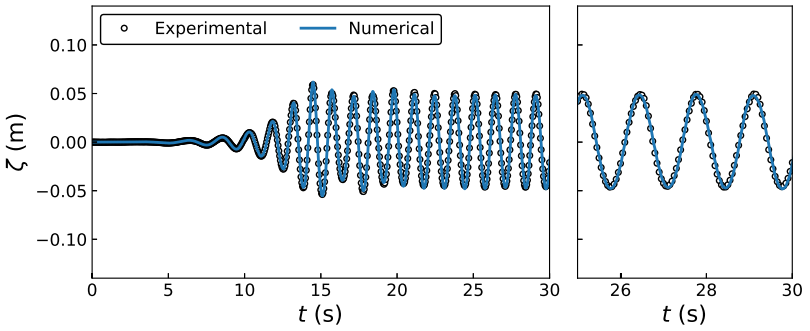

(a) $k\zeta_a = 0.10$

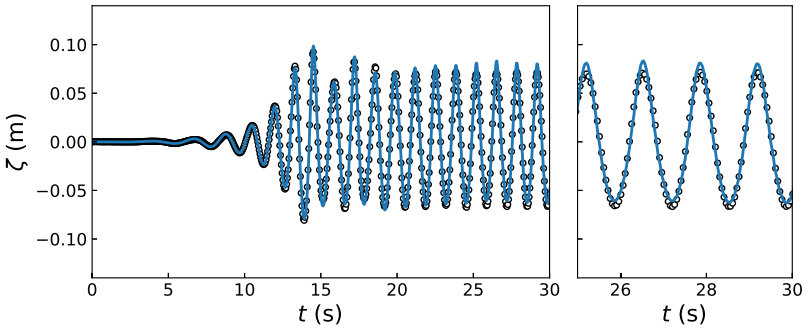

(b) $k\zeta_a = 0.15$

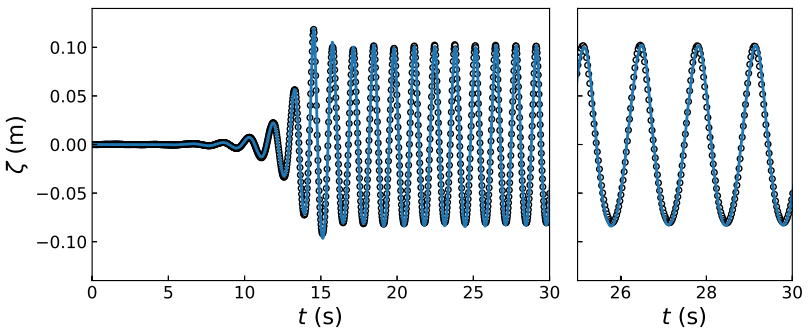

(c) $k\zeta_a = 0.20$

Figure 4.10: Time series of wave elevation for periodic deep-water waves with steepness $k\zeta_a = \{0.10, 0.15, 0.20\}$ in a wave probe located 12 m from the position of the wavemaker. The experimental results are from Lugni (1999) and the numerical results are from the present analysis.

While the waves with $k\zeta_a = 0.10$ are close to linear, the waves with $k\zeta_a = 0.20$ are relatively steep with significant trough-to-crest asymmetry. The results in Figure 4.10 do therefore show that, knowing the exact details of the wavemaker signal, the numerical method used here is fully capable of reproducing non-linear deep-water waves accurately over a long time scale.

4.3 Propagation of Steep Periodic Waves and Growth of the Leading Wave

Baarholm (2001) performed experiments with periodic, steep waves in a wave flume $13.5\ m$ m long, $0.6\ m$ wide and with a water depth h equal to $1.0\ m$ with the objective of studying wave impacts on deck structures with low clearance to the still-water level. The wave elevation was measured in a single wave probe that we here assume was located in the middle of the tank, although Baarholm states that the location of the wave probe sometimes was changed between cases. The three cases described in Table 4.2 are considered. In order to get an impression of how steep these waves are, the crest amplitudes are plotted together with the breaking criterion given by expression (4.6) in Figure 4.11. Clearly, the case n30_004, that also has the highest value of the steepness estimate $k\zeta_c$, is closest to the breaking limit. Here ζ_c represents the crest amplitude, consistent with the notation used by Baarholm (2001).

Table 4.2: Selected cases from Baarholm (2001), with the same notation as used in the reference, for propagation of steep periodic waves. ω is the angular wave frequency, λ is the wavelength, ζ_c is the crest amplitude and k is the wave number. It is noted that, near breaking, ζ_c is not equal to half the wave height.

Case	$\omega\ (s^{-1})$	$\lambda\ (m)$	$\zeta_c\ (m)$	$k\zeta_c\ (-)$
d03_003	6.28	1.56	0.080	0.322
n30_004	6.28	1.56	0.093	0.375
n30_008	5.03	2.41	0.089	0.232

The waves in the experiments were generated by a flap-type wavemaker hinged $0.1\ m$ above the sea bed. Neither the stroke or the ramp period of the wavemaker is known. We here assume a ramp time of $5\ s$, while the wavemaker's angular stroke $s_{wm,a}$ is iterated on until a satisfactory agreement with the experiments is reached. The following values are used for $s_{wm,a}$: $3.209°$ for d03_003, $3.638°$ for n30_004 and $4.498°$ for n03_008. The frequency of the flap motion is taken equal to ω in Table 4.2. The time step Δt and grid spacing $\Delta x = \Delta z$ are set to $0.02\ s$ and $0.05\ m$, respectively, for all three cases. Similar grid spacings are used in the stationary background grid and in the body-fixed grid moving with the motion of the flap-type wavemaker. This ensures at least 30 time steps per wave period and at least 31 grid points per wavelength. The latter is consistent with the recommendations given towards the end of Section 4.1. The length of the wave tank is increased to $16.5\ m$ in the numerical analysis, in order to allow for a $6\ m$ long numerical beach with damping coefficient $\nu_{max} = 2.0\ s^{-1}$ to be located

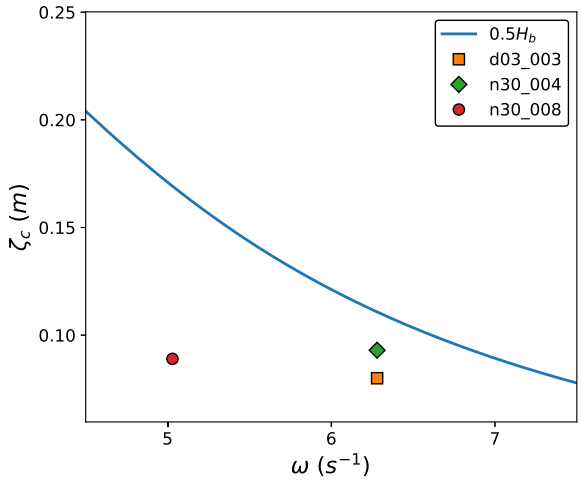

Figure 4.11: Waves from Table 4.2 plotted together with the breaking criterion given by expression (4.6). H_b is the breaking-wave height and ζ_c is the crest amplitude. It is noted that near breaking, $\zeta_c \neq 0.5H_b$.

at the opposite side of the wavemaker without disturbing the wave measured in the middle of the tank.

The wave elevation in the probe located $6.25\ m$ from the position of the wavemaker at rest is compared with the experimental results in Figure 4.12. Considering that there is uncertainty related to both the wavemaker signal and the position of the wave probe used in the experiments, the agreement between the numerical and experimental results is satisfactory. The largest deviations are observed for the case n30_004, i.e. the case closest to breaking in Figure 4.11. To propagate such steep waves accurately represents a challenge also in experimental work, and it is likely that at least some of the observed differences between the experimental and numerical wave elevation are due to this.

In relation with the present analysis, it is discovered that several wavelengths away from the wavemaker, the crest of the leading wave in the wave train may grow very steep and even cause numerical instability. In order to further examine this phenomenon, the case d03_003 is revisited by elongating the wave tank to $25\ m$, leaving the other simulation parameters unchanged. Snapshots of the wave elevation plotted as a function of distance from the wavemaker are shown in Figure 4.13. As indicated by the envelope curve, the crest-amplitude starts to grow approximately 5λ from the wavemaker. Shortly after $t = 17\ s$, the simulation becomes unstable and breaks down due to the rapid increase of the leading-wave crest.

In order for the simulation to remain stable, the stroke of the wavemaker is reduced by 25%. The envelope curve in Figure 4.14 clearly shows that the leading wave systematically increases with distance from the wavemaker, and the magnitude of the crest increases more than the magnitude of the trough.

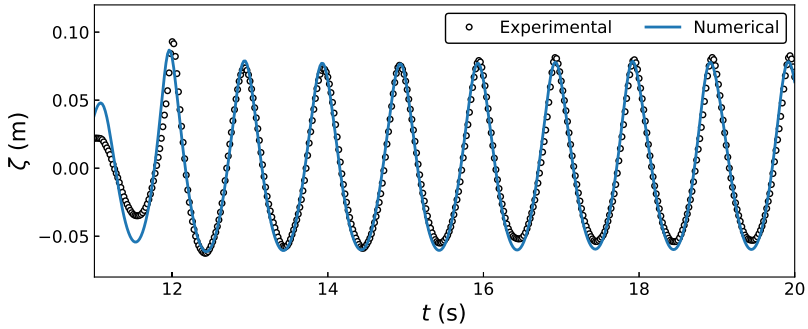

(a) Case d03_003

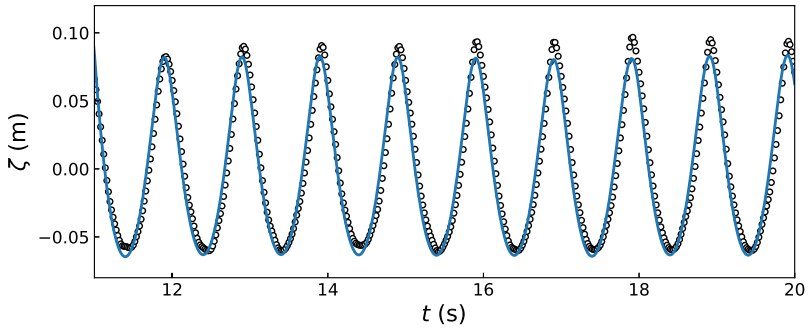

(b) Case n30_004

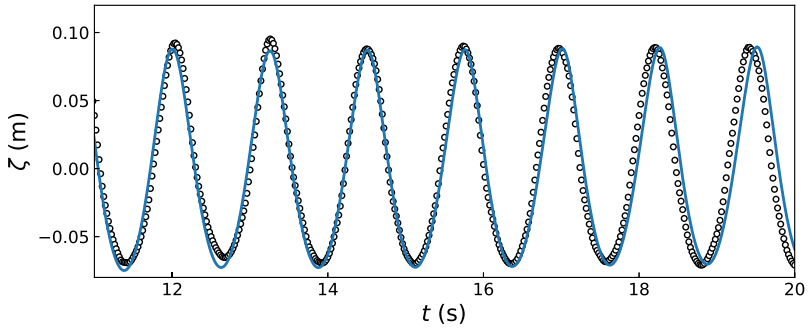

(c) Case n30_008

Figure 4.12: Time series of wave elevation for the cases in Table 4.2 studied experimentally by Baarholm (2001). The wave elevation is plotted in a wave probe located $6.25\ m$ from the position of the wavemaker. It is noted that B-spline interpolation is used to increase the spatial sampling density of the experimental results.

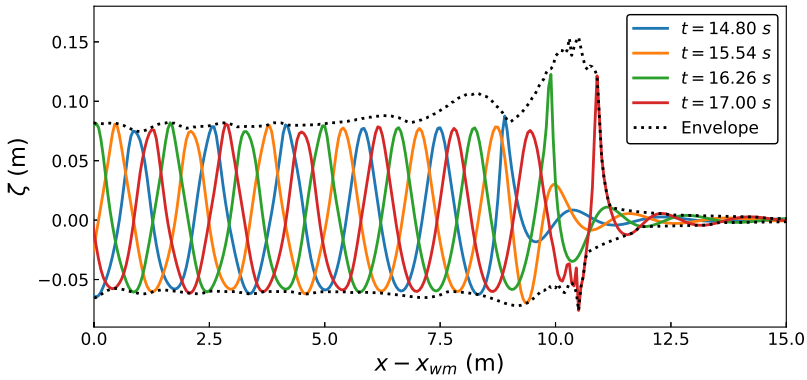

Figure 4.13: Snapshots of wave elevation at different time instances t plotted as a function of distance from the position x_{wm} of the wavemaker for case d03_003 in a $25\ m$ long wave tank. The envelope curve indicates the minimum and maximum wave elevation at each x location for any t.

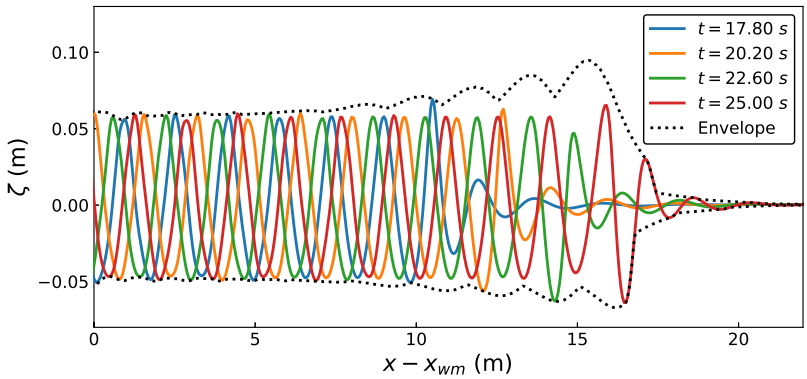

Figure 4.14: Snapshots of wave elevation at different time instances t plotted as a function of distance from the position x_{wm} of the wavemaker for case d03_003 with 25% reduced wavemaker stroke in a $25\ m$ long wave tank. The envelope curve indicates the minimum and maximum wave elevation at each x location for any t.

By studying different configurations of the numerical beach, and different tank lengths, it is ruled out that the observed growth of the leading wave in Figure 4.14 is related to wave reflections. However, it is found that increasing the ramp-up time for the wavemaker may postpone the time until the leading wave shows significant growth. The growth of the leading wave in a wave train was also found by Clamond and Grue (2000), who performed numerical simulations of the phenomenon motivated by experimental observations. As the authors point out, this behaviour is not captured by higher-order analytical wave theories. They

observed that the amplitude of the leading wave had an oscillatory trend, amplifying with time until the point of breaking. The latter is interpreted as the time when numerical instability occurs, similar to the scenario in Figure 4.13. It is likely that the growth of the leading wave is due to non-linear dispersion related to the transient ramp-up of the wavemaker, leading to focusing of energy near the front of the wave train. Indeed, the fact that modifying the wavemaker ramp-up time influences the behaviour supports such argument. Being outside the scope of the present work, the phenomenon is not further examined.

4.4 Non-Linear Dispersion in Periodic Shallow-Water Waves

The experimental work of Chapalain et al. (1992) is now considered. Generating waves with a harmonically oscillating piston-type wavemaker in a $35.54\ m$ long and $0.55\ m$ wide wave channel with water depth h set equal to $0.4\ m$, they studied the transformation of long waves with moderate steepness due to non-linear interaction between different harmonic modes in shallow water. The motion of the wavemaker is described by

$$s_{wm}(t) = -s_{wm,a} \cos \omega_{wm} t, \tag{4.7}$$

where $s_{wm,a}$ is the wavemaker stroke and ω_{wm} is the angular oscillation frequency. Numerical analyses are performed for the two cases in Table 4.3. Uniform grids with grid spacing $\Delta x = \Delta z = 0.08\ m$ are used for both cases, giving approximately 60 and 85 grid points per wavelength for cases A and C, respectively, with the wavelength estimated from the finite-water depth linear dispersion relation. This is a finer grid than strictly found necessary in Section 4.1, however, we here anticipate that higher-order wave components arise as the waves propagate. The time step is taken as $\Delta t = 0.08\ s$, giving more than 30 time steps per wave period for both the examined cases.

Table 4.3: Selected cases from Chapalain et al. (1992), with the same notation as used in the reference, for propagation of shallow-water waves. $s_{wm,a}$ and ω_{wm} are the wavemaker stroke and angular frequency, respectively, used in (4.7).

Case	$s_{wm,a}\ (m)$	$\omega_{wm}\ (s^{-1})$
A	0.078	2.5133
C	0.113	1.7952

Chapalain et al. (1992) do not give any information regarding the start-up of the wavemaker. In the numerical analysis, a ramp function as defined in the expression (3.32) is used together with a ramp time $T_{ramp} = 2 \cdot 2\pi/\omega_{wm}$. No beach was used on the opposite side of the wavemaker in the experiments, which according to the authors is to avoid parasitic wave reflections. Thus, only the wave elevation in the first $25\ m$ of the channel was used in post-processing of the experimental waves. This gives a sufficient time window to perform harmonic analysis before the waves are reflected back from the tank wall opposite of the wavemaker.

In the numerical analysis, the accuracy of the post-processing improves by having longer time series before reflected waves start to influence the wave elevation in the first $25\ m$ of the channel. A $45\ m$ long numerical wave tank is therefore used in the analysis. In order to be consistent with the experiments, no numerical damping zone is used.

The wave-elevation time series is recorded in fixed wave probes distributed over the first $25\ m$ of the tank. For each of these time series, the first four harmonic wave amplitudes $\zeta_a^{(i)}, i = 1, ..., 4$ are calculated by Fourier analysis. Only the steady-state part of the wave elevation in each probe is used, i.e. the part of the time series after initial transient waves have passed, and before waves are reflected back. The present results are compared with the experimental results, in addition to the numerical results by Shao and Faltinsen (2012). They also used the HPC method, but in contrast to the present work, the grid was stretched vertically to deform with the motion of the free surface.

The harmonic wave amplitudes are plotted as a function of distance from the wavemaker in Figure 4.15. For case A, the results from the present analysis are found to be in reasonable agreement with the experiments except for an apparent phase shift in the 2^{nd} harmonic. This phase shift is also to some extent seen in the results by Shao and Faltinsen (2012), who predict slightly lower values for the 1^{st} harmonic compared to the present analysis. Larger differences between the present results and the experimental results are observed for case C, particularly for the 1^{st} harmonic where the difference increases with distance from the wavemaker. A possible explanation is viscous dissipation in the experiments. Shao and Faltinsen (2012) added an artificial dissipation term in the free-surface conditions to model this, resulting in a better agreement with the experiments for the 1^{st} harmonic away from the wavemaker.

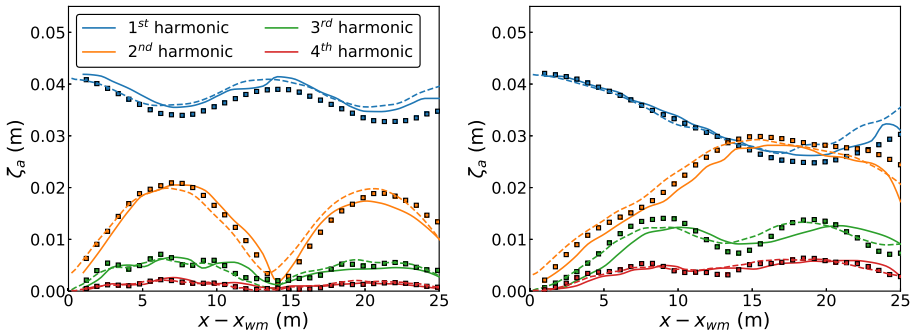

(a) Case A

(b) Case C

Figure 4.15: Harmonic wave amplitudes for shallow-water wave cases defined in Table 4.3 plotted as function of distance from the nominal position x_{wm} of the piston-type wavemaker. Full lines indicate the experimental results by Chapalain et al. (1992), square symbols indicate the numerical results by Shao and Faltinsen (2012) and the dashed lines indicate the results obtained in the present analysis.

Due to the dimensions of the wave channel where the experiments were performed, there are some possible sources of uncertainty. Due to the narrowness of the channel, non-negligible viscous effects may arise from the side walls. The length of the tank, and the fact that no beach was present to prevent wave reflections, restrict the duration of the time signal used in the Fourier analysis. Theoretically, the analysis requires at least one full steady-state oscillation to give accurate estimates of the Fourier amplitudes. However, because the wave signal measured in an experiment will always to some degree be polluted, it is reasonable to assume that the accuracy of the estimated Fourier amplitudes increases with the number of oscillation periods used in the analysis. No further efforts are here made to quantify the level of uncertainty in the experiments. The qualitative agreement between the experimental and numerical results does nevertheless indicate that the present method is able to predict the non-linear transfer of energy between different harmonic modes in shallow-water conditions.

4.5 Solitary Wave in Shallow Water

A solitary wave can be described as a single wave crest that travels over a long distance with a constant wave profile. Its existence was first reported by Russell (1844), and several theories have since been suggested to describe solitary waves. We here consider the 9^{th} order approximate solution by Fenton (1972) as an analytical reference solution. The free-surface elevation ζ is expanded in a series with a non-dimensional parameter $\epsilon = A/h$, where A is the amplitude of the solitary wave and h is the water depth. Fenton (1972) concluded that his solution can be accurate for ϵ up to 0.75, however, a practical limit seems to be around 0.6. We here pursue the method proposed by Wu et al. (2014) to generate the solitary wave by a moving piston-type wavemaker that extends all the way down to the seabed. The velocity of the piston is taken equal to the average horizontal fluid-particle velocity under the solitary wave at the instantaneous position of the piston. This can be approximated as

$$\dot{s}_{wm} = \left. \frac{c\zeta}{h+\zeta} \right|_{x=s_{wm}}, \tag{4.8}$$

where c and ζ are the phase speed and surface elevation given by the analytical solution, respectively. The position s_{wm} of the wavemaker is obtained by letting the analytical wave crest initially be located far upstream of the wavemaker, and integrating (4.8) in time as the analytical wave travels towards and beyond the wavemaker. The procedure is further elaborated in Hanssen et al. (2018). One should be aware that this way of generating a solitary wave is approximate, because it assumes that the horizontal fluid-particle velocity is uniform across the water depth at the position of the wavemaker. Wu et al. (2014) claim that (4.8) in combination with Fenton's 9^{th} order solution enables accurate numerical simulations for ϵ up to 0.4. In the following analysis, the free-surface is modelled with the semi-Lagrangian formulation described in Section 3.2.1.

The wavelength associated with the solitary wave is estimated as $\lambda = 2\pi/k$,

where k is the wave number suggested by Rayleigh (Wu et al., 2014) as

$$k = \sqrt{\frac{3A}{4h^2(h+A)}}. \tag{4.9}$$

Numerical analyses are performed for ϵ in the range $0.2-0.6$. A single grid spacing $\Delta x = \Delta z$ is used for all cases, both in the stationary background grid and in the body-fixed grid moving with the piston-type wavemaker, so that $95 \leq \Delta x/\lambda \leq 142$. The time step is fixed at $\Delta t = 0.015\ s$, so that a Courant-Friedrichs-Lewy (CFL) condition (Courant et al., 1928) on the form

$$CFL = \frac{c\Delta t}{\Delta x} \leq 1.0 \tag{4.10}$$

to ensure numerical stability is always satisfied. The water depth is set to $h = 0.4\ m$, and the length of the tank is $30\ m$ without any numerical damping zone. As a consequence, only the part of the time series before the solitary wave reaches the tank wall opposite of the wavemaker is considered in the post-processing. The properties of the considered waves based on the analytical solution and the resulting CFL number in the numerical simulations are summarized in Table 4.4.

Table 4.4: Properties of solitary waves simulated numerically. A is the wave amplitude, λ is the wavelength, c is the phase speed and CFL is the Courant-Friedrichs-Lewy number.

ϵ	0.2	0.3	0.4	0.5	0.6
$A\ (m)$	0.08	0.12	0.16	0.20	0.24
$\lambda\ (m)$	7.11	6.04	5.43	5.03	4.74
$c\ (m/s)$	2.17	2.25	2.33	2.41	2.48
$CFL\ (-)$	0.65	0.68	0.70	0.72	0.74

The free-surface elevation is shown at two different time instants for $0.2 \leq \epsilon \leq 0.6$ in Figure 4.16. For ϵ up to 0.4, both the amplitude, phase and wave form of the numerical solution compare well with the analytical solution. For the two highest values of ϵ, the wave amplitudes are lower than the corresponding analytical values. At the first time instant, noticeable trailing waves follow after the solitary crest for $\epsilon > 0.4$. These are not visible at the later time instant, because the trailing waves travel with lower velocity than the solitary crest as seen in the space-time plots in Figure 4.17. A phase difference that is increasing with time can also be noticed. This indicates that the phase speed in the numerical solution is slightly lower than the analytical value when $\epsilon > 0.4$.

The errors observed in the numerical solution for $\epsilon > 0.4$ are believed to be due to the use of a piston-type wavemaker that forces the horizontal fluid-particle velocity to be uniform for $-h \leq z \leq \zeta$ at the position of the wavemaker, which is unphysical when ϵ increases and non-linear effects become more significant. This is illustrated in Figure 4.18, where the horizontal fluid-particle velocity u_x computed with a 3^{rd} order approximate solution given by Fenton (1972) is plotted as

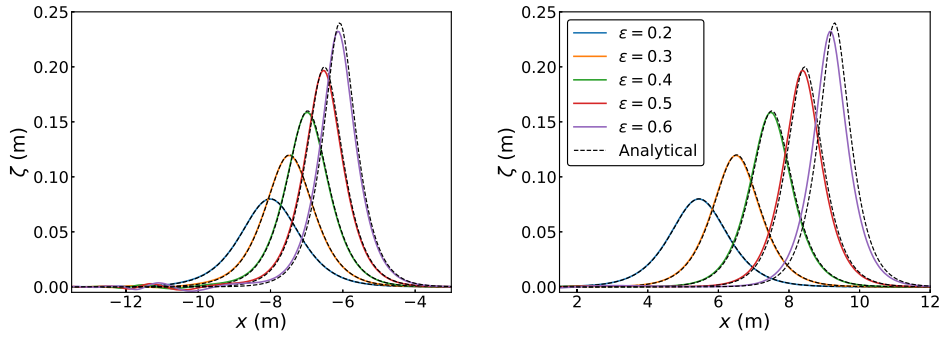

(a) $t = 6.22\ s$ (b) $t = 12.44\ s$

Figure 4.16: Wave elevation for solitary waves with $0.2 \leq \epsilon \leq 0.6$ as function of the horizontal coordinate x at two different time instants. x has origin in the middle of the tank. The analytical solution is the 9^{th} order solution by Fenton (1972).

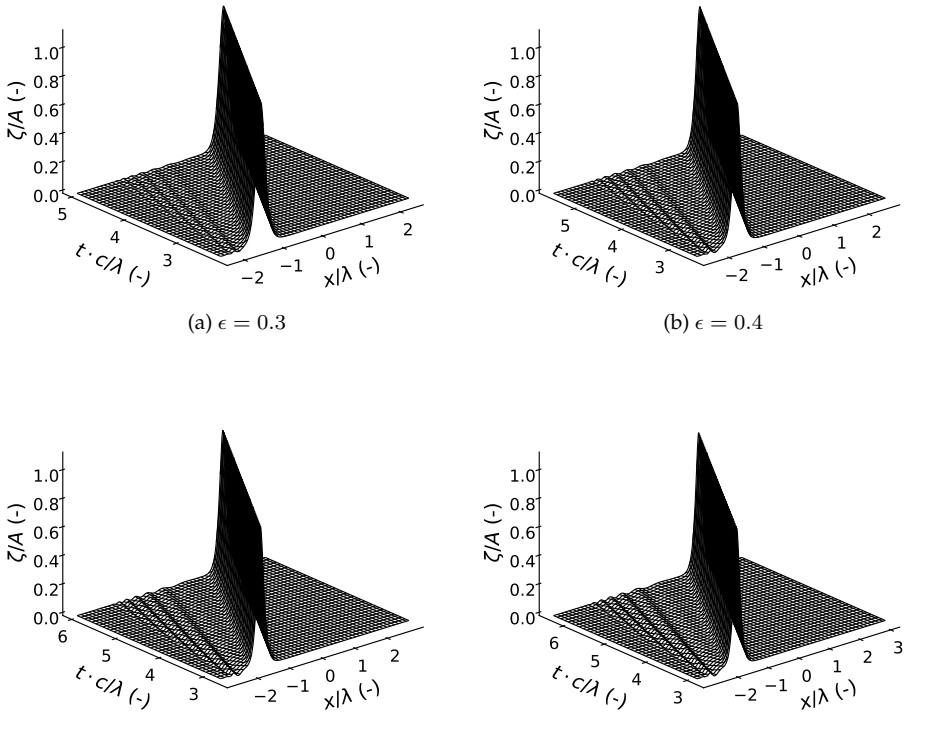

(a) $\epsilon = 0.3$ (b) $\epsilon = 0.4$

(c) $\epsilon = 0.5$ (d) $\epsilon = 0.6$

Figure 4.17: Space-time plot of free-surface elevation for solitary waves with $0.3 \leq \epsilon \leq 0.6$. x has origin in the middle of the tank.

a function of the vertical coordinate z. For $\epsilon \leq 0.4$, the velocity profile can be approximated with reasonable accuracy by a uniform profile. For $\epsilon > 0.4$, however, u_x depends more strongly on z. This can be understood by noticing that the terms depending on z in the approximate representation of u_x are 2^{nd} and 3^{rd} order with respect to ϵ. Thus, when the horizontal fluid-particle velocity is forced to be uniform at the position of the wavemaker for higher values of ϵ in the numerical solution, dispersion errors may cause both the trailing waves and phase lag observed in the numerical results. This hypothesis is supported by the findings of Zhou et al. (2016), who simulated solitary waves by specifying initial conditions. By using a higher-order initial condition, they were able to simulate solitary waves with $\epsilon = 0.5$ more accurately than when applying a lower-order initial condition. Indeed, by using the present numerical code with a modified Neumann-boundary condition for the velocity potential at the wavemaker, Tong et al. (2019) were able to simulate a solitary wave with ϵ up to 0.6 with good accuracy. This confirms that the errors observed here for $\epsilon > 0.4$ are related to the wave generation rather than the fundamental features of the numerical method.

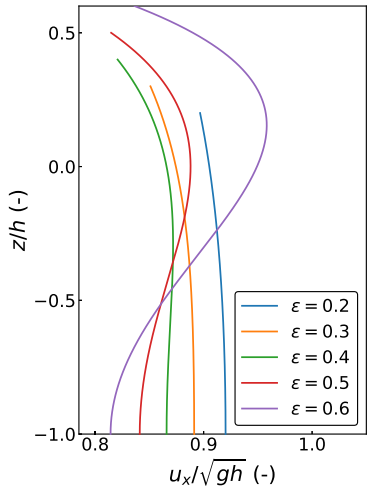

Figure 4.18: Horizontal fluid particle velocity u_x under crest of a solitary wave with $0.2 \leq \epsilon \leq 0.6$ estimated from 3^{rd} order approximate solution given by Fenton (1972). The velocity is normalized against $\sqrt{gh}$, where g and h are the acceleration of gravity and the water depth, respectively.

4.6 Propagation of a Wave Packet Resulting in a Steep Focused Wave

The focused wave group studied by Dommermuth et al. (1988) is now considered. They performed experiments in a $25\ m$ long, $0.7\ m$ wide and $0.6\ m$ deep water channel equipped with a piston-type wavemaker. In the experiments, the wavemaker was programmed to generate waves with different wavelengths re-

sulting in an amplified and eventually plunging crest at a certain location and time. The channel was equipped with a damping beach starting at a distance $19.5\ m$ away from the wavemaker. The wave elevation was measured in nine wave probes located between $3.17h$ and $12.17h$ from the wavemaker, where h is the water depth. In the experiments, the breaking wave occurred at the focus point approximately $12.08h$ away from the wavemaker at a non-dimensional time instant $t\sqrt{g/h} \approx 52.15$.

We here perform simulations with waves generated by a piston-type wavemaker with the displacement signal shown in Figure 4.19. The depth h is set equal to that in the experiments, while the length of the tank is set to $15\ m$. A sketch of the tank is given in Figure 4.20, also indicating the locations of the nine wave probes used in the analysis. Due to the nature of the experiments, wave reflections do not represent a major concern. Nevertheless, a numerical beach of length $8h$ with $\nu_{max} = 2.0\ s^{-1}$ is located on the opposite side of the wavemaker. This means that the numerical beach starts at a distance $17h$ from the wavemaker, i.e. well beyond the wave-focus point. Uniform grids with three different grid spacings are considered. The grid spacing is the same in both the stationary background grid and in the grid fixed to the wavemaker. The free-surface is modelled with the semi-Lagrangian formulation described in Section 3.2.1. As can be seen from Table 4.5, where the main simulation parameters are listed, a fixed time step is used independent of the grid refinement. This time step is chosen so that the CFL number based on the individual piston-frequency component with the largest velocity is always less than unity.

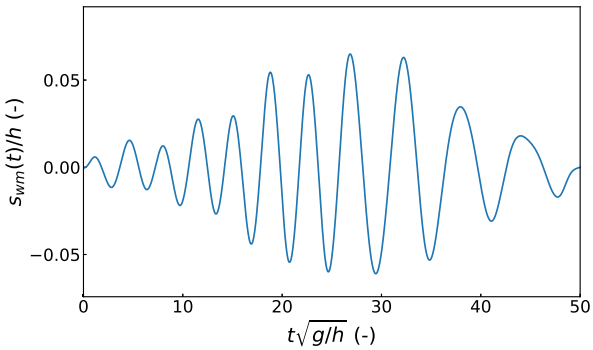

Figure 4.19: Time history of piston-wavemaker displacement s_{wm} to generate a focused wave.

The time series of the wave elevation in the nine wave probes obtained with the three different grid refinements are compared to the experimental results by Dommermuth et al. (1988) in Figure 4.21. The first thing that stands out is that, while the simulations with the medium and fine grids break down close to the time of wave breaking in the experiments ($t\sqrt{g/h} \approx 52.15$), the simulation with the coarse grid does not. This is possibly because the coarsest grid effectively filters out instabilities that are associated with the initiation of wave breaking, so

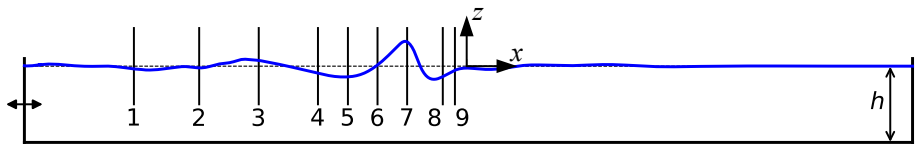

Figure 4.20: Sketch of wave tank with water depth h used in numerical analysis to propagate a focused wave. The shown free-surface elevation corresponds to non-dimensional time $t\sqrt{g/h} = 50.0$. The horizontal positions of the wave probes with indices 1-9 are given as $(x - x_{wm})/h = \{3.17, 5.00, 6.67, 8.33, 9.17, 10.00, 10.83, 11.83, 12.17\}$, where x_{wm} is the position of the piston-type wavemaker at rest. The global Oxz coordinate system is located in the middle of the computational domain with origin in the still waterline. The x and z-axes are not in scale 1:1.

Table 4.5: Settings used in the numerical simulations for the focused-wave experiments by Dommermuth et al. (1988). Δx and Δz are the grid spacings in horizontal and vertical direction, respectively, Δt is the time step, h is the water depth and g is the acceleration of gravity.

Refinement	$\Delta x/h\ (-)$	$\Delta z/h\ (-)$	$\Delta t\sqrt{g/h}\ (-)$
Coarse	0.08	0.08	
Medium	0.06	0.06	0.05
Fine	0.04	0.04	

that the free surface remains a single-valued function of the horizontal coordinate, which is required in the present method. However, Wang and Faltinsen (2018) showed that also such scenarios can be modelled within the framework of the HPC method by applying a fully-Lagrangian free-surface model with local grid refinements. In the probes located some distance from the focus point where the physical wave breaking occurred, i.e. Figure 4.21 (a) - (f), there are insignificant differences between the numerical results for the different grid refinements prior to the wave breaking. In the probes closer to the focus point, i.e. Figure 4.21 (g) - (i), the free-surface elevation with the coarse grid differs slightly from the medium grid. The results with the medium and fine grids are visually in good agreement throughout, indicating that the medium grid gives approximately converged results.

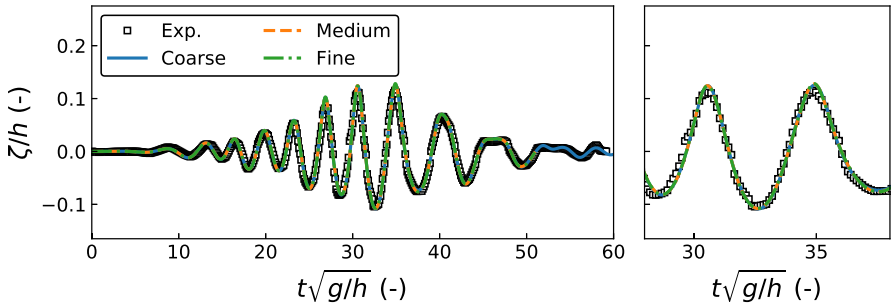

(a) $(x - x_{wm})/h = 3.17$

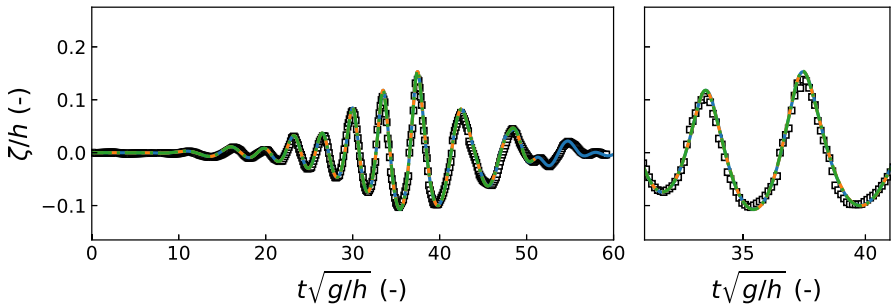

(b) $(x - x_{wm})/h = 5.00$

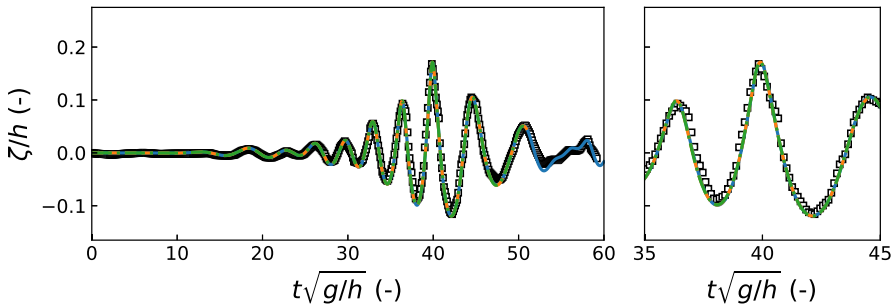

(c) $(x - x_{wm})/h = 6.67$

Figure 4.21: Time series of wave elevation for a focused wave in nine probes located between $3.17h$ and $12.17h$ from the wavemaker that at rest is located at $x = x_{wm}$. Numerical results with three different grid refinements are compared with the experimental results by Dommermuth et al. (1988).

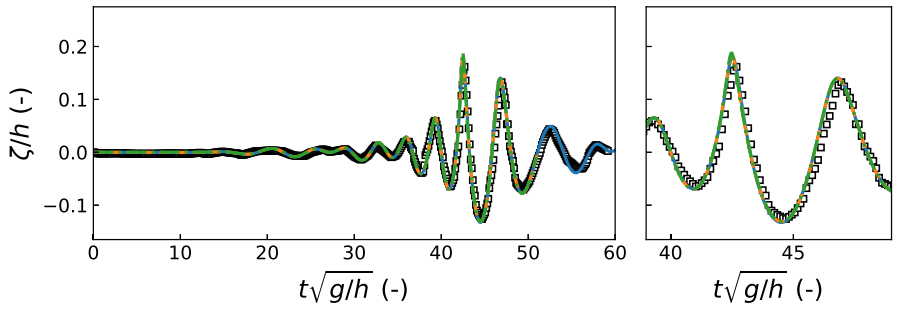

(d) $(x - x_{wm})/h = 8.33$

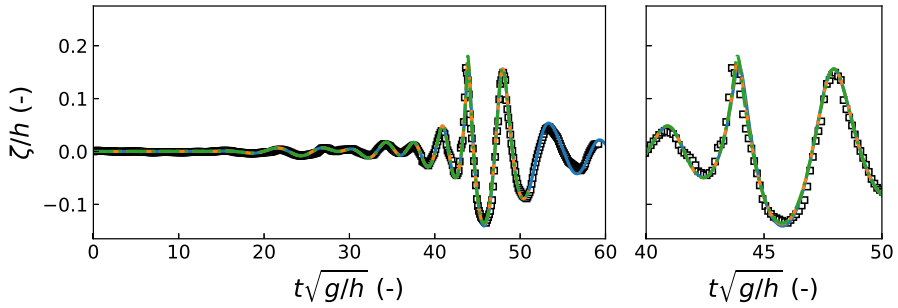

(e) $(x - x_{wm})/h = 9.17$

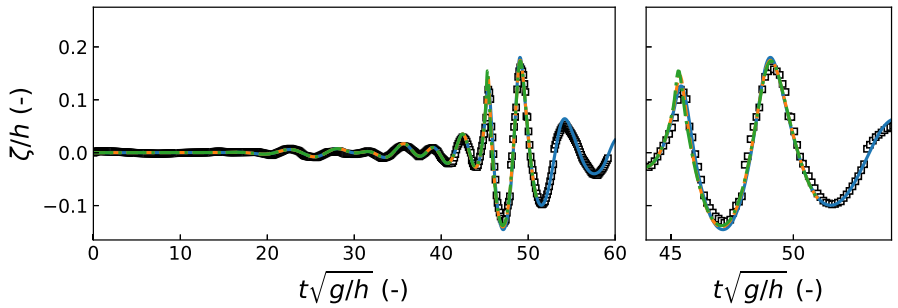

(f) $(x - x_{wm})/h = 10.00$

Figure 4.21: Continued.

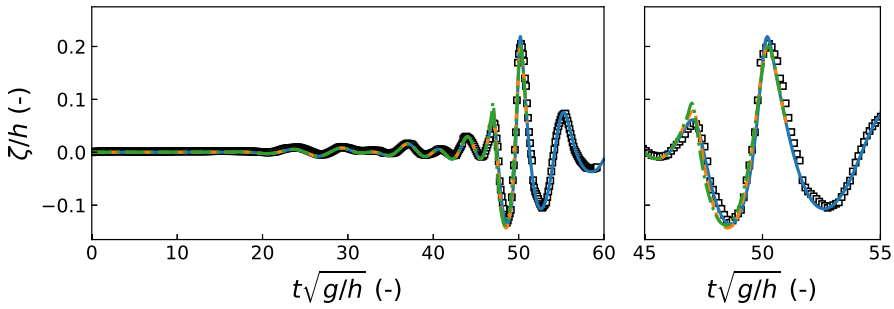

(g) $(x - x_{wm})/h = 10.83$

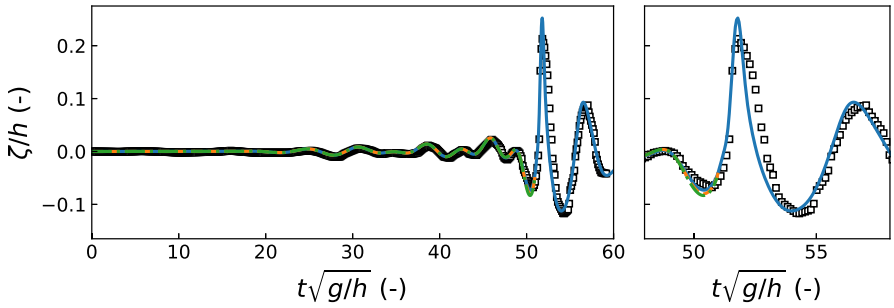

(h) $(x - x_{wm})/h = 11.83$

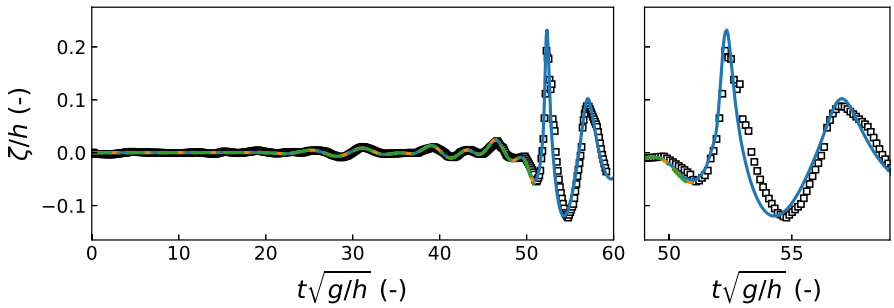

(i) $(x - x_{wm})/h = 12.17$

Figure 4.21: Continued.

To represent an overturning wave numerically represents an additional challenge with respect to modelling, and requires a finer spatial discretization as well as a smaller time step. Moreover, the scenario when the overturning wave reattaches to the free surface underneath cannot be accounted for in a potential-flow model. In many cases it may therefore be of interest to study waves that are close to breaking, or where the actual breaking is either localized or not of primary concern, without actually modelling the overturning wave. The physical process of wave breaking is associated with dissipation of energy, and several numerical schemes have been proposed to artificially suppress wave breaking in an attempt to account for this energy dissipation in potential-flow models. Two methods are outlined by Subramani (2000), where in the first, an additional pressure term is added in the dynamic free-surface condition (DFSC). The second method consists in replacing the free surface of the breaking wave with a smoothed profile. This method has similarities with the method proposed by Wang et al. (1995), where the top layer of a wave crest close to breaking is "peeled" off in order to avoid unwanted wave breaking. Also relevant in this framework is the work by Paulsen et al. (2014), where a Savitsky-Golay filter is applied locally on the free surface close to where breaking is expected.

All the above methods represent means to remove energy from the wave crest in order to avoid wave breaking in a pragmatic manner. Inspired by the work of Subramani (2000), we here use the method of adding a dissipative term $\mu_b(x,t)$ in the DFSC. In the semi-Lagrangian formulation outlined in Section 3.2.1, that is used in the present analysis, the DFSC in the inertial reference frame given by expression (3.14) is reformulated with the dissipative term as

$$\frac{\delta\varphi_{P_m}}{\delta t} = -\frac{1}{2}|\nabla\varphi|^2 - gz + \frac{\delta z_{P_m}}{\delta t}\frac{\partial\varphi}{\partial z} - \nu(x,t)(\varphi-\varphi_{ref}) - \mu_b(x,t). \tag{4.11}$$

Here, $\boldsymbol{P}_m = (x_{P_m}, z_{P_m})$ is the position of a free-surface marker expressed in the inertial coordinate system, where the horizontal x-axis and the vertical z-axis have origin in the center of the computational domain and in the still free surface, respectively. $\nu(x,t)$ is a linear damping coefficient associated with a numerical damping zone. The wave breaking here occurs at a location outside the numerical beach, i.e. $\nu(x,t) = 0$ when $\mu_b(x,t) \neq 0$. If wave breaking is identified in a marker with horizontal coordinate x_0, the contribution to $\mu_b(x,t)$ due to this is defined as

$$\mu_b(x,t;x_0) = \mu_{max}\theta_b(x,x_0)|\nabla\varphi|^2 sign(\frac{\partial\varphi}{\partial z}), \tag{4.12}$$

where μ_{max} is an empirical coefficient and $sign(\partial\varphi/\partial z) = 1$ if $\partial\varphi/\partial z \geq 0$ and $sign(\partial\varphi/\partial z) = -1$ otherwise. $\theta_b(x,x_0)$ is an envelope function on the form

$$\theta_b(x,x_0) = \begin{cases} \frac{1}{2}\left[1.0 + \cos\frac{\pi(x-x_0)}{L_0}\right] & |x-x_0| \leq L_0 \\ 0 & |x-x_0| > L_0 \end{cases}, \tag{4.13}$$

with L_0 the half-length of the envelope. Because wave breaking can be identified at several markers $i = 1, ..., N$ that are close to each other, the total dissipative

term $\mu_b(x,t)$ is accumulated from the individual contributions given by (4.12):

$$\mu_b(x,t) = \sum_{i=1}^{N} \mu_b(x,t;x_0 = x_{P_m,i}). \tag{4.14}$$

The parameters μ_{max} and L_0 in (4.12) must be determined empirically. For the present case it is found that taking L_0 as 10-15% of the local wavelength of the breaking wave represents a reasonable initial guess. However, it is believed that the optimal choice for L_0 will depend on the type of wave breaking. In order to determine the final value of μ_{max}, a suggested strategy is to start out with a small value $\mu_{max} << 1$ and re-perform the analysis where wave breaking originally occurred. If the numerical analysis still becomes unstable, μ_{max} should be increased incrementally until the simulation becomes stable. If, on the other hand, the simulation is stable with the initial guess for μ_{max} but results in a clearly non-physical free-surface profile, μ_{max} should be decreased incrementally until a good compromise is found. If reference results are not available, it is obviously not straightforward to judge the goodness of such compromise. Evaluation of additional properties such as conservation of fluid energy and fluid mass, as done by Hanssen et al. (2018), can be helpful in this respect. If an adequate value for μ_{max} cannot be established, the choice of L_0 can be revisited. A reasonable value for μ_{max} is found to be 0.1 for the present case.

In order to identify the position(s) x_0 in (4.12), a criterion to detect wave breaking must be established. Following Barthelemy et al. (2015), wave breaking can be considered a threshold process where the threshold is defined by the ratio γ_b between the horizontal fluid-particle velocity $\partial\varphi/\partial x$ and the local phase speed $c(x,t)$. Using a threshold level for γ_b in the range $0.85 - 0.86$, Barthelemy et al. (2015) were able to successfully predict wave breaking. Seiffert and Ducrozet (2016) confirmed that a threshold level of $0.84 - 0.86$ for γ_b identifies the onset of wave breaking for various focused-wave cases. We here identify wave breaking when $\gamma_b > 0.86$. The local phase speed is given as

$$c(x,t) = \sqrt{\frac{g \tanh\left[k(x,t)h\right]}{k(x,t)}}, \tag{4.15}$$

where h is the water depth and $k(x,t)$ is the local wave number. Following Seiffert and Ducrozet (2016), the latter is determined by first taking the Hilbert transform of the free-surface elevation, $H(\zeta)$, at time t:

$$k(x,t) = \frac{1}{\zeta^2 + H(\zeta)^2}\left(\zeta\frac{\partial H(\zeta)}{\partial x} - H(\zeta)\frac{\partial \zeta}{\partial x}\right). \tag{4.16}$$

The derivative $\partial H(\zeta)/\partial x$ is taken from a numerically fitted B-spline representation of $H(\zeta)$ through all free-surface markers. (4.16) must be evaluated at each time step, but is not found to give any significant increase in the total computational time involved in the analysis.

Although the breaking criterion described above is able to detect the time and location of breaking observed in the experiments with good accuracy (Hanssen

et al., 2018), criteria that are more straightforward to implement have been suggested by other authors. For instance, Snyder and Kennedy (1983) statistically described the probability of wave breaking in a random sea state using the negative vertical acceleration of the free surface as criterion. By estimating the relevant spectral parameters from the significant wave height and period, Greenhow (1989) demonstrated a practical use of the method that can easily be combined with wave scatter diagrams. Applying the vertical acceleration of the free surface as breaking criterion directly in a non-linear simulation may indeed represent an attractive alternative to the one used here, particularly if the method is extended to 3D. However, the relevant threshold level for the acceleration and the accuracy of the criterion would require further investigation.

The medium-grid case, that originally resulted in an unstable simulation close to the time of wave breaking in the experiments in Figure 4.21, is revisited with the above breaking-identification and suppression schemes included. As shown in Figure 4.22, the simulation now remains stable throughout. Compared with the coarse-grid case, where the simulation did not originally break down, the free-surface profile differs close to the location and time of wave breaking mainly in that the magnitude of the free-surface elevation is lower. However, some time after the breaking, the numerical medium-grid results with breaking-suppression are similar to the coarse-grid results. This indicates that the suppression scheme successfully modifies the properties of the waves locally in space and time, without significantly influencing the behaviour of the solution thereafter.

The performance of the breaking-suppression scheme is here tested for a case where a plunging breaker was observed in the experiments. This can be considered a violent type of wave breaking, that is expected to be challenging to suppress numerically in a sound manner. However, plunging breakers will in practice only be studied with potential-flow methods in local types of analyses where e.g. the wave kinematics associated with impact loads on structures are of interest. Having demonstrated that the scheme is able to ensure numerical stability even for the challenging case of a plunging breaker, indicates that it may represent an attractive method for cases involving less violent wave-breaking mechanisms. As an example, spilling breakers may occur due to locally steep waves in an irregular sea state. If the wave breaking is not expected to be important for the quantities under consideration, that may e.g. be the slowly-varying wave drift loads on a moored structure, a breaking-suppression scheme can be an useful mean to promote numerical stability in a non-linear analysis.

A clear weakness of the proposed breaking-suppression scheme in practical applications is that the empirical coefficients involved in the dissipative term (4.12) are determined by a labour-intensive, manual tuning process. In order to make the method more practical, it is necessary to relate these coefficients more strongly to the physical properties of the instantaneous wave. This would enable the coefficients to be changed dynamically during a simulation, but in order to establish such relations, more research is required. It would also be of interest to determine if, and how, the method can be applied to 3D problems.

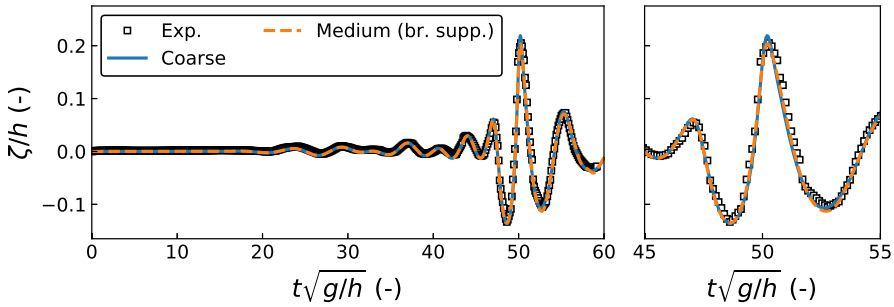

(a) $(x - x_{wm})/h = 10.83$

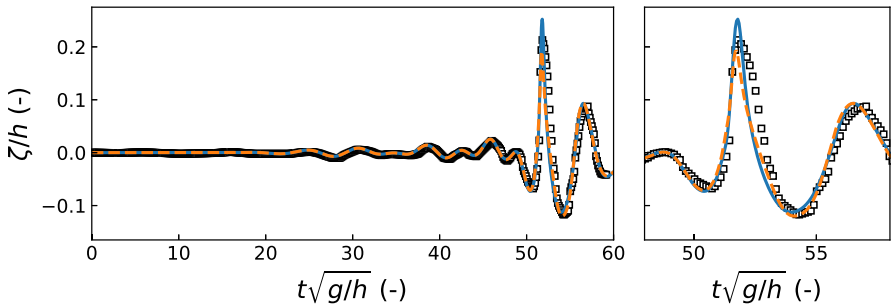

(b) $(x - x_{wm})/h = 11.83$

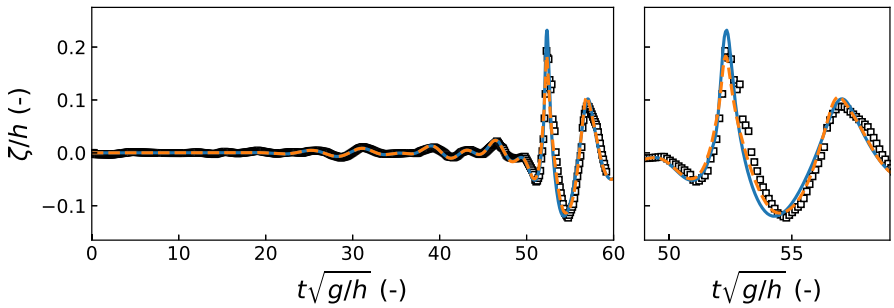

(c) $(x - x_{wm})/h = 12.17$

Figure 4.22: Time series of wave elevation for a focused wave in the three probes closest to the focus point. Numerical results with coarse grid and with medium grid including a scheme to suppress wave breaking are compared with the experimental results by Dommermuth et al. (1988).

4.7 Summary

Using the numerical method introduced in Chapter 3, wave-propagation problems involving various non-linear mechanisms have been examined. Periodic waves with wave steepness $k\zeta_a$ between 0.1 and 0.4 in finite water depth, propagating in an infinitely long wave tank modelled by a restricted computational domain with periodic boundary conditions, were first considered. The steepness $k\zeta_a = 0.1$ represents a wave close to linear, while the wave with $k\zeta_a = 0.4$ is close to breaking. The waves were generated by specifying the initial properties of the free surface, allowing us to study the wave-propagating capabilities of the method without disturbances from a wavemaker. The numerical error was computed by considering a high-order stream-function theory as analytical solution. For all values of $k\zeta_a$, the waves were simulated over 40 wave periods, with the number of grid points required to obtain a certain level of accuracy increasing with increasing wave steepness. The spatial convergence of the numerical error of the free-surface elevation and potential was, with a few exceptions, approximately 3^{rd} order or better in the grid spacing. For $k\zeta_a = 0.4$, numerical instabilities of sawtooth-type were observed for the finest grids. By applying a high-order spatial filter to smooth the free surface, the simulations were able to continue for 40 wave periods, although with increasing numerical errors. It was found that 30 grid points per wavelength generally is sufficient to give accurate simulations for waves with steepness up to approximately $k\zeta_a = 0.3$.

Propagation of steep waves generated by a flap-type wavemaker was examined for several cases with wave steepness $k\zeta_a$ in the range 0.1 to 0.38. Excellent comparison with experimental results was found for the cases with $k\zeta_a$ up to 0.2, where the exact time histories of the wavemaker used in the experiments were enforced in the numerical analysis. For the higher values of $k\zeta_a$, where simulations were compared to experiments with different origin, the particulars of the wavemaker motion were unknown and thus estimated by manual iteration. With this in mind, and disregarding the initial transient of the wave elevation, the comparison with experimentally measured wave elevations was reasonable. By extending the length of the wave tank beyond that used in the experiments, it was seen that the amplitude of the leading wave in a steep wave train increased as the waves propagated. It is likely that this behaviour is due to non-linear dispersion effects caused by the transient ramp-up of the wavemaker.

By studying long waves in shallow water generated by a piston-type wavemaker, the non-linear transfer of energy between different harmonic modes was investigated. Comparing the first four harmonic amplitudes with both experimental and numerical reference results, it was demonstrated that the numerical method is able to account for non-linear wave-wave interactions in shallow water.

Solitary waves with amplitude-to-depth ratios ϵ between 0.2 and 0.6 were generated by a piston-type wavemaker. Compared with a high-order approximate solution, accurate numerical results were obtained for ϵ up to 0.4. For higher values of ϵ, trailing waves with non-negligible amplitudes were observed, along with notable errors in phase speed and wave amplitude. It was argued that the errors observed for $\epsilon > 0.4$ were due to the fact that waves were generated by a piston-type wavemaker, that forces the horizontal fluid-particle velocity to be uniform

over the depth, rather than caused by than the numerical method itself.

At last, a focused wave group that in experiments resulted in a plunging breaker at the focus point, was examined. Simulations were performed with a coarse, medium and fine grid, where the medium grid was observed to give numerically converged results when considering the wave elevation close to the wave-focusing point. Up to the point of breaking, good agreement with experimental results was demonstrated. The two simulations with the finest grids became numerically unstable close to the time of breaking in the experiments, while the simulation with the coarsest grid did not. This is likely because this grid effectively filters out the small instabilities that initiate the physical process of wave breaking. Inspired by this observation, a scheme to suppress wave breaking was proposed, that enabled the simulation with the medium grid to remain numerically stable throughout. This represents a pragmatic measure to improve numerical robustness when modelling waves close to breaking, or where the breaking is localized or not of primary concern. More work is however required to relate the empirical parameters in the model to physical properties.

Having shown that the numerical method is able to propagate periodic waves with high steepness, solitary waves and long waves in shallow water, with distinct non-linear features, we consider a wave-radiation and a wave-diffraction problem in the next chapter in order to examine the method's ability to deal with free surface-body interaction problems.

Chapter 5

Wave Radiation and Diffraction Studies

The previous chapter showed that the immersed boundary-overlapping grid method (IBOGM) described in Chapter 3 is able to accurately simulate propagating waves with various non-linear and dispersive mechanisms. The method's ability to handle water-body interaction is examined next.

First, a circular cylinder undergoing forced harmonic heave motions in still water, that corresponds to a wave-radiation problem, is considered. This problem has two numerically challenging non-linear features, namely that the body has non-vertical geometry in the intersection points between the free surface and the body, and that local non-linear wave behaviour develops close to the body for high oscillation frequencies. Thereafter, a fixed ship section in beam-sea incident waves with different wave heights and frequencies is considered. This corresponds to a wave-diffraction problem, where non-linearity is mainly related to the incident wave and the modification of this as it approaches the body.

The analysis of the heaving cylinder was documented in Hanssen et al. (2017).

5.1 Forced Heave Motion of a Semi-Submerged Circular Cylinder in Still Water

The forced harmonic heave motions of a half-submerged, circular cylinder in still water studied experimentally by Tasai and Koterayama (1976) is considered. The non-dimensional heave amplitude is given as $\epsilon_{\eta_3} = \eta_{3a}/R$, where η_{3a} is the heave amplitude and $R = 0.1\ m$ is the cylinder radius. The forced heave motion is given as

$$\eta_3(t) = -\eta_{3a} \sin \omega t, \tag{5.1}$$

where ω is the angular oscillation frequency. Since no incident waves are present, this corresponds to a wave-radiation problem, where the heave added mass coefficient A_{33} and damping coefficient B_{33} can be estimated from the time series of the vertical water force $F_3(t)$ on the cylinder. Following Sun (2007), $F_3(t)$ can be

expanded in a Fourier series,

$$F_3(t) = F_{3,0} + \sum_{n=1}^{\infty} F_{3,n} \sin(n\omega t + \delta_n), \tag{5.2}$$

with $F_{3,n}$ and δ_n the n^{th} order force amplitude and phase angle, respectively. The force amplitudes can be estimated from the actual time series $F_3(t)$ as follows:

$$\begin{aligned} F_{3,0} &= \frac{1}{mT}\int_{t_0}^{t_0+mT} F_3(t)dt \equiv a_{3,0} \\ F_{3,n}\sin\delta_n &= \frac{2}{mT}\int_{t_0}^{t_0+mT} F_3(t)\cos(n\omega t)dt \equiv a_{3,n} \\ F_{3,n}\cos\delta_n &= \frac{2}{mT}\int_{t_0}^{t_0+mT} F_3(t)\sin(n\omega t)dt \equiv b_{3,n} \end{aligned} \qquad n \geq 1. \tag{5.3}$$

$T = 2\pi/\omega$ is here the oscillation period and $m \geq 1$ is an integer. The integrals in (5.3) are estimated through numerical integration, and the integration limits are taken so that $F_3(t)$ has steady-state behaviour for $t_0 \leq t < t_0 + mT$. The added mass coefficient is found from the 1^{st} order Fourier component that is 180° out of phase with the heave acceleration,

$$A_{33} = \frac{b_{3,1} - C_{33}\eta_{3a}}{-\omega^2\eta_{3a}}, \tag{5.4}$$

where the hydrostatic restoring coefficient is defined as $C_{33} = \rho g D$ with ρ the water density, g the acceleration of gravity and $D = 2R$ the cylinder's diameter. The damping coefficient is found from the 1^{st} order Fourier component that is 180° out of phase with the heave velocity,

$$B_{33} = \frac{a_{3,1}}{\omega\eta_{3a}}. \tag{5.5}$$

In addition we compute the mean force $F_3^{(0)}$ and the 2^{nd} order force amplitude $F_{3,2}$ as

$$F_3^{(0)} = a_{3,0} - \rho g S_0 \tag{5.6}$$

and

$$F_{3,2} = \sqrt{a_{3,2}^2 + b_{3,2}^2}, \tag{5.7}$$

where $S_0 = 0.5\pi R^2$ is the mean submerged area of the cylinder.

5.1.1 Definition of Cases

Eight oscillation frequencies are studied numerically for a single heave amplitude $\epsilon_{\eta_3} = 0.2$ in a computational domain that is symmetric about the vertical axis through the cylinder center, as illustrated in Figure 5.1. The dimensions of the wave tank used for each of the eight frequencies are summarized in Table 5.1, where the length of the tank L_{tank} is set equal to 10 times the wavelength λ estimated from the linear deep-water dispersion relation, and the water depth h is approximately equal to or larger than 0.5λ.

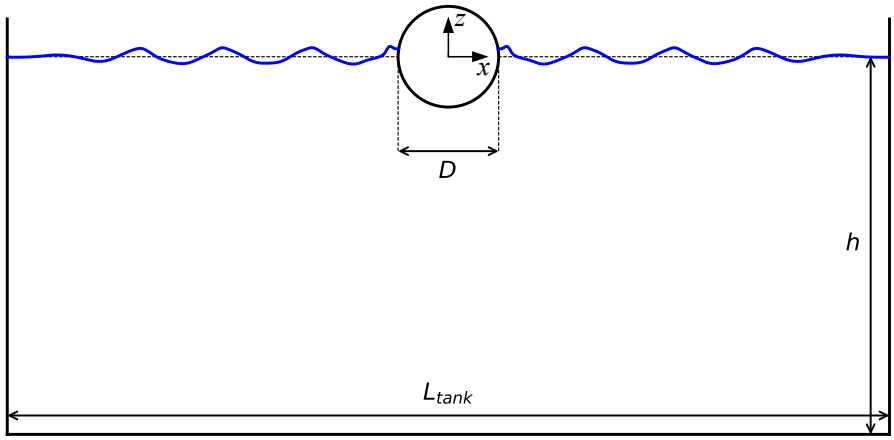

Figure 5.1: Sketch of wave tank with length L_{tank} and water depth h used in numerical analysis of circular free-surface piercing cylinder undergoing forced heave motions. The global Oxz coordinate system is located in the middle of the computational domain with origin in the still waterline, and the computational domain is symmetrical about the z-axis.

Table 5.1: Length L_{tank} and depth h of wave tank used in numerical analysis of cylinder undergoing forced heave motion with non-dimensional amplitude $\epsilon_{\eta 3} = 0.2$ and non-dimensional frequency $\omega^2 R/g$. λ is the wavelength estimated from the linear deep-water dispersion relation.

$\omega^2 R/g\ (-)$	$\lambda\ (m)$	$L_{tank}\ (m)$	$h\ (m)$
0.20	3.15	31.47	1.50
0.40	1.56	15.62	1.50
0.60	1.05	10.53	1.50
0.80	0.79	7.90	1.50
1.01	0.62	6.19	1.50
1.19	0.53	5.29	1.50
1.38	0.46	4.56	1.50
1.61	0.39	3.30	1.50

5.1.2 Numerical Setup

Examples of the stationary background grid used to model the flow in the majority of the computational domain, and the body-fixed grid used to refine the flow locally close to the oscillating cylinder, are shown in Figure 5.2 and Figure 5.3, respectively. The meaning of the different node types indicated in the two grids are discussed in detail in Section 3.2, and thus not repeated here. The free surface is described with the hybrid formulation in Section 3.2.1, so that the free-surface markers at the wave-body intersections move in a fully-Lagrangian manner and thus never separate from the body surface, while the markers in the background

grid are semi-Lagrangian and thus restricted to move in parallel with the inertial z-axis. The horizontal velocity component of the remaining markers in the body-fixed grid, i.e. those not at the wave-body intersections, decays linearly from the horizontal velocity component at the closest wave-body intersection point towards zero at the boundary of the body-fixed grid. The spacing between free-surface markers in the body-fixed grid is significantly smaller than in the stationary background grid, where the markers are distributed so that their horizontal positions coincide with the vertical grid nodes.

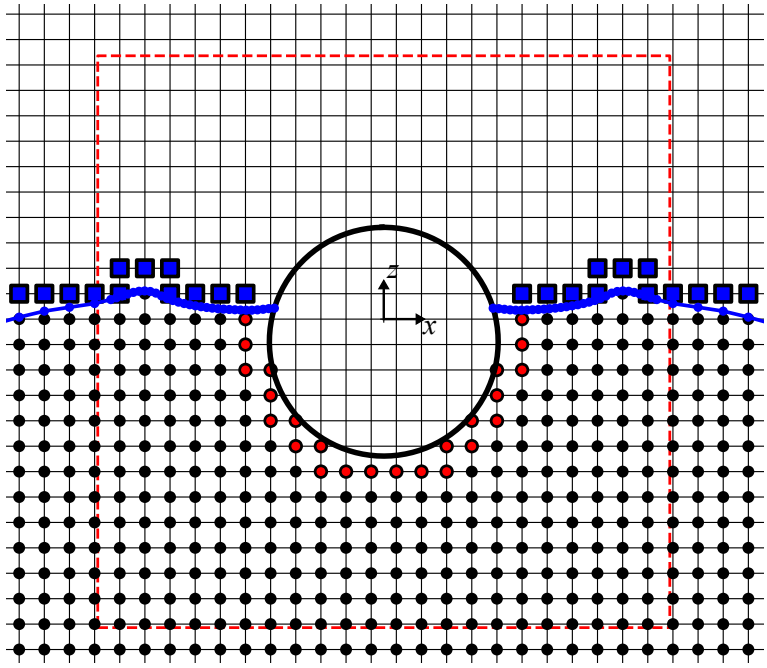

Figure 5.2: Portion of stationary background grid where the fluid variables are modelled in the inertial reference frame associated with the Oxz coordinate system. The different node types are explained in Section 3.2. The free-surface markers are indicated with blue circles, and the instantaneous boundaries of the body-fixed grid that follows the cylinder's motion are indicated with red dashed lines.

The grid density in the two grids, the extent of the body-fixed grid and the time step chosen for the cases in Table 5.1 are listed in Table 5.2. All of the grids are uniform with square cells. The grid spacing Δx in the stationary background grid is chosen so that there are 18 grid nodes per wavelength λ. This is found sufficient, since the radiated waves some distance from the cylinder have mild steepness. The length L_{bf} of the body-fixed grid, equal to the grid height, is taken so that it is always larger than or equal to $5R$. The grid spacing Δx_{bf} in the body-fixed grid is taken so that there are never less than five grid nodes per R, which is considered a minimum value to ensure a proper representation of the cylinder geometry modelled as an immersed boundary. With increasing oscillation frequency, the number

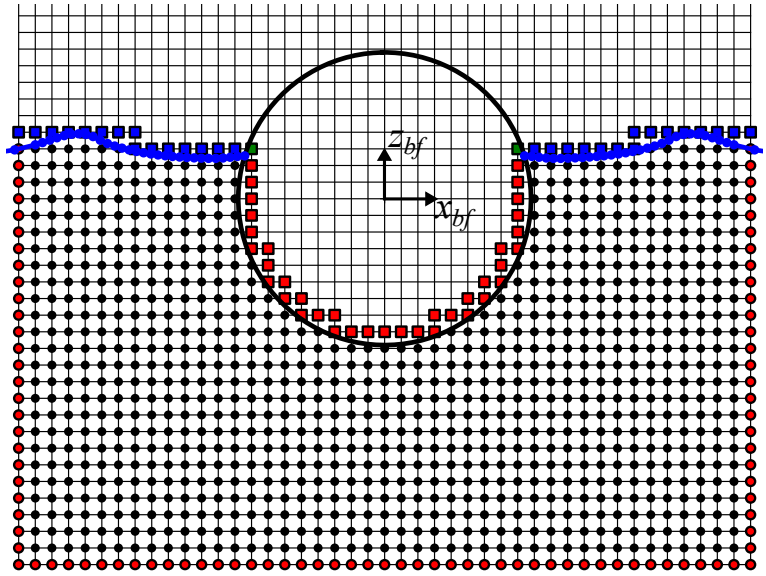

Figure 5.3: Portion of body-fixed grid following the cylinder's motion where the fluid variables are modelled in the body-fixed reference frame associated with the $Ox_{bf}z_{bf}$ coordinate system. The different node types are explained in Section 3.2. The free-surface markers are indicated with blue circles.

of grid points per cylinder is increased towards $R/\Delta x_{bf} = 9$. This is because the higher oscillation frequencies involve stronger non-linearities. For the same reason, the number of time steps per oscillation period is increased from 55 for the lowest frequency towards 200 for the two highest oscillation frequencies.

Table 5.2: Simulation parameters used in numerical analysis of cylinder undergoing forced heave motion with non-dimensional amplitude $\epsilon_{\eta_3} = 0.2$ and non-dimensional frequency $\omega^2 R/g$. L_{bf} is the dimension of the square body-fixed grid, Δx and Δx_{bf} are the uniform grid spacings of the square cells in the stationary background grid and body-fixed grid, respectively, Δt is the time step and $T = 2\pi/\omega$ is the heave oscillation period.

$\omega^2 R/g\ (-)$	$L_{bf}\ (m)$	$\Delta x\ (m)$	$\Delta x_{bf}\ (m)$	$T/\Delta t\ (-)$
0.20	2.00	0.176	0.017	55
0.40	1.00	0.087	0.014	70
0.60	0.85	0.059	0.013	85
0.80	0.70	0.044	0.012	85
1.01	0.60	0.035	0.012	150
1.19	0.50	0.030	0.012	150
1.38	0.50	0.025	0.011	200
1.61	0.50	0.022	0.011	200

The ratio $\Delta x/\Delta x_{bf}$ ranges from 10 for $\omega^2 R/g = 0.20$ to 2 for $\omega^2 R/g = 1.61$. This demonstrates how the IBOGM enables us to significantly refine the solution close to the body, while using square cells throughout, in an efficient manner. The temporal and spatial discretization used in the analysis are confirmed through convergence checks for $\omega^2 R/g = 1.61$.

For the highest oscillation frequencies in Table 5.1, large curvatures of the free surface occasionally develop close to the wave-body intersection points so that the jet-cutting scheme described in Section 3.2.8 is invoked to ensure numerical stability. An example of how the free surface close to the wave-body intersection points behaves just before and immediately after the jet cutting is performed is shown in Figure 5.4.

5.1.3 Results

The added mass and damping coefficients and the mean and 2^{nd} order forces derived from the heave-force time series with expressions (5.4) - (5.7) are compared with reference results from various sources in Figure 5.5. The theoretical results for A_{33} and B_{33} are derived by Tasai and Koterayama (1976) with a linear theory, while the theoretical results for $F_3^{(0)}$ and $F_{3,2}$ are computed by Papanikolaou (1980) using a 2^{nd} order theory. The experimental results are by Tasai and Koterayama (1976), while the results by Sun (2007) are obtained from a non-linear boundary element method (BEM). All the reference results are taken from the curves presented by Sun (2007).

The present results are generally found to be in good agreement with the reference results. Some differences can be observed for the mean heave force, where there is also some scatter in the experimental data. The differences between the IBOGM and Sun (2007) for $F_3^{(0)}$, in particular for the largest oscillation frequencies, may be due to small differences in the flow near the wave-body intersection points. Since the mean force is low relative to the other forces, it is sensitive to the time window used to average the time series. This is an error source in the present results as well as in the experimental results and in the results by Sun (2007).

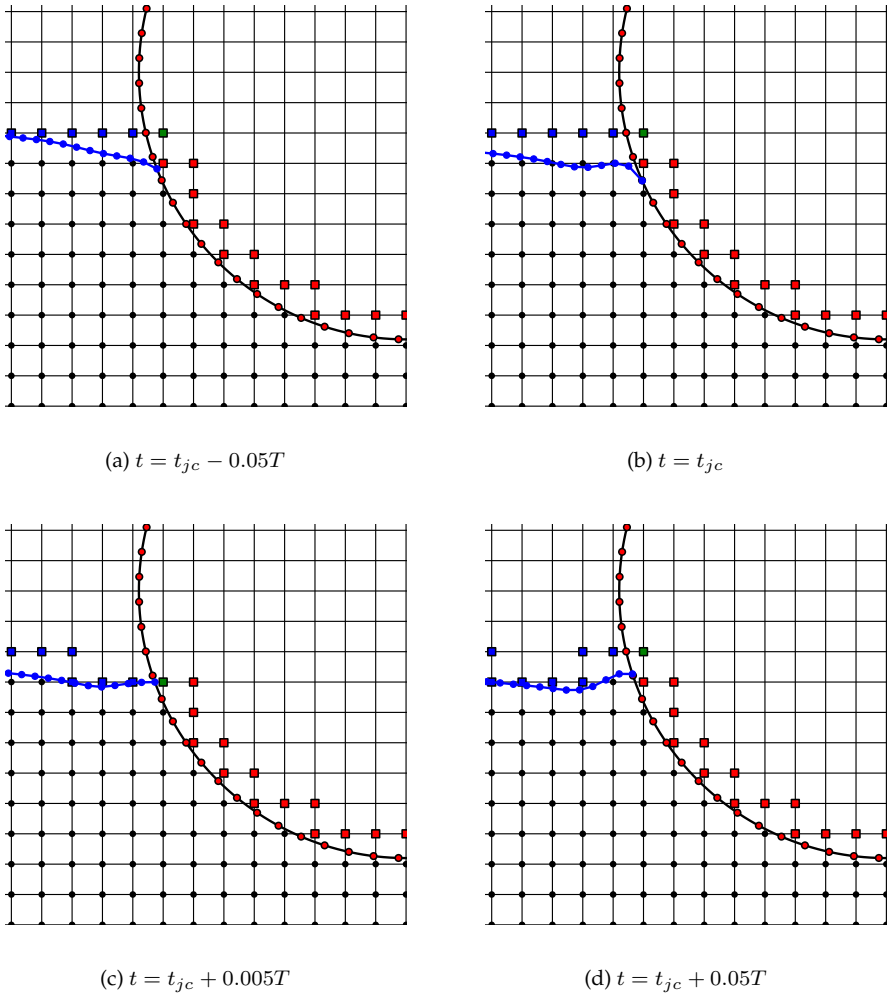

(a) $t = t_{jc} - 0.05T$

(b) $t = t_{jc}$

(c) $t = t_{jc} + 0.005T$

(d) $t = t_{jc} + 0.05T$

Figure 5.4: Jet-cutting scheme invoked for heaving cylinder triggered by the angle between the free surface and body boundary becoming less than 5° at $t = t_{jc}$. The free-surface profile is shown for time instants $t = t_{jc} - 0.05T \leq t \leq t_{jc} + 0.05T$, where $T = 2\pi/\omega$ is the oscillation period of the forced heave motion.

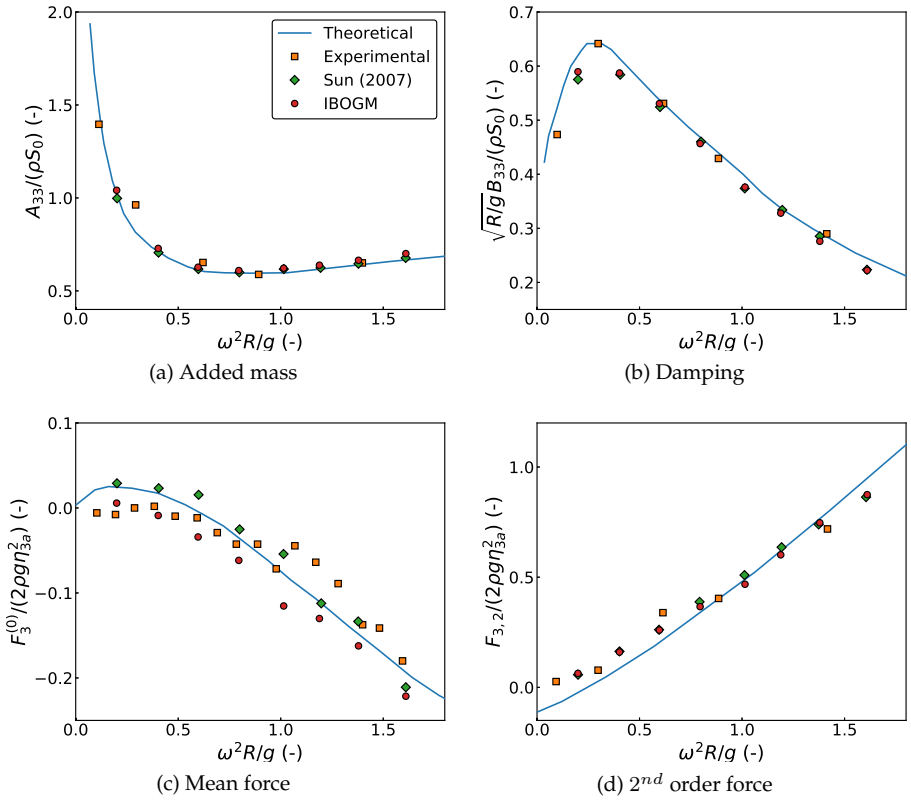

(a) Added mass

(b) Damping

(c) Mean force

(d) 2^{nd} order force

Figure 5.5: Added mass and damping coefficients and mean and 2^{nd} order forces in heave for cylinder undergoing forced heave motion with non-dimensional amplitude $\epsilon_{\eta_3} = 0.2$ and non-dimensional frequency $\omega^2 R/g$. The theoretical results for A_{33} and B_{33} are given by Tasai and Koterayama (1976) and by Papanikolaou (1980) for $F_3^{(0)}$ and $F_{3,2}$. The experimental results are given by Tasai and Koterayama (1976). The results by Sun (2007) are computed by a non-linear BEM, and the present results are denoted *IBOGM*.

The case with $\omega^2 R/g = 1.61$ is found to be the most numerically challenging case in Table 5.1 because large free-surface curvatures develop close to the cylinder. Therefore, this case is further examined. The time series of the heave force on the cylinder is compared with results from the analysis by Sun (2007) in Figure 5.6. Even though the forced heave motion is harmonic, the resulting force is clearly non-linear as seen through the existence of higher-order harmonics. The behaviour of the two time series is globally consistent, although there are some differences, particularly in the troughs. Bearing in mind that this is a numerically challenging case, and that two different numerical methods are compared, differences of this magnitude are nevertheless considered acceptable.

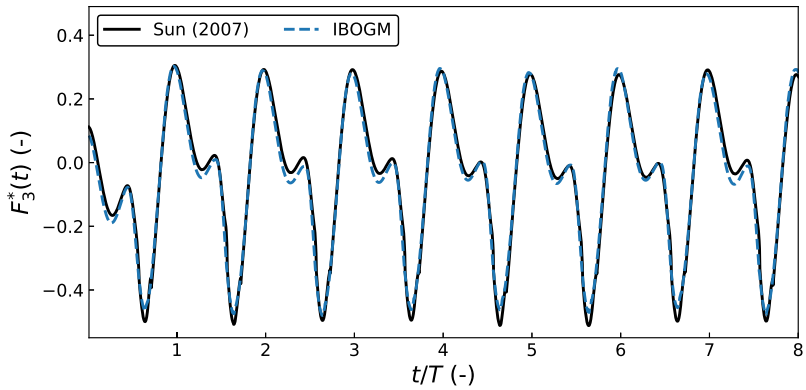

Figure 5.6: Non-dimensional heave force $F_3^*(t) = (F_3(t) - \rho g S_0)/(2\rho g R \eta_{3a})$ for cylinder undergoing forced heave motion with non-dimensional amplitude $\epsilon_{\eta_3} = 0.2$ and non-dimensional frequency $\omega^2 R/g = 1.61$. Present IBOGM results are compared with non-linear BEM results by Sun (2007).

Snapshots showing the free-surface elevation around the cylinder are compared with Sun (2007) in Figure 5.7. Both close to the wave-body intersection points and further away from the cylinder, the two solutions are in good agreement. This indicates that the numerical modelling of the flow at the wave-body intersection points is reasonable, even in the case where significant non-linear behaviour of the free surface is observed locally. It is noted that the results by Sun in Figures 5.6 and 5.7 were not given explicitly in Sun (2007), but have been obtained through personal communication.

The wave-radiation problem studied here shows that the IBOGM used in the present work is able to predict the linear added mass and damping forces, as well as higher-order forces, with good accuracy for a surface-piercing body with non-vertical sides oscillating in still water.

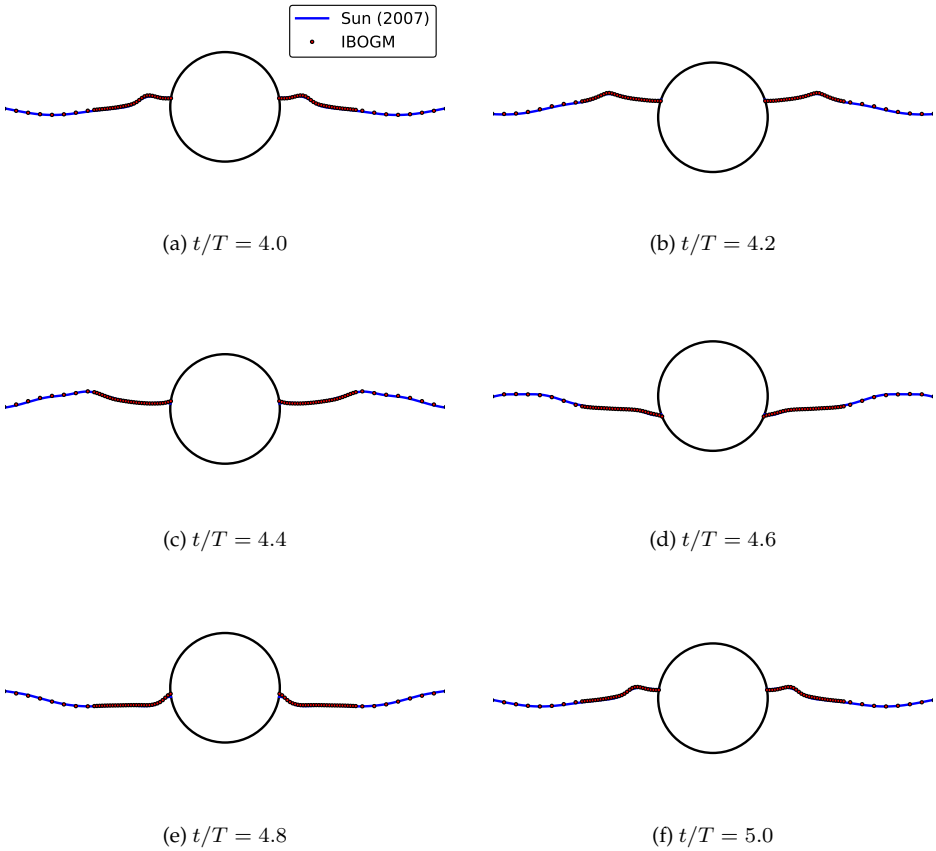

(a) $t/T = 4.0$ (b) $t/T = 4.2$

(c) $t/T = 4.4$ (d) $t/T = 4.6$

(e) $t/T = 4.8$ (f) $t/T = 5.0$

Figure 5.7: Free-surface profile plotted at different time instants through heave cycle of cylinder undergoing forced heave motion with non-dimensional amplitude $\epsilon_{\eta_3} = 0.2$ and non-dimensional frequency $\omega^2 R/g = 1.61$. Present IBOGM results are compared with non-linear BEM results by Sun (2007).

5.2 Fixed Two-Dimensional Ship Section in Beam-Sea Regular Waves

The previous section dealt with an oscillating body in still water, corresponding to a wave-radiation problem. We now consider a wave-diffraction problem, with a fixed 2D ship section in beam-sea regular waves with different amplitudes and frequencies. This scenario was studied numerically by Tanizawa et al. (1999) and experimentally by Nojiri and Murayama (1975)[1]. The latter work also includes theoretical results based on a linear theory. The same case is used further to examine a freely floating body in the next chapter.

The layout of the wave tank used is shown in Figure 5.8. In the present nu-

[1] In Japanese.

merical study, we set the length of the tank to $L_{tank} = 8\lambda$ and the water depth to $h = \lambda$, where λ is the wavelength based on the linear dispersion relation. Forces and moments are reported in the global coordinate system with z-axis positive upwards, x-axis positive in the wave-propagation direction and y-axis orthogonal to the ship section. Waves are generated by a moving flap-type wavemaker hinged at half the water depth. The 2D ship section is placed in the middle of the tank, and is characterized by a breadth $B = 0.50\ m$, a draught $d = 0.25\ m$ and a bilge radius $0.064\ m$. The vertical center of gravity, that is only relevant when the body is free to move, is $KG = 0.135\ m$. This case is studied in the next chapter. Since the analysis is performed in 2D, the length L_s of the ship section in y direction used to normalize results is taken as unity. The characteristic values of the ship section are chosen to be consistent with Nojiri and Murayama (1975). Towards the ends of the tank, numerical beaches are used to prevent reflection of waves back into the tank. On the side opposite of the wavemaker, artificial damping is added in the kinematic and dynamic free-surface conditions operating on the total wave signal. Next to the wavemaker, artificial damping terms are added for the reflected wave, which is taken as the total wave minus the incident wave predicted by linear wavemaker theory as given by e.g. Dean and Dalrymple (1991). The advantage of using this approach is that also irregular waves can be handled in a straightforward manner without the need to perform an additional simulation to obtain the incident-wave signal. The theory behind the numerical beaches is given in Appendix B, including a dedicated investigation of the performance of the beach next to the wavemaker. The lengths of the numerical damping zones are here taken as $L_{beach} = 2\lambda$ on both sides of the tank. It is noted that the length of the tank used in the present analysis is 2λ longer than in the analysis by Tanizawa et al. (1999). This is related to the length of the numerical damping zones. If L_{tank} was set to 6λ, the numerical damping zones would have to be shortened and their associated dissipation coefficients increased. Studies performed here indicate that this is unfavourable, since it easily leads to wave reflections from the damping zones themselves. However, the distance from the end of the numerical damping zones to the ship section is similar to in Tanizawa et al. (1999).

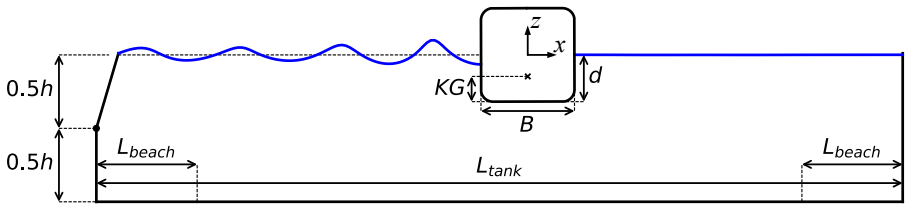

Figure 5.8: Sketch of wave tank with length L_{tank} and water depth h for a fixed 2D ship section in beam-sea regular waves. Waves are generated by a flap-type wavemaker hinged at half the water depth. Numerical damping zones with equal lengths L_{beach} are located at both ends of the tank. B, d and KG indicate the breadth, draught and vertical center of gravity of the body, respectively. The global, Earth-fixed Oxz coordinate system is located in the middle of the computational domain with origin in the still waterline.

5.2.1 Definition of Cases

The simulation cases are characterized by the non-dimensional wave frequency $\xi_B = \omega^2 B/2g = kB/2$, where ω is the angular wave frequency, g is the acceleration of gravity and k is the wave number as given by the linear dispersion relation assuming deep-water conditions. Taking Tanizawa et al. (1999) as reference, two wave heights ($H = 1\ cm$ and $H = 7\ cm$) are simulated for each wave frequency. The wave frequencies for each wave height are listed in Table 5.3. The steepness $k\zeta_A$ of the waves increases with ξ_B, and is so that significant wave non-linearities (trough-crest asymmetry) can be expected for the largest $k\zeta_A$ values.

Table 5.3: Simulation cases for a fixed 2D ship section in beam-sea waves. $\xi_B = \omega^2 B/2g$ and ω are the non-dimensional and dimensional wave frequencies, respectively, k is the wave number and $k\zeta_A$ is the wave steepness based on the linear wave amplitude ζ_A.

ξ_B $(-)$	k (m^{-1})	ω (s^{-1})	$k\zeta_{A,H=1cm}$ $(-)$	$k\zeta_{A,H=7cm}$ $(-)$
0.250	1.000	3.132	0.005	0.035
0.500	2.000	4.429	0.010	0.070
0.550	2.200	4.645	0.011	0.077
0.600	2.400	4.851	0.012	0.084
0.650	2.600	5.049	0.013	0.091
0.700	2.800	5.240	0.014	0.098
0.750	3.000	5.424	0.015	0.105
1.000	4.000	6.263	0.020	0.140
1.250	5.000	7.002	0.025	0.175
1.500	6.000	7.671	0.030	0.210
1.750	7.000	8.285	0.035	0.245
2.000	8.000	8.857	0.040	0.280

5.2.2 Numerical Setup

For all cases in Table 5.3, a time step $\Delta t = T/45$ is used, where T is the incident wave period. The ramp time of the wavemaker is set to $t_{ramp} = 4T$. Simulations are performed with duration $20T$, since it is found that steady-state conditions for wave loads are obtained already after approximately $12 - 14$ wave periods. Three grids are present, namely a stationary background grid and two overlapping grids fixed to the wavemaker and the body, respectively. All the grids are uniform with square cells. The grid spacing in the background grid and in the wavemaker-fixed grid is set to $\lambda/25$. The extent of the ship section-fixed grid varies with the wavelength, but is never smaller than $2.5B$. The grid spacing in this grid is taken as $min(B/12, \lambda/25)$. An example of the entire computational grid used in the analysis is shown in Figure 5.9 (a) at the initial time step, and with emphasis on the regions around the body-fixed grids on the wavemaker and on the ship section in (b) and (c). The free surface is described with the fully Lagrangian formulation

in Section 3.2.1 with markers uniformly distributed in x direction with marker spacing Δd_m. Δd_m is generally set equal to the grid spacing Δx_{bf} in the body-fixed grid on the body, but is in the same way as in Section 4.5 restricted by a CFL requirement in order to ensure numerical stability. The CFL requirement is here formulated as

$$CFL = \frac{u_m \Delta t}{\Delta d_m} \leq 1.0, \tag{5.8}$$

where u_m is a characteristic velocity related to the linear phase speed $c = \omega/k$. As a result, the marker spacing is increased to $\Delta d_m = 2\Delta x_{bf}$ for the case $\xi_B = 0.25$.

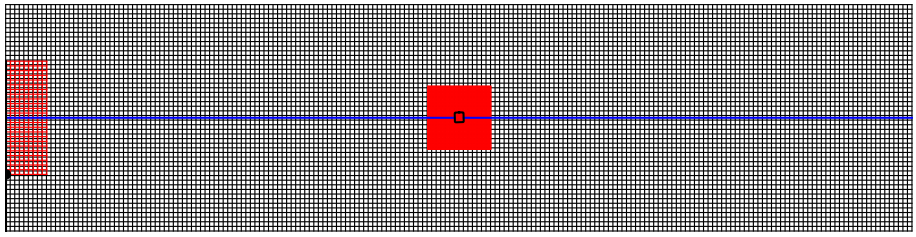

(a) Entire domain

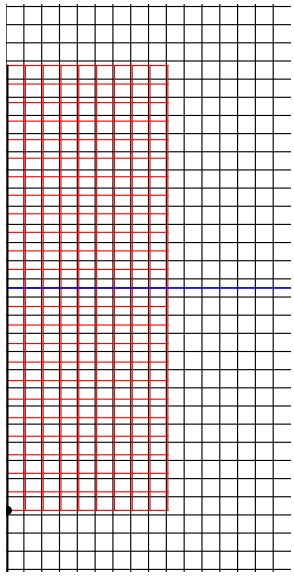

(b) Close up of wavemaker

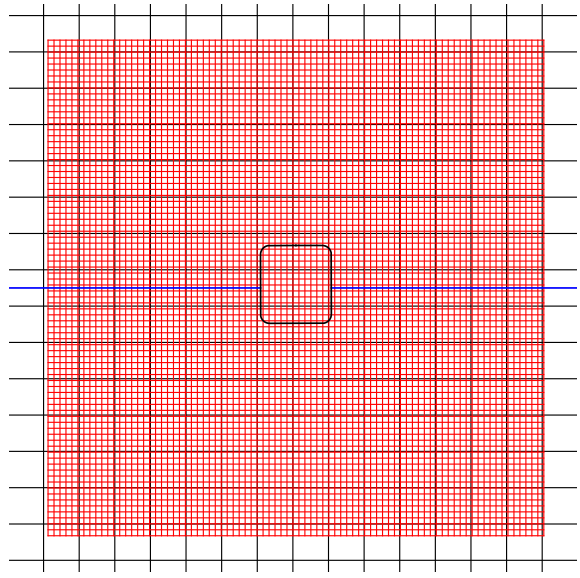

(c) Close up of body

Figure 5.9: Example of grids used for the case $\xi_B = 0.25$ shown at the initial time $t = 0$. The stationary background grid is indicated with black grid lines, while the body-fixed grids are indicated with red grid lines.

In order to ensure that the numerical modelling is adequate, an analysis of fluid energy and fluid volume in the tank as a function of time is given in Appendix D for a few of the cases in Table 5.3.

5.2.3 Results

It is noted that we here refer to the forces in x and z direction as sway and heave forces, respectively, and to the moment about the y axis as the roll moment. This notation is chosen because the examined structure is a ship section.

The time history of the non-dimensional sway force, heave force and roll moment for three wave frequencies $\xi_B = (0.5, 1.0, 2.0)$ are shown in Figure 5.10 with wave heights $H = 1\ cm$ and $H = 7\ cm$. It is evident that the non-linearity increases with the wave frequency, especially for the largest wave height. This is seen as crest-to-trough asymmetry and through the presence of higher-order harmonic components in the time series. Since the body is restrained from moving, these non-linearities can be attributed to the non-linearity of the incident waves and wave-body interactions without any contribution from floater motions.

A Fourier analysis is performed over the last 4 wave periods of the wave load time histories to derive transfer functions. Figure 5.11 shows the transfer functions for the mean sway wave drift force $F_x^{(0)}$ as well as for the 1^{st} order sway force $F_x^{(1)}$, heave force $F_z^{(1)}$ and roll moment $M_y^{(1)}$. The results of the present analysis are compared with experimental results and numerical results from a linear theory, both by Nojiri and Murayama (1975). For the mean wave drift force, theoretical results are from a 2^{nd} order theory based on the linear solution by Nojiri and Murayama (1975). The wave height used in the experiments is unknown to the present author. The results from a fully non-linear boundary element method (BEM) by Tanizawa et al. (1999) for $H = 7\ cm$ are also included. For the mean wave drift force they provide two estimates, respectively, from direct pressure integration (DPI) and from conservation of fluid momentum (CFM) through Maruo's formula, explained in Appendix C. In the present work, the mean wave drift force is evaluated from DPI and from CFM, using the *exact* method described in Appendix C with vertical control surfaces located a distance 0.5λ away from the body's center. While Maruo's formula is a 2^{nd} order theory, the exact method does not truncate the solution to any specific order. The difference between approximate methods, such as Maruo's formula, and the exact method for estimating the mean wave drift force will be further elaborated in the next chapter dealing with freely-floating body motions.

Figure 5.11 (a) shows that the mean wave drift force obtained with DPI and with CFM are consistent with each other with the present IBOGM. For wave frequencies $\xi_B \geq 1.0$, the mean wave drift force obtained with the IBOGM, especially for $H = 7\ cm$, becomes smaller than the theoretical value and those estimated by Tanizawa et al. (1999). This tendency can also be observed for the 1^{st} order sway force and roll moment, and is believed to be due to increasing wave non-linearity. Indeed, the same qualitative trend is also observed in the experimental results. For later discussions when the body is freely floating, it is pointed out that the mean wave drift force obtained from direct pressure integration by Tanizawa et al. (1999) is in close agreement with the present results for low and intermediate wave frequencies, and remains in fair agreement with the linear results for all wave frequencies.

Transfer functions for the $1^{st} - 4^{th}$ order wave loads found from Fourier analysis are shown in Figure 5.12. It is clearly seen that the higher-order components

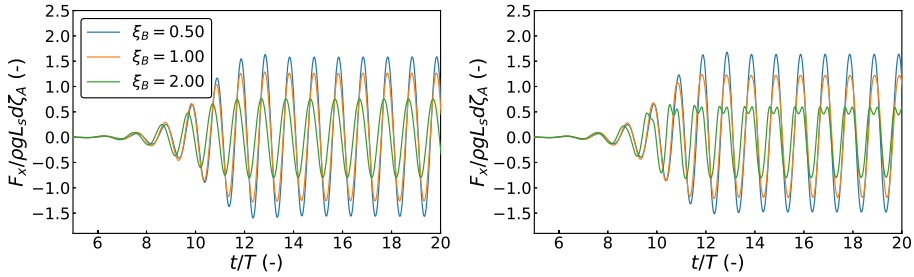

(a) Sway force ($H = 1\ cm$)

(b) Sway force ($H = 7\ cm$)

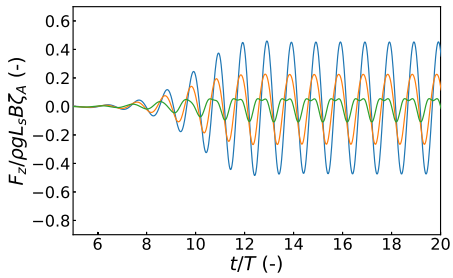

(c) Heave force ($H = 1\ cm$)

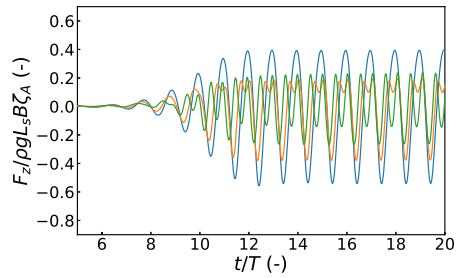

(d) Heave force ($H = 7\ cm$)

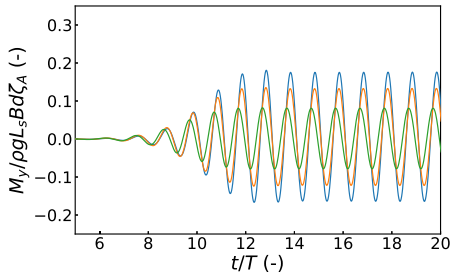

(e) Roll moment ($H = 1\ cm$)

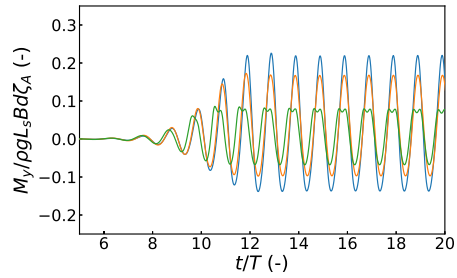

(f) Roll moment ($H = 7\ cm$)

Figure 5.10: Non-dimensional wave load time series for fixed 2D ship section in beam-sea waves for non-dimensional wave frequencies $\xi_B = (0.5, 1.0, 2.0)$.

increase when ξ_B increases for $H = 7\ cm$. Considering the mean wave drift force in Figure 5.11, it is plausible that the decreasing drift force for higher wave frequencies can be related to higher-order effects. It is not clear why this trend is not observed in the results by Tanizawa et al. (1999) using direct pressure integration, although it could be due to the way of generating the incident wave in their work. It is understood that in their analysis, the incident waves are generated by imposing a fluid velocity corresponding to linear wave theory at a fixed control surface. Furthermore, it is stated that the wave tank is 6λ long, which means that the distance between the surface where the incident wave is generated and where

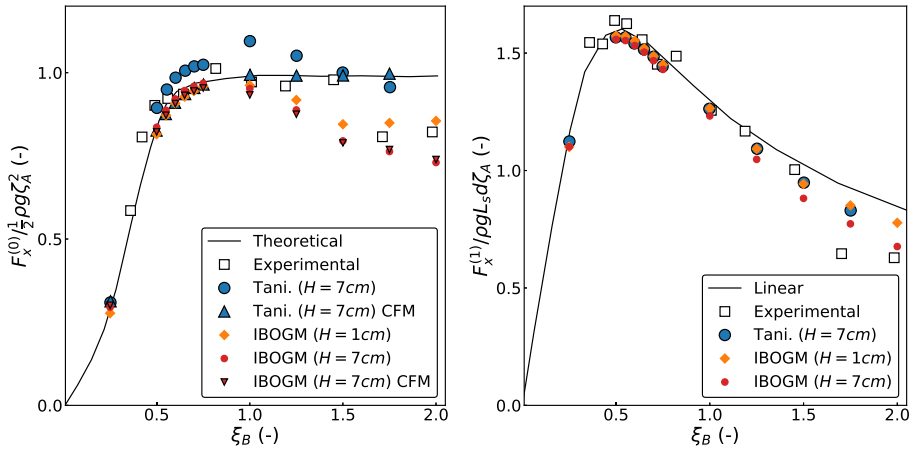

(a) Mean sway drift force

(b) 1^{st} order sway force

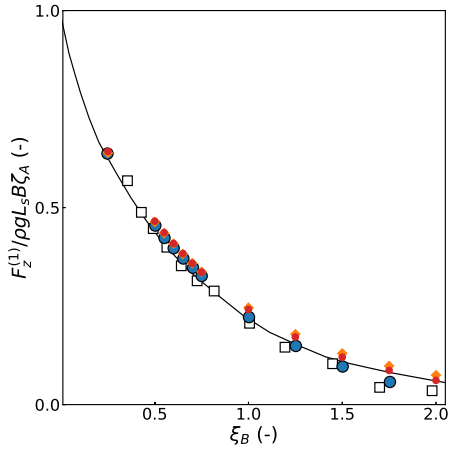

(c) 1^{st} order heave force

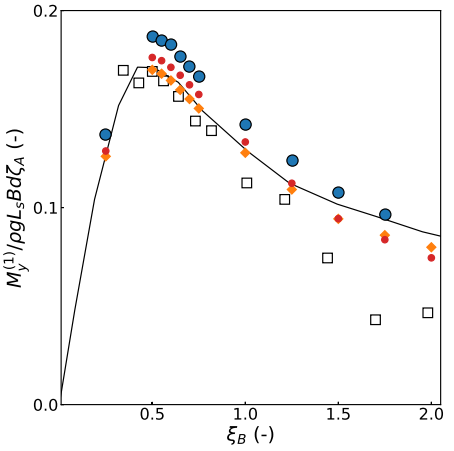

(d) 1^{st} order roll moment

Figure 5.11: Wave load transfer functions for fixed 2D ship section in beam-sea waves. The results from the present IBOGM are compared with experimental, linear and theoretical results by Nojiri and Murayama (1975) and non-linear BEM results by Tanizawa et al. (1999). The results in (a) denoted *CFM* are estimated from conservation of fluid momentum, using the exact method in the IBOGM and Maruo's formula in Tanizawa et al.'s results.

the body is located is one wavelength shorter than in the present analysis. It is possible that this distance is too short for wave non-linearities to fully develop, since they initially impose the incident wave as a linear wave. In connection with the present analysis, it has been found that the magnitude of higher-order wave load components indeed depends on the distance between the wavemaker and the body.

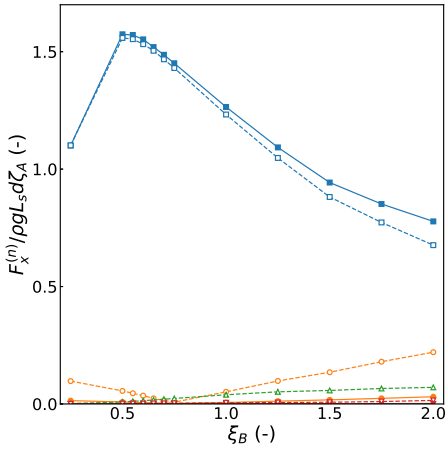

(a) sway force

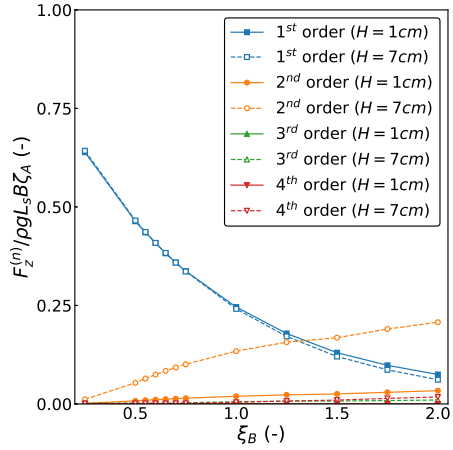

(b) Heave force

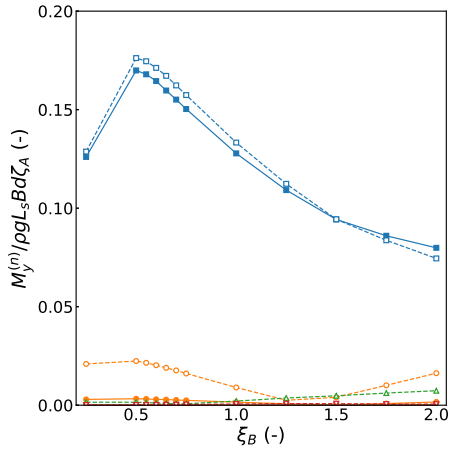

(c) Roll moment

Figure 5.12: Transfer function for $1^{st} - 4^{th}$ order wave loads for fixed 2D ship section in beam-sea waves from IBOGM analysis.

5.3 Summary

In this chapter the immersed boundary-overlapping grid method (IBOGM) proposed in Chapter 3 has been applied to wave-radiation and wave-diffraction problems.

First, a circular cylinder undergoing forced, harmonic heave motion in still water with different oscillation frequencies was analyzed. Added mass and damping coefficients, as well as the mean and 2^{nd} order heave forces, were derived and shown to compare well with analytical, experimental and numerical reference results. The 2^{nd} order force amplitude was seen to increase with oscillation frequency, indicating increased non-linearity. For the highest oscillation frequencies, strong non-linear features of the radiated waves developed locally close to the body. This leads to small angles between the free surface and the body surface, so that a jet-cutting scheme had to be invoked in the potential-flow analysis. It was shown that this scheme ensures numerical stability, and a free-surface profile that is consistent with results from a different numerical method. The results indicate that the present numerical method is able to account for free surface-body interactions for bodies with non-vertical walls through the free surface, and that it remains numerically robust even when strong free-surface non-linearities are present close to the body.

Thereafter, a fixed 2D ship section in beam-sea incident waves with different amplitudes and frequencies was considered. The 1^{st} order wave loads, as well as the mean wave drift force in sway, were compared to theoretical, experimental and numerical reference results. When the wave steepness was high, significant high-order components were present in the time series of the wave loads on the body. For higher wave frequencies, and in particular for the waves with largest amplitude, the mean wave drift force was found to deviate from theoretical and numerical reference results, but in qualitative agreement with the experimental results. It was argued that the difference from theoretical and numerical reference results were related to higher-order load components due to increasing wave steepness. Indeed, the 2^{nd} order sway force was found to increase with wave steepness. It was shown that the mean wave drift force obtained from integration of the fluid pressure over the instantaneous wetted body surface was consistent with results estimated from conservation of fluid momentum using an exact method, i.e. without any additional approximations.

The studies in the previous chapter, involving propagation of non-linear waves, and the present chapter, involving water-body interactions with either radiation or diffraction effects, highlighted important features and capabilities of the numerical method. The next chapter combines all these phenomena through examining incident waves interacting with a freely floating body. This chapter also investigates available methods to estimate the mean wave drift force, showing significant individual differences under certain conditions.

Chapter 6

A Freely Floating Body in Waves

The 2D ship section in regular beam-sea waves, studied as fixed in Section 5.2, is now examined as a freely floating body. The numerical setup is similar, except for the addition of a linear stiffness and damping in sway. With these included, the total external force vector $\boldsymbol{F}_{bf,ext}$ in the equation of translational motion in (3.35) in Section 3.2.10 includes an additional force vector defined as

$$\boldsymbol{F}_{bf,add} = -\boldsymbol{\Lambda}_{i\to b} \cdot (\boldsymbol{B}^l \cdot \dot{\boldsymbol{R}}_0 + \boldsymbol{C} \cdot \boldsymbol{R}_0), \tag{6.1}$$

where $\boldsymbol{R}_0$ and $\dot{\boldsymbol{R}}_0$ are the position and velocity of the body's center of gravity in the inertial reference frame, respectively. $\boldsymbol{\Lambda}_{i\to b}$ is the rotation matrix defined in equation (2.1). $\boldsymbol{B}^l$ is a linear damping matrix defined as

$$\boldsymbol{B}^l = \begin{pmatrix} B^l_{22} & B^l_{23} \\ B^l_{32} & B^l_{33} \end{pmatrix}, \tag{6.2}$$

and $\boldsymbol{C}$ is a stiffness matrix

$$\boldsymbol{C} = \begin{pmatrix} C_{22} & C_{23} \\ C_{32} & C_{33} \end{pmatrix}. \tag{6.3}$$

The damping and stiffness forces are applied in the body's center of gravity, and all terms except B^l_{22} and C_{22} are set equal to zero in (6.2) and (6.3). The values of the linear sway damping and stiffness are set equal to the values used in the experiments by Nojiri and Murayama (1975), respectively $B^l_{22} = 19.8\ Nsm^{-1}$ and $C_{22} = 197.58\ Nm^{-1}$. As indicated in (6.1), the damping and stiffness forces relate to the body motion in the inertial coordinate system. This is in order to be consistent with the experimental setup. The body's roll moment of inertia, also set equal to the value used in the experiments, is $I_{yy} = 4.0145\ kgm^2$. The vertical center of gravity, already defined in Section 5.2, is $KG = 0.135\ m$. The effect of adding quadratic roll damping will also be investigated. In that case, an additional roll moment $M_{y,add} = -B^l_{55}\dot{\eta}_5|\dot{\eta}_5|$, where $\dot{\eta}_5$ is the roll velocity, is added to the equation of angular motion in (3.35).

The dimensions of the numerical wave tank are equal to those discussed in connection with Figure 5.8, and are therefore not repeated here. The remainder of the numerical setup, including the spatial and temporal discretization, is similar

to in Section 5.2 except for the duration of the simulations. This is here taken as $60T$, where T is the incident wave period. This is to allow for the transient phase of the body motions to die out so that the time signals used in Fourier analysis have reached steady state. It is however to be noted that the decay of transient motions is a function of both wave frequency and amplitude, and especially low-frequency sway motions may decay slowly. This can in a few cases make the simulation time required to achieve true steady-state conditions as high as $100T$ or more. The choice of $60T$ as simulation duration is thus taken as a reasonable compromise under the assumption that the presence of small low-frequency sway motions will have little or negligible influence on the quantities of interest. In this connection one could argue that some quadratic sway damping would have been appropriate in order to increase the decay rate of low-frequency motions. The reason for not applying this in the present work is in order to stay as consistent as possible with the analysis by Tanizawa et al. (1999), where such damping is not mentioned. Transfer functions of wave loads and motions are derived from Fourier analysis of the time histories after the simulations are completed. As a general rule, the time window used in the Fourier analysis is $40T \leq t < 60T$. Minor adjustments are made to the time window for a few cases in order to have a time signal that is visually at steady state in the Fourier analysis.

Results from the immersed boundary-overlapping grid method (IBOGM) are compared with the experiments and numerical results based on a linear theory by Nojiri and Murayama (1975) and non-linear BEM results by Tanizawa et al. (1999) and by Koo and Kim (2004). Results from recent dedicated numerical simulations with the non-linear BEM used by Greco (2001) are considered for a further in-depth assessment of the IBOGM.

6.1 Definition of Cases

Compared with the cases analyzed for the fixed body in Section 5.2, an intermediate wave height $H = 3\ cm$ is added for the freely floating body. In addition, a larger number of wave frequencies is considered in the wave-frequency range $0.5 \leq \xi_B \leq 0.6$ that includes the body's natural heave and roll frequencies. The complete set of cases for the freely floating body is shown in Table 6.1. It is noted that the wave frequencies $\xi_B = 0.525$ and $\xi_B = 0.575$ are only simulated for wave heights $H = 1\ cm$ and $H = 3\ cm$. For the largest wave height $H = 7\ cm$, the heave and roll motions for these particular wave frequencies become so large that the simulations break down. Results from these simulations are hence omitted. It is also noted that results for wave frequency $\xi_B = 0.5$ with $H = 7\ cm$ are omitted by Tanizawa et al. (1999), citing that this case lead to numerical divergence. Furthermore, Koo and Kim (2004) do not include non-linear results for $0.4 < \xi_B < 0.6$.

Table 6.1: Simulation cases for a freely floating 2D ship section in beam-sea waves. $\xi_B = \omega^2 B/2g$ and ω are the non-dimensional and dimensional wave frequencies, respectively, k is the wave number and $k\zeta_A$ is the wave steepness based on the linear wave amplitude ζ_A.

ξ_B $(-)$	k (m^{-1})	ω (s^{-1})	$k\zeta_{A,H=1cm}$ $(-)$	$k\zeta_{A,H=3cm}$ $(-)$	$k\zeta_{A,H=7cm}$ $(-)$
0.250	1.000	3.132	0.005	0.015	0.035
0.500	2.000	4.429	0.010	0.030	0.070
0.525	2.100	4.538	0.011	0.032	-
0.550	2.200	4.645	0.011	0.033	0.077
0.575	2.300	4.749	0.012	0.035	-
0.600	2.400	4.851	0.012	0.036	0.084
0.650	2.600	5.049	0.013	0.039	0.091
0.700	2.800	5.240	0.014	0.042	0.098
0.750	3.000	5.424	0.015	0.045	0.105
1.000	4.000	6.263	0.020	0.060	0.140
1.250	5.000	7.002	0.025	0.075	0.175
1.500	6.000	7.671	0.030	0.090	0.210
1.750	7.000	8.285	0.035	0.105	0.245
2.000	8.000	8.857	0.040	0.120	0.280

6.2 Comparison with Linear Numerical, Theoretical and Experimental Results

The transfer functions for the mean sway wave drift force and 1^{st} order rigid-body motions in sway, heave and roll from the IBOGM for all the cases in Table 6.1 are compared with the linear and theoretical results by Koo and Kim (2004) and the experimental results by Nojiri and Murayama (1975) in Figure 6.1. The motion amplitudes in sway, heave and roll, denoted η_{1a}, η_{3a} and η_{5a}, respectively, are taken in, and about, the body's center of gravity in the inertial reference frame. The mean wave drift force by Koo and Kim (2004) is based on a 2^{nd} order theory.

For wave frequencies around $\xi_B = 0.5$, that is close to the body's natural heave and roll frequencies, the IBOGM motions display non-linear behaviour. This is evident by the fact that the normalized response amplitudes decrease with increasing wave height. It is believed that the non-linear behaviour of the heave motion is partially due to coupled effects as a result of large roll motions. Another likely contributing factor is an increase of the 2^{nd} order heave wave-excitation force with increasing wave height. This was clearly observed in Figure 5.12 when the body was restrained from moving. Although the peak of the heave transfer function increases with decreasing wave height, it is consistently lower than the linear results. A possible explanation for this is that even for $H = 1\ cm$ the roll motion is close to 10°. Hence, the assumption of small body motions, which is central in a linear approximation, is never fulfilled for frequencies close to resonance.

The experimental results indicate that the roll damping around resonance is

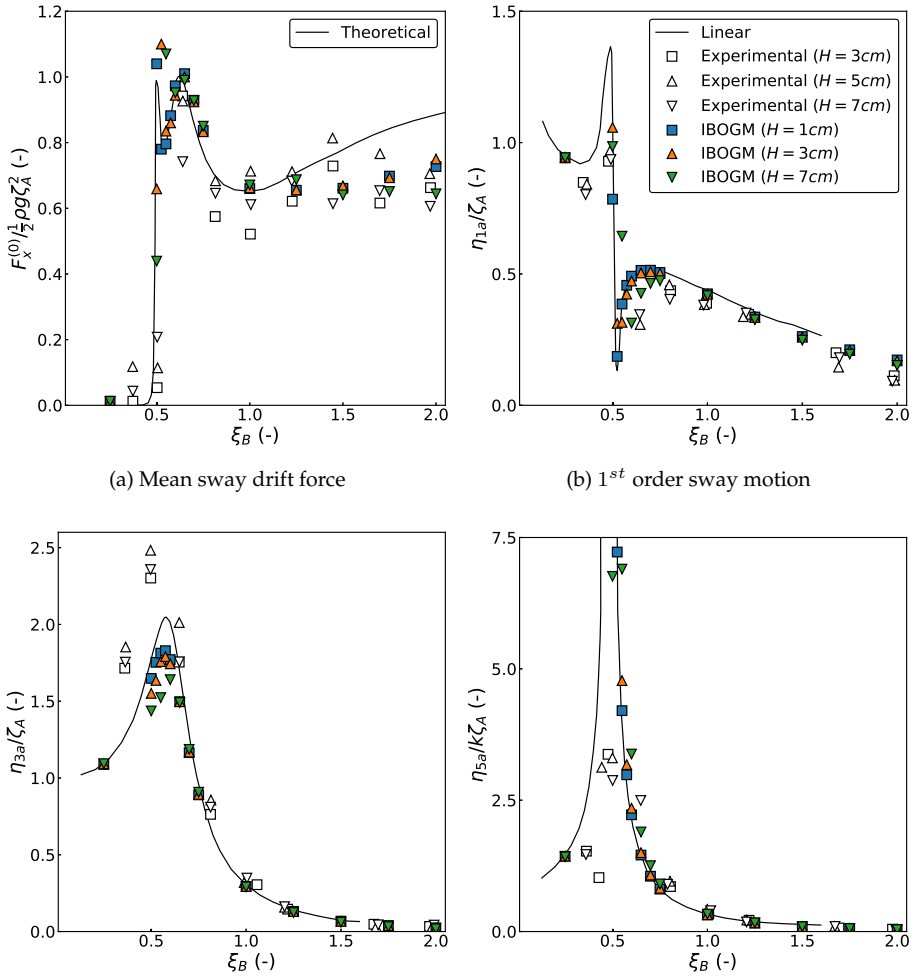

(a) Mean sway drift force

(b) 1^{st} order sway motion

(c) 1^{st} order heave motion

(d) 1^{st} order roll motion

Figure 6.1: Transfer functions for a freely floating 2D ship section in beam-sea waves. The results from the present IBOGM are compared with linear and theoretical results by Koo and Kim (2004) and experimental results by Nojiri and Murayama (1975). The mean wave drift force $F_x^{(0)}$ is in the IBOGM obtained from direct integration of fluid pressure.

significantly greater than that in the numerical analysis, with a response amplitude less than half that of the IBOGM results for $H = 7\ cm$. As a consequence, the effect of adding quadratic roll damping in the IBOGM analysis is examined in Section 6.2.1. In connection with the experimental results, it is here pointed out that the paper by Nojiri and Murayama (1975) is largely written in Japanese. As a consequence, the details of the experimental setup are not fully understood, nor is it possible to assess the experimental uncertainty. As far as possible, the paper by Tanizawa et al. (1999) is used to complement the missing information from the experiments.

The normalized sway motion from the IBOGM analysis agrees well with the linear theory, except in the frequency range $0.6 \leq \xi_B < 1.0$ for $H = 7\ cm$ where the IBOGM predicts notably lower 1^{st} order sway motions. This trend is also observed in the experimental results. Moreover, the experimental results show significantly higher heave response and lower roll response than both the linear analysis and the IBOGM analysis for wave frequencies below heave resonance. The reason for this is not well understood, most notably because the details of the experimental procedure and related uncertainties are not known.

For the mean wave drift force, the same behaviour is observed as for the fixed body in Figure 5.11 both in the IBOGM analysis and in the experimental results. That is, for higher wave frequencies, the mean drift force becomes smaller than the theoretical results. For the IBOGM, the difference increases with increasing wave height, indicating non-linear behaviour. Moreover, since the 1^{st} order motions are moderate for $\xi_B > 1.0$, it is likely that the observed trend is mainly related to non-linearity of the incident waves. It is to be noted that the normalized drift force in the IBOGM analysis has an amplitude larger than unity for all wave heights around $\xi_B = 0.50$, which is not possible according to 2^{nd} order theory. This indicates non-linear effects in the IBOGM analysis, likely related to large-amplitude 1^{st} order heave and roll motions. Indeed, normalized mean wave drift forces above unity were not observed for the fixed body in Figure 5.11. One should also keep in mind that the absolute value of the mean drift force is much smaller than the 1^{st} order wave force, which makes the Fourier analysis more sensitive towards the choice of time window. Although the time windows used in the present analysis are selected carefully, this should nevertheless be considered as a source of uncertainty in processing both experimental and simulated time signals. The mean wave drift force is here obtained by direct integration of fluid pressure over the instantaneous wetted body surface. It is sometimes claimed that this method is less accurate than estimating the mean wave drift force from conservation of fluid method. As it will be shown in Section 6.2.2, however, the direct pressure integration is considered to be the most accurate method in the present analysis.

To further understand the behaviour of the transfer functions in Figure 6.1, the transfer functions for the $1^{st} - 4^{th}$ order wave loads for the freely floating body for all wave heights are computed in Figure 6.2. One should keep in mind that these are total wave loads obtained from integration of the fluid pressure over the instantaneous wetted body surface, and therefore include both wave excitation, radiation and restoring loads. Indeed, the amplitudes of both the 2^{nd} and 3^{rd} order sway force are non-negligible around $\xi_B = 0.5$. For higher wave frequencies, and with increasing wave height, the 2^{nd} order sway force increases while the

1^{st} order amplitudes decrease. This trend is similar to the trend observed for the fixed body in Figure 5.12. Also for the heave force and roll moment an increase of the higher-order load components, accompanied with reduced 1^{st} order loads, occurs. This is most notably seen for the roll moment, where the normalized 1^{st} order component for $H = 7\ cm$ is approximately half of that for $H = 1\ cm$. Moreover, the peak frequency is shifted towards the heave natural frequency, which indicates a non-linear heave-roll coupling. Due to the increase of higher-order components in Figure 6.2, one may question whether a 1^{st} or 2^{nd} order analysis is sufficient to estimate the wave loads and resulting body motions close to heave and roll resonance for high waves, or to estimate the mean wave drift force for steep waves associated with high ξ_B values.

6.2.1 Influence of Roll Damping

Near resonance, the roll motion is clearly over-predicted in the IBOGM analysis in Figure 6.1 compared with the experimental results. As explained by Faltinsen (1993), the potential roll damping is small for a typical ship cross section at roll resonance. The discrepancy between the experimental and numerical results is therefore likely due to viscous roll damping. Thus, in order to examine the influence that roll damping has on coupled motions and on the mean wave drift force near roll resonance, quadratic roll damping is added in the IBOGM analysis with $H = 7\ cm$ and with wave frequencies ξ_B densely distributed in the range $0.425 - 0.575$. Two values of the quadratic roll-damping coefficient B_{55}^q are considered, corresponding to equivalent linear roll damping coefficients $B_{55}^{l,eq}$ approximately equal to 3% and 5% of the critical roll damping $B_{55,cr}$ at the roll resonance frequency $\xi_B = 0.5$, respectively. In estimating the critical roll damping the added roll inertia is neglected so that $B_{55,cr} = 2\sqrt{I_{yy}C_{55}}$. C_{55} is the hydrostatic roll stiffness $\rho g \nabla GM_5$, where ∇ is the volume displacement and GM_5 is the metacentric height. In steady-state conditions, and with motions oscillating with a single frequency ω, $B_{55}^{l,eq}$ is linked to B_{55}^q through

$$B_{55}^{l,eq} = B_{55}^q |\eta_{5a}| \frac{8\omega}{3\pi}, \tag{6.4}$$

see e.g. Faltinsen (1993). η_{5a} is the roll amplitude (in radians), here taken as the maximum observed roll motion during a simulation without quadratic roll damping. The corresponding quadratic damping coefficients B_{55}^q are $1\ kgm^2$ and $2\ kgm^2$, respectively.

Transfer functions for the mean sway wave drift force and 1^{st} order rigid-body motions for the simulations with quadratic roll damping are shown in Figure 6.3. Clearly, the analysis with $B_{55}^q = 2\ kgm^2$ gives roll amplitudes closest to the experiments near resonance. The roll damping has a significant influence also on sway and heave motions, confirming that there are significant coupling effects between the motion in these three degrees of freedom. With increasing roll damping, the heave amplitudes move towards the linear results, but tend to converge against a lower response in the same way as the results with decreasing wave height in Figure 6.1. The added roll damping reduces sway amplitudes for $\xi_B < 0.5$ and

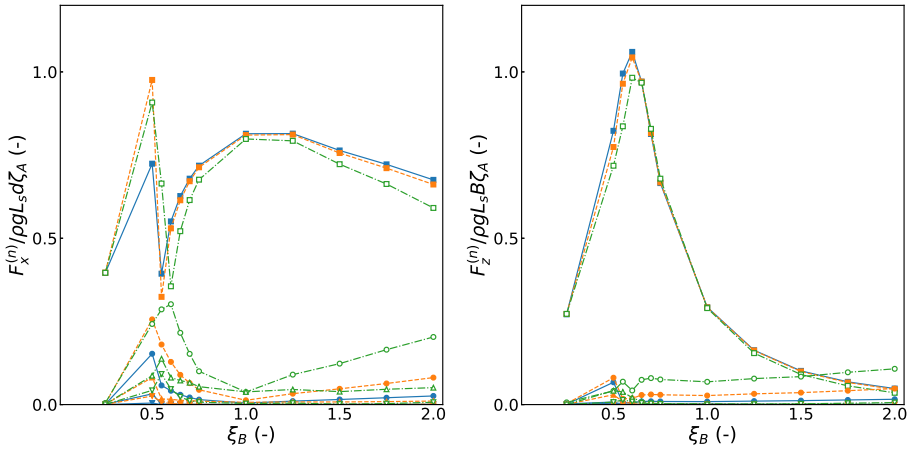

(a) Sway force

(b) Heave force

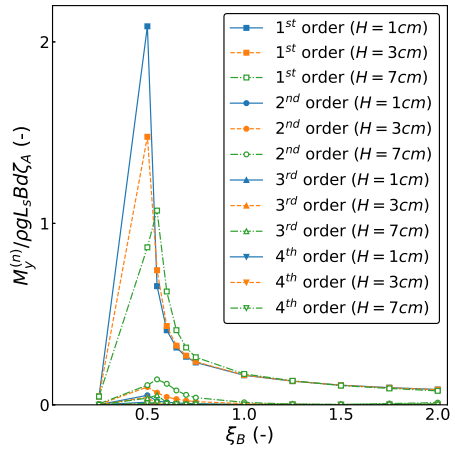

(c) Roll moment

Figure 6.2: Transfer function for $1^{st} - 4^{th}$ order wave loads for a freely floating 2D ship section in beam-sea waves from IBOGM analysis.

increases sway amplitudes for $\xi_B > 0.5$. However, the sway response does generally not agree with the linear results. In combination with the fact that the IBOGM analysis gives lower heave amplitudes than the linear results, this may indicate that non-linear effects are important in this frequency range also when roll damping is added. Here it can be noted that, even though roll motions are reduced, the roll amplitudes are still as large as $\eta_{5a} \approx 15°$. It is also clear that adding roll damping does not make the mean wave drift force converge towards the theoretical curve, although it is seen to have a significant influence, with reduced values of $F_x^{(0)}$ when increasing the roll damping for $\xi_B \geq 0.5$. The latter is an observation

of practical importance when analysing ship-shaped floaters that are exposed to large roll motions. In particular if the ship has bilge keels, the viscous damping may be significant. If the ship behaviour is analyzed using perturbation theory, the motion coupling effects observed in the present simulations may not be captured. Similarly, if the wave drift force in addition is based on a 2^{nd} order approximation, it may not be accurately calculated. Validation against model test data of high quality is thus suggested as appropriate in these scenarios.

The discussion above suggests that adding roll damping does not necessarily make the results of the non-linear IBOGM analysis approach the linear or theoretical solution. The roll motions are still significant near resonance, and the added roll damping appears to influence the coupling between sway, heave and roll motions. For a further investigation, the normalized amplitudes of the $1^{st} - 4^{th}$ order sway force components are plotted in Figure 6.4. The magnitudes of all components decrease with increasing roll damping. However, the relative decrease of the 1^{st} order component is stronger than that of the 2^{nd} order component around $\xi_B = 0.5$. One may therefore say that the 2^{nd} order force component becomes more important when non-linear roll damping is added. Moreover, the 1^{st} order component is smaller with $B^q_{55} = 2\ kgm^2$ than with $B^q_{55} = 1\ kgm^2$ for $\xi_B < 0.525$, but larger for $\xi_B > 0.525$. This supports the claim that adding roll damping in the non-linear analysis does not necessarily make the problem more linear-like for wave frequencies close to roll resonance.

6.2.2 Conservation of Fluid Momentum versus Direct Pressure Integration for Estimation of the Mean Wave Drift Force

Until now we have presented the mean sway drift force obtained from integration of the fluid pressure over the wetted body surface, often denoted as direct pressure integration (DPI). It is also possible to obtain the mean wave drift force from conservation of fluid momentum (CFM). In analysis based on perturbation theory, this method is traditionally considered more robust than DPI (DNV GL, 2017). In the context of fully non-linear time domain analysis, this conclusion is less obvious. In the following, three methods for estimating the mean wave drift force from CFM are investigated:

- Exact evaluation of the fluid momentum.
- A 2^{nd} order approximate method.
- Maruo's formula.

The drift force from the 2^{nd} order approximate method is expressed as

$$F_x^{(0)} = \frac{1}{4}\rho g(\zeta_A^2 + \zeta_R^2 - \zeta_T^2)\left[1 + \frac{2kh}{sinh2kh}\right], \tag{6.5}$$

where ζ_A is the incident wave amplitude taken as $H/2$, ζ_R is the reflected wave amplitude found from a reconstruction of the wave signal using the method described in Appendix E and the transmitted wave amplitude ζ_T is taken as the wave amplitude measured in a wave probe located between the body and the numerical beach on the opposite side of the wavemaker. Maruo's formula follows

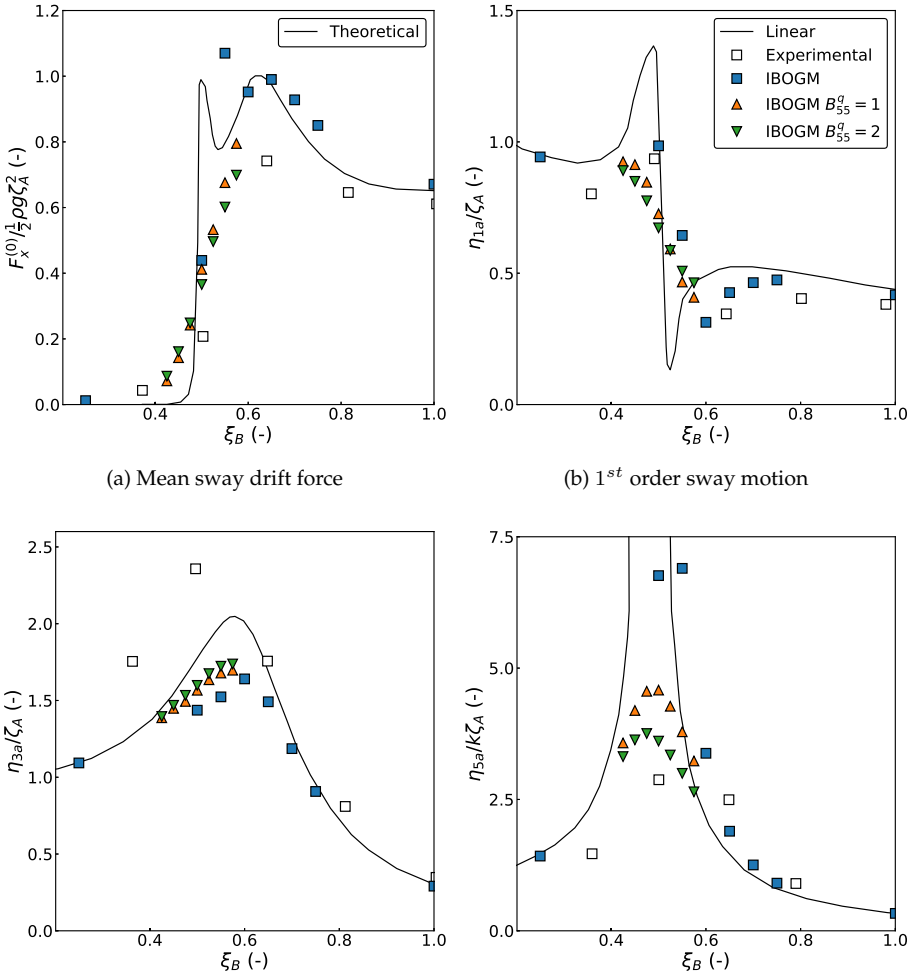

(a) Mean sway drift force

(b) 1^{st} order sway motion

(c) 1^{st} order heave motion

(d) 1^{st} order roll motion

Figure 6.3: Transfer functions for a freely floating 2D ship section in beam-sea waves. The linear and theoretical results are from Koo and Kim (2004), and the experimental results are from Nojiri and Murayama (1975) with $H = 7\ cm$. The IBOGM results without and with quadratic roll damping coefficients $B_{55}^q = 1\ kgm^2$ and $B_{55}^q = 2\ kgm^2$ are all for $H = 7\ cm$, and with the mean wave drift force $F_x^{(0)}$ obtained from direct integration of fluid pressure.

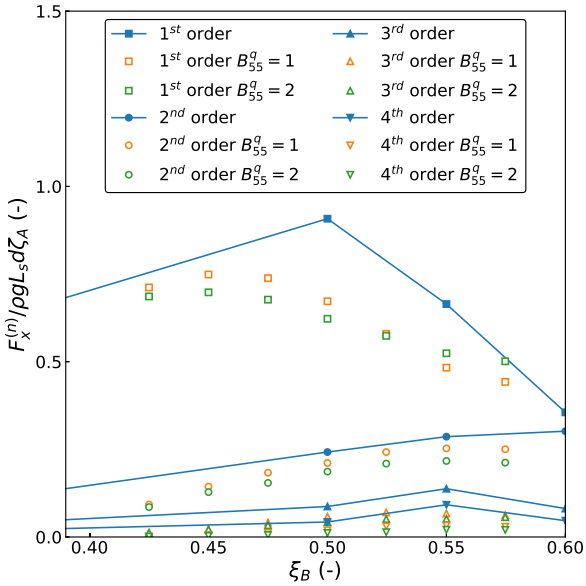

Figure 6.4: Transfer function for $1^{st} - 4^{th}$ order sway forces for a freely floating 2D ship section in beam-sea waves from IBOGM analysis with $H = 7\ cm$. Comparison of analysis without and with quadratic roll damping coefficients $B_{55}^q = 1\ kgm^2$ and $B_{55}^q = 2\ kgm^2$.

directly from (6.5) by in addition assuming that fluid energy is conserved,

$$F_x^{(0)} = \frac{1}{2}\rho g \zeta_A^2 (1 - C_T^2)\left[1 + \frac{2kh}{sinh2kh}\right]. \tag{6.6}$$

Here, C_T is the wave transmission coefficient defined as ζ_T/ζ_A. Both (6.5) and (6.6) make use of the same assumptions as in linear theory, i.e. that non-linear parameters such as the wave amplitude and body motions are small and can be approximated by truncated series around their mean values. While the exact method requires that the fluid-momentum flux across control surfaces is evaluated during the simulation, the methods in (6.5) and (6.6) only require time histories of the wave elevation. The exact method is therefore computationally somewhat more expensive. The theories behind the methods are elaborated in Appendix C.

The mean wave drift force estimated from CFM is compared to theoretical results and DPI for $H = 1\ cm$ in Figure 6.5, for $H = 3\ cm$ in Figure 6.6 and for $H = 7\ cm$ in Figure 6.7. The results for $\xi_B = 0.525$ and $\xi_B = 0.575$ are omitted for all wave heights, since these frequencies resulted in unstable simulations for the largest wave height. The mean wave drift force from the exact CFM formulation is evaluated with the vertical control surfaces located a distance 0.5λ and λ from the initial center of the body. In addition to the CFM results, the mean wave drift force is also estimated from the mean sway position $\overline{x}$ of the body, i.e. $F_x^{(0)} = C_{11}\overline{x}$. This simple estimate can be done because there are no other environmental loads

than those due to waves, so that the mean offset is solely due to wave action. As it can be seen, the mean wave drift force obtained from DPI is consistent with the offset estimate for most frequencies. Notable differences can only be seen for a few frequencies around $\xi_B = 0.5$, and are likely related to the significant higher-order sway force components seen in Figure 6.2 in this frequency range. From this argument, the mean sway drift force obtained from DPI can be considered consistent with the mean offset of the body.

For $\xi_B \geq 1.0$, the mean wave drift force from the exact CFM mostly agrees with DPI for all wave heights, and shows small or negligible differences with respect to the location of vertical control surfaces. For ξ_B closer to the natural heave and roll frequencies, the mean wave drift force from the exact CFM tends to be significantly lower than from DPI, and with different results depending on the location of the vertical control surfaces. The results obtained with the vertical control surface located closer to the body are generally closer to the results from DPI around $\xi_B = 0.5$. The results for the fixed body in Figure 5.11, on the other hand, showed that the mean wave drift force from exact CFM remains in excellent agreement with DPI for all frequencies. The observed differences between the exact CFM and DPI here are thus related to large body motions. Results from the 2^{nd} order approximate method (6.5) show no consistent agreement with neither the theoretical results nor with results from DPI, and the degree of correlation varies with both wave height and frequency. The results obtained with Maruo's formula (6.6) are qualitatively consistent with the theoretical results and in fair agreement with the results from DPI up to $\xi_B = 1.0$. However, Maruo's formula never predicts normalized drift forces above unity.

The results here indicate that the mean wave drift force is most reliably obtained from DPI. The exact CFM results agree well with DPI when wave-frequency motions are limited, but give smaller wave drift forces around the heave and roll resonance frequencies. More research is required to fully understand these discrepancies. However, the results indicate that they are associated with large body motions.

The approximate formulas (6.5) and (6.6) appear inappropriate to estimate the mean wave drift force, especially for the highest waves. Significant differences are observed both close to the heave and roll resonance frequencies, where rigid-body motions are large, and for higher wave frequencies, associated with steep waves. Clearly, the underlying assumptions in deriving these formulas are violated in both these scenarios. One should therefore be careful to use such approximate formulas in relation with non-linear simulations, since important non-linear effects may not be adequately captured. Estimating the mean wave drift force from the mean position of the body appears to be a more robust method in this respect, generally giving results in close agreement with DPI. However, this approach is not possible if other environmental loads, such as wind and current, are included, since the body motion is then not only due to wave action.

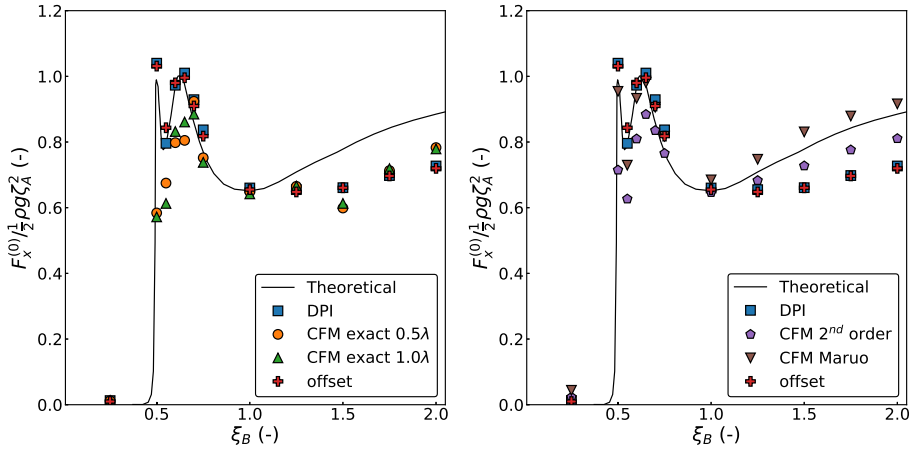

(a) Exact CFM (b) Approximate CFM

Figure 6.5: Mean sway wave drift force for a freely floating 2D ship section in beam-sea waves for $H = 1\ cm$. The theoretical results are from Koo and Kim (2004), the results denoted *DPI* are from direct pressure integration, the results denoted *CFM* are from conservation of fluid momentum using either *exact* or 2^{nd} order approximate formulations (including Maruo's formula), and the results denoted *offset* are estimated from the mean sway offset.

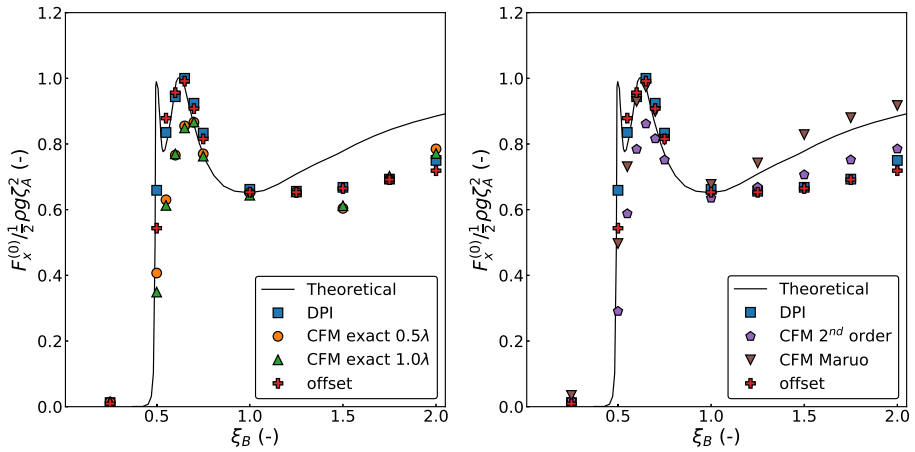

(a) Exact CFM (b) Approximate CFM

Figure 6.6: Same as Figure 6.5 with $H = 3\ cm$.

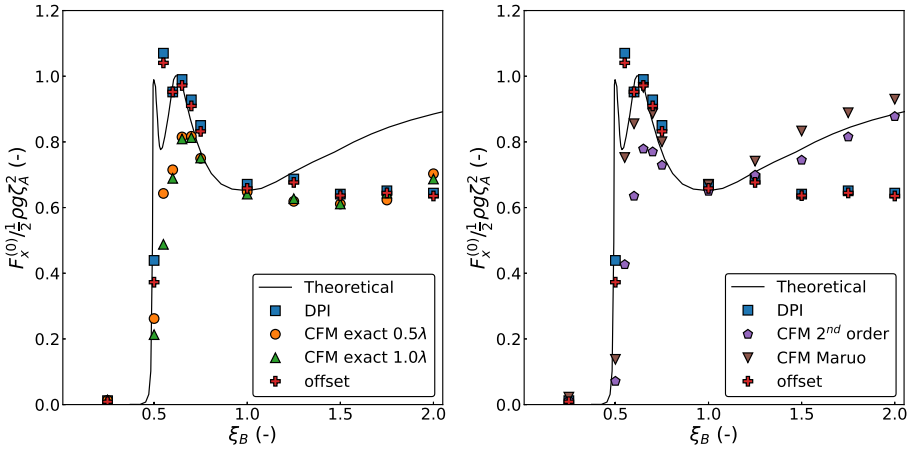

(a) Exact CFM

(b) Approximate CFM

Figure 6.7: Same as Figure 6.5 with $H = 7\ cm$.

6.3 Comparison with Greco's Non-Linear Numerical Results

Not all the details from the numerical reference results examined in this chapter are available. Therefore, a verification is performed against dedicated studies with a fully non-linear potential-flow solver. The cases with $H = 7\ cm$ in Table 6.1, except for a few wave frequencies, are analyzed using the BEM code developed by Greco (2001). This was originally used to study highly non-linear wave-on-deck problems, including extensive validation against experimental data. The numerical wave tank is similar to Figure 5.8, including the length and depth of the tank. The numerical setup, including the duration of the simulation, the length and formulation of the numerical beaches, the geometry of the body and the inertia, damping and restoring coefficients, are similar to the IBOGM analysis. The required time step in the BEM was found to be half of that used in the IBOGM analysis in order to obtain numerically stable simulations for the most challenging cases with large body motions. The incident waves are generated by an identical moving flap with the same wavemaker signal as in the IBOGM analysis. As in the present work, the time derivative of the velocity potential φ is obtained by solving an auxiliary boundary value problem (BVP) for this variable. The Fourier analysis to obtain transfer functions are performed by the present author using the same methodology as in post-processing of results from the IBOGM analysis in order to remove this as a source of uncertainty. The major difference between the two analyses is thus that Greco (2001) uses a BEM as potential-flow solver and that the two BVPs for φ and for its time derivative are solved in an Earth-fixed inertial reference frame. The simulations performed with Greco's code are therefore considered as an independent verification of the IBOGM analysis using a fundamentally different potential-flow solver from the one in the present work, but with identical boundary conditions.

Transfer functions for the mean sway drift force and 1^{st} order rigid-body motions are compared between the two analyses in Figure 6.8, where also the linear and theoretical results by Koo and Kim (2004) and the experimental results by Nojiri and Murayama (1975) are included. All the non-linear and experimental results are for $H = 7\ cm$. Figure 6.1 showed that the sway motion in the IBOGM analysis for $H = 7\ cm$ deviated from the linear solution as well as from results with smaller wave heights in the frequency range $0.6 \leq \xi_B < 1.0$. This behaviour of the IBOGM results is confirmed by Greco's analysis. Also the amplitudes of the 1^{st} order heave and roll motions in the frequency range close to resonance are qualitatively in good agreement, even though minor differences are visible.

The analysis by Greco includes the mean sway drift force evaluated by CFM using the exact method described in Appendix C. The included CFM results from both the IBOGM analysis and Greco's analysis are with the vertical control surfaces located 0.5λ from the initial position of the body's center. For $\xi_B > 1.0$, the deviation of the mean wave drift force from theoretical results observed in the IBOGM analysis, also indicated by the experiments, is reproduced by Greco. The results obtained with CFM in Greco's analysis show the same qualitative behaviour as in the IBOGM analysis. In particular, the difference between DPI and CFM around $\xi_B = 0.5$ is observed also in Greco's results. The mean wave drift force obtained with DPI is generally in good agreement between the IBOGM and Greco's analysis, except for in the frequency range $0.5 \leq \xi_B \leq 0.7$ around the heave and roll natural frequencies. It is believed that the difference in the mean wave drift force between the two analyses in this frequency range is related to the minor differences observed in the 1^{st} order heave motion, since the mean wave drift force depends strongly on the relative motions between the body and the free surface. When the relative motions are large, differences in numerical techniques for dealing with the wave-body intersection points in the two analyses may also be a source of uncertainty (reference is made to Figure 6.11).

The difference between the IBOGM analysis and Greco's analysis close to heave and roll resonance is further examined by comparing time histories of wave loads and motions for $\xi_B = 0.5$ in Figure 6.9. While the loads and responses in heave and roll are in good agreement, differences are observed for sway. The crests in the sway force are in excellent agreement, while the behaviour and magnitude of the troughs differ. This explains why the mean wave drift force in the two analyses differ.

Figure 6.10, shows that the difference in sway behaviour at $\xi_B = 0.5$ is associated with a larger 3^{rd} order sway force in the IBOGM analysis than in Greco's analysis. This may be due to the local flow close to the wave-body intersection points, since the body has large heave and roll motions. Another possible explanation is that the HPC method, used as potential-flow solver in the IBOGM, is a higher-order method with better spatial accuracy than the BEM.

A detailed analysis of the wave elevation close to the ship section, and the dynamic pressure distribution over the instantaneous wetted body surface, for $\xi_B = 0.5$ is presented in Figure 6.11. Here, snapshots are shown for different time instants over two complete wave periods towards the end of the simulation. Considering the large rigid-body motions, the agreement between the two methods is deemed satisfactory. It appears that there is a small phase difference between

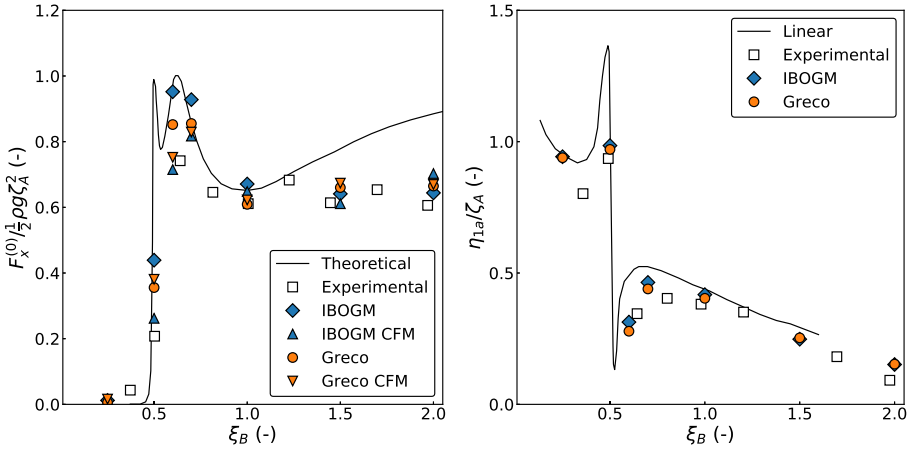

(a) Mean sway drift force

(b) 1^{st} order sway motion

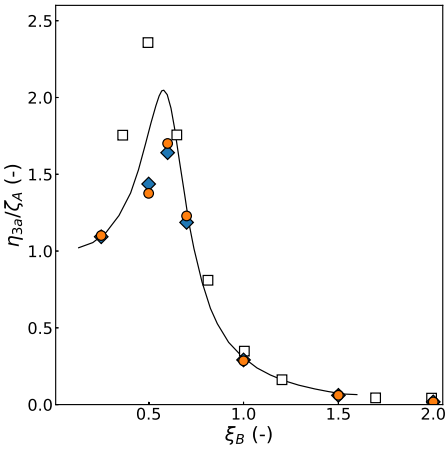

(c) 1^{st} order heave motion

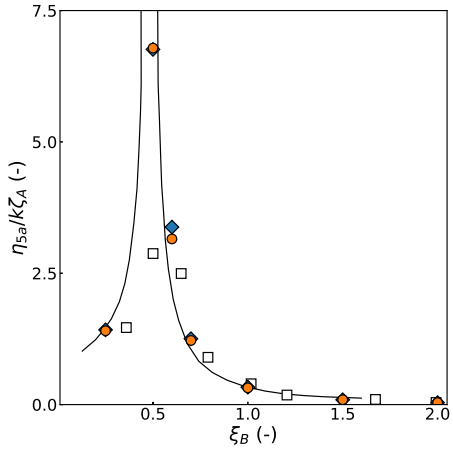

(d) 1^{st} order roll motion

Figure 6.8: Transfer functions for a freely floating 2D ship section in beam-sea waves. IBOGM analysis compared with the linear and theoretical results by Koo and Kim (2004), the experimental results by Nojiri and Murayama (1975) and the non-linear BEM results by Greco. All the non-linear and experimental results are for $H = 7\ cm$. The mean wave drift force $F_x^{(0)}$ in the IBOGM and Greco results is obtained from both DPI and CFM.

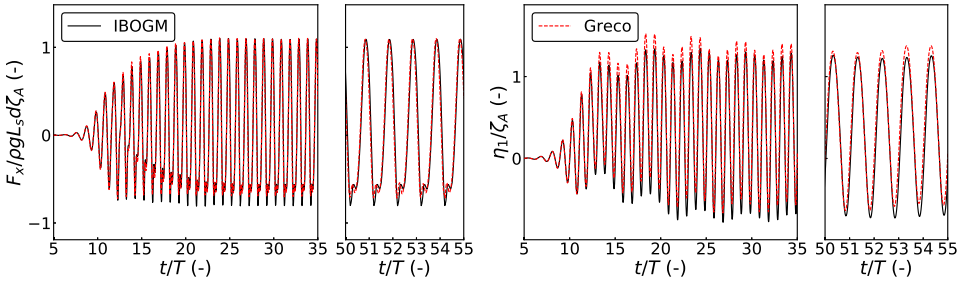

(a) Sway force

(b) Sway motion

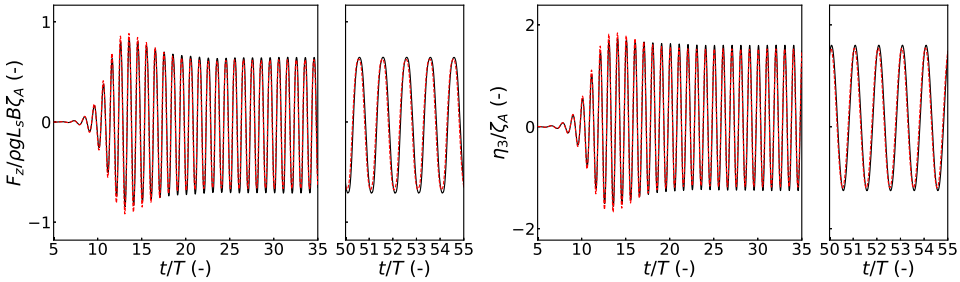

(c) Heave force

(d) Heave motion

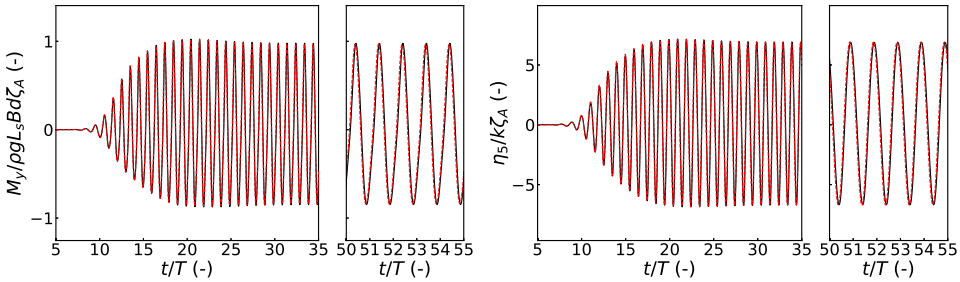

(e) Roll moment

(f) Roll motion

Figure 6.9: Comparison of wave load and motion response time series from IBOGM analysis and non-linear BEM analysis by Greco for a freely floating 2D ship section in beam-sea waves for $\xi_B = 0.50$, $H = 7\ cm$.

the two simulations, however, this is mostly related to the fact that the results are generally not reported at the exact same time instants. This can be seen in the small sub plots that indicate the time instant of the two simulations in the sway-force time series. These show that, when the time of the snapshots coincide, e.g. at $t/T \approx 52.9$, the phase difference is small. The pressure distribution over the wetted surface clearly has local differences, but is qualitatively consistent. Two likely explanations for the difference in pressure distribution is 1) that the refinement of the body boundary in the IBOGM method is dictated by the grid spacing in

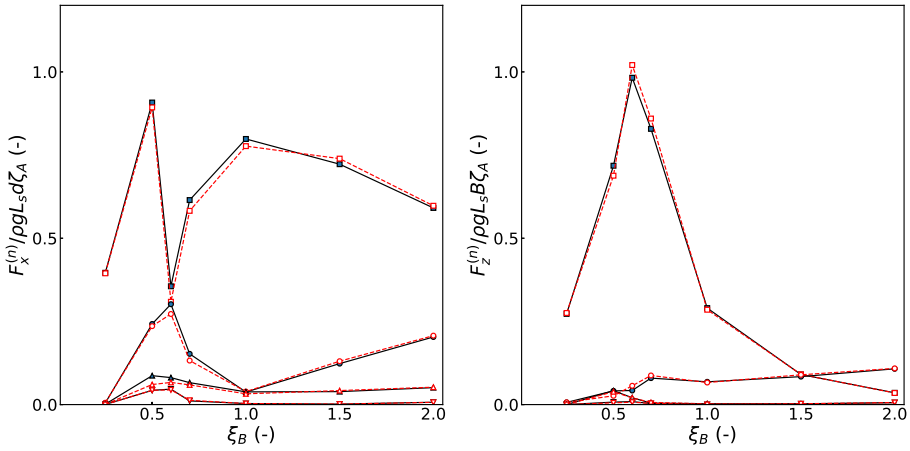

(a) Sway force

(b) Heave force

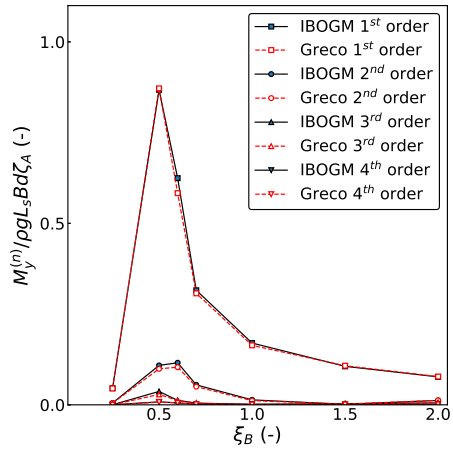

(c) Roll moment

Figure 6.10: Transfer function for $1^{st} - 4^{th}$ order wave loads for freely floating 2D ship section in beam-sea waves from IBOGM analysis compared with the non-linear BEM by Greco with $H = 7\ cm$.

the body-fixed grid, while points can be distributed arbitrarily in the BEM, and 2) that the IBOGM has higher spatial accuracy than the BEM. The local flow at the body boundary in the IBOGM can be refined in an efficient manner by e.g. modelling the body-fixed grid with an octree technique. This is suggested as a further improvement of the IBOGM, that would enhance its general applicability.

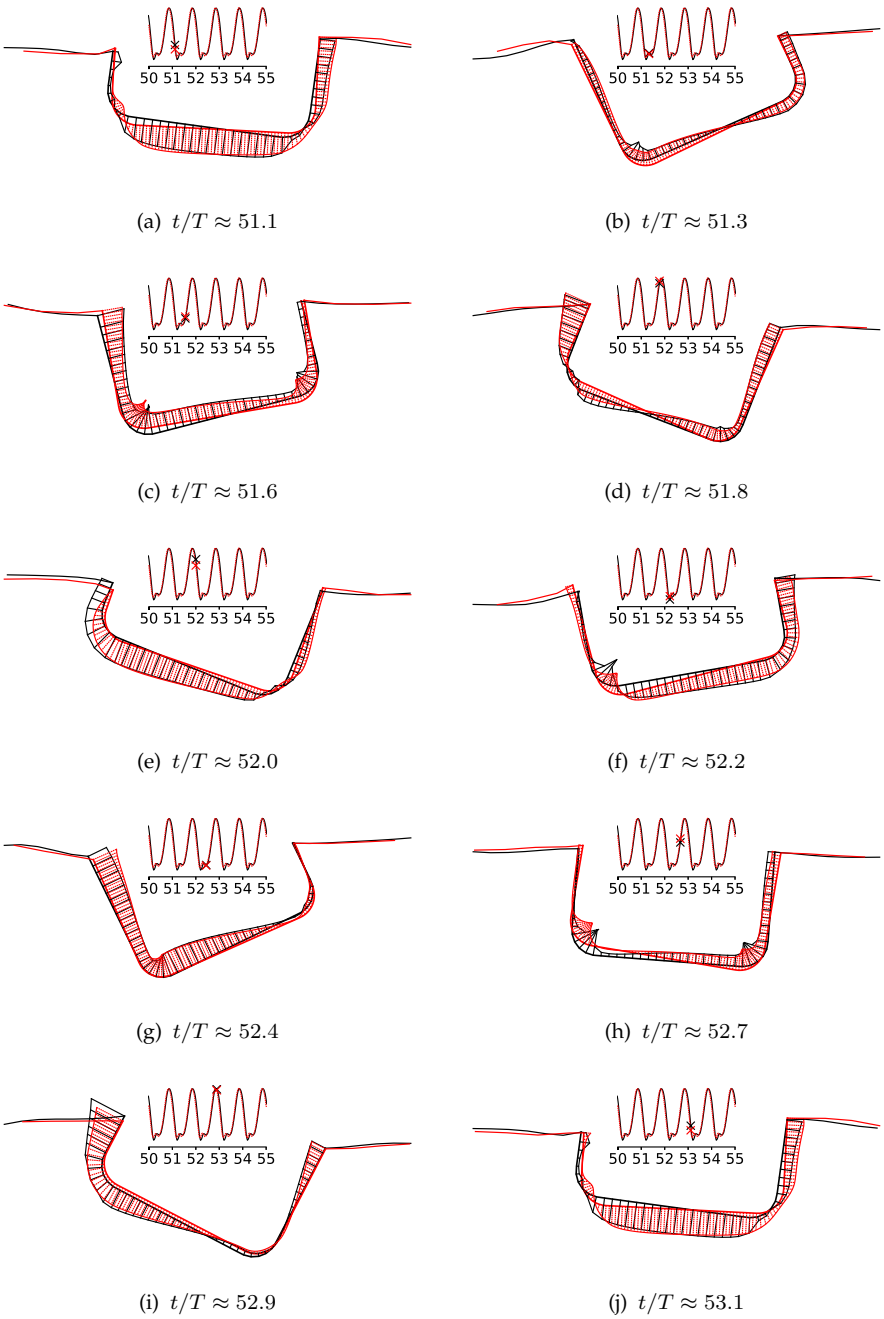

(a) $t/T \approx 51.1$ (b) $t/T \approx 51.3$

(c) $t/T \approx 51.6$ (d) $t/T \approx 51.8$

(e) $t/T \approx 52.0$ (f) $t/T \approx 52.2$

(g) $t/T \approx 52.4$ (h) $t/T \approx 52.7$

(i) $t/T \approx 52.9$ (j) $t/T \approx 53.1$

Figure 6.11: Dynamic pressure distribution and free-surface elevation at different time instances for $H = 7\ cm$, $\xi_B = 0.5$ for IBOGM analysis (black) and Greco's non-linear BEM analysis (red). The corresponding time instants in the sway force time series are indicated.

6.4 Comparison with other Non-Linear Numerical Results

We now compare the present IBOGM analysis with the non-linear analysis by Tanizawa et al. (1999) and Koo and Kim (2004) for $H = 7\ cm$. Both use a fully non-linear numerical wave tank based on BEM, and both solve an auxiliary BVP for the time derivative of φ. While Tanizawa et al. (1999) use a computational domain 6λ long with 1λ long numerical beaches on both sides, Koo and Kim (2004) use a domain similar to the one used in the IBOGM analysis illustrated in Figure 5.8. In both cases, it appears that the incident waves are generated by applying a velocity flux on a fixed position rather than having a physical wavemaker. The spatial and temporal discretization used by Koo and Kim (2004) is somewhat finer than that used by Tanizawa et al. (1999). Transfer functions for the mean sway wave drift force as well as 1^{st} order rigid-body motions are plotted in Figure 6.12, where also the linear and theoretical results by Koo and Kim (2004) and experimental results by Nojiri and Murayama (1975) are included for reference. Results near roll resonance were not given by Tanizawa et al. (1999), stating that these diverged due to large roll motions. The mean wave drift force in the latter reference is presented both from DPI and from CFM using Maruo's formula (6.6). Koo and Kim (2004) do not include results for the roll resonance frequency $\xi_B = 0.5$, for which no particular explanation is given. However, given that they predict larger roll response at $\xi_B = 0.6$ than in the IBOGM analysis, it can be speculated that this case resulted in numerical instability.

Away from the heave and roll resonance frequencies, all the numerical results give 1^{st} order motions in good agreement. Close to the natural frequencies, Koo and Kim (2004) predict lower sway and larger heave and roll motions than the IBOGM analysis. More significant differences are found when considering the mean wave drift force. Based on the few plotted points, the results from DPI by Tanizawa et al. (1999) show a diverging trend from both the theoretical and experimental results, and the correlation is generally unsatisfactory. Also the mean wave drift force by Koo and Kim (2004) compares poorly with the theoretical and experimental results. In particular, the mean wave drift force at $\xi_B = 0.6$ is 50% larger than the theoretical value. On the other hand, the results computed with Maruo's formula by Tanizawa et al. (1999) agree well with the theoretical values for all the plotted frequencies. As a consequence, they claim that the method of DPI is not reliable, and that the results computed from Maruo's formula are more trustworthy. The investigation of different methods to estimate the mean wave drift force in Section 6.2.2 do however contradict this conclusion. In particular, it was shown that using approximate methods such as Maruo's formula in connection with non-linear simulations is questionable, and that the mean wave drift force estimated from DPI agrees best with the mean sway offset of the body.

A substantial effort has been devoted to investigate the difference between the DPI results from Tanizawa et al. (1999) and from Koo and Kim (2004) and the present IBOGM analysis. The major finding from this is that the mean wave drift force, in particular near roll resonance, is sensitive to the body-boundary condition used when solving the auxiliary BVP for the time derivative of φ, and that this may be a contributing factor to the conclusions drawn by Tanizawa et al. (1999). This is elaborated in the next section.

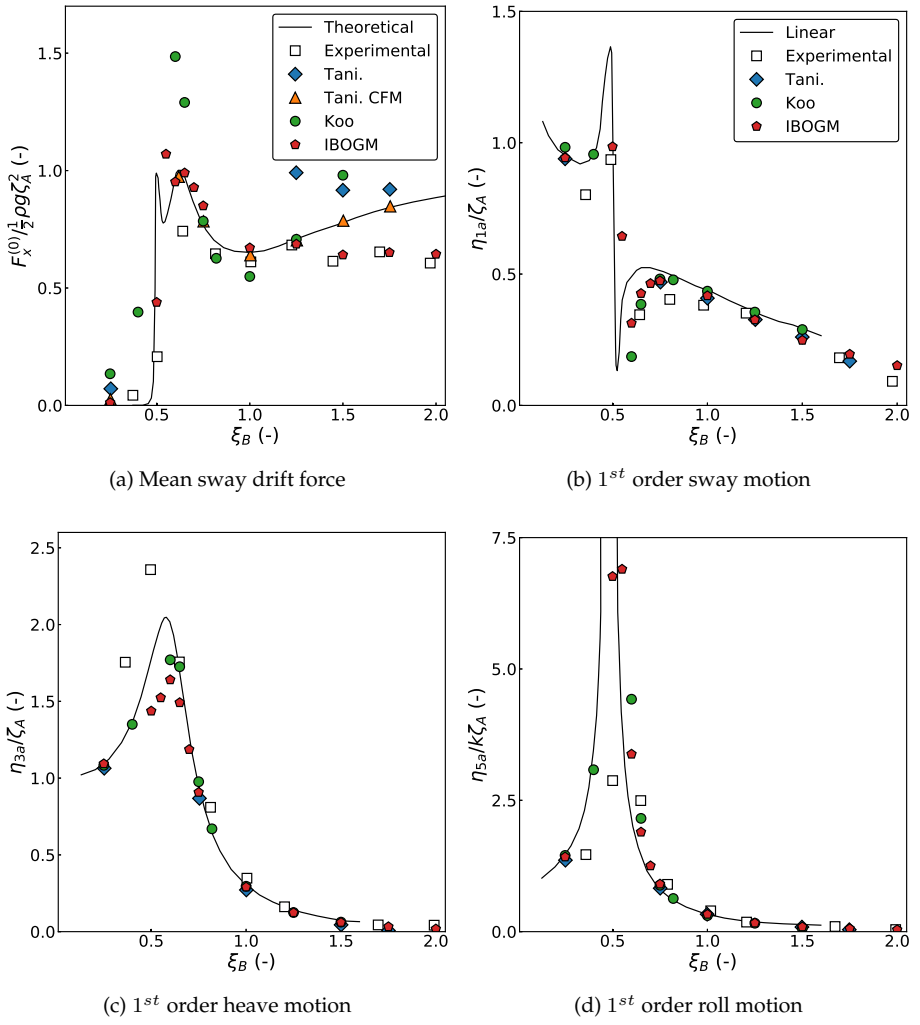

(a) Mean sway drift force

(b) 1^{st} order sway motion

(c) 1^{st} order heave motion

(d) 1^{st} order roll motion

Figure 6.12: Transfer functions for a freely floating 2D ship section in beam-sea waves. IBOGM analysis compared with the linear and theoretical results by Koo and Kim (2004), the experimental results by Nojiri and Murayama (1975), the non-linear BEM results by Tanizawa et al. (1999) and the non-linear BEM results by Koo and Kim (2004). All the non-linear and experimental results are for $H = 7\ cm$. In addition to DPI, the mean wave drift force $F_x^{(0)}$ obtained by CFM based on Maruo's formula is included from Tanizawa et al. (1999).

6.5 Sensitivity towards the Body-Boundary Condition for the Time Derivative of φ

A key aspect in computing the pressure on the body boundary is to reliably estimate the time derivative of the velocity potential φ that goes into the Bernoulli equation discussed in Section 2.3.2. When this estimate is obtained by solving an auxiliary BVP for the time derivative of φ, posing the correct body-boundary condition is of key importance. As it will be shown through a sensitivity analysis, the mean sway wave drift force close to roll resonance is sensitive to errors in this body-boundary condition. In the following discussion it is to be noted that Tanizawa has been one of the pioneers in defining the BVP for the time derivative of φ, and both Koo and Kim (2004) and other authors use the implementation in his papers. An apparent difference between this formulation and the one derived herein is highlighted, and its consequences are investigated.

6.5.1 Comparison of Formulations

In equation (2.10) in Section 2.2.2, it was stated that the acceleration of a fixed point P on the surface of a moving rigid body is given as

$$\frac{d^2\boldsymbol{R}}{dt^2} = \ddot{\boldsymbol{R}}_0 + \boldsymbol{\omega} \times \dot{\boldsymbol{R}}_0 + \dot{\boldsymbol{\omega}} \times \boldsymbol{r} + \boldsymbol{\omega} \times (\boldsymbol{\omega} \times \boldsymbol{r}),$$

where all the time derivatives on the right-hand side are relative to the body-fixed reference frame. $\dot{\boldsymbol{R}}_0$ and $\ddot{\boldsymbol{R}}_0$ are the velocity and acceleration, respectively, of the body's center of rotation that is here taken as the body's center of gravity, $\boldsymbol{r}$ is a vector from the body's center of rotation to P and $\boldsymbol{\omega}$ is the angular velocity vector. We note that all the $\boldsymbol{\omega}\times$ terms in the above equation are due to the time rate of change of unit vectors in the body-fixed coordinate system seen by an inertial observer. In the present work, where the BVP for the time derivative of φ is formulated in the body-fixed reference frame, these terms were hence omitted in the body-boundary condition given by equation (2.35) in Section 2.3.4 as

$$\nabla \frac{D_{BO}\varphi}{Dt} \cdot \boldsymbol{n} = (\ddot{\boldsymbol{R}}_0 + \dot{\boldsymbol{\omega}} \times \boldsymbol{r}) \cdot \boldsymbol{n},$$

where D_{BO}/Dt is the time derivative following a point P moving with the body and $\boldsymbol{n}$ is the normal vector in P. It is implicit that all the vectors in the above equation are given in the body-fixed reference frame.

Tanizawa et al. (1999) state a body-boundary condition for the Eulerian time derivative $\partial\varphi/\partial t$ that is derived in Tanizawa (1995). We here repeat the main steps of this derivation, starting by defining a variable

$$\Phi = \frac{\partial\varphi}{\partial t} + \frac{1}{2}(\nabla\varphi)^2. \tag{6.7}$$

Φ is called the acceleration potential, in that the acceleration of a fluid particle is given by its gradient $\nabla\Phi$. In deriving the relevant boundary condition, we considered a fixed point on the body surface. We now initially consider a point that is not

fixed, but that instead slides along the body. Hence, the Neumann body-boundary condition for Φ can be written as

$$\nabla\Phi \cdot \boldsymbol{n} = (\ddot{\boldsymbol{R}}_0 + \ddot{\boldsymbol{r}} + \dot{\boldsymbol{\omega}} \times \boldsymbol{r} + \boldsymbol{\omega} \times \dot{\boldsymbol{R}}_0 + 2\boldsymbol{\omega} \times \dot{\boldsymbol{r}} + \boldsymbol{\omega} \times (\boldsymbol{\omega} \times \boldsymbol{r})) \cdot \boldsymbol{n}. \tag{6.8}$$

By using the definition of the material derivative following a fluid particle, $D/Dt = \partial/\partial t + \nabla\varphi \cdot \nabla$, it can be shown that

$$\nabla\Phi = \nabla(\frac{\partial\varphi}{\partial t} + \frac{1}{2}(\nabla\varphi)^2) = \nabla\frac{\partial\varphi}{\partial t} + \nabla\varphi \cdot \nabla(\nabla\varphi) = \frac{D(\nabla\varphi)}{Dt}. \tag{6.9}$$

The gradient of Φ is hence equivalent to the material derivative of the fluid velocity $\nabla\varphi$. The body-boundary condition for the Lagrangian time derivative of φ for a fluid particle sliding on the body surface in the inertial reference frame is hence

$$\frac{D(\nabla\varphi)}{Dt} \cdot \boldsymbol{n} = (\ddot{\boldsymbol{R}}_0 + \boldsymbol{\omega} \times \dot{\boldsymbol{R}}_0 + \ddot{\boldsymbol{r}} + \dot{\boldsymbol{\omega}} \times \boldsymbol{r} + 2\boldsymbol{\omega} \times \dot{\boldsymbol{r}} + \boldsymbol{\omega} \times (\boldsymbol{\omega} \times \boldsymbol{r})) \cdot \boldsymbol{n}. \tag{6.10}$$

If we now assume that the point is fixed on the body surface rather than sliding along it, (6.10) becomes

$$\frac{D(\nabla\varphi)}{Dt} \cdot \boldsymbol{n} = (\ddot{\boldsymbol{R}}_0 + \boldsymbol{\omega} \times \dot{\boldsymbol{R}}_0 + \dot{\boldsymbol{\omega}} \times \boldsymbol{r} + \boldsymbol{\omega} \times (\boldsymbol{\omega} \times \boldsymbol{r})) \cdot \boldsymbol{n}. \tag{6.11}$$

The body-boundary condition for $\nabla\Phi$ given in Equation (11) of Tanizawa (1995) reads

$$\boldsymbol{n} \cdot \boldsymbol{a} = \boldsymbol{n} \cdot (\boldsymbol{a}_0 + \dot{\boldsymbol{\omega}} \times \boldsymbol{r}) + \boldsymbol{n} \cdot \boldsymbol{\omega} \times (\boldsymbol{\omega} \times \boldsymbol{r}) + \boldsymbol{n} \cdot [\boldsymbol{a}] + \boldsymbol{n} \cdot 2\boldsymbol{\omega} \times [\boldsymbol{v}], \tag{6.12}$$

where $\boldsymbol{a} = \nabla\Phi$, $[\boldsymbol{v}] = \dot{\boldsymbol{r}}$ and $[\boldsymbol{a}] = \ddot{\boldsymbol{r}}$. Tanizawa (1995) states that $\boldsymbol{a}_0 + \dot{\boldsymbol{\omega}} \times \boldsymbol{r}$ is the acceleration due to the translational and angular acceleration of the body. There are two ways to interpret this: If $\boldsymbol{a}_0 = \ddot{\boldsymbol{R}}_0 + \boldsymbol{\omega} \times \dot{\boldsymbol{R}}_0$, $\boldsymbol{a}_0$ is the acceleration of the body's center of rotation as observed from the inertial reference frame. If, on the other hand, $\boldsymbol{a}_0 = \ddot{\boldsymbol{R}}_0$, it is the acceleration of the body's center of rotation observed from the body-fixed reference frame. In the former interpretation, the expression in (6.12) is consistent with (6.10). Thus, in order for (6.12) to be formally correct, one must take $\boldsymbol{a}_0$ as $\ddot{\boldsymbol{R}}_0 + \boldsymbol{\omega} \times \dot{\boldsymbol{R}}_0$. Tanizawa et al. (1999) use (6.12) as body-boundary condition in their numerical implementation. Furthermore, the body-boundary condition for Φ stated in Equation (28) in Koo and Kim (2004) is the same as that used by Tanizawa (1995).

As highlighted in the above discussion, it is crucial that $\boldsymbol{a}_0$ is interpreted in the correct way in order for the body-boundary condition to be consistent. In the following, it will be shown that correctly accounting for the non-linear term $\boldsymbol{\omega} \times \dot{\boldsymbol{R}}_0$ has a significant effect on the mean sway wave drift force when heave and roll motions are large.

6.5.2 Sensitivity Study

The influence of the $\boldsymbol{\omega} \times \dot{\boldsymbol{R}}_0$ term in the body-boundary condition for the time derivative of φ is studied by modifying the original body-boundary condition in

the body-fixed reference frame defined above into

$$\nabla \frac{D_{BO}\varphi}{Dt} \cdot \boldsymbol{n} = (\ddot{\boldsymbol{R}}_0 - \boldsymbol{\omega} \times \dot{\boldsymbol{R}}_0 + \dot{\boldsymbol{\omega}} \times \boldsymbol{r}) \cdot \boldsymbol{n}. \tag{6.13}$$

In the inertial reference-frame interpretation, this corresponds to disregarding the $\boldsymbol{\omega} \times \dot{\boldsymbol{R}}_0$ term. The analysis is repeated for $H = 7\ cm$, modifying the body-boundary condition for the time derivative of φ into (6.13), with otherwise unchanged conditions. With this, the simulation with non-dimensional wave frequency $\xi_B = 0.55$ became unstable and is hence not included in the discussion to follow.

Motion time histories for non-dimensional wave frequencies $\xi_B = (0.5, 1.0, 1.5)$ and incident wave height $H = 7\ cm$ are here considered. The results from the present analysis are compared with time series shown by Tanizawa et al. (1999). Despite stating that the simulation for $\xi_B = 0.5$ diverged due to large angular motions, they nevertheless present time series for this case in their paper. The time series for this case as well as for the two other frequencies are thus included in the comparison, although the accuracy of the reproduced curves is limited[1]. With this in mind, the comparison is only interpreted in a qualitative sense.

For the wave frequency close to heave and roll resonance, $\xi_B = 0.5$, Figure 6.13 shows that the modified boundary condition leads to a significant increase in the mean sway offset in the IBOGM simulations. The effect on wave frequency motions is much smaller, with limited changes to the heave and roll response. The transient sway response in the simulations by Tanizawa et al. (1999) is much larger than in the present simulation. This can be partially explained by difference in the ramp function used for the incident waves, as well as in the strategy to generate them. However, the sway transient phase from Tanizawa et al. (1999) is somehow closer to the IBOGM solution with modified body-boundary condition. Moreover, they are associated with similar mean offsets in steady-state condition, in both cases larger than predicted with the original body-boundary condition.

Figures 6.14 and 6.15 show that the influence of the modified body-boundary condition is much smaller for $\xi_B = 1.0$, and practically invisible for $\xi_B = 1.5$. This is because the heave and roll motions for $\xi_B = 1.0$ and $\xi_B = 1.5$ are much smaller than for $\xi_B = 0.5$, so that the non-linear term $\boldsymbol{\omega} \times \dot{\boldsymbol{R}}_0$ becomes orders of magnitude smaller for these frequencies. The general trend of the sway motion in the IBOGM simulations compares qualitatively well with Tanizawa et al. (1999) for $\xi_B = 1.0$ and $\xi_B = 1.5$, although the mean sway offset is lower. In the steady-state part of the time series, the relative difference in mean sway offset between the two sets of simulations, $(\overline{\eta}_{1,Tani} - \overline{\eta}_{1,IBOGM})/\overline{\eta}_{1,Tani}$, is estimated as approximately 0.03 for $\xi_B = 0.5$, 0.21 for $\xi_B = 1.0$ and 0.25 for $\xi_B = 1.5$. Although the reason for this difference is not fully understood, it is qualitatively consistent with Figure 6.12 where the mean wave drift forces estimated from the IBOGM analysis are approximately 30% lower than those reported by Tanizawa et al. (1999) using DPI in the frequency range $1.25 \leq \xi_B \leq 1.75$.

[1] Time series are captured from plots in Tanizawa et al. (1999) with low resolution.

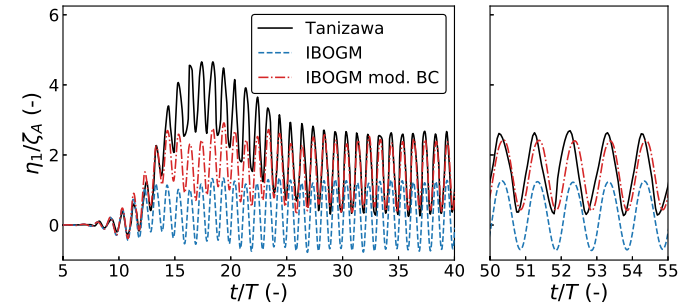

(a) Sway

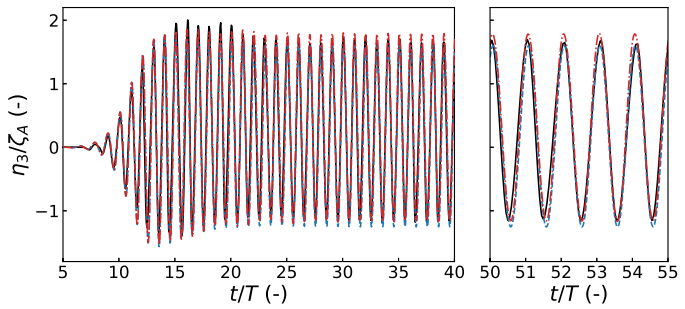

(b) Heave

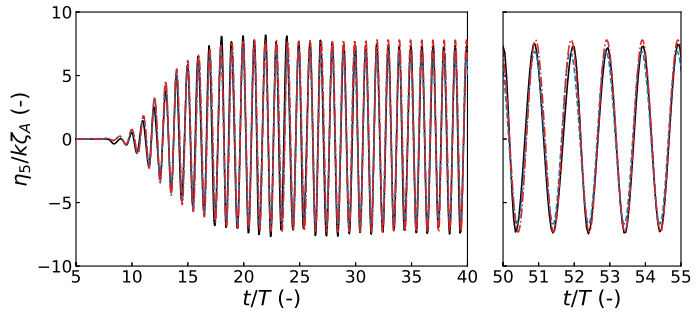

(c) Roll

Figure 6.13: Comparison of motion series for $\xi_B = 0.5$, $H = 7\ cm$. The results denoted *Tanizawa* are from Tanizawa et al. (1999), and the *IBOGM mod. BC* results are obtained with (6.13) as body-boundary condition in the IBOGM analysis. Note that the roll motion from Tanizawa et al. (1999) is plotted with the opposite sign as in their paper.

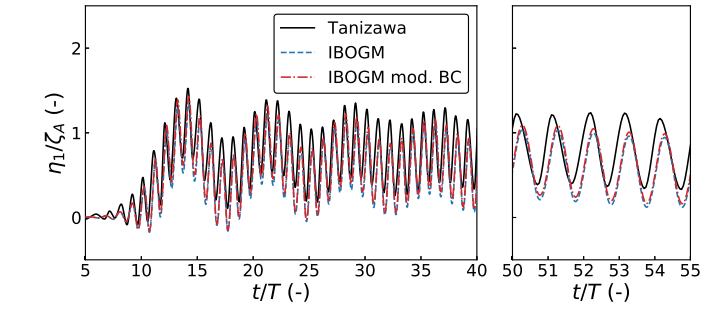

(a) Sway

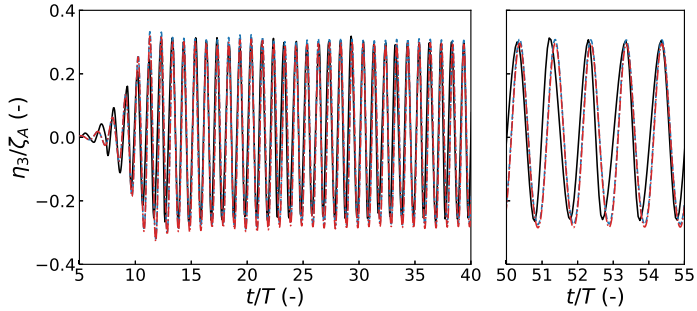

(b) Heave

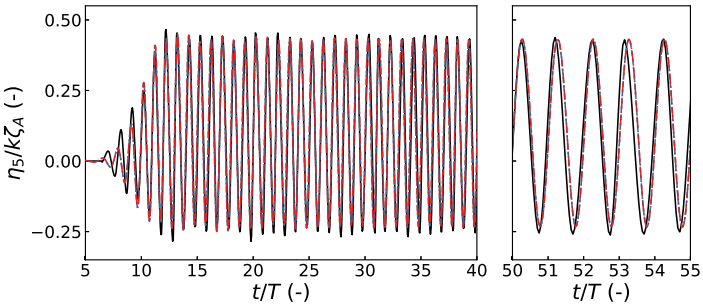

(c) Roll

Figure 6.14: Same as Figure 6.13 with $\xi_B = 1.0$, $H = 7\ cm$.

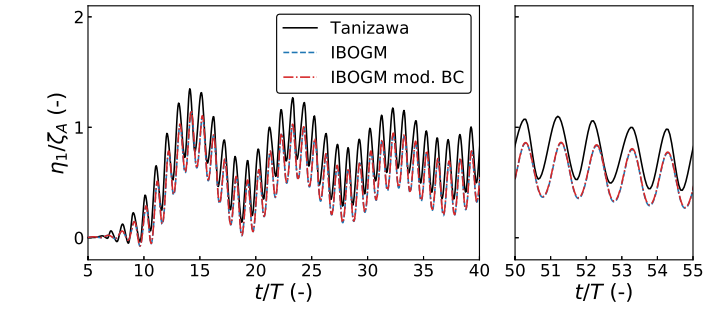

(a) Sway

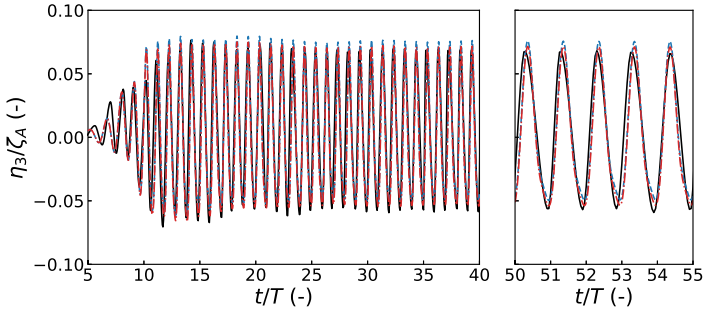

(b) Heave

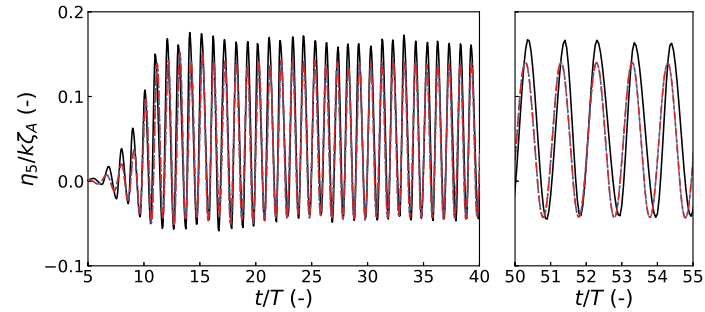

(c) Roll

Figure 6.15: Same as Figure 6.13 with $\xi_B = 1.5$, $H = 7\ cm$.

Transfer functions for the mean sway wave drift force as well as 1^{st} order rigid-body motions for $H = 7\ cm$ are shown in Figure 6.16, where the mean wave drift force is estimated from DPI in all the non-linear numerical results. No visible difference is seen in the IBOGM results with the two body-boundary conditions for $\xi_B > 1.0$, where heave and roll motions are moderate. In general, the modified body-boundary condition shows limited influence on wave-frequency motions, with only a small increase in sway, heave and roll motions around $\xi_B = 0.5$. It is therefore not evident from only considering the wave-frequency motions that the the body-boundary condition in (6.13) is erroneous. Dramatic differences are however seen in the mean wave drift force for $\xi_B < 1.0$. Close to the heave resonance frequency, at $\xi_B = 0.6$, where also the roll motion is large, the mean wave drift force is close to three times higher than the theoretical value when the modified body-boundary condition is used. The results by Koo and Kim (2004) show the same trend in a qualitative sense, but in their case the mean wave drift force never becomes higher than approximately 1.5 times the theoretical value. Tanizawa et al. (1999) do not provide results from direct pressure integration in this frequency range, noting that they believe their results from DPI to be unreliable. However, since the mean steady-state sway offset in Figure 6.13 is comparable to the IBOGM analysis with modified body-boundary condition, it is plausible that the mean wave drift force also is comparable for $\xi_B = 0.5$.

Figure 6.16, and the fact that Koo and Kim (2004) use the formulation of Tanizawa (1995) to solve for the acceleration potential, would suggest that they may have interpreted $\boldsymbol{a}_0$ in (6.12) as the acceleration in the body-fixed reference frame instead of in the inertial reference frame, as it should be. In that case, the claim made by Tanizawa et al. (1999) that the mean wave drift force estimated from DPI is inaccurate, would be questionable. However, one must keep in mind that there are several factors that may influence the mean wave drift force estimated from a time domain analysis, related to e.g. spatial and temporal discretization. The mean wave drift force is small compared to the 1^{st} order wave force, and is sensitive to the time window used to average the force. Furthermore, if for some reason there are spikes in the wave force time history with duration in the order of one time step, these may influence the estimate of $F_x^{(0)}$ without notably affecting the sway motion. Differences may also be present in other boundary conditions used in the BVP for the time derivative of φ, such as the free-surface boundary condition, that have not been investigated here. Another possible reason for the disagreement could be in the different fluid-body motions coupling strategy adopted, i.e. intrinsic in the case of Koo and Kim (2004) and iterative in the IBOGM analysis. Nevertheless, the present study shows that the mean wave drift force is sensitive to the body-boundary condition used in the BVP, whereas 1^{st} order motions are relatively insensitive.

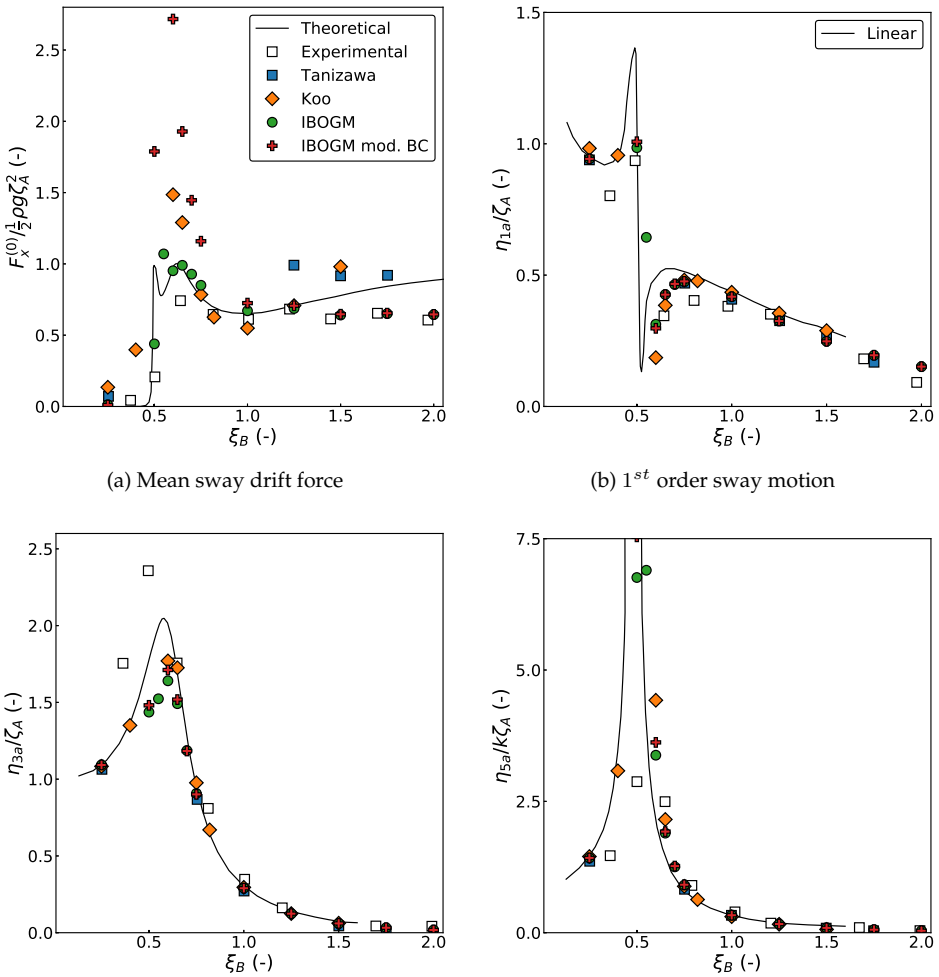

(a) Mean sway drift force

(b) 1^{st} order sway motion

(c) 1^{st} order heave motion

(d) 1^{st} order roll motion

Figure 6.16: Transfer functions for a freely floating 2D ship section in beam-sea waves. Original IBOGM analysis and IBOGM analysis with (6.13) as body-boundary condition compared with the linear and theoretical results by Koo and Kim (2004), the experimental results by Nojiri and Murayama (1975), the non-linear BEM results by Tanizawa et al. (1999) and the non-linear BEM results by Koo and Kim (2004). All the non-linear and experimental results are for $H = 7\ cm$, and the mean wave drift force $F_x^{(0)}$ is obtained from DPI in all non-linear analyses.

6.6 Summary

A freely floating 2D ship section in beam-sea regular waves has been considered in a range of wave frequencies and in different wave heights. Numerical analyses were performed with the fully non-linear immersed boundary-overlapping grid method (IBOGM) developed in the present work, with particular focus on non-linear effects due to large wave steepness and large rigid-body motions. It was found that both when rigid-body motions are large, close to heave and roll resonance, and when the waves are steep, the mean sway wave drift force deviates from the 2^{nd} order theoretical value.

Compared with experiments, the roll damping was found to be underestimated in the numerical analysis, probably due to viscous effects in the experiments. The roll response in the numerical analysis was brought closer to the experimental results by adding quadratic roll damping, with best agreement when the added damping corresponded to an equivalent linearized damping level approximately equal to 5% of the critical damping near resonance. The additional roll damping was found to also influence sway and heave motions through coupling effects, as well as the mean sway wave drift force. An interesting observation is that adding roll damping to reduce motions did not necessarily mean that the system behaved more linearly. In particular, it was found that the 1^{st} order wave force in sway relatively speaking was reduced more than the 2^{nd} order force when the quadratic roll damping increased.

The method of direct pressure integration (DPI) to estimate the mean wave drift force was compared to using conservation of fluid momentum (CFM). Three different CFM methods were considered, including an exact method, where no additional approximations are made, and two 2^{nd} order approximate methods including the widely used Maruo's formula. The mean wave drift force was also estimated from the mean sway position of the body. In general, it was found that the latter method gave consistent results with DPI. The exact CFM method was found to give results that were consistent with DPI, but with differences observed close to heave and roll resonance. Although the reason for this is not fully understood, it is likely related to large body motions. It is clear that the 2^{nd} order approximate methods may neglect important non-linear contributions, and should be used with care in connection with non-linear simulations.

The IBOGM was verified against dedicated analyses carried out with the non-linear boundary element method (BEM) solver developed by Greco (2001). Satisfactory agreement was observed, even for the most challenging scenarios involving significant heave and roll motions of the body.

Compared against other available non-linear numerical results by Tanizawa et al. (1999) and Koo and Kim (2004), mean wave drift forces of significantly different magnitudes were observed close to heave and roll resonance. Tanizawa et al. (1999) claimed that the method of DPI to estimate the mean wave drift force was inaccurate, although the mean wave drift force estimated for DPI was in good agreement with reference results when the body was restrained from moving in their work. An in-depth investigation revealed that a non-linear term in the body-boundary condition for the auxiliary boundary value problem (BVP) used to estimate the time derivative of the velocity potential significantly influences the

mean wave drift force when rigid-body motions are large, but has only a moderate influence on 1^{st} order rigid-body motions. A sensitivity analysis showed that, by neglecting such non-linear term, the mean wave drift force may be significantly over-estimated close to heave and roll resonance. Tanizawa et al. (1999) and Koo and Kim (2004) use the same body-boundary condition in this BVP, and by neglecting the non-linear term in the IBOGM analysis, a similar steady-state mean sway offset as in Tanizawa et al. (1999) was obtained at roll resonance. Furthermore, the transfer function of the mean wave drift force from the IBOGM analysis with the modified body-boundary condition showed qualitatively similar behaviour as in Koo and Kim (2004), although with different magnitudes. Since the IBOGM analysis with the correctly posed body-boundary condition compared well with Greco's independent analysis, it is possible that Tanizawa et al. (1999) and Koo and Kim (2004) have neglected the non-linear term in their body-boundary conditions. Either way, the analysis showed that when an auxiliary BVP is solved to estimate the time derivative of the velocity potential, the mean wave drift force is sensitive towards the imposed body-boundary condition. Since the linear quantities are much less sensitive, it may be misleading to only consider these when determining the adequacy of a numerical solution. This should be kept in mind during validation and verification of a non-linear numerical implementation.

The roll response near resonance represents an example where viscous effects may matter. In order to properly account for these, a viscous-flow solver is required. In the next chapter, a strategy to couple the present IBOGM solver with an existing viscous-flow solver is proposed. By doing this, viscous effects can be accounted for where they matter, while benefiting from the strengths of the present potential-flow solver elsewhere.

Chapter 7

Coupling with a Viscous-Flow Solver through Domain-Decomposition

Potential-flow methods are generally able to propagate waves in an accurate and efficient manner. However, there are scenarios where they are insufficient. Two examples of this examined in the present thesis are the focused and eventually breaking wave in Chapter 4, and the roll motion for a freely floating body near resonance in Chapter 6. In the former case, we were able to suppress the wave breaking numerically in order to make the simulation more robust. The details of the process where the overturning wave impacts the underlying free surface, leading to circulation and vortical structures (Battjes, 1988), is on the other hand outside the validity of potential flow. For the freely floating body, the simulated roll response near resonance was approximately twice as large as in experiments, which indicated that there were viscous effects leading to roll damping in the latter.

In order to deal properly with wave breaking and fragmented flows, and with important viscous effects, a Navier-Stokes solver is required. Navier-Stokes solvers are however more computationally expensive than potential-flow solvers, and may be less accurate in propagating free-surface waves due to numerical dissipation. To benefit from the strengths of both classes of solvers, an increasing interest in coupling potential-flow and Navier-Stokes solvers is seen lately. In this framework, a Navier-Stokes solver can be applied where viscous effects matter, while a potential-flow solver can be used in the remaining part of the considered fluid domain. An example of this is given by Colicchio et al. (2006), where a 2D strong domain-decomposition (DD) strategy between a level-set Navier-Stokes (LS-NS) solver and a non-linear potential-flow solver based on the boundary element method (BEM) was devised to analyze a dam-breaking problem and subsequent wave impact on a vertical wall. Here, we propose a DD scheme to couple the same LS-NS solver as used by Colicchio et al. (2006), but with single-phase (water) formulation as proposed by Colicchio et al. (2011), with the immersed boundary-overlapping grid method (IBOGM) developed in the present work. A version of the LS-NS code modified for the present application has been provided by Colicchio, where the exchange of information and control of the time-integration pro-

cess is managed through external ASCII files.

A version of the DD scheme proposed in the following was initially presented in Hanssen et al. (2019).

7.1 Level-Set Navier-Stokes Solver

A complete overview of the theory behind the applied LS-NS solver can be found in Colicchio et al. (2006) and Colicchio et al. (2011). A short summary of key aspects is given in the following. It is here emphasized that for the present work, a modified version of the LS-NS solver has been provided by Colicchio where the communication of fluid variables is managed by reading from and writing to ASCII files in a dedicated information interface. The LS-NS solver is therefore coupled with the potential-flow solver as a standalone program, and has not been implemented numerically by the present author.

The governing equations for the fluid problem are the continuity equation,

$$\nabla \cdot \boldsymbol{V} = 0, \tag{7.1}$$

and the Navier-Stokes equations,

$$\frac{\partial \boldsymbol{V}}{\partial t} + (\boldsymbol{V} \cdot \nabla)\boldsymbol{V} = -\frac{\nabla p}{\rho} + \frac{2\nabla \cdot (\mu \boldsymbol{D})}{\rho} + \boldsymbol{g}. \tag{7.2}$$

The equations are here formulated in Eulerian form in the Earth-fixed, inertial coordinate system, where $\boldsymbol{V}$ is the water particle velocity, p is the pressure, ρ is the density, μ is the dynamic viscosity, $\boldsymbol{D}$ is the rate-of-strain tensor and $\boldsymbol{g}$ is the acceleration of gravity vector. (7.1) and (7.2) are solved on a staggered, stationary Cartesian grid by a 2^{nd} order finite difference method (FDM) in space, and with a 2^{nd} order projection method in time. In the staggered spatial scheme, the horizontal and vertical velocity components are defined, respectively, on the center of the vertical and horizontal cell sides, while the pressure is defined in the cells' center. In the temporal scheme, a predictor step is first performed to estimate $\boldsymbol{V}^{*n+1}$ and $p^{*n+1/2}$. These are the initial "guesses" for the fluid pressure and velocity at time $t = t_n + \Delta t$ and $t_n + 0.5\Delta t$, respectively, where Δt is the time step and $t_n = n\Delta t$. This is followed by a corrector step, where the divergence-free velocity $\boldsymbol{V}^{n+1}$ and pressure $p^{n+1/2}$ are obtained.

The air-water interface, which corresponds to the free surface in the single-phase (water) formulation, is defined by the level-set function ϕ which represents the signed distance from the free surface so that $\phi < 0$ in the water, $\phi > 0$ outside the water and $\phi = 0$ on the exact position of the interface. The free surface evolution is captured in time through solving the following equation:

$$\frac{\partial \rho}{\partial \phi}\left(\frac{\partial \phi}{\partial t} + \boldsymbol{V} \cdot \nabla \phi\right) = 0. \tag{7.3}$$

As mentioned above, the LS-NS solver used in the present work represents a single-phase incompressible method, where only the water-phase is modelled. The pressure in the air is set to zero with a smooth transition from the pressure in the water, and with the water velocity extended in air.

7.2 Domain-Decomposition Scheme

The general idea of the proposed DD between the potential-flow IBOGM and LS-NS solvers is illustrated for the two problems described in the introduction of the chapter in Figure 7.1. In (a), we know the position where a breaking wave will develop, either from experiments or from potential-flow analysis, and locate a LS-NS domain around this region. The waves on either sides of the breaking-wave region are propagated by the IBOGM solver. This is of interest if we for instance would like to estimate the fluid kinematics in the overturning wave. In (b), a LS-NS domain is located around the position of a rolling ship section, covering the region where significant fluid vorticity due to flow separation from the ship's bilges is generated. On either sides of the ship section, the waves are propagated by the IBOGM solver. In this way, the particular flow phenomena can be studied in an efficient manner. There are several other examples where such DD strategy is beneficial, including lowering and lifting of subsea modules through the splash zone, and viscous contributions to wave drift loads on a semi-submersible. The latter problem was highlighted in the introduction given in Section 1.1.

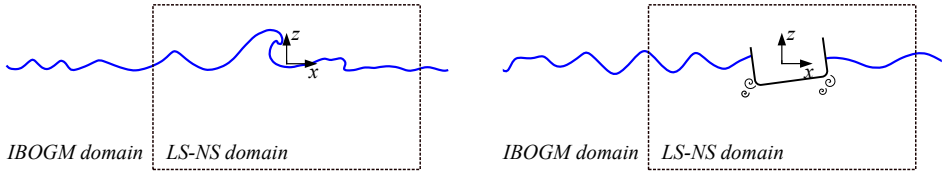

(a) Breaking wave (b) Flow separation from ship bilges

Figure 7.1: Two relevant scenarios for coupling of a IBOGM and LS-NS solvers. The global Oxz coordinate system is located in the middle of the LS-NS domain with origin in the still waterline.

Following Colicchio et al. (2006), the proposed DD involves an overlapping between the two solvers to allow a more relaxed, robust and accurate coupling of the solutions. The details of the spatial and temporal coupling in the proposed DD scheme are given next.

7.2.1 Spatial Coupling Scheme

We here describe the spatial coupling scheme, i.e. how information is exchanged between the two solvers at a given time instant. A principal outline of the two domains is shown in Figure 7.2, where the LS-NS domain is indicated in grey and with the global Oxz coordinate system shared by both solvers located in the middle of the LS-NS domain with origin in the still waterline. The domains are overlapped, so that information is exchanged between the two solvers at locations that are separated in space. In the case examined in the figure, the overlapping region has a thickness equal to eight nodes of the LS-NS domain. The IBOGM solver can have a coarser mesh than the LS-NS domain, provided that this is suitable for an accurate solution of the problem.

Two classes of intersection boundaries are defined in Figure 7.2: At the LS-NS→IBOGM boundary, the pressure and velocity, as well as the free-surface intersection with the vertical sides of the boundary, are written from the LS-NS solver to the IBOGM solver. The LS-NS→IBOGM boundary points, indicated with red pentagons with black borders, are predefined, so that variables are also written above the free surface. The values above the free surface are however never used by the IBOGM solver. At the IBOGM→LS-NS boundary, the data are written from the IBOGM solver to the LS-NS solver. More specifically, the water-velocity components and pressure are provided consistently with the LS-NS staggered grid, i.e. the horizontal water velocity $\partial\varphi/\partial x$ is written in the points indicated with green dots, the vertical water velocity $\partial\varphi/\partial z$ is written in the points indicated with blue x's and the water pressure is written in the points indicated with red +'s. In addition, the free-surface elevation is written to the LS-NS solver in the points indicated with blue circles with black borders. In the points above the instantaneous IBOGM free-surface position, the pressure and fluid velocities are set to zero. The LS-NS solver needs information on more grid layers than the IBOGM solver to properly estimate the gradients involved in convective terms.

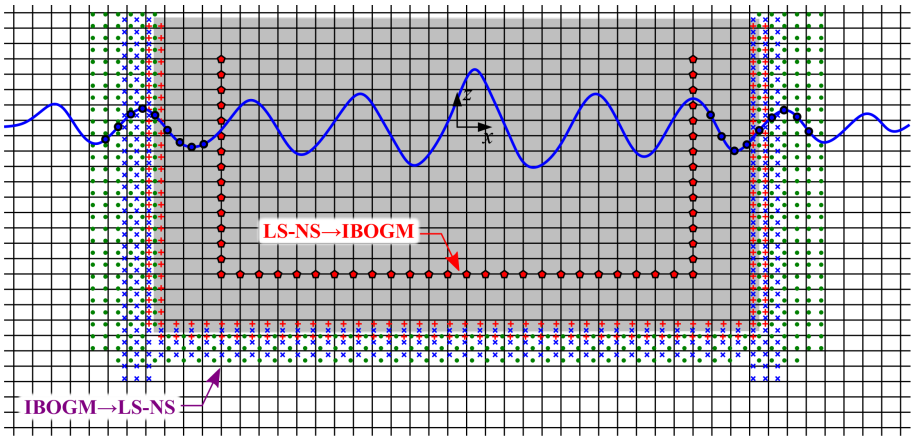

Figure 7.2: Principal outline of spatial coupling scheme. The black lines indicate the IBOGM grid, while the grey area indicates the LS-NS domain.

Boundary Conditions from LS-NS to IBOGM Solver

As indicated in Figure 7.2, the IBOGM grid is fitted to the LS-NS→IBOGM boundary. The details of a highlighted part of the IBOGM grid around the LS-NS→IBOGM boundary are shown in Figure 7.3. As in Section 3.2, the IBOGM domain is constituted by an active (yellow) and an inactive (grey) part. The subset of cells where the free surface is considered as an immersed boundary are blue-shaded with ghost nodes above the free surface in their upper parts. The grid region enclosed by the LS-NS→IBOGM boundary is always inactive for the IBOGM solver. In the nodes indicated with red squares with black borders, boundary conditions from the LS-NS solver are imposed. In the BVP for the velocity po-

tential, we impose Neumann conditions in the grid nodes that coincide with the LS-NS→IBOGM boundary and are below the free surface. Considering a particular node with coordinates (x, z) and with normal vector $\boldsymbol{n}(x, z)$ pointing into the active IBOGM domain, the Neumann condition for the velocity potential is stated as

$$\sum_{i=1}^{8}\left[\sum_{j=1}^{8} c_{j,i}\nabla f_j\left(\overline{x},\overline{z}\right)\cdot\boldsymbol{n}(x,z)\right]\varphi_i = \boldsymbol{V}(x,z)\cdot\boldsymbol{n}(x,z), \tag{7.4}$$

where $\boldsymbol{V}(x, z)$ is the fluid velocity given by the LS-NS solver in the corresponding point. $(\overline{x}, \overline{z})$ are the node's coordinates in the local coordinate system in a cell that contains the node along one of its sides. In the BVP for the time derivative of the velocity potential, we impose Dirichlet conditions in the form

$$\varphi_{t,i} = \varphi_t(x, z), \tag{7.5}$$

where i is the global index of a node on a LS-NS→IBOGM boundary and $\varphi_t(x, z)$ is estimated from the pressure given by the LS-NS solver in (x, z) through expression (7.9) in the next section. Since the points along the LS-NS→IBOGM boundary are fixed in space, the cells used to impose the boundary conditions can be predetermined at the beginning of the simulation.

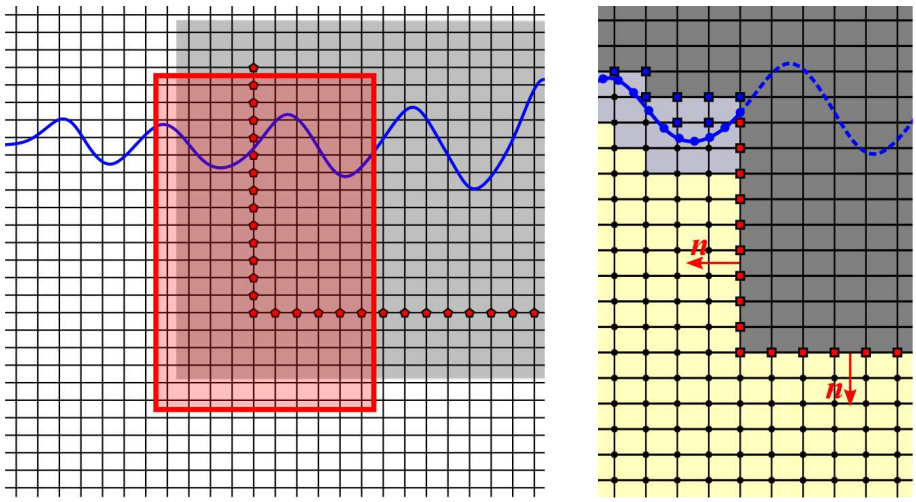

(a) Highlighted part of IBOGM domain

(b) IBOGM domain details

Figure 7.3: Details of IBOGM domain close to the LS-NS→IBOGM boundary. Yellow and grey cells indicate the active and inactive parts of the instantaneous computational domain. Boundary conditions from the LS-NS solver are imposed in the nodes indicated by red squares with black borders.

A consequence of imposing Neumann conditions for the velocity potential and Dirichlet conditions for its time derivative along the LS-NS→IBOGM boundary,

is that the coefficient matrices for the two respective global matrix systems differ. Although associated with a slight increase in computational cost, this choice is made because it is found to enhance the robustness of the coupled numerical solution over time.

Boundary Conditions from IBOGM to LS-NS Solver

In the points along the IBOGM→LS-NS boundary where velocities are passed from the IBOGM solver as boundary conditions for the LS-NS solver, these are estimated from the known velocity potential in the IBOGM domain by using (3.2) in Section 3.1.1:

$$\frac{\partial \varphi}{\partial x}(x,z)_{u_x} = \sum_{i=1}^{8}\left[\sum_{j=1}^{8} c_{j,i}\frac{\partial f_j}{\partial x}\left(\overline{x},\overline{z}\right)_{u_x}\right]\varphi_i,$$

$$\frac{\partial \varphi}{\partial z}(x,z)_{u_z} = \sum_{i=1}^{8}\left[\sum_{j=1}^{8} c_{j,i}\frac{\partial f_j}{\partial z}\left(\overline{x},\overline{z}\right)_{u_z}\right]\varphi_i.$$

$(x,z)_{u_x}$ and $(x,z)_{u_z}$ are the coordinates of a point where the horizontal and vertical velocity component are estimated, respectively. $(\overline{x},\overline{z})_{u_x}$ and $(\overline{x},\overline{z})_{u_z}$ are the corresponding local coordinates in the cells where the expressions are evaluated. To estimate the pressure in the points $(x,z)_p$ along the IBOGM→LS-NS boundary where this is passed to the LS-NS solver, we use (3.2) and (3.4) in Section 3.1.1 to estimate the velocity and the time derivative of the velocity potential,

$$\frac{\partial \varphi}{\partial x}(x,z)_p = \sum_{i=1}^{8}\left[\sum_{j=1}^{8} c_{j,i}\frac{\partial f_j}{\partial x}\left(\overline{x},\overline{z}\right)_p\right]\varphi_i,$$

$$\frac{\partial \varphi}{\partial z}(x,z)_p = \sum_{i=1}^{8}\left[\sum_{j=1}^{8} c_{j,i}\frac{\partial f_j}{\partial z}\left(\overline{x},\overline{z}\right)_p\right]\varphi_i.$$

$$\varphi_t(x,z)_p = \sum_{i=1}^{8}\left[\sum_{j=1}^{8} c_{j,i} f_j\left(\overline{x},\overline{z}\right)_p\right]\varphi_{t,i}.$$

The pressure is evaluated by using these in the Bernoulli equation (2.20).

Since the points along the IBOGM→LS-NS boundary are fixed in space, the eight cells that contain each of them need only to be determined once at the beginning of the simulation. Generally, the cell where a particular IBOGM→LS-NS point is closer to the cell's center is chosen. When evaluating the expressions, a check is performed to ensure that all the cell nodes are part of the instantaneous active IBOGM computation domain. This may lead to a different choice of cell for some of the points just beneath the free surface. Since the points are fixed in space, the associated HPC coefficients also only need to be determined once. By utilizing this, the computational efficiency of the IBOGM is enhanced.

7.2.2 Temporal Coupling Scheme

In the IBOGM simulations presented in Chapter 4 - 6, the 4^{th} order Runge-Kutta scheme (RK4) given by (3.33) was applied to evolve the solution in time. Here, since the LS-NS solver uses a 2^{nd} order predictor-corrector temporal scheme, a 2^{nd} order Runge-Kutta midpoint scheme (RK2) is used for the time evolution of the free surface properties in the IBOGM solver. For a general variable y with time derivative given in the form $\dot{y} = \dot{y}(y,t)$, the evolution from the known state $y_n = y(t_n)$ at time $t_n = n\Delta t$ to the unknown state at $t_{n+1} = t_n + \Delta t$ is given as

$$y_{n+1} = y_n + \Delta t k_{2,y}, \tag{7.6}$$

where Δt is the constant time step, set equal in the IBOGM and LS-NS solvers. The coefficient $k_{2,y}$ is given as

$$k_{2,y} = \dot{y}(y_n + 0.5\Delta t k_{1,y}, t_n + 0.5\Delta t), \tag{7.7}$$

where $k_{1,y} = \dot{y}(y_n, t_n)$. Since the free surface is the only boundary evolved in time in the IBOGM domain using (7.6) and (7.7), y here represents the position and velocity potential, respectively, for the free-surface markers. The free surface is described with the hybrid formulation in Section 3.2.1, where the free-surface marker at the wavemaker moves in a fully-Lagrangian manner and thus never separates from the wavemaker surface, while the markers in the background grid towards the LS-NS domain are semi-Lagrangian and thus restricted to move along trajectories parallel to the inertial z-axis.

The temporal coupling scheme between the two solvers is illustrated schematically in Figure 7.4. Starting from a time t_n, where the solution in both domains is known, the first IBOGM RK2 sub step is performed, during which the free-surface elevation is frozen (i.e. not updated). First, the time derivative of the free-surface velocity potential is estimated from the dynamic free-surface condition, and the first RK2 sub step is performed to estimate the free-surface potential at $t_n + 0.5\Delta t$. In relation with (7.7), the first RK2 sub step consists of an Euler step expressed as $y_n + 0.5\Delta t k_{1,y}$. Since the pressure and velocity from LS-NS along the LS-NS→IBOGM boundary are only known up to t_n, the values at $t_n + 0.5\Delta t$ are extrapolated through

$$\begin{aligned} p^{n+1/2} &= \frac{1}{2}(3p^n - p^{n-1}), \\ \boldsymbol{V}^{n+1/2} &= \frac{1}{2}(3\boldsymbol{V}^n - \boldsymbol{V}^{n-1}), \end{aligned} \tag{7.8}$$

where p^{n-1} and $\boldsymbol{V}^{n-1}$ are the pressure and velocity at $t_n - \Delta t$, respectively. Furthermore, we use the Bernoulli equation (2.20) to estimate the time derivative of the velocity potential:

$$\varphi_t^{n+1/2} = -\frac{p^{n+1/2}}{\rho} - \frac{1}{2}(\boldsymbol{V}\cdot\boldsymbol{V})^{n+1/2} - gz. \tag{7.9}$$

ρ and g are here the water density and the acceleration of gravity, respectively, and the atmospheric pressure is set to zero. Although not relevant in the present

work, it is noted that the latter cannot be done in case of gas-cavity entrainment. In this way, the boundary conditions described above for the velocity potential φ and its time derivative φ_t in the IBOGM domain become available at $t_n + 0.5\Delta t$, and corresponding boundary value problems (BVP) can be solved. From these, the fluid pressure $p_{RK2,1}^{n+1/2}$ along the IBOGM→LS-NS boundary for the LS-NS domain can be estimated, as required for the predictor step.

The LS-NS predictor step is performed next, after which the pressure and velocity $p^{*n+1/2}$ and $\boldsymbol{V}^{*n+1}$ are obtained along the LS-NS→IBOGM boundary. The free-surface position is frozen during the predictor step. The second IBOGM RK2 sub step is then performed, where the time derivatives of the free-surface position and velocity potential are estimated from the kinematic and dynamic free-surface conditions from the solution at $t_n + 0.5\Delta t$ obtained after the first RK2 sub step. These time derivatives constitute $k_{2,y}$ in (7.7). (7.6) is used to integrate the free-surface position and velocity potential to their states at $t_n + \Delta t$. Since the pressure after the LS-NS predictor step is known up to $t_n + 0.5\Delta t$, this is extrapolated to $t_n + \Delta t$ through

$$p^{n+1} = 2p^{*n+1/2} - p^n, \tag{7.10}$$

and the time derivative of the velocity potential φ_t^{n+1} is estimated from the Bernoulli equation in the same way as in (7.9). The BVPs for φ and φ_t at $t_n + \Delta t$ in the IBOGM domain are solved, and from their solutions the pressure $p_{RK2,2}^{n+1}$ and velocity $\nabla\varphi_{RK2,2}^{n+1}$ can be estimated along the IBOGM→LS-NS boundary. $p_{RK2,2}^{n+1/2}$ is then obtained by interpolation in time so that the corrector step can be performed. In addition, the free-surface elevation, at and near the IBOGM→LS-NS boundary, is given from the IBOGM solver to the LS-NS solver.

To complete the DD time step, the LS-NS corrector step is performed, giving the pressure $p^{n+1/2}$ and velocity $\boldsymbol{V}^{n+1}$. A time extrapolation of the pressure is performed to estimate p^{n+1} along the LS-NS→IBOGM boundary. At this stage, both the LS-NS and the IBOGM solvers update their free-surface configuration at $t_n + \Delta t$.

The above algorithm is carried out until the end of the simulation defined as $t = t_{end}$.

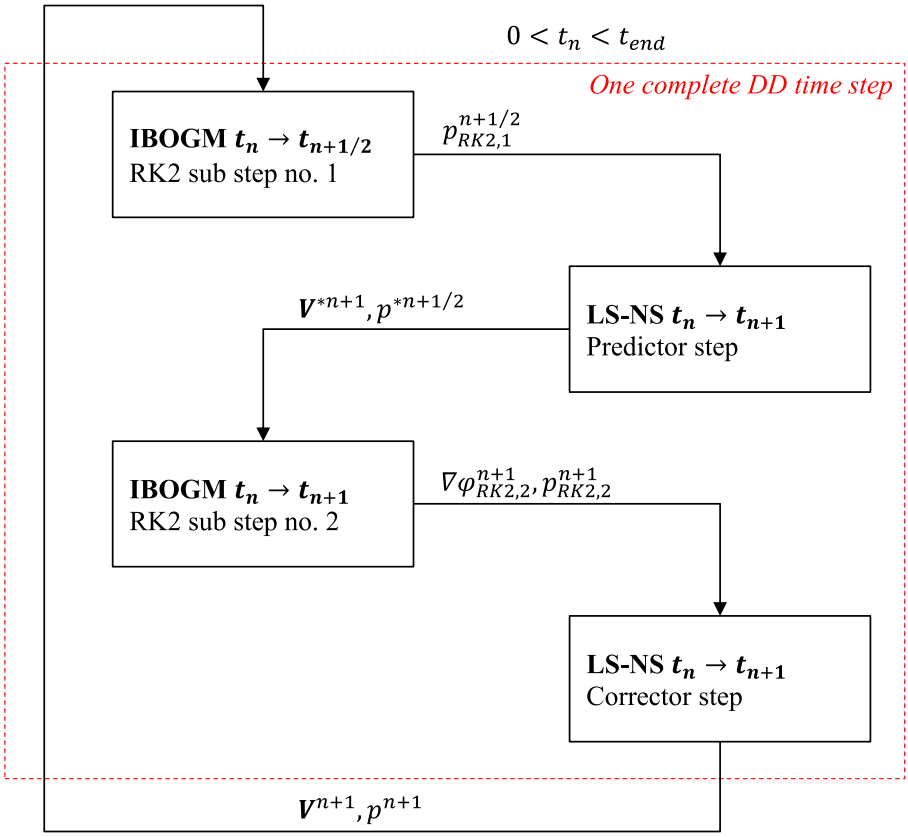

Figure 7.4: Temporal coupling scheme for IBOGM-LS-NS DD.

7.3 A Numerical Example considering Propagation of Periodic Waves

When different solvers are coupled in a DD, and in particular in a strong coupling like the one proposed here, proper exchange of information between the solvers is of key importance. By this we mean that the variables that are communicated are consistent in space and time, and that they are interpreted correctly. A numerical test case is defined, where the objective is to examine the performance of the DD in a condition when no significant viscous-flow phenomena are anticipated inside the LS-NS domain. Periodic waves with frequency $\omega = 4.429\ s^{-1}$, amplitude $\zeta_A = 0.035\ m$, wavelength $\lambda = 3.14\ m$ and steepness $k\zeta_A = 0.07$ are generated in the IBOGM domain by a flap-type wavemaker and propagated through the LS-NS domain and out in the IBOGM domain on the other side. The numerical setup is shown in Figure 7.5, where the water depth is $h = \lambda$, implying deep-water conditions. The total length of the numerical domain is $L_{tank} = 18\ m$, corresponding to approximately 5.7 wavelengths. A numerical beach with length $L_{beach} = 2\lambda$ and with a damping coefficient $\nu_{max} = 2.0\ s^{-1}$ is placed on the op-

posite side of the wavemaker in order to prevent wave reflections from the tank wall. In this test case, the LS-NS domain has dimensions $L_{LS-NS} = 4.0\ m$ and $H_{LS-NS} = 2.5\ m$. The distance from the bottom of the LS-NS domain to the still waterline is $h_{LS-NS} = 2.2\ m$. The left boundary of the LS-NS domain is located $4\ m$, corresponding to a little more than one wavelength, from the position of the wavemaker.

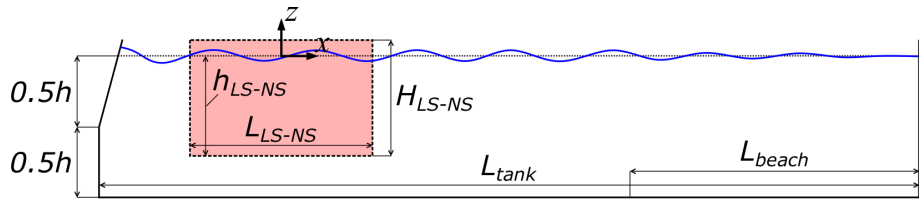

Figure 7.5: Sketch of computational domain used in numerical DD simulation. The global Oxz coordinate system is located in the middle of the LS-NS domain, indicated by the red transparent region, and with origin in the still waterline.

The uniform grid size $\Delta x = \Delta z$ in the IBOGM solver is approximately equal to $0.125\ m$, giving $\lambda/\Delta x \approx 25$. The cell size in the LS-NS solver is $\Delta x = \Delta z \approx 0.02\ m$, or $\lambda/\Delta x \approx 157$. The time step, equal in the two solvers, is $\Delta t = 0.0025\ s$. This gives $T/\Delta t \approx 567$, where $T = 2\pi/\omega$ is the incident wave period. Sensitivity studies have shown that both the cell size in the LS-NS solver and the time step can be increased, but the parameters given here are found to be slightly more favourable overall for the considered case. The ramp period of the wavemaker is set to $t_{ramp} = 4T$.

As a reference for the free-surface elevation, a potential-flow simulation is performed with the IBOGM solver without the presence of the LS-NS solver, otherwise using the same computational domain as illustrated in Figure 7.5. Snapshots of the free-surface elevation at different time instants $4.2 \leq t/T \leq 14.1$ are shown in Figure 7.6. The two simulations are initially in good agreement at $t/T = 4.2$, while a slight phase shift and amplitude reduction of the wave inside the LS-NS domain can be observed at $t/T = 5.6$. After $t/T = 8.5$, which coincides with the time where the waves entering the LS-NS domain becomes stationary, the phase shift introduced in the LS-NS domain is approximately constant. This suggests that the phase shift may be associated with the initial transient waves. No sensitivity studies are performed to examine the effect of the wavemaker ramp period, although this may be instructive. The wave elevation in the IBOGM domain left of the LS-NS domain is in good agreement with the pure potential-flow simulation throughout, although a moderate increase in wave height can be seen towards $t/T = 14.1$. This shows that the wave reflection from the LS-NS domain is small. Apart from the phase shift introduced in the LS-NS domain, the wave form on the right side of the LS-NS domain agrees well with the pure potential-flow simulation, although with a slight reduction in wave amplitude.

To further investigate the observations in Figure 7.6, the dynamic pressure and velocity fields are examined at three different time instants in Figures 7.7 - 7.9. With dynamic pressure we here refer to the total pressure, that is zero at the in-

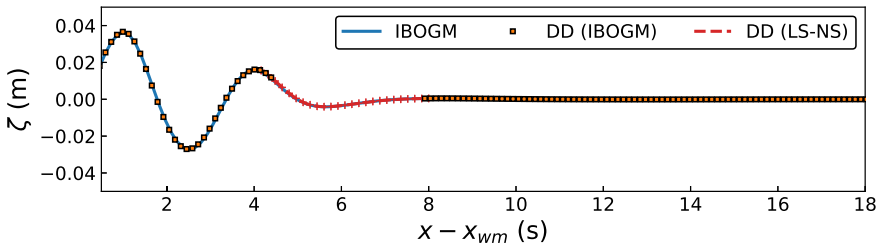

(a) $t/T = 4.2$

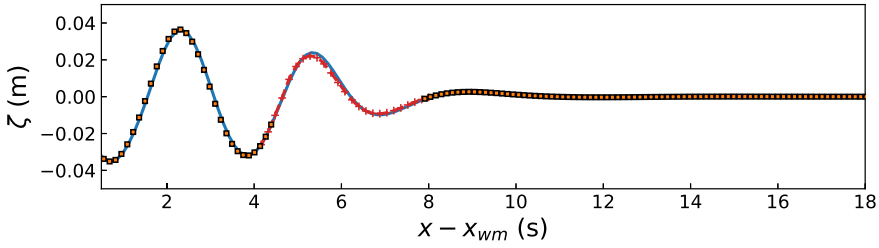

(b) $t/T = 5.6$

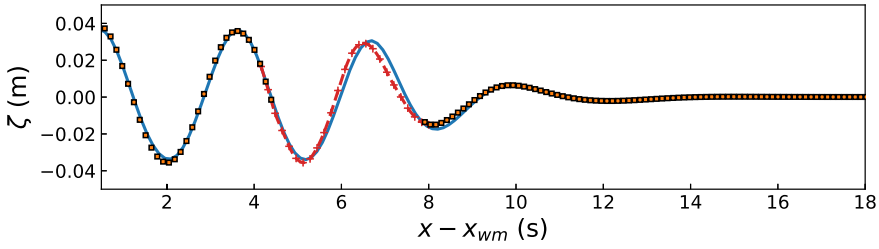

(c) $t/T = 7.0$

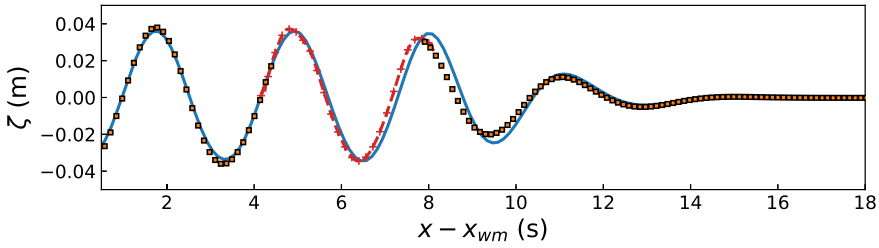

(d) $t/T = 8.5$

Figure 7.6: Snapshots of wave elevation plotted as a function of distance from the initial position of the wavemaker x_{wm}. Comparison of results between potential theory (IBOGM) and the DD, where DD (IBOGM) and DD (LS-NS) represent respectively the solution in the IBOGM and LS-NS domain.

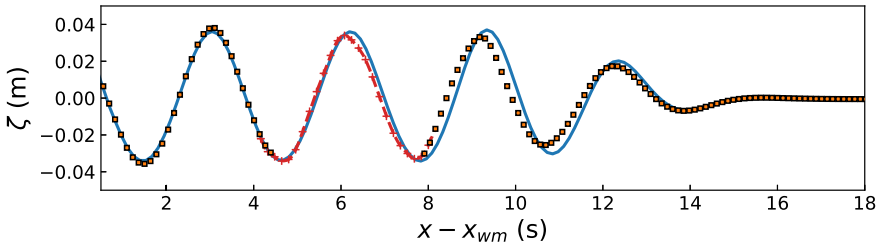

(e) $t/T = 9.9$

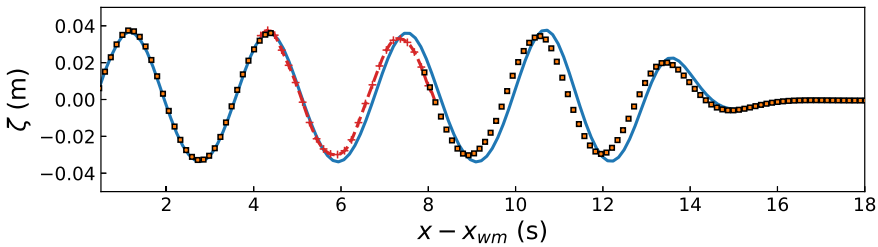

(f) $t/T = 11.3$

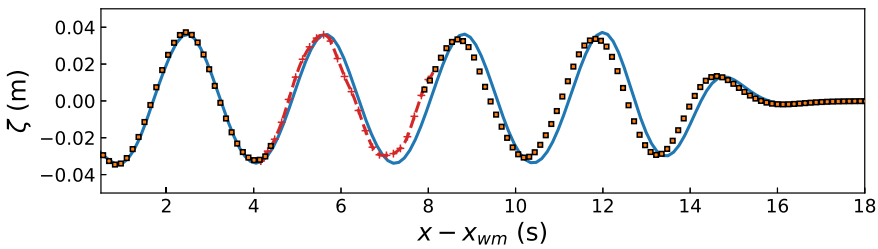

(g) $t/T = 12.7$

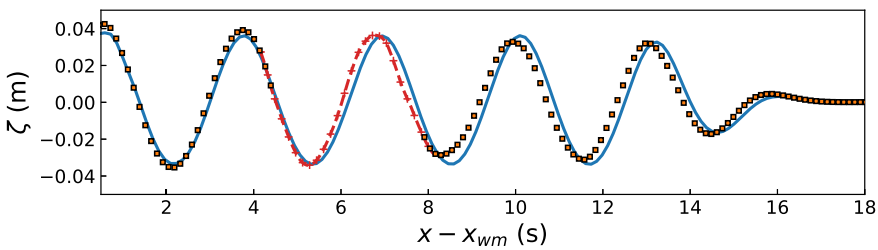

(h) $t/T = 14.1$

Figure 7.6: Continued.

stantaneous free surface, minus the hydrostatic pressure. The pressure generally appears smoothly varying between the solvers, although minor differences may be hidden due to the contour scale in the plots. A more systematic investigation of the consistency in pressure fields between the two solvers should be performed as future work. Although the velocity fields computed by the IBOGM and LS-NS solvers are comparable inside the overlapping regions, small differences in the direction and magnitude of the velocity vectors are seen moving towards the free surface, see e.g. Figure 7.8 c). An explanation for this may be that only the normal velocity from the LS-NS solver is specified as a boundary condition for φ along the LS-NS→IBOGM boundary (see Figure 7.3). In particular, differences may occur when the flow direction in the LS-NS domain is predominantly parallel to the boundary. Considering alternative strategies to more rigorously specify both the horizontal and vertical velocity as boundary conditions in the IBOGM solver along the LS-NS→IBOGM boundary simultaneously is thus expected to enhance the consistency between the velocity fields in the two solvers, particularly in and near the the overlapping region.

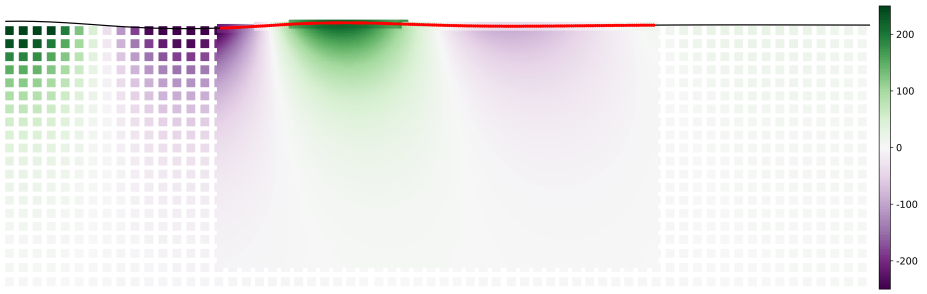

(a) Dynamic pressure

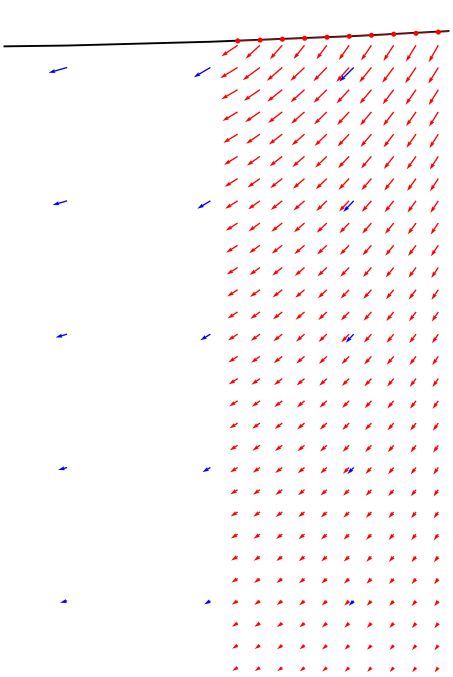

(b) Velocity (left overlapping region)

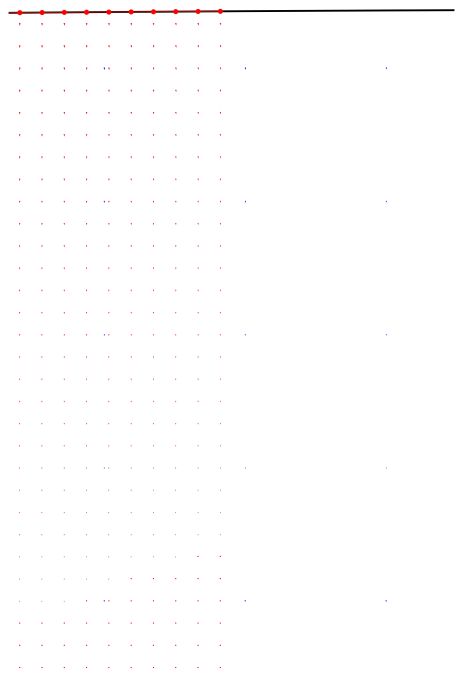

(c) Velocity (right overlapping region)

Figure 7.7: Dynamic pressure and velocity field at $t/T = 5.6$. The red and blue velocity vectors are from the LS-NS and IBOGM solutions, respectively. The free surface inside the LS-NS domain is indicated with red markers.

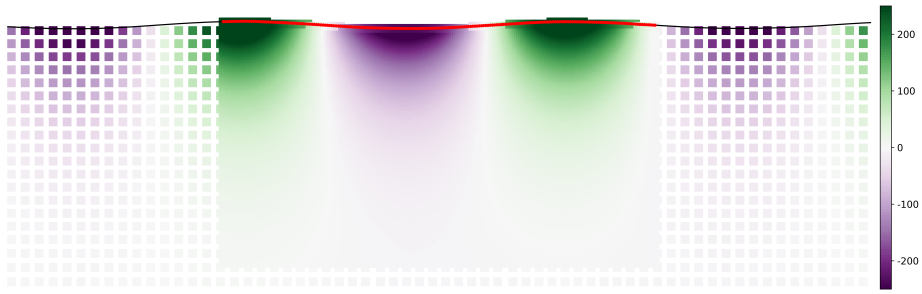

(a) Dynamic pressure

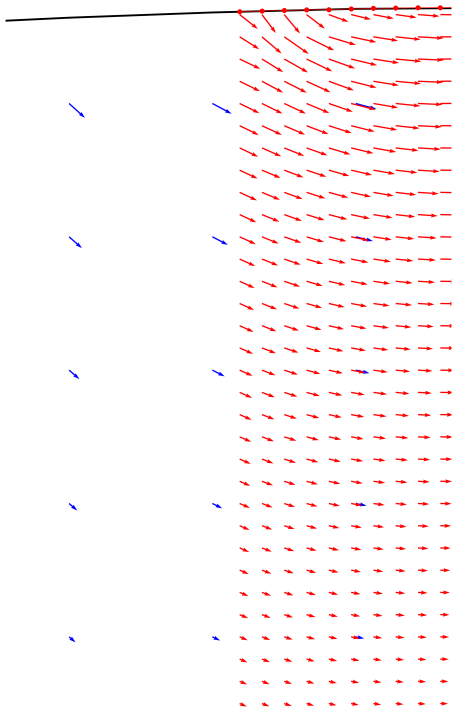

(b) Velocity (left overlapping region)

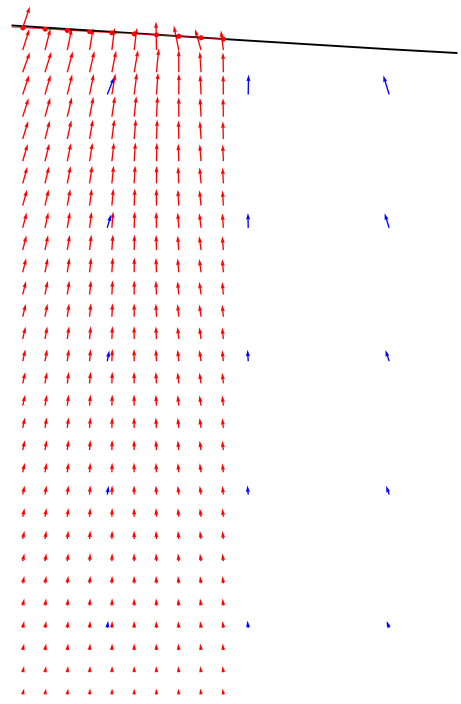

(c) Velocity (right overlapping region)

Figure 7.8: Dynamic pressure and velocity field at $t/T = 11.3$. The red and blue velocity vectors are from the LS-NS and IBOGM solutions, respectively. The free surface inside the LS-NS domain is indicated with red markers.

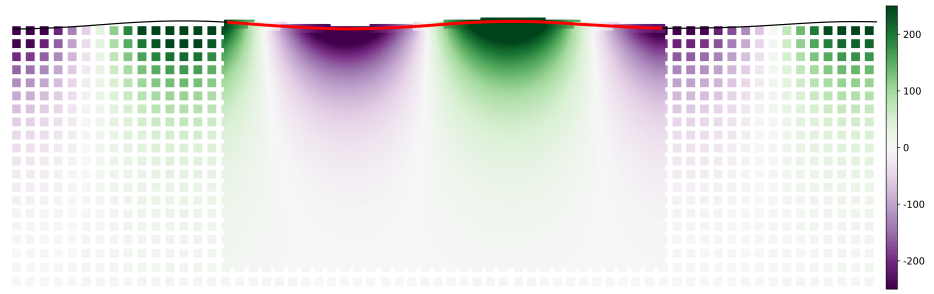

(a) Dynamic pressure

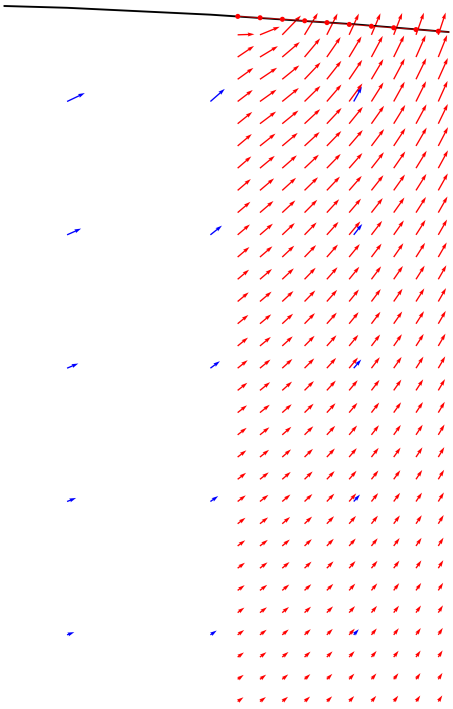

(b) Velocity (left overlapping region)

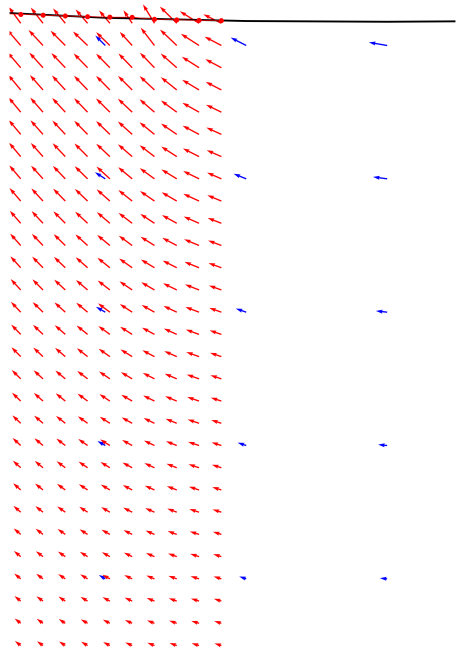

(c) Velocity (right overlapping region)

Figure 7.9: Dynamic pressure and velocity field at $t/T = 14.1$. The red and blue velocity vectors are from the LS-NS and IBOGM solutions, respectively. The free surface inside the LS-NS domain is indicated with red markers.

7.4 Future Perspectives

Figure 7.6 showed that with the present implementation of the DD, the amplitude and phase of the propagating periodic waves examined in the previous section were slightly modified in the LS-NS domain compared with a pure potential-flow solution. This is likely related to somewhat inconsistent solution fields in and near the overlapping region between the two solvers illustrated in Figures 7.7 - 7.9. The case considered here is conceptually similar to that illustrated in Figure 7.1 a), with the exception that the waves have low steepness and are not breaking inside the LS-NS domain. However, the exchange of information between the two solvers is similar irrespective if wave breaking occurs or not, or if viscous-flow phenomena associated with a body such as illustrated in Figure 7.1 b) are present inside the LS-NS domain. One must however be cautious to select the LS-NS domain large enough to prevent vorticity from being convected to the LS-NS→IBOGM boundary, since potential-flow theory assumes irrotational flow.

Although the present results are considered promising, the consistency between the two solvers needs to be further enhanced before investigations of relevant phenomena such as illustrated in Figure 7.1 can be pursued. In order to achieve this, the following activities are suggested:

1. Introducing techniques that allow the fluid velocity in both horizontal and vertical direction to be specified simultaneously as boundary conditions for the IBOGM solver along the LS-NS→IBOGM boundary, as well as other strategies to ensure a more accurate exchange of information between the two solvers.
2. A systematic parameter investigation of the size of the overlapping region between the IBOGM and LS-NS domains, both relative to the grid spacing in the IBOGM solver, the cell size in the LS-NS solver and the characteristic wavelength.
3. Systematic numerical convergence studies, considering both the temporal and spatial discretization.

In performing the above activities, the solution in the two solvers should be compared quantitatively in the overlapping region. Also conservation of physical properties such as energy and mass should be investigated.

7.5 A Note on the Challenges in Coupling Different Solvers

Combining a potential-flow solver and a Navier-Stokes solver in a strong DD scheme like the one outlined here is indeed a challenging task. In particular, since the governing equations differ in the two solvers, to properly exchange information at the intersection between their respective domains is not straightforward. An initial attempt was made as part of the present research to couple the IBOGM solver with the open-source Navier-Stokes solver InterFOAM included in OpenFOAM version 5.0 (www.openfoam.org). The spatial coupling scheme was comparable to that in Figure 7.2, with overlapping domains, and where the *externalCoupled* boundary condition included in OpenFOAM was used to impose

the boundary conditions from the IBOGM solver to InterFOAM. Similarly, OpenFOAM *probes* were defined where variables were written from InterFOAM to the IBOGM solver.

There are distinct differences between InterFOAM and the LS-NS solver above:

1. InterFOAM uses the volume of fluid (VOF) method to capture the free surface.
2. InterFOAM uses the finite volume method (FVM) to discretize the Navier-Stokes equation.

Compared with the level-set function, the VOF gives a less sharp description of the free-surface position. Moreover, it poses more challenges in exchanging the free-surface position and the velocity close to the free surface from the IBOGM to the NS solver. While in the FDM velocities are defined at cell sides and the pressure is defined in the cell center, both velocities and pressure are defined in the cell center in the FVM. As a consequence, it was not possible to impose both velocity and pressure from the IBOGM solver to InterFOAM, because this created large velocity and pressure gradients in the InterFOAM domain even when the water was practically at rest. The reason for this is that imposing velocity and pressure in a single point makes the solution over-determined. As a consequence, only the velocity was imposed as boundary condition from the IBOGM solver. Moreover, it was generally found that the velocity field just inside the InterFOAM domain was not fully consistent with the imposed boundary field. It is thus questioned whether the *externalCoupled* boundary condition in OpenFOAM works as it is intended to. Indeed, the available documentation for this boundary condition is scarce. The philosophy behind the temporal coupling scheme between the IBOGM solver and InterFOAM was similar to Figure 7.4. However, since we did not attempt to intervene with the source code of OpenFOAM, we were not able to impose boundary conditions for InterFOAM other than at the beginning of each time step. This made the coupling less controllable than in the coupling with the LS-NS solver, which is likely to contribute to a less accurate solution.

Attempts were made to propagate regular waves with moderate steepness generated in the IBOGM domain through the InterFOAM domain in the same way as in Section 7.3, with the InterFOAM domain configured in a similar way as illustrated in Figure 7.4. Both spatial and temporal convergence studies were performed without being able to obtain an accurate solution. In general, waves were reflected from the InterFOAM domain in opposite direction of the wave propagation, as well as internally in the InterFOAM domain. In other words, the incident waves were not properly propagated neither in nor out of the InterFOAM domain. In addition, the InterFOAM solution was slow to converge, resulting in excessive computational time.

The unsuccessful attempt to couple the IBOGM and InterFOAM solvers described here illustrates a fundamental difficulty beyond the fact that the governing equations differ. Because the InterFOAM solver was used as an isolated standalone solver, we could not control the solver's behaviour at the different stages of each time step. This is in contrast with the LS-NS solver, were we explicitly control the boundary conditions for both the predictor and corrector steps. One

would imagine that the same obstacle remains also if a potential-flow solver is coupled with other commercial NS solvers, unless one is able and willing to modify the solver's source code. This does not mean that such endeavour is without purpose for particular scenarios. For instance, Siddiqui et al. (2018) were able to radiate waves from a heaving ship section in OpenFOAM to an exterior potential-flow domain where the HPC method was used as solver. However, in their case the coupling was weak in the sense that it did not allow for a proper two-way transfer of information.

7.6 Summary

A domain-decomposition (DD) scheme to couple the potential-flow solution from the immersed boundary-overlapping grid method (IBOGM) developed in the present work with the viscous-flow solution from an existing level-set Navier-Stokes (LS-NS) solver in a strong way has been proposed. This means that the two solvers exchange information mutually in terms of velocity, pressure and free-surface elevation, both at the beginning and during each time step of the simulation. A purpose-fitted version of the LS-NS solver was made available for the present work, allowing the exchange of information between the two solvers to be managed through external ASCII files. After outlining the details of the spatial and temporal coupling schemes, a numerical test case was presented in order to examine the DD's ability to properly exchange information between the two solvers. The case consisted in propagating periodic waves with low steepness through the LS-NS domain, that was located in the interior of the IBOGM domain. Without having performed systematic convergence studies, the results showed that the general form of the waves remained intact when compared with a pure potential-flow solution, and with little reflections from the LS-NS domain back towards the wavemaker. However, a slight phase shift and reduction in wave amplitude were observed. It was indicated that these were due to small inconsistencies in the solution fields in the overlapping region between the two solvers. Developing strategies to enhance the exchange of information between the two solvers was thus suggested as further work. Although the case considered here did not involve violent wave phenomena nor viscous wave-body interactions inside the LS-NS domain, the exchange of information between the two solvers is similar also for these scenarios. Hence, by improving the DD for the considered test case, no additional challenges are expected dealing also with these types of cases.

Towards the end, an unsuccessful attempt to couple the IBOGM solver with the open-source Navier-Stokes solver OpenFOAM, used as a standalone solver, was described. This highlighted the challenges in coupling two solvers using different sets of governing equations to describe the flow, and where two-way exchange of information other than at the beginning of each time step of the simulation is impossible.

Chapter 8

Summary and Further Work

Non-linear wave propagation and wave-body interaction problems have been examined numerically. The main purpose of the work has been to develop a fully non-linear numerical framework to study these problems in an efficient and accurate manner, and to identify important non-linear wave-body interaction effects. The main features of the numerical framework are summarized in Section 8.1, while main findings from the investigation of wave-body interaction effects are given in Section 8.2. In Section 8.3, the original contributions of the present work, in the opinion of the author, are highlighted. Relevant topics for further work are proposed in Section 8.4.

8.1 Numerical Framework

A numerical method capable of simulating fully non-linear potential-flow problems in 2D has been proposed. The recently developed harmonic polynomial cell (HPC) method, shown to have high accuracy and to be numerically efficient, is used to solve the governing Laplace equation for the velocity potential. The HPC method is a field method, so that the entire fluid domain has to be discretized. A study has shown that, in order to benefit from the high-order accuracy of the HPC method, Cartesian grids with square cells are preferable. To easily model arbitrary boundaries in an accurate manner using square cells, an immersed boundary method has been applied. Because the HPC method is an interpolation method, no additional interpolation schemes were required in doing this. To refine the fluid flow locally where needed, and to allow for moving bodies, a technique using overlapping Cartesian, body-fixed grids was used. Inside the overlapping grids, the fluid problem is modelled in a non-inertial, body-fixed reference frame, while the majority of the fluid domain is modelled in a stationary background grid. In the latter, the fluid problem is considered in the Earth-fixed inertial reference frame. The combined method was denoted as an immersed boundary-overlapping grid method (IBOGM). With this, complex boundaries can be modelled accurately solely using Cartesian grids, without increasing the total number of grid nodes and computational time unnecessarily.

An auxiliary boundary value problem (BVP) was solved for the time deriva-

tive of the velocity potential, which is required in order to estimate the pressure and the resulting loads on a body. It was shown that, using the IBOGM, the boundary conditions on moving bodies are simplified compared to modelling the problem in an inertial reference frame. The terms that are numerically challenging in the inertial reference frame are instead accounted for in a more straightforward way in the coupling between the body-fixed grids and the stationary background grid.

Techniques to account for small angles developing between the free surface and rigid boundaries, as well as wave breaking, have been introduced to improve the method's numerical robustness.

It is found that the proposed IBOGM essentially preserves the numerical efficiency of the HPC method. However, a drawback is that the global coefficient matrix in the BVP solved at each time instant is time-dependent due to the motion of immersed boundaries and the overlapping between different grids. This is not beneficial with respect to computational efficiency. Numerical techniques have been introduced to minimize the additional computational cost related to this, utilizing the fact that the majority of the cells in the water domain are unaffected.

The method has been validated and verified against experimental and numerical reference results in a systematic manner. A range of wave-propagation problems with different sources of non-linearity, both in deep and shallow water, were first examined. It was shown that the method is able to accurately model steep waves close to breaking. By applying a wave-breaking suppression scheme, even a plunging breaker was modelled. Thereafter, a heaving circular cylinder in still water and a fixed ship section in regular waves were considered. The distinct non-linear features in the former problem are related to the non wall-sided geometry of the body, and to small angles developing near the intersection between the free surface and the cylinder for high oscillation frequencies. The fixed ship section in regular waves represents a non-linear wave-diffraction problem. For a freely floating ship section in regular waves, the IBOGM analysis was compared with an independent analysis performed with a non-linear boundary element method (BEM). The simulation parameters and boundary conditions were, as far as possible, similar in the two solvers. Identical post-processing of the results from both analyses was performed in order to remove this as a source of uncertainty. The results between the two solvers were in good agreement, even when the rigid-body heave and roll motions of the ship section were large.

A domain-decomposition (DD) strategy to couple the IBOGM with an existing level-set Navier-Stokes (LS-NS) solver based on laminar flow has been outlined. The exchange of information between the two solvers was examined for a simple wave-propagation case. This serves as a basis for future research, considering scenarios where viscous effects due to e.g. wave breaking or wave-body interaction matter in restricted regions.

8.2 Numerical Investigation of Wave-Body Interaction Problem

A freely floating ship section in regular waves with different frequencies and heights was systematically examined with the IBOGM. The results were compared to experimental and linear and non-linear numerical reference results, with particular focus on non-linear effects due to large wave steepness and large rigid-body motions. With roll amplitudes up to 30° near resonance for the highest waves, the mean wave drift force in sway was found to be larger than predicted by 2^{nd} order theory. For steep waves away from resonance frequencies, the mean wave drift force was significantly lower than from 2^{nd} order theory. This was also observed when the body was fixed, and is therefore likely related to non-linearities in the incident waves and their interaction with the body.

Near resonance, the predicted roll motions were considerably larger than in the experiments, which was explained by lack of viscous damping in the potential-flow analysis. By adding quadratic damping, the roll motion was brought closer to the experiments with amplitudes of approximately 15°. Also sway and heave motions, as well as the mean wave drift force, were significantly modified, which indicated strong coupling effects. An important observation was that the problem not necessarily became more linear by adding roll damping. In particular it was seen that the relative decrease of the 2^{nd} order sway force was smaller than that of the 1^{st} order component.

Different methods to estimate the mean wave drift force were investigated, showing that the results obtained with direct pressure integration (DPI) generally were consistent with the mean sway motion of the ship section. The mean wave drift force was also estimated from conservation of fluid momentum (CFM) with an exact formulation and with 2^{nd} order approximations, including the widely used Maruo's formula. With the exact formulation, the CFM results were in good agreement with DPI other than when wave-frequency rigid-body motions were large. This was also observed in the independent BEM analysis. The results from 2^{nd}-order approximate CFM methods compared poorly with DPI and experiments. It was concluded that approximate CFM methods should be used with caution in connection with fully non-linear simulations.

The finding that DPI is more accurate than CFM methods differs from statements made by other authors, who claimed that the mean wave drift force estimated from DPI was unreliable in their analyses. Through performing a sensitivity analysis with the IBOGM, however, it was shown that this conclusion may have been drawn on a false basis. In particular, the mean wave drift force was highly sensitive to a non-linear term in the body-boundary condition in the BVP for the time derivative of the velocity potential. It was shown that this non-linear term may have been wrongly accounted for in the reference results. Indeed, by neglecting this non-linear term in the IBOGM analysis, a similar steady-state sway motion as in one of the reference publications was obtained with the wave frequency equal to the roll resonance frequency. The non-linear term did on the other hand not have a significant influence on the wave-frequency body motions. It was therefore warned against judging a non-linear numerical implementation solely on the basis of 1^{st} order quantities.

8.3 Original Contributions

In relation with the fully non-linear numerical method implemented in 2D, novel concepts include:

- *Time derivative of the velocity potential in HPC method*: It was shown that in the HPC method the time derivative of the velocity potential can be computed with the same local expression inside a cell as the velocity potential. The boundary conditions differ between the two.
- *HPC method in a body-fixed reference frame*: It was shown that the formulation of the velocity potential is similar in an inertial and in a body-fixed reference frame. The formulation of the time derivative of the velocity potential, on the other hand, differs due to a convective term associated with the velocity of the body-fixed reference frame.
- *Immersed boundary modelling*: The free surface and the boundary of rigid bodies were modelled as immersed boundaries in Cartesian grids, that can either be inertial or body-fixed, with ghost nodes outside the water domain. It was demonstrated that, since the HPC method is formulated as an interpolation method, no additional interpolation schemes need to be constructed. It was therefore claimed that the proposed immersed-boundary modelling is natural in the context of the HPC method. The immersed-boundary modelling applies in both the boundary value problem for the velocity potential and of its time derivative. The formulation would be straightforward to implement also for an elastic body, tracking its flexible motions with markers in a body-fixed grid like we here have done for the free surface.
- *Overlapping computational domains*: Using multiple overlapping computational domains, where the numerical problem can be formulated in different reference frames, the solution could be refined locally. The solutions in the different domains were coupled in an implicit manner with little additional computational cost.
- *Combination of immersed boundaries and overlapping domains*: By combining the immersed-boundary and overlapping domain modelling, square cells could be used throughout in analysis involving wave-body interaction problems. Moreover, using overlapping domains, the grid could be refined locally without increasing the total number of cells in the whole domain unnecessarily. The combined method, denoted as an immersed boundary-overlapping grid method, allows for accurate and efficient modelling of wave-body interaction problems.
- *Simplified body-boundary condition for time derivative of velocity potential*: By considering the numerical problem for the time derivative of the velocity potential on moving rigid bodies in a body-fixed reference frame, problematic terms in the body-boundary condition, involving higher-order spatial derivatives, were avoided. These were instead accounted for in a more straightforward manner near the intersecting boundaries between different computational domains.

- *Coupling with Navier-Stokes solver*: The first attempt to couple a potential-flow solver based on the HPC method with a Navier-Stokes solver while accounting for non-linear free-surface effects was documented. The exchange of information is handled through an overlapping zone that includes the free surface. Initial results were promising, although further work is required to optimize the exchange of information between the two solvers.

With respect to the examined interactions between waves and a floating body, the following findings were documented:

- *Higher-order loads*: When large resonant rigid-body motions occurred, non-negligible high-order components were identified in the hydrodynamic loads on the body. High-order components were also significant in steep incident waves, even with frequencies far away from any resonance frequency.
- *Effect of adding damping near resonance*: Quadratic roll damping was added near resonance to bring the roll motion closer to experimental results. While this leads to reduced roll motions, it did not in general make the system's behaviour more linear. In particular, the relative importance of the 2^{nd} order sway force was found to increase when the roll damping increased.
- *Strong motion coupling effects*: Near heave and roll resonance, the 1^{st} order heave motion was consistently lower than predicted by linear theory. The discrepancy increased with increasing wave height, and was reduced with increased roll damping. Also the 1^{st} order sway motion was influenced by the roll damping. This indicated strong coupling effects between sway, heave and roll.
- *Mean wave drift force*: The normalized mean wave drift force was larger than the 2^{nd} order theoretical value of unity near heave and roll resonance. This is likely due to non-linear effects. For higher wave frequencies, the mean wave drift force was consistently lower than predicted by 2^{nd} order theory. This was also observed in experimental reference results.
- *Estimation of mean wave drift force*: Estimating the mean wave drift force from direct integration of fluid pressure gave results consistent with the horizontal offset of the body. Other than near heave and roll resonance, the mean wave drift force from conservation of fluid momentum using an exact formulation was in good agreement with direct pressure integration. Approximate 2^{nd} order methods, such as the widely used Maruo's formula, did not reproduce the results from direct pressure integration well. This is possibly because such approximate methods neglect higher-order effects that matter for large motions and in steep incident waves.
- *The body-boundary condition for the time derivative of the velocity potential*: By comparing with other sources providing results from non-linear numerical simulations, a large discrepancy was seen in the mean wave drift force near heave and roll resonance. It was speculated whether this may be related to an inconsistency in the body-boundary condition used in those studies when estimating the time derivative of the velocity potential. Performing a sensitivity study with a similar inconsistency in the body-boundary condition showed qualitatively the same type of behaviour. However, the influ-

ence on 1^{st} order rigid-body motions was insignificant. It was noted that also other aspects may contribute to the observed discrepancies.

8.4 Suggested Further Work

During the present work, several aspects that deserve additional attention have been identified:

- In order to generalize the proposed numerical method, it should be extended to 3D applications. Indeed, 3D applications of the HPC method have been demonstrated by other authors. It is expected that the numerical techniques here developed in 2D, such as the immersed-boundary modelling and overlapping between different computational domains, are applicable also in 3D without major modifications.
- In the immersed-boundary modelling, the numerical refinement of a boundary is governed by the density of the grid in the vicinity of the boundary. Further work is required to refine such boundaries, when needed, in an efficient manner. An appealing strategy in this respect is to introduce octree techniques, where the grid size is reduced locally by dividing cells into several smaller ones. In this way, a boundary can be refined while still using Cartesian grids with square cells, and without increasing the total number of cells excessively. Another strategy is to introduce several layers of smaller overlapping grids. Using octree grids can be viewed as a particular version of this.
- Although the immersed-boundary modelling and overlapping domains provide several benefits with respect to computational efficiency, a drawback is that the size and topology of the global coefficient matrix changes during the analysis. Numerical techniques to reconstruct the global coefficient matrix in an efficient manner have been presented, but there is still room for improvement. Such means should be further investigated. Furthermore, the computational method can be made more efficient by optimizing it for parallel computation, or by facilitating it for graphical processor units (GPU). The method can also be made more efficient by e.g. implementing an adaptive time-stepping scheme, where the time step is adjusted throughout the analysis.
- Adaptive methods are also attractive in relation with grid refinements, i.e. refining the grid locally when this is required. A relevant application could e.g. be to refine the grid in the vicinity of a steep wave crest.
- The body-boundary condition for the time derivative of the velocity potential depends on the body's motion. At the same time, the body motion depends on the fluid pressure, that again depends on the time derivative of the velocity potential. This recursive dependence was here accounted for by applying an iterative scheme. A more elegant strategy that has been implemented by other authors is to couple the two problems implicitly. More work is required to implement such strategy in the present numerical framework.

- When body motions were large, the mean wave drift force estimated from conservation of fluid momentum and from direct integration of fluid pressure differed. Further research is required to explain this discrepancy between the two methods.
- An attempt was made to implement a non-reflective boundary condition through a multi-transmitting formula on the vertical tank wall on the opposite side of the wavemaker. However, a steady drift was observed in the wave elevation. Applying such boundary condition is appealing from a computational-efficiency viewpoint because it removes the requirement of a numerical damping zone to prevent wave reflections, so that the extent of the computational domain can be reduced accordingly. Further research to successfully implement such boundary condition in the present numerical framework is therefore proposed.
- It was demonstrated that, by applying a breaking-suppression scheme, wave breaking could be avoided in the numerical analysis. This is attractive to improve numerical robustness in simulations where wave breaking may occur, but is not of primarily importance. The parameters involved in the scheme were determined through trial and error until reasonable values were obtained. For such scheme to be practical for general scenarios, the scheme's parameters should be determined as a function of physical quantities such as e.g. the wave steepness.
- Many offshore structures have non-wall sided hull geometry in the free-surface region. This can be expected to influence both the floater motions and wave drift loads, and should be further examined. Similarly, wave drift loads on structures moored in shallow water should be investigated in a fully non-linear framework. The numerical method proposed in this thesis can be directly applied to both these scenarios.
- The present analysis is performed for periodic, monochromatic waves. Going forward, irregular waves should be investigated. In particular, it is of interest to study how non-linear effects influence the slowly-varying drift loads and resulting motions of moored structures.
- More research is required to increase the accuracy of the scheme proposed to couple the potential-flow solver with a Navier-Stokes solver. This can be achieved through systematic parameter investigations and enhanced strategies to ensure consistent information exchange between the two solvers. The potential of doing so is considerable, allowing for proper treatment of viscous effects where they matter combined with the accurate and efficient wave-propagation abilities demonstrated by the potential-flow solver. Through a further extension to 3D, such strategy could be used to investigate several problems of practical relevance. Examples of such scenarios include wave drift loads on semi-submersibles in severe sea states, where it is found that viscous contributions are significant, and determination of environmental windows for lowering and lifting of complex subsea structures through the free-surface zone in waves.

References

Aksnes, V., Berthelsen, P. A., and Da Fonseca, N. (2015). On the need for calibration of numerical models of large floating units against experimental data. In *The Twenty-fifth International Ocean and Polar Engineering Conference*. International Society of Offshore and Polar Engineers.

Baarholm, R. J. (2001). *Theoretical and experimental studies of wave impact underneath decks of offshore platforms*. PhD thesis, Norwegian University of Science and Technology.

Bandyk, P. J. and Beck, R. F. (2011). The acceleration potential in fluid–body interaction problems. *Journal of Engineering Mathematics*, 70(1-3):147–163.

Bardazzi, A., Lugni, C., Antuono, M., Graziani, G., and Faltinsen, O. M. (2015). Generalized hpc method for the poisson equation. *Journal of Computational Physics*, 299:630–648.

Barthelemy, X., Banner, M., Peirson, W., Fedele, F., Allis, M., and Dias, F. (2015). On the local properties of highly nonlinear unsteady gravity water waves. part 2. dynamics and onset of breaking. *Journal of Fluid Mechanics (submitted) http://arxiv. org/abs/1508.06002*.

Battjes, J. (1988). Surf-zone dynamics. *Annual Review of Fluid Mechanics*, 20(1):257–291.

Bingham, H. B. and Zhang, H. (2007). On the accuracy of finite-difference solutions for nonlinear water waves. *Journal of Engineering Mathematics*, 58(1-4):211–228.

Chapalain, G., Cointe, R., and Temperville, A. (1992). Observed and modeled resonantly interacting progressive water-waves. *Coastal engineering*, 16(3):267–300.

Clamond, D. and Grue, J. (2000). Dynamics of the transient leading part of a wave train. In *The 15th International Workshop on Water Waves and Floating Bodies*.

Colicchio, G., Greco, M., and Faltinsen, O. M. (2006). A bem-level set domain-decomposition strategy for non-linear and fragmented interfacial flows. *International journal for numerical methods in engineering*, 67(10):1385–1419.

Colicchio, G., Greco, M., and Faltinsen, O. M. (2011). Domain-decomposition strategy for marine applications with cavity entrapments. *Journal of Fluids and Structures*, 27(4):567–585.

Courant, R., Friedrichs, K., and Lewy, H. (1928). Über die partiellen differenzengleichungen der mathematischen physik. *Mathematische annalen*, 100(1):32–74.

Dean, R. G. and Dalrymple, R. A. (1991). *Water wave mechanics for engineers and scientists*. World Scientific Publishing Company.

Dev, A. and Pinkster, J. (1995). Viscous mean drift forces on moored semi-submersibles. In *The Fifth International Offshore and Polar Engineering Conference*. International Society of Offshore and Polar Engineers.

DNV GL (2017). *Recommended Practice DNVGL-RP-C205. Environmental Conditions and Environmental Loads*.

DNV GL (2018). *Offshore Standard DNVGL-OS-E301. Position Mooring*.

Dommermuth, D. G., Yue, D. K., Lin, W., Rapp, R., Chan, E., and Melville, W. (1988). Deep-water plunging breakers: a comparison between potential theory and experiments. *Journal of Fluid Mechanics*, 189:423–442.

Ducrozet, G., Bingham, H. B., Engsig-Karup, A. P., and Ferrant, P. (2010). High-order finite difference solution for 3d nonlinear wave-structure interaction. *Journal of Hydrodynamics, Ser. B*, 22(5):225–230.

Eatock Taylor, R. (1996). Analysis of non-linear wave-body interactions using finite elements. In *Waves and Nonlinear Processes in Hydrodynamics*, pages 51–62. Springer.

Engsig-Karup, A. P., Bingham, H. B., and Lindberg, O. (2009). An efficient flexible-order model for 3d nonlinear water waves. *Journal of computational physics*, 228(6):2100–2118.

Faltinsen, O. M. (1993). *Sea loads on ships and offshore structures*. Cambridge university press.

Faltinsen, O. M., Landrini, M., and Greco, M. (2004). Slamming in marine applications. *Journal of Engineering Mathematics*, 48(3-4):187–217.

Faltinsen, O. M. and Timokha, A. N. (2009). *Sloshing*. Cambridge University Press Cambridge.

Faltinsen, O. M. and Zhao, R. (1991). Flow predictions around high-speed ships in waves. *Mathematical approaches in hydrodynamics*, pages 265–288.

Fenton, J. (1972). A ninth-order solution for the solitary wave. *Journal of fluid mechanics*, 53(2):257–271.

Fonseca, N., Ommani, B., Stansberg, C., Bøckmann, A., Birknes-Berg, J., Nestegård, A., Hauteclocque, G. d., and Baarholm, R. (2017). Wave forces and low frequency drift motions in extreme seas: Benchmark studies. In *Offshore Technology Conference*.

Fonseca, N. and Stansberg, C. T. (2017a). Wave drift forces and low frequency damping on the exwave fpso. In *ASME 2017 36th International Conference on Ocean, Offshore and Arctic Engineering*. American Society of Mechanical Engineers.

Fonseca, N. and Stansberg, C. T. (2017b). Wave drift forces and low frequency damping on the exwave semi-submersible. In *ASME 2017 36th International Conference on Ocean, Offshore and Arctic Engineering*. American Society of Mechanical Engineers.

Fonseca, N., Stansberg, C. T., Nestegård, A., Bøckmann, A., and Baarholm, R. (2016). The EXWAVE JIP: Improved procedures to calculate slowly varying wave drift forces on floating units in extreme seas. In *ASME 2016 35th International Conference on Ocean, Offshore and Arctic Engineering*. American Society of Mechanical Engineers.

Fredriksen, A. G. (2015). *A numerical and experimental study of a two-dimensional body with moonpool in waves and current*. PhD thesis, Norwegian University of Science and Technology.

Greco, M. (2001). *A two-dimensional study of green-water loading*. PhD thesis, Norwegian University of Science and Technology.

Greenhow, M. (1989). A probability distribution of breaking wave crest height based on a crest-acceleration threshold method. *Ocean Engineering*, 16(5-6):537–544.

Hanssen, F.-C. W., Bardazzi, A., Lugni, C., and Greco, M. (2018). Free-surface tracking in 2d with the harmonic polynomial cell method: Two alternative strategies. *International Journal for Numerical Methods in Engineering*, 113(2):311–351.

Hanssen, F.-C. W., Colicchio, G., and Greco, M. (2019). Severe wave-body interactions: a potential-flow hpc method and its strong domain-decomposition coupling with a level-set navier-stokes solver. In *The 34th International Workshop on Water Waves and Floating Bodies*.

Hanssen, F.-C. W., Greco, M., and Faltinsen, O. M. (2017). Wave-body interaction with overlapping structured grids in the hpc method. In *The 32nd International Workshop on Water Waves and Floating Bodies*.

Hanssen, F.-C. W., Greco, M., and Shao, Y.-L. (2015). The harmonic polynomial cell method for moving bodies immersed in a cartesian background grid. In *ASME 2015 34th International Conference on Ocean, Offshore and Arctic Engineering*. American Society of Mechanical Engineers.

Hughes, S. A. (1993). *Physical models and laboratory techniques in coastal engineering*. World Scientific.

Kim, C., Clement, A., and Tanizawa, K. (1999). Recent research and development of numerical wave tanks-a review. *International Journal of Offshore and Polar Engineering*, 9(04).

Koo, W. and Kim, M.-H. (2004). Freely floating-body simulation by a 2d fully nonlinear numerical wave tank. *Ocean Engineering*, 31(16):2011–2046.

Kristiansen, T. and Faltinsen, O. M. (2011). Gap resonances analyzed by a domain-decomposition method. In *The 26th International Workshop on Water Waves and Floating Bodies*.

Kristiansen, T., Ommani, B., Berget, K., and Baarholm, R. (2015). An experimental and numerical investigation of a box-shaped object in moonpool: A three-dimensional study. In *ASME 2015 34th International Conference on Ocean, Offshore and Arctic Engineering*. American Society of Mechanical Engineers.

Kvitrud, A. (2014a). Anchor line failures - Norwegian continental shelf - 2010-2014. Report, Petroleum Safety Authority Norway.

Kvitrud, A. (2014b). Lessons learned from norwegian mooring line failures 2010–2013. In *ASME 2014 33rd International Conference on Ocean, Offshore and Arctic Engineering*. American Society of Mechanical Engineers.

Liang, H., Faltinsen, O. M., and Shao, Y.-L. (2015). Application of a 2d harmonic polynomial cell (hpc) method to singular flows and lifting problems. *Applied Ocean Research*, 53:75–90.

Longuet-Higgins, M. S. (1977). The mean forces exerted by waves on floating or submerged bodies with applications to sand bars and wave power machines. *Proceedings of the Royal Society of London. A. Mathematical and Physical Sciences*, 352(1671):463–480.

Longuet-Higgins, M. S. and Cokelet, E. (1976). The deformation of steep surface waves on water-I. a numerical method of computation. *Proc. R. Soc. Lond. A*, 350(1660):1–26.

Lugni, C. (1999). *An investigation on the interaction between free-surface waves and freely-floating bodies*. PhD thesis, University of Rome "La Sapienza".

Ma, Q. and Yan, S. (2009). Qale-fem for numerical modelling of non-linear interaction between 3d moored floating bodies and steep waves. *International Journal for Numerical Methods in Engineering*, 78(6):713–756.

Ma, S., Hanssen, F.-C. W., Siddiqui, M. A., Greco, M., and Faltinsen, O. M. (2018). Local and global properties of the harmonic polynomial cell method: In-depth analysis in two dimensions. *International Journal for Numerical Methods in Engineering*, 113(4):681–718.

Maruo, H. (1960). The drift on a body floating in waves. *J. Ship Res.*, 4(3):1–10.

Mei, C. C., Stiassnie, M., and Yue, D. K.-P. (2005). *Theory and applications of ocean surface waves: nonlinear aspects*. World scientific.

Newman, J. N. (1977). *Marine hydrodynamics*. The MIT press.

Noble Denton Europe (2006). Floating production system JIP FPS mooring integrity. Technical report, Research report 444 prepared for the Health and Safety Executive (HSE).

Nojiri, N. and Murayama, K. (1975). A study on the drift force on two-dimensional floating body in regular waves (in Japanese). *Transactions of the West-Japan Society Naval Architect*, 51:131–152.

Papanikolaou, A. (1980). Second-order theory of oscillating cylinders in a regular steep wave. In *Proc. 13th Symp. on Nav. Hydrodyn.*, pages 303–331.

Paulsen, B. T., Bredmose, H., and Bingham, H. B. (2014). An efficient domain decomposition strategy for wave loads on surface piercing circular cylinders. *Coastal Engineering*, 86:57–76.

Pinkster, J. (1980). *Low frequency second order wave exciting forces on floating structures*. PhD thesis, Delft University of Technology.

Rienecker, M. and Fenton, J. (1981). A fourier approximation method for steady water waves. *Journal of Fluid Mechanics*, 104:119–137.

Robaux, F. and Benoit, M. (2018). Modeling nonlinear wave-body interaction with the harmonic polynomial cell method combined with the immersed boundary method on a fixed grid. In *The 33rd International Workshop on Water Waves and Floating Bodies*.

Russell, J. S. (1844). Report on waves. In *14th meeting of the British Association for the Advancement of Science*, volume 311, page 1844.

Savitzky, A. and Golay, M. J. (1964). Smoothing and differentiation of data by simplified least squares procedures. *Analytical chemistry*, 36(8):1627–1639.

Seiffert, B. and Ducrozet, G. (2016). Deep water wave-breaking in a high-order spectral model. In *The 31th International Workshop on Water Waves and Floating Bodies*.

Shao, Y.-L. (2010). *Numerical potential-flow studies on weakly-nonlinear wave-body interactions with/without small forward speeds*. PhD thesis, Norwegian University of Science and Technology.

Shao, Y.-L. and Faltinsen, O. M. (2012). Towards efficient fully-nonlinear potential-flow solvers in marine hydrodynamics. In *Proceedings of the 31st International Conference on Ocean, Offshore and Arctic Engineering (OMAE), Rio de Janeiro, Brazil*, pages 369–380.

Shao, Y.-L. and Faltinsen, O. M. (2014a). Fully-nonlinear wave-current-body interaction analysis by a harmonic polynomial cell method. *Journal of Offshore Mechanics and Arctic Engineering*, 136:031301–1.

Shao, Y.-L. and Faltinsen, O. M. (2014b). A harmonic polynomial cell (hpc) method for 3d laplace equation with application in marine hydrodynamics. *Journal of Computational Physics*, 274:312–332.

Siddiqui, M. A., Greco, M., Colicchio, G., and Faltinsen, O. M. (2018). Validation of damaged ship hydrodynamics by a domain decomposition approach using the harmonic polynomial cell method and openfoam. In *The 33rd International Workshop on Water Waves and Floating Bodies*.

Snyder, R. and Kennedy, R. (1983). On the formation of whitecaps by a threshold mechanism. part I: basic formalism. *J. phys. Oceanogr.*, 13:1482–1492.

Stansberg, C., Yttervik, R., and Nielsen, F. (1998). Wave drift forces and responses in storm waves. In *Proceedings of PRADS'98 Conference*, pages 1005–1012.

Stansberg, C. T., Hoff, J. R., Hermundstad, E. M., and Baarholm, R. (2013). Wave drift forces and responses in current. In *ASME 2013 32nd International Conference on Ocean, Offshore and Arctic Engineering*. American Society of Mechanical Engineers.

Stansberg, C. T., Kaasen, K. E., Abrahamsen, B. C., Nestegård, A., Shao, Y.-L., and Larsen, K. (2015). Challenges in wave force modelling for mooring design in high seas. In *Offshore Technology Conference*.

Strand, I. M. (2018). *Sea Loads on Closed Flexible Fish Cages*. PhD thesis, Norwegian University of Science and Technology.

Subramani, A. K. (2000). *Computations of highly nonlinear free-surface flows, with applications to arbitrary and complex hull forms*. PhD thesis, University of Michigan.

Sun, H. (2007). *A boundary element method applied to strongly nonlinear wave-body interaction problems*. PhD thesis, Norwegian University of Science and Technology.

Tanizawa, K. (1995). A nonlinear simulation method of 3d body motions in waves. *Journal of the Society of Naval Architects of Japan*, 178:96–105.

Tanizawa, K., Minami, M., and Naito, S. (1999). Estimation of wave drift force by numerical wave tank. In *The Ninth International Offshore and Polar Engineering Conference*. International Society of Offshore and Polar Engineers.

Tasai, F. and Koterayama, W. (1976). Nonlinear hydrodynamic forces acting on cylinders heaving on the surface of a fluid. *Research Institute for Applied Mechanics, Kyushu University, Fukuaka, Japan, Technical Report*, (77).

Tong, C., Shao, Y.-L., Hanssen, F.-C. W., Li, Y., Xie, B., and Lin, Z. (2019). Numerical analysis on the generation, propagation and interaction of solitary waves by a harmonic polynomial cell method. *Wave Motion*, 88:34–56.

Vinje, T. and Brevig, P. (1981). *Breaking waves on finite water depths: a numerical study*. Ship Research Institute of Norway Marine Technology Center.

Wang, J. and Faltinsen, O. M. (2018). A harmonic polynomial method based on cartesian grids with local refinement for complex wave-body interactions. In *The 33rd International Workshop on Water Waves and Floating Bodies*.

Wang, P., Yao, Y., and Tulin, M. P. (1995). An efficient numerical tank for non-linear water waves, based on the multi-subdomain approach with bem. *International journal for numerical methods in fluids*, 20(12):1315–1336.

Wichers, J. E. W. (1988). *A simulation model for a single point moored tanker*. PhD thesis, Delft University of Technology.

Wu, G. and Eatock Taylor, R. (1994). Finite element analysis of two-dimensional non-linear transient water waves. *Applied Ocean Research*, 16(6):363–372.

Wu, N.-J., Tsay, T.-K., and Chen, Y.-Y. (2014). Generation of stable solitary waves by a piston-type wave maker. *Wave Motion*, 51(2):240–255.

Yan, S. and Ma, Q. (2007). Numerical simulation of fully nonlinear interaction between steep waves and 2d floating bodies using the qale-fem method. *Journal of Computational physics*, 221(2):666–692.

You, J. (2012). *Numerical studies on wave forces and moored ship motions in intermediate and shallow water*. PhD thesis, Norwegian University of Science and Technology.

Zhang, W. (2009). Non-reflecting simulation for fully nonlinear irregular wave radiation. In *The 24th International Workshop on Water Waves and Floating Bodies*.

Zhou, B., Wu, G., and Meng, Q. (2016). Interactions of fully nonlinear solitary wave with a freely floating vertical cylinder. *Engineering Analysis with Boundary Elements*, 69:119–131.

Zhu, W., Greco, M., and Shao, Y.-L. (2017). Improved hpc method for nonlinear wave tank. *International Journal of Naval Architecture and Ocean Engineering*, 9(6):598–612.

Appendix A

Boundary Condition for Time Derivative of φ on Moving Rigid Boundaries

In problems where fluid forces and moments on a body are required, the time derivative of the velocity potential φ must be estimated in order to calculate the pressure. In the present work, an auxiliary boundary value problem is solved for this variable. The body-boundary condition imposed in this problem is here elaborated on. The time derivative of φ is considered as the time derivative following the motion of the body,

$$\frac{D_{BO}\varphi}{Dt} = \frac{\partial \varphi}{\partial t} + (\boldsymbol{u}_P \cdot \nabla)\varphi, \tag{A.1}$$

where $\boldsymbol{u}_P$ is the velocity of a point P on the surface of, and moving with, the rigid body. This is defined as $\boldsymbol{u}_P = \dot{\boldsymbol{x}} + \boldsymbol{\omega} \times \boldsymbol{r}$, where $\dot{\boldsymbol{x}}$ is the translational body velocity in the center of rotation, $\boldsymbol{\omega}$ is the rotational velocity vector of the body and $\boldsymbol{r}$ is the position vector of P relative to the center of rotation.

The objective in the following is to define a proper Neumann boundary condition on the surface of the body for $D_{BO}\varphi/Dt$. We here start from the corresponding boundary condition for the velocity potential, given as

$$\nabla\varphi \cdot \boldsymbol{n} = \boldsymbol{u}_P \cdot \boldsymbol{n}. \tag{A.2}$$

A.1 Derivation of the Body-Boundary Condition

When we in the following refer to the body-fixed reference frame, this is what can be denoted as the *true* body-fixed reference frame. This is emphasized in order to avoid confusion, as one may find that in some cases the term body-fixed refers to a quantity defined in the body-fixed coordinate system, yet evaluated relative to an inertial observer.

The body-boundary condition for $D_{BO}\varphi/Dt$ follows from taking the time derivative of (A.2) following the motion of the body, i.e.

$$\frac{D_{BO}}{Dt}(\nabla\varphi \cdot \boldsymbol{n}) = \frac{D_{BO}}{Dt}(\boldsymbol{u}_P \cdot \boldsymbol{n}). \tag{A.3}$$

Expanding this, we get

$$\frac{D_{BO}(\nabla\varphi)}{Dt} \cdot \boldsymbol{n} + \nabla\varphi \cdot \frac{D_{BO}\boldsymbol{n}}{Dt} = \frac{D_{BO}\boldsymbol{u}_P}{Dt} \cdot \boldsymbol{n} + \boldsymbol{u}_P \cdot \frac{D_{BO}\boldsymbol{n}}{Dt}. \tag{A.4}$$

It is of key importance to note that while in the inertial reference frame we have $D_{BO}\boldsymbol{n}/Dt = \boldsymbol{\omega} \times \boldsymbol{n}$, it is zero in the body-fixed reference frame. This is because the time derivative of $\boldsymbol{n}$ in the inertial reference frame reflects the time rate of change of the unit axes of the body-fixed reference frame. This is not seen by an observer in the body-fixed reference frame. Hence, the boundary condition, written in the body-fixed reference frame becomes

$$\frac{D_{BO}(\nabla\varphi)}{Dt} \cdot \boldsymbol{n} = \frac{D_{BO}\boldsymbol{u}_P}{Dt} \cdot \boldsymbol{n}. \tag{A.5}$$

It has already been shown in Chapter 2 that the right-hand side of this equation is written $(\ddot{\boldsymbol{R}}_0 + \dot{\boldsymbol{\omega}} \times \boldsymbol{r}) \cdot \boldsymbol{n}$. However, in order to have a Neumann condition for $D_{BO}\varphi/Dt$, we must express the left-hand side as $\nabla(D_{BO}\varphi/Dt) \cdot \boldsymbol{n}$ instead of $D_{BO}(\nabla\varphi)/Dt \cdot \boldsymbol{n}$. This is rigorously proved by Greco (2001) and later by Sun (2007) in the inertial reference frame. In the present work we show this when the problem is solved in the body-fixed reference frame. For an observer in this reference frame, $D_{BO}\varphi/Dt$ thus corresponds to the Eulerian time derivative of φ. The change from $D_{BO}(\nabla\varphi)/Dt$ to $\nabla(D_{BO}\varphi/Dt)$ in the body-fixed reference frame is thus analogue with the change between $\partial(\nabla\varphi)/\partial t$ and $\nabla(\partial\varphi/\partial t)$ for a fixed point in the inertial reference frame. Consequently, the body-boundary condition for $D_{BO}\varphi/Dt$ in the body-fixed reference frame is

$$\nabla\frac{D_{BO}\varphi}{Dt} \cdot \boldsymbol{n} = (\ddot{\boldsymbol{R}}_0 + \dot{\boldsymbol{\omega}} \times \boldsymbol{r}) \cdot \boldsymbol{n}. \tag{A.6}$$

It is emphasized that $\ddot{\boldsymbol{R}}_0$ is the acceleration in the center of gravity observed from the body-fixed reference frame. If we instead let the problem be observed from an inertial, Earth-fixed reference frame, the corresponding boundary condition would be

$$\nabla\frac{D_{BO}\varphi}{Dt} \cdot \boldsymbol{n} = (\ddot{\boldsymbol{R}}_0 - \boldsymbol{\omega} \times \dot{\boldsymbol{R}}_0 + \dot{\boldsymbol{\omega}} \times \boldsymbol{r}) \cdot \boldsymbol{n}. \tag{A.7}$$

This expression is similar to the one given in equation (32) in Bandyk and Beck (2011). In this case, $\ddot{\boldsymbol{R}}_0 = d^2\boldsymbol{R}_0/dt^2$ is the acceleration of the center of gravity in the inertial reference frame. We note that $d^2\boldsymbol{R}_0/dt^2 - \boldsymbol{\omega} \times \dot{\boldsymbol{R}}_0$ coincides with the acceleration of the center of gravity in the body-fixed reference frame, see for this the acceleration terms in the left-hand sides of (2.11) and (2.12) in Chapter 2. Therefore, (A.6) and (A.7) are equivalent. This is confirmed by the consistency between the present results and those from the BEM by Greco (2001) for a floating body in waves, discussed in Chapter 6.

To further elaborate, the boundary condition for the Eulerian time derivative $\partial\varphi/\partial t = \varphi_t$ in the inertial reference can according to equation (18) in Bandyk and Beck (2011) be written as

$$\begin{aligned}\nabla\varphi_t \cdot \boldsymbol{n} = (\ddot{\boldsymbol{R}}_0 + \dot{\boldsymbol{\omega}} \times \boldsymbol{r}) \cdot \boldsymbol{n} + (\boldsymbol{\omega} \times \boldsymbol{n}) \cdot (\dot{\boldsymbol{R}}_0 - \nabla\varphi) \\ - \left[(\dot{\boldsymbol{R}}_0 + \boldsymbol{\omega} \times \boldsymbol{r}) \cdot \nabla(\nabla\varphi)\right] \cdot \boldsymbol{n},\end{aligned} \tag{A.8}$$

where all time derivatives are relative to the inertial reference frame. Clearly, the right-hand side of (A.8) contains 2^{nd} order spatial derivatives of φ. These are not straightforward to evaluate, and may be a source for numerical inaccuracies. By instead formulating the boundary condition for $D_{BO}\varphi/Dt$, either in the body-fixed reference frame as in (A.6) or in the inertial reference frame as in (A.7), this is avoided.

A.2 Special Considerations for HPC Implementation using Overlapping Grids

To prove the derivation of (A.6), we use the numerical expression for the gradient of the velocity potential inside a cell in the HPC method:

$$\nabla\varphi\left(\overline{x},\overline{z}\right) = \sum_{i=1}^{8}\left[\sum_{j=1}^{8} c_{j,i}\nabla f_j\left(\overline{x},\overline{z}\right)\right]\varphi_i. \tag{A.9}$$

$c_{j,i}$ are here coefficients, f_j are harmonic polynomials and φ_i is the velocity potential in node i of the cell. $(\overline{x},\overline{z})$ are the coordinates of a fixed point in the cell in the local cell coordinate system, i.e. they do not change as a function of time. This is also true for the gradient operator ∇, since everything in the equation is resolved along the axes of the body-fixed coordinate system. Taking the time derivative of the right-hand side of (A.9), and noting that none of the terms inside the bracket on the right-hand side depend on time, we get

$$\frac{D_{BO}}{Dt}\left(\sum_{i=1}^{8}\left[\sum_{j=1}^{8} c_{j,i}\nabla f_j\left(\overline{x},\overline{z}\right)\right]\varphi_i\right) = \sum_{i=1}^{8}\left[\sum_{j=1}^{8} c_{j,i}\nabla f_j\left(\overline{x},\overline{z}\right)\right]\frac{D_{BO}\varphi_i}{Dt}. \tag{A.10}$$

Thus, the order change between the gradient operator and time-derivative operator is allowed.

An important consequence is that, while the solution field for φ is consistent between the inertial and body-fixed reference frame, this is not true for the time derivative of φ. While the Eulerian time derivative $\partial\varphi/\partial t$ is solved for in the inertial background grid, $D_{BO}\varphi/Dt$ is solved for in the body-fixed grid. Thus, when numerically coupling the solutions in the different grids, the following relation is applied:

$$\frac{D_{BO}\varphi}{Dt} = \frac{\partial\varphi}{\partial t} + \boldsymbol{u}_P \cdot \nabla\varphi. \tag{A.11}$$

The last term on the right-hand side is easily evaluated once φ is known. Furthermore, $\boldsymbol{u}_P$ is the rigid-body velocity of the body-fixed grid in the point where the two time derivatives are coupled.

An advantage of solving for different time derivatives in the different grids, is that computationally challenging terms in the Neumann condition on the body surface discussed in connection with (A.8) are avoided. The continuity of the solution across the grids with different reference frames is ensured by instead taking the coupling into account through Dirichlet conditions.

Appendix B

Numerical Beaches

If simulations are carried out for a sufficiently long time in a numerical wave tank, waves will be reflected from the tank walls. Other than in special applications, such as comparing simulations with experimental data without wave-damping devices, this is highly undesirable. In order to avoid influence from reflected waves, the wave tank would accordingly need to be very long, which leads to excessive computational time. As an alternative, numerical beaches or damping zones are used as effective means to prevent that waves are reflected from tank walls. This allows for long-time simulations without unreasonably long computational domains. The term numerical beach is used as an analogy to the damping beaches often used for the same purpose in laboratory experiments.

The theory of the numerical beaches applied in the present work is outlined in the following. Two types of beaches are illustrated by Figure B.1. One is referred to as *upwave*, and is located next to the wavemaker. The purpose of the upwave beach is to dissipate waves reflected from and radiated by a surface-piercing body, which otherwise will reach the wavemaker and from thereon reflect back into the tank. This is mainly an issue in 2D simulations, since the reflected and radiated waves in 3D will decay moving away from the body. The other beach is located next to the tank wall on the opposite side of the wavemaker, and is thus referred to as *downwave*.

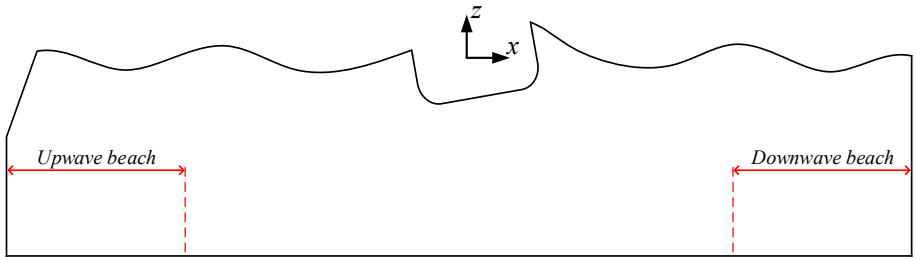

Figure B.1: Numerical wave tank with upwave and downwave damping zones.

B.1 Theory

Inside a numerical damping zone, damping terms are added to the dynamic and kinematic free-surface conditions. The fully Lagrangian dynamic and kinematic free-surface conditions including damping terms are written in an inertial, Earth-fixed Oxz coordinate system as

$$\frac{D\varphi}{Dt} = \frac{1}{2}|\nabla\varphi|^2 - gz - \nu(x,t)(\varphi - \varphi_{ref}), \tag{B.1}$$

$$\frac{D\boldsymbol{x}}{Dt} = \nabla\varphi - \nu(x,t)(\boldsymbol{x}\cdot\boldsymbol{k} - \zeta_{ref}), \tag{B.2}$$

where $\boldsymbol{x} = (x, z)$ and φ are the position of and velocity potential in a fluid particle on the free surface $z = \zeta(x)$, respectively. φ_{ref} and ζ_{ref} are reference values for the velocity potential and free-surface elevation. g is the acceleration of gravity, $\boldsymbol{k}$ is the unit vector in z direction and $\nu(x,t)$ is the damping coefficient associated with the numerical beach. This is defined as $\nu(x,t) = \nu(x)\delta(t_0)$, where $\delta(t_0)$ is a step function which is zero for $t \leq t_0$ and 1 for $t > t_0$. t_0 is the time when the beach is activated, and has a non-zero value only for the upwave beach in order to ensure that the transient waves associated with start up of the wavemaker are not affected.

$\nu(x)$ is taken from Greco (2001) and is defined as

$$\nu(x) = \begin{cases} 0 & x \leq x_0 \\ \nu_{max}(-2\xi^3 + 3\xi^2) & x_0 < x \leq x_1 \text{ (downwave)} \\ \nu_{max}(1 + 2\xi^3 - 3\xi^2) & x_0 < x \leq x_1 \text{ (upwave)} \\ \nu_{max} & x > x_1, \end{cases} \tag{B.3}$$

where ν_{max} is an empirically chosen coefficient. x_0 and x_1 are the start and end-point of the beach as illustrated in Figure B.2. ξ is an auxiliary normalized coordinate defined as

$$\xi = \frac{x - x_0}{L_{beach}}, \tag{B.4}$$

where $L_{beach} = x_1 - x_0$ is the length of the beach. As a general guidance L_{beach} can be taken as two times the characteristic wavelength. There is a close relation between ν_{max} and L_{beach}: If L_{beach} is too short, ν_{max} has to be set to a high value in order to dissipate the waves. However, a high ν_{max} may lead to wave reflections from the beach itself. Reasonable values for ν_{max} is generally found to be in the range $2 - 4\ s^{-1}$.

It can be noted that the direction of the coordinate ξ for the upwave beach differs from the formulation by Greco (2001). However, since also $\nu(x)$ in (B.3) is formulated differently for the upwave beach, it can be shown that the two formulations indeed are equivalent.

The damping terms in (B.1) and (B.2) are similar also when the free-surface conditions are not stated in the Lagrangian form. They remain unchanged also when the problem is formulated in a body-fixed reference frame, i.e. x would still be defined in the inertial reference frame.

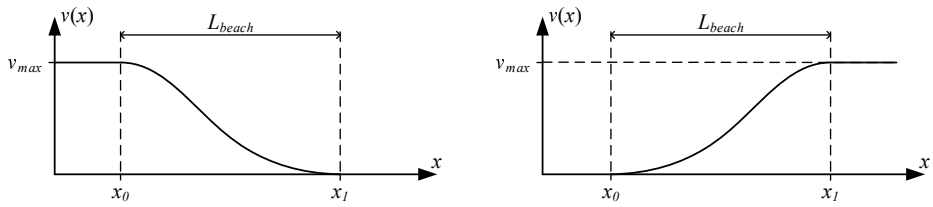

(a) Upwave beach (b) Downwave beach

Figure B.2: Damping coefficients for numerical beaches as a function of the auxiliary coordinate ξ.

B.1.1 Choosing Reference Solutions

The reference values φ_{ref} and ζ_{ref} in (B.1) and (B.2) require some additional attention. Their purpose is to ensure that only the desired parts $\varphi - \varphi_{ref}$ and $z - \zeta_{ref}$ of the wave are dissipated. For the downwave beach, the entire wave should be damped, i.e. $\varphi_{ref} = \zeta_{ref} = 0$. On the upwave side, however, only the wave component propagating towards the wavemaker should be operated on by the beach. φ_{ref} and ζ_{ref} should consequently represent the incident wave generated by the wavemaker. In the following we will for simplicity use the term reflected waves for all waves propagating in opposite direction of the incident wave.

There are several possibilities to obtain φ_{ref} and ζ_{ref} or to directly identify the reflected waves, for instance

1. performing a simulation without a body in the tank, taking the velocity potential and free-surface elevation measured in the region of the beach as reference solution
2. using some analytical wave theory to describe the incident waves
3. using control algorithms to identify the reflected waves and modify the signal of the wavemaker to counteract them.

While the first option above can be considered the most accurate, it is impractical because it involves a significant increase in computational cost. The last option listed requires knowledge of control theory and is outside the scope of the present work. The second option is thus pursued in the present work.

Several non-linear wave theories exist that can be used to describe incident waves generated by the wavemaker, such as Stokes 2^{nd} or 5^{th} order theory or stream function theory. Most of the available non-linear theories are however restricted to regular waves. In the present work the reference solution has thus been obtained from linear wavemaker theory, which is particularly attractive because it describes both regular and irregular waves in a straightforward manner. This is similar to the approach by Tanizawa et al. (1999), with the exception that we here also include standing wave modes close to the wavemaker.

B.1.2 Linear Wavemaker Theory

The linear wavemaker theory described below is taken from Dean and Dalrymple (1991), but is modified due to a difference in the definition of normal vectors and to allow for a flap wavemaker hinged at an arbitrary water depth. We define an inertial, Earth-fixed coordinate system Oxz with origin in the nominal position of the wavemaker and in the still water level as shown in Figure B.3.

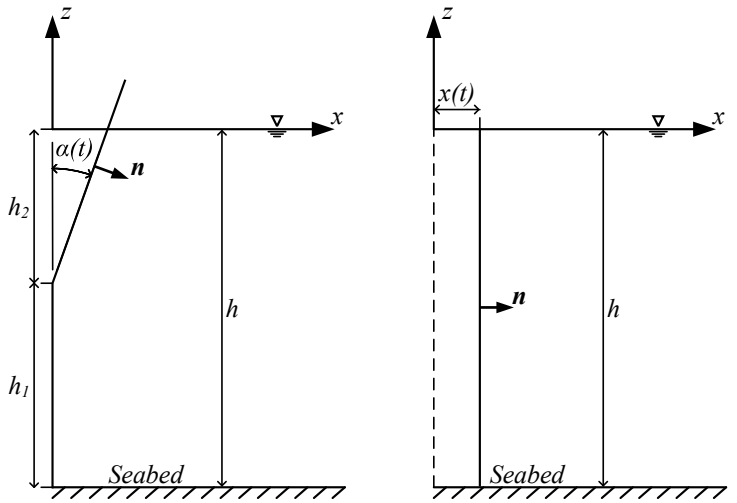

(a) Flap wavemaker (b) Piston wavemaker

Figure B.3: Flap and piston type wavemakers.

The velocity potential for the wave generated by the wavemaker is represented as

$$\varphi(x,z,t) = A_p \cosh[k(h+z)] \sin(kx - \omega t + \theta) + \sum_{n=1}^{\infty} C_n e^{-k_s(n)x} \cos[k_s(n)(h+z)] \cos(\omega t + \theta), \tag{B.5}$$

where the first part is associated with the propagating wave and the second part is associated with standing waves. h is here the water depth, ω and k are the wave frequency and wave number of the propagating wave, $k_s(n)$ is the wave number associated with the n^{th} standing mode and θ is a phase angle. The standing waves decay fast as a function of the distance from the wavemaker, and it is thus sufficient to truncate the summation to only include a few (e.g. 5) terms. The wave number k is found from the linear dispersion relation,

$$\omega^2 = gk \tanh(kh), \tag{B.6}$$

while $k_s(n)$ is found from the following expression:

$$\omega^2 = -gk_s(n) \tan(k_s(n)h). \tag{B.7}$$

(B.7) has an infinite number of solutions, each giving a different $k_s(n)$. However, as already stated, we here restrict ourself to consider a limited number of standing wave modes. The amplitudes A_p and C_n associated with the propagating wave and the standing wave modes are given as

$$A_p = \frac{1}{2}\frac{\int_{-h}^{0} S(z)\omega\cosh[k(h+z)]dz}{k\int_{-h}^{0}\cosh^2[k(h+z)]dz}, \tag{B.8}$$

$$C_n = -\frac{1}{2}\frac{\int_{-h}^{0} S(z)\omega\cos[k_s(n)(h+z)]dz}{k_s(n)\int_{-h}^{0}\cos^2[k_s(n)(h+z)]dz}. \tag{B.9}$$

The function $S(z)$ describes the wavemaker stroke, and depends on the type of wavemaker. For a piston type wavemaker, the instantaneous position of the flap is defined as $x(t) = x_a\sin(\omega t+\theta)$ where x_a is the piston displacement amplitude. Then angular displacement of a flap type wavemaker is defined as $\alpha(t) = \alpha_a\sin(\omega t+\theta)$, where α_a is the flap angular displacement amplitude. With reference to Figure B.3, $S(z)$ is then defined as

$$S(z) = \begin{cases} 2x_a & \text{(piston wavemaker)} \\ 2h_2\tan(\alpha_a)(1+\dfrac{z}{h_2}) & z \geq -h_1 \\ 0 & z < -h_1. \end{cases} \quad \text{(flap wavemaker)} \tag{B.10}$$

The reference value φ_{ref} for the upwave numerical beach is determined by evaluating (B.5) at the linearised free-surface position $z = 0$, while the free-surface elevation $\zeta_{ref} = \zeta$ is found from the linearised dynamic free-surface condition:

$$\begin{aligned}\varphi_{ref}(x,t) = {} & A_p\cosh(kh)\sin(kx-\omega t+\theta)+ \\ & \sum_{n=1}^{\infty} C_n e^{-k_s(n)x}\cos(k_s(n)h)\cos(\omega t+\theta),\end{aligned} \tag{B.11}$$

$$\begin{aligned}\zeta_{ref}(x,t) = {} & \frac{\omega A_p}{g}\cosh(kh)\cos(kx-\omega t+\theta)+ \\ & \frac{\omega}{g}\sum_{n=1}^{\infty} C_n e^{-k_s(n)x}\cos(k_s(n)h)\sin(\omega t+\theta).\end{aligned} \tag{B.12}$$

In the case of irregular waves, solutions for each individual wave component applying the above equations are linearly superimposed.

B.2 Numerical Examples for Performance of Upwave Beach

In order to study wave-body interactions in a numerical wave tank applying an upwave numerical beach, it is crucial that the beach effectively dissipates waves reflected from the body without modifying the incident wave. Indeed, one may question the application of the reference solution based on linear wavemaker theory. A verification study is therefore performed, in which waves are generated

with a flap type wavemaker in a numerical wave tank without a body. We focus on the wave elevation measured in the two wave probes illustrated in Figure B.4, one located inside the upwave numerical beach and one in the middle of the tank.

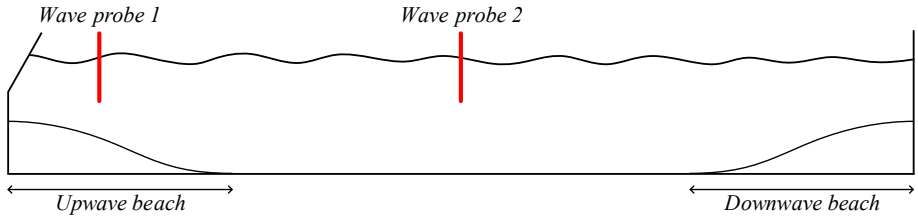

Figure B.4: Sketch of numerical wave tank with flap type wavemaker used in verification study.

Simulations are carried out for both regular and irregular waves with low and high steepness. Each case is performed with a downwave beach, with an upwave beach and with both a downwave and an upwave beach. The simulations are carried out long enough for the waves to be reflected several times across the tank. A temporal ramp function is applied to the wavemaker motion for $0 \leq t \leq t_{ramp}$ in order to prevent numerical instabilities due to impulsive waves. t_0 in (B.1) and (B.2) is chosen accordingly to allow the initial transient waves due to this to pass by the numerical beach before the beach is activated. In doing so, one must take into consideration the length of the beach and the phase speed of the propagating waves. For irregular waves, the choice should be based on the shortest harmonic wave component, i.e. the wave component with the lowest phase speed.

An overview of the simulation cases, both for regular and irregular waves, is given in Table B.1, where $k\zeta_A$ is the wave steepness, L is the tank length, λ is the wavelength and c is the phase speed. For the irregular waves, the information is listed for each of the three harmonic components that the wavemaker signal is composed of. The length of the wave tank is set to $8\lambda_{char}$, where λ_{char} is the characteristic wave length which is taken as λ for the regular wave cases and as the wave length of the longest wave component in the irregular wave cases. The length of all beaches is set equal to $2\lambda_{char}$ and with $\nu_{max} = 2.5\ s^{-1}$. Only the sloped part of the beach is included, i.e. the part between x_0 and x_1 in Figure B.2. The quantities L/c and L_{beach}/c indicate how long time the wave will use to propagate across the length of the tank and across the beach, respectively. Transient waves generated during start up of the wavemaker may however propagate with a different velocity.

Selected results for the cases in Table B.1 are discussed below. The main focus is to ensure that the upwave beach is able to successfully dissipate reflected waves, and that it does not significantly change the propagating wave away from the wavemaker. The two wave probes shown in Figure B.4 are considered. These are located approximately $1.1\lambda_{char}$ and $4.0\lambda_{char}$ away from the wavemaker.

Table B.1: Simulation cases for assessment of the performance of upwave beaches.

Case	$k\zeta_A$ $(-)$	L_{beach}/λ $(-)$	L/c (s)	L_{beach}/c (s)	t_{ramp} (s)	t_0 (s)
Reg low	0.04	2.00	6.00	1.50	2.25	4.25
Reg high	0.29					
	0.04	3.21	9.63	2.41	2.85	6.05
Irr low	0.03	2.50	8.49	2.12		
	0.02	2.00	7.60	1.90		
	0.22	3.21	9.63	2.41		
Irr high	0.08	2.50	8.49	2.12		
	0.04	2.00	7.60	1.90		

B.2.1 Regular Waves

Figure B.5 shows the results for regular waves with a downwave beach compared with the results obtained with both an upwave and downwave beach. Since waves are dissipated by the downwave beach in both cases, no waves are reflected from the downwave tank wall. We can therefore assess how the upwave beach affects the propagating wave. The black vertical line indicates the time it takes for the propagating wave starting from the wavemaker at t_0 to arrive at the position of the wave probe assuming that it propagates with the linear phase speed c. With low steepness, the wave is essentially unaffected by the upwave beach in both wave probes. This is as expected, since a wave with such low steepness is close to linear. For the higher steepness, it is clear that the wave is modified in the probe located in the middle of the upwave beach when this is activated. For the probe located in the middle of the tank, however, the waves generated with and without the upwave beach are in close agreement when steady state is settled after approximately $9s$. This means that the propagating wave has regained its nonlinear properties away from the upwave beach, even though a linear wavemaker-theory solution is enforced close to the wavemaker. This clearly indicates that the upwave beach can be applied in simulations with relatively steep regular waves with a body in the tank, as long as this is placed some distance away from the wavemaker. Typically, the position of the body will be close to the middle of the tank.

Next we focus on the upwave beach's ability to dissipate reflected waves. In Figure B.6 results for the regular wave with low steepness are shown with a downwave and upwave beach at two probes inside the upwave beach. In addition to probe 1, probe 0, which is not shown in Figure B.1, is located approximately $0.15L_{beach}$ away from the wavemaker. The red vertical line indicates the time when the wave is reflected from the downwave tank wall to the wavemaker and back to the position of the probe if a downwave beach is not present. While the results for probe 1 eventually show some discrepancies as a result of reflection from the downwave tank wall, they remain in close agreement in probe 0. This indicates that the upwave beach fully dissipates the reflected wave close to the wavemaker, leaving only the incident wave. The beach thus works as intended.

One should note that the wave in the simulation without a downwave beach is fully reflected from the tank wall. This is obviously not always the case in simulations with a body in the tank.

B.2.2 Irregular Waves

Figure B.7 shows the results for irregular waves with a downwave beach compared with the results obtained with both an upwave and downwave beach. The vertical lines here indicate arrival times for the fastest travelling wave component in the irregular wave train estimated from its phase speed. As for the regular waves, the waves are insignificantly modified by the upwave beach when the wave steepness is small. With the higher steepness, the waves measured in the probe inside the upwave beach are modified when the beach is activated. The difference is clearly dependent on the instantaneous wave steepness in the location of the probe, i.e. how well the instantaneous wave is described by linear theory. For the probe in the middle of the tank, larger differences are observed for the case of irregular waves than for regular waves. Based on the results in probe 1, this is likely because the upwave beach introduces some dispersion effects. Still, the largest crests and smallest troughs are deemed to be in acceptable agreement.

B.2.3 Discussion

The results in Figures B.5 - B.7 show that, even though the upwave beach uses linear wavemaker theory as a reference solution, it is successful in dissipating reflected waves without significantly affecting the incident wave towards the middle of the tank. For regular waves, this holds true for waves with both low and high steepness. For irregular waves, it is seen that the upwave beach may slightly modify the incident waves in the middle of the tank if the wave steepness is high. Thus, in case an upwave beach is used in simulations with steep irregular waves, it is considered good practice to verify that the generated waves behave as intended at the location of interest on a case to case basis. Depending on the problem definition, this may involve comparisons similar to Figure B.7, deriving wave- and wave-group spectra, or deriving the crest distribution function.

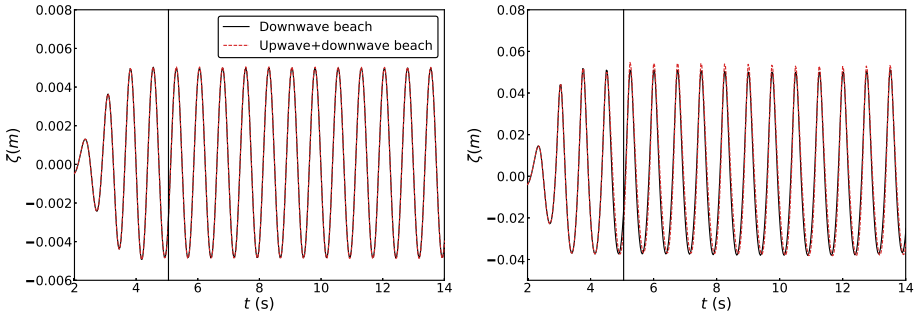

(a) Probe 1 (low steepness)

(b) Probe 1 (high steepness)

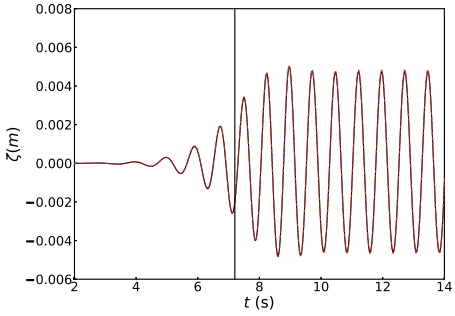

(c) Probe 2 (low steepness)

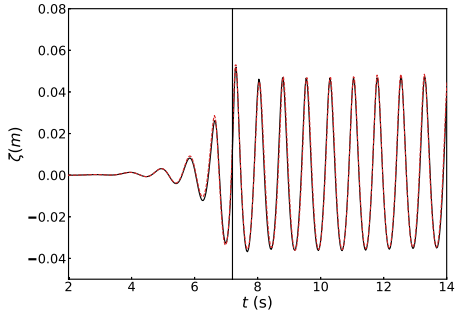

(d) Probe 2 (high steepness)

Figure B.5: Time series of wave elevation in probes 1 and 2 for regular waves with low and high steepness.

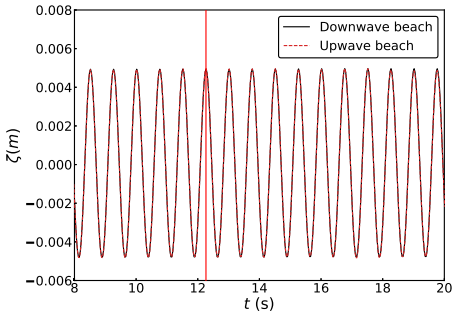

(a) Probe 0 (low steepness)

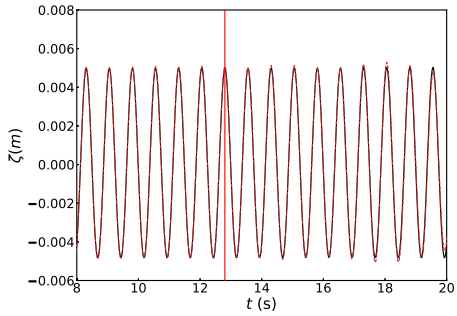

(b) Probe 1 (low steepness)

Figure B.6: Time series of wave elevation in probes 0 and 1 for regular waves with low steepness.

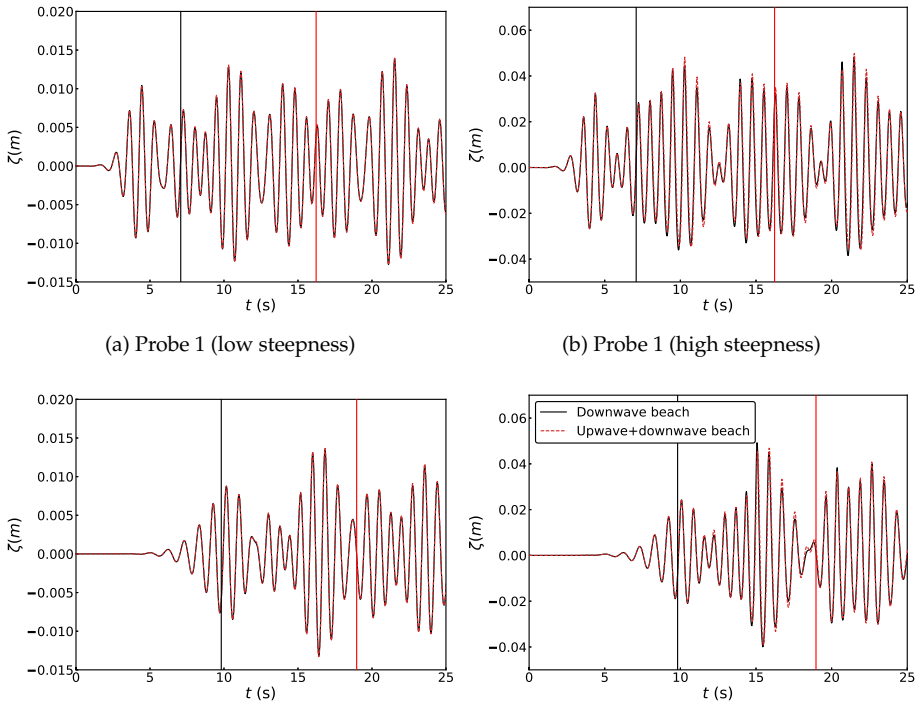

(a) Probe 1 (low steepness)

(b) Probe 1 (high steepness)

(c) Probe 2 (low steepness)

(d) Probe 2 (high steepness)

Figure B.7: Time series of wave elevation in probes 1 and 2 in for irregular waves with low and high steepness.

Appendix C

Wave Drift Force from Conservation of Fluid Momentum

Within potential-flow theory, the mean wave drift forces on a body can be obtained by conservation of fluid momentum in a closed control volume (3D), or closed control surface (2D), surrounding the body. Different methods to determine the mean horizontal wave drift forces are discussed here. One is an exact formulation, where no assumptions regarding the order of the problem are made. The others are 2^{nd} order approximations with and without assuming conservation of fluid energy.

C.1 Exact Method

Following Faltinsen and Timokha (2009), the fluid momentum $\boldsymbol{M}(t)$ inside a control volume $Q(t)$ bounded by a closed control surface $S_{Q(t)}$ is written as

$$\boldsymbol{M}(t) = \int_{Q(t)} \rho \boldsymbol{u} dQ, \tag{C.1}$$

where $\boldsymbol{u} = \nabla\varphi$ is the fluid velocity vector. The problem is formulated in an inertial, Earth-fixed coordinate system. Since we here operate in the xz plane, we can imagine that the control volume has unit length in the y direction, and that all variables are uniform along this axis. With this, the integral in y dimension can be omitted. We define $Q(t)$ bounded by $S_{Q(t)}$ in Figure C.1 so that it surrounds the body at its initial position, and located so that the body never intersects $S_{Q(t)}$ during the simulation. The normal vectors $\boldsymbol{n}$ on $S_{Q(t)}$ are defined pointing out from $Q(t)$. $S_{Q(t)}$ is separated into vertical control sides $S_{1,2}$ extending up to the instantaneous free surface ζ, a flat bottom S_0, the instantaneous wetted body surface S_B and the instantaneous free surface $S_{\zeta\pm}$ on either side of the body.

By using Reynolds transport theorem, the definition of the Euler equations and the generalized Gauss theorem, the time derivative of the volume integral in (C.1) can be rewritten as a surface integral over $S_{Q(t)}$:

$$\frac{d\boldsymbol{M}(t)}{dt} = -\int_{S_Q} p\boldsymbol{n} dS - \rho g \int_{S_Q} z\boldsymbol{n} dS - \rho \int_{S_Q} \boldsymbol{u}(u_n - U_{sn}) dS. \tag{C.2}$$

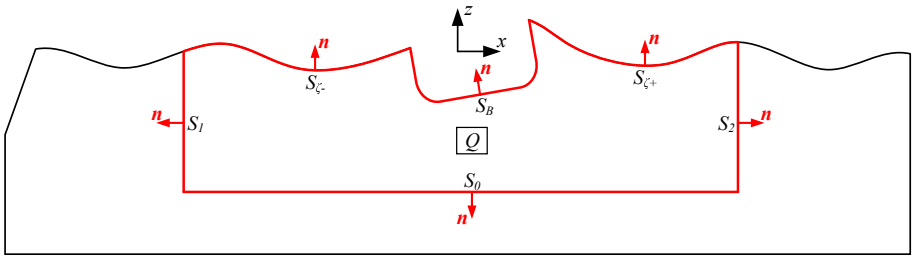

Figure C.1: Control volume $Q(t)$ for evaluation of fluid momentum bounded by control surface $S_Q(t) = S_{0,1,2} + S_B + S_{\zeta\pm}$.

Here, p is the fluid pressure relative to the atmospheric pressure as defined by the Bernoulli equation, $u_n = \nabla\varphi \cdot \boldsymbol{n}$ is the local normal component of the fluid velocity on the surface $S_{Q(t)}$ and U_{sn} is the local normal velocity of the surface $S_{Q(t)}$ itself.

For convenience, we define S_0 to coincide with the seabed. As a consequence, we have that $u_n = U_{sn} = 0$ on S_0. On the vertical sides $S_{1,2}$, we have that $U_{sn} = 0$ since their x positions are fixed. Due to the dynamic and kinematic free surface conditions we have that $p = 0$ and $u_n = U_{sn}$ on $S_{\zeta\pm}$, and on S_B it follows from the body-boundary condition that $u_n = U_{sn}$. With this, (C.2) can be written as

$$\frac{d\boldsymbol{M}(t)}{dt} = -\int_{S_B} p\boldsymbol{n}dS - \int_{S_{0,1,2}} p\boldsymbol{n}dS - \rho g \int_{S_Q} z\boldsymbol{n}dS - \rho \int_{S_{1,2}} u_n \boldsymbol{u}dS. \tag{C.3}$$

The first term on the right hand side of (C.3) is recognized as the fluid force $\boldsymbol{F}(t)$ on the body, hence

$$\boldsymbol{F}(t) = -\frac{d\boldsymbol{M}(t)}{dt} - \int_{S_{0,1,2}} p\boldsymbol{n}dS - \rho g \int_{S_Q} z\boldsymbol{n}dS - \rho \int_{S_{1,2}} u_n \boldsymbol{u}dS. \tag{C.4}$$

In regular waves and under steady-state conditions, the average momentum flux over n periods T of oscillation is zero,

$$\overline{\frac{d\boldsymbol{M}(t)}{dt}} = \frac{1}{nT}\int_{t_0}^{t_0+nT} \frac{d\boldsymbol{M}(t)}{dt}dt = 0, \tag{C.5}$$

where t_0 is some time instant when steady-state conditions have been achieved and $n \geq 1$. Using (C.5), and noting that the third term in the right hand side of (C.4) only gives a contribution in vertical direction, the mean wave force in x direction can be expressed as

$$\overline{F_x} = -\overline{\int_{S_{1,2}} pn_x dS} - \rho\overline{\int_{S_{1,2}} u_n \varphi_x dS}. \tag{C.6}$$

n_x and φ_x are here the x components of $\boldsymbol{n}$ and $\nabla\varphi$, respectively, and the overbar denotes time averaging over n periods of oscillation. In a non-linear simulation, the integrals in the right-hand side of (C.6) must be evaluated at each time step

and stored as a time series. The time averaging is performed as post-processing after the simulation is completed. It is emphasized that the integrals over $S_{1,2}$ must be evaluated up to the instantaneous free surface ζ without any approximation. After the simulation is completed, the time average is taken over an appropriate steady-state time window $t_0 \leq t < t_0 + nT$ in the same way as when the mean wave drift force is obtained from direct pressure integration. In the present work we typically use $n \geq 5$ in (C.6), and the resulting mean wave drift force is denoted as *exact*.

C.2 2^{nd} Order Approximate Method

The same type of analysis that gives the mean wave drift force in (C.6) can be performed within the framework of perturbation theory. By assuming incident regular waves, and that the floating body oscillates in steady-state conditions around a mean position, the problem is truncated so that effects up to 2^{nd} order are included. The mean wave drift force in x direction can then be written as

$$F_x^{(0)} = \frac{1}{4}\rho g(\zeta_A^2 + \zeta_R^2 - \zeta_T^2)\left[1 + \frac{2kh}{sinh2kh}\right], \tag{C.7}$$

see e.g. Faltinsen (1993). The second term inside the brackets represents a correction for finite water depth. ζ_A, ζ_R and ζ_T are amplitudes of the incident, reflected and transmitted wave, respectively, k is the wave number and h is the water depth. The mean wave drift force obtained from (C.7) is referred to as 2^{nd} *order* in the present work.

By in addition assuming that the average work done by the body over one period of oscillation is zero, (C.7) can be expressed as

$$F_x^{(0)} = \frac{1}{2}\rho g\zeta_A^2(1 - C_T^2)\left[1 + \frac{2kh}{sinh2kh}\right], \tag{C.8}$$

where C_T is the wave transmission coefficient defined as ζ_T/ζ_A. (C.8) is a version of the well-known Maruo's formula, where the finite-water depth correction was derived by Longuet-Higgins (1977). Maruo's formula was published in 1960 (Maruo, 1960), and has since been extensively applied. One may speculate that much of the popularity gained by the formula is due to its elegance and simplicity. The mean wave drift force obtained from (C.8) is denoted *Maruo* in the present work.

Maruo's formula can also be written by means of ζ_R, but the form in (C.8) is more convenient for post-processing of results from a time domain analysis, since it may be difficult to separate the incident and reflected wave amplitudes.

It is emphasized that the assumptions made in deriving Maruo's formula are the same as in linear theory, i.e. that non-linear parameters such as the wave amplitude and body motions are small parameters that can be approximated by truncated series around their mean values. The squared wave amplitudes involved in the formula are therefore connected with linear incident waves and linear wave-body interactions.

Appendix D

Conservation of Fluid Properties

The framework used to evaluate fluid energy and fluid volume in a non-linear numerical wave tank is outlined in the following. It is noted that the derivations assume a general 3D scenario, even though the present work solely addresses 2D analysis. One should therefore read this appendix as if the problem is defined with unit length and uniform properties in y direction.

D.1 Fluid Energy

With reference to Figure D.1, the fluid energy inside the control volume $Q(t)$ and the energy flux across control surfaces $S_{Q(t)}$ are evaluated.

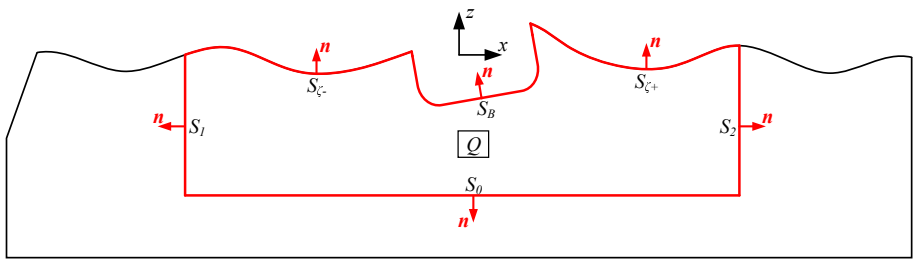

Figure D.1: Control volume $Q(t)$ for evaluation of fluid properties bounded by control surface $S_Q(t) = S_{0,1,2} + S_B + S_{\zeta\pm}$.

The total kinetic and potential fluid energy $E(t)$ inside $Q(t)$ is

$$E(t) = \rho \int_{Q(t)} \left[gz + \frac{1}{2} \nabla\varphi \cdot \nabla\varphi \right] dQ, \tag{D.1}$$

in which ρ is the fluid density, g is the acceleration of gravity and φ is the velocity potential. It is however impractical to evaluate the gradient of the velocity potential anywhere inside $Q(t)$. The expression (D.1) is therefore transformed into a

surface integral over $S_Q(t)$,

$$E(t) = \rho \int_{S_{Q(t)}} \left[\frac{1}{2} g z^2 \boldsymbol{n} \cdot \boldsymbol{k} + \frac{1}{2} \varphi \nabla \varphi \cdot \boldsymbol{n} \right] dS, \tag{D.2}$$

where $\boldsymbol{k}$ is the unit vector in z-direction and $\boldsymbol{n}$ is the normal vector defined in Figure D.1.

Starting from (D.1) and using the Reynolds transport theorem, the energy flux across $S_{Q(t)}$ can be written as

$$\dot{E}(t) = \frac{dE(t)}{dt} = \int_{S_{Q(t)}} \left[\rho \frac{\partial \varphi}{\partial t} (u_n - U_{sn}) - p U_{sn} \right] dS, \tag{D.3}$$

where $u_n = \nabla \varphi \cdot \boldsymbol{n}$, p is the fluid pressure given by the Bernoulli equation and U_{sn} is the normal velocity of the boundary itself. Details of the derivation are given by Faltinsen and Timokha (2009). We let S_0 coincide with the seabed, so that on this boundary $u_n = U_{sn} = 0$. On $S_{\zeta\pm}$ we have that $u_n = U_{sn}$ and $p = 0$ due to the kinematic and dynamic free-surface conditions, respectively, and on S_B we have $u_n = U_{sn}$ due to the body-boundary condition. $U_{sn} = 0$ on the vertical side walls $S_{1,2}$. (D.3) then reduces to

$$\dot{E}(t) = \rho \int_{S_{1,2}} \frac{\partial \varphi}{\partial t} u_n dS - \int_{S_B} p u_n dS. \tag{D.4}$$

The last term in (D.4) can be recognized as the work done by the body on the water.

(D.2) and (D.4) are evaluated at every time step of the simulation for the instantaneous computational domain $S_{Q(t)}$.

In evaluating the results of (D.2), we define a quantity

$$E_{m0} = \frac{1}{nT} \int_{t_0}^{t_0 + nT} E(t) dt, \tag{D.5}$$

where T is the wave period, $t = t_0$ is a time instant when steady-state behaviour is obtained and $n \geq 1$ is an integer. Furthermore, we define the running-average energy

$$E_m(t) = \frac{1}{T} \int_{t-T}^{t} E(t) dt, \tag{D.6}$$

which can be calculated for $t \geq T$. The relative change of fluid energy inside $Q(t)$ can then be assessed through the parameter

$$\epsilon_E(t) = \frac{E_m(t) - E_{m0}}{E_{m0}}. \tag{D.7}$$

The energy flux (D.4) is assessed relative to the wave power P_w in a linear, propagating wave,

$$\epsilon_{\dot{E}}(t) = \frac{\dot{E}_m(t)}{P_w}, \tag{D.8}$$

where $\dot{E}_m(t)$ is a running average of the energy flux similar to expression (D.6). P_w is defined by Faltinsen and Timokha (2009) as

$$P_w = \frac{1}{4}\rho g^2 \frac{\zeta_a^2}{\omega}, \tag{D.9}$$

in which ζ_a is the incident wave amplitude and ω is the angular wave frequency. Note that these definitions imply that both ϵ_E and $\epsilon_{\dot{E}}$ are time-dependent parameters.

D.2 Fluid Volume

Conservation of fluid volume is assessed by the integral of the free-surface elevation $\zeta(t)$. The relative error of the fluid volume is defined through the parameter

$$\epsilon_V(t) = \frac{V_m(t)}{V_0}. \tag{D.10}$$

V_0 is the approximate initial fluid volume in the tank, given as the product between the tank length L and the water depth h, while $V_m(t)$ is the running average, defined in a similar way as in expression (D.6), of the integrated wave elevation $V(t)$ in the tank:

$$V(t) = \int_L \zeta(x,t)dx. \tag{D.11}$$

$V(t)$ represents the change in volume due to the wave elevation, meaning that $V(t) = 0$ when no waves are present. In comparison, the total volume at any given time instant is expressed as $V_0 + V(t)$. $V_m(t)$ is thus connected with the mean change of volume due to waves, equal to zero if the volume is fully conserved.

D.3 Numerical Examples for Ship Section in Beam-Sea Waves

Examples of how fluid properties are conserved for the 2D ship section in beam-sea waves analysed in Chapter 5 and 6 are here given. The influence of wave steepness and large body motions is emphasised.

Three non-dimensional wave frequencies $\xi_B = (0.5, 1.0, 2.0)$ are considered for wave heights $H = 2\zeta_a = (1cm, 7cm)$, where ξ_B is defined in Chapter 5. The case $\xi_B = 2.0$, $H = 7cm$ has a wave steepness $k\zeta_a = 0.28$, which implies significant wave non-linearity. $\xi_B = 0.5$ is close to the natural heave and pitch frequency of the body, which implies large motions when the body is freely floating.

Results for a fixed and a freely floating body are plotted side by side in Figures D.2 - D.4. $\epsilon_{\dot{E}}(t)$ is seen to oscillate around a mean value close to zero towards the end of the time series, with amplitudes that do not change significantly with either wave height nor wave frequency in the case of a fixed body. For the freely floating body, the oscillation amplitudes of the energy flux are larger, which can be explained by the fact that the body exerts work on the fluid when allowed to oscillate. Indeed, the amplitudes are largest close to the motion resonance frequencies. The mean value of $\epsilon_{\dot{E}}(t)$ over the last two oscillation periods examined

in the figures are listed in Table D.1. The mean energy flux relative to the wave power is seen to be relatively insensitive to both wave height and frequency for the fixed body. For the freely floating body, the mean values decrease away from the natural motion frequencies, but do not show strong dependency on the wave height except for at $\xi_B = 0.5$.

Table D.1: Mean value of $\epsilon_{\dot{E}}(t)$ over last two wave periods.

ξ_B	Fixed body		Floating body		
	$H = 1\ cm$	$H = 7\ cm$	$H = 1\ cm$	$H = 3\ cm$	$H = 7\ cm$
0.5	3.56E-03	5.03E-03	4.38E-02	1.73E-01	1.34E-01
1.0	7.50E-03	9.03E-03	1.54E-02	1.95E-02	2.57E-02
2.0	5.05E-03	-1.81E-02	1.91E-02	1.55E-02	-1.48E-03

$\epsilon_E(t)$ also oscillates around close to zero in the last part of the time series, but the oscillation amplitudes increase with wave height. The order of magnitude of $\epsilon_E(t)$ is comparable for the fixed and freely floating body. The same can be said for $\epsilon_V(t)$, other than for at $\xi_B = 0.5$ where values are higher for the freely floating body. The mean value of $\epsilon_V(t)$ is seen to always be less than $1.5 \cdot 10^{-4}$ towards the end of the time series, which is deemed acceptable considering that the largest wave with highest frequency has significant non-linear characteristics.

One should be aware that the notable shifts that can be seen in all of the evaluated properties at $t/T \approx 10$, in particular for steep waves, are correlated with the time the numerical beach next to the wavemaker has been activated. As discussed in Appendix B, this enforces a linear free-surface elevation in a confined region close to the wavemaker, which is why the influence is more evident when wave non-linearity increases.

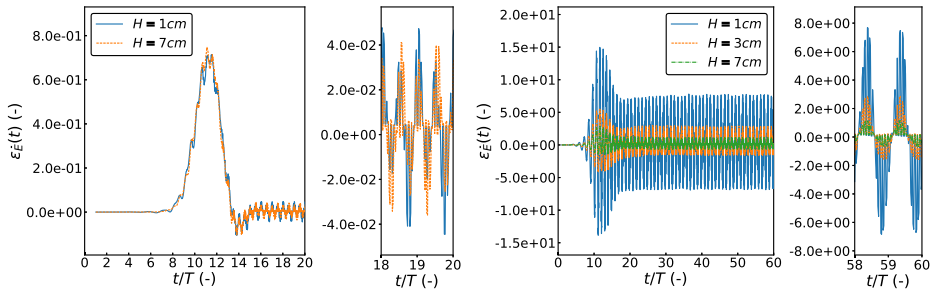

(a) $\epsilon_{\dot{E}}(t)$, fixed body

(b) $\epsilon_{\dot{E}}(t)$, floating body

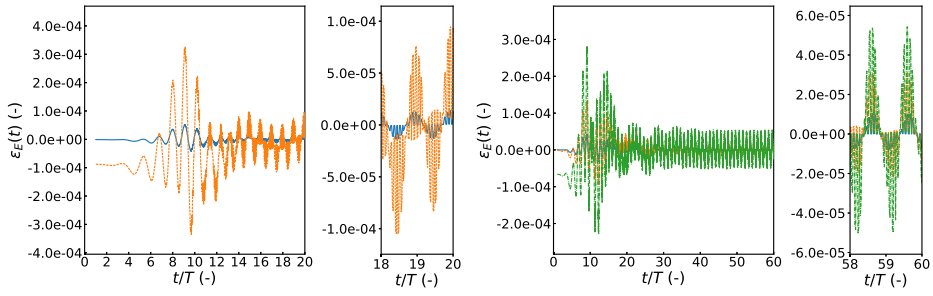

(c) $\epsilon_E(t)$, fixed body

(d) $\epsilon_E(t)$, floating body

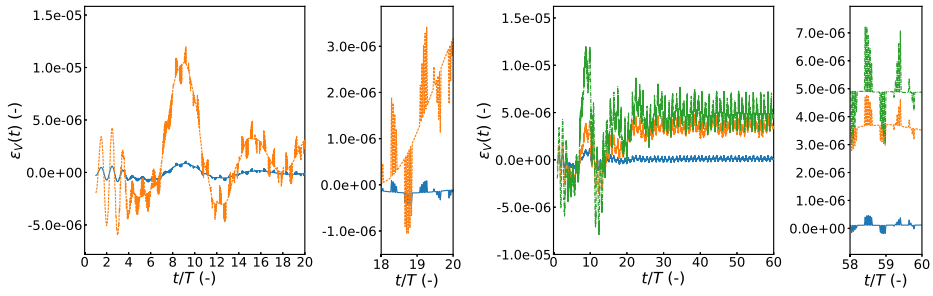

(e) $\epsilon_V(t)$, fixed body

(f) $\epsilon_V(t)$, floating body

Figure D.2: Conservation of fluid properties, fixed and freely floating body with non-dimensional wave frequency $\xi_B = 0.5$.

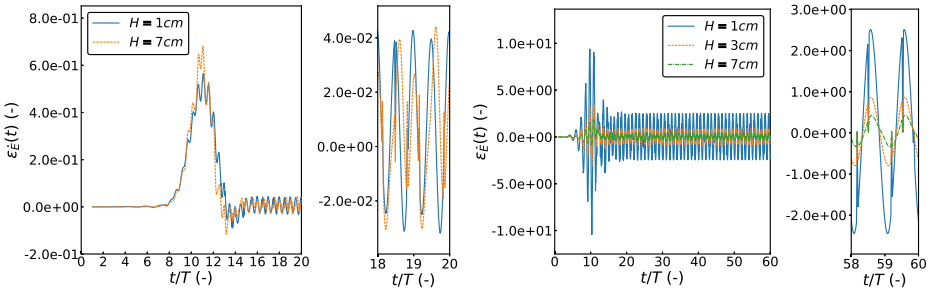

(a) $\epsilon_{\dot{E}}(t)$, fixed body

(b) $\epsilon_{\dot{E}}(t)$, floating body

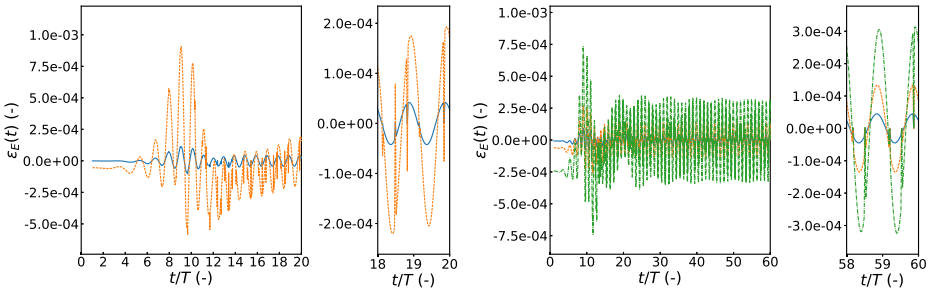

(c) $\epsilon_E(t)$, fixed body

(d) $\epsilon_E(t)$, floating body

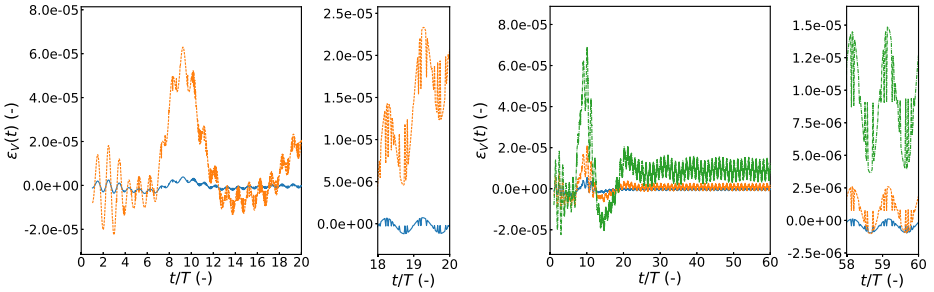

(e) $\epsilon_V(t)$, fixed body

(f) $\epsilon_V(t)$, floating body

Figure D.3: Conservation of fluid properties, fixed and freely floating body with non-dimensional wave frequency $\xi_B = 1.0$.

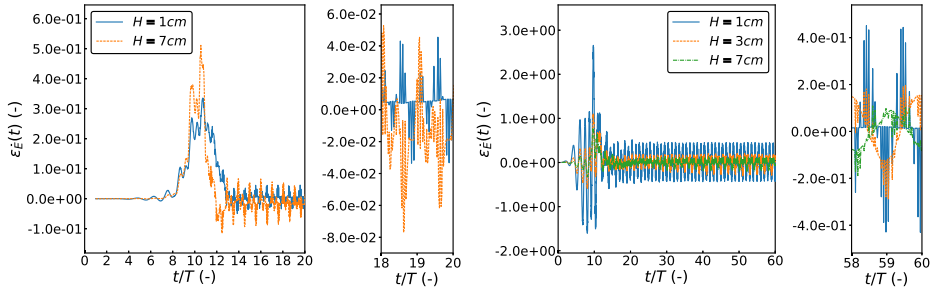

(a) $\epsilon_{\dot{E}}(t)$, fixed body

(b) $\epsilon_{\dot{E}}(t)$, floating body

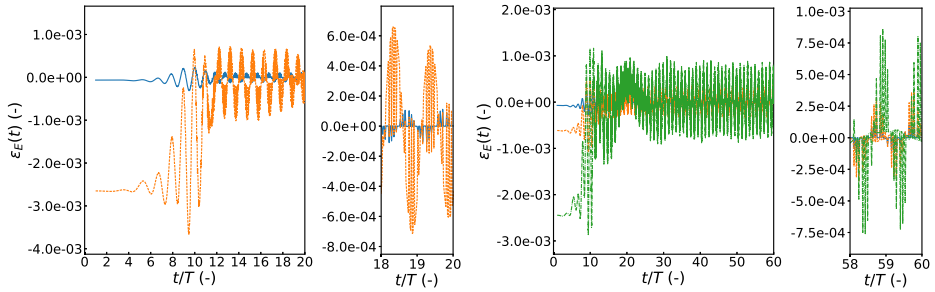

(c) $\epsilon_E(t)$, fixed body

(d) $\epsilon_E(t)$, floating body

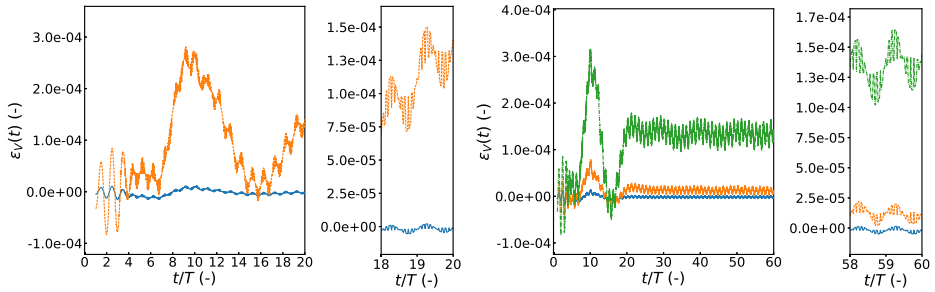

(e) $\epsilon_V(t)$, fixed body

(f) $\epsilon_V(t)$, floating body

Figure D.4: Conservation of fluid properties, fixed and freely floating body with non-dimensional wave frequency $\xi_B = 2.0$.

Appendix E

Reconstruction of Reflected Waves

Hughes (1993) outlines three strategies to reconstruct irregular, reflected waves in a wave tank using

1. a horizontal array of two or more wave probes,
2. a vertical array of probes measuring wave elevation and fluid velocities or
3. a single probe measuring fluid velocities in horizontal and vertical direction.

In the present work the second strategy is used, i.e. measuring the free surface elevation in a probe and the fluid velocity in a fixed point in the water underneath. The probe is located between the wavemaker and the body. Care is taken so that the probe is not located inside the zone of the numerical damping zone next to the wavemaker. A principal sketch showing the position of the wave and velocity probes is shown in Figure E.1. We here always locate the velocity probe a distance $0.20\lambda - 0.25\lambda$ below the still water level, where λ is the characteristic wavelength. The velocity probe must not be so far down in the fluid that velocities are negligible, nor located too close to the free surface so that it is in danger of getting out of water.

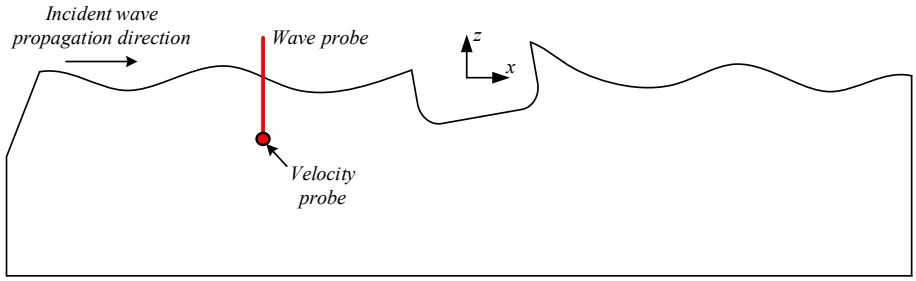

Figure E.1: Conceptual sketch of wave and velocity probe used to reconstruct reflected waves.

E.1 Theory

The analysis follows from assuming constant water depth h and linear wave theory. The time-varying velocity potential in the fluid is expressed through a sum of harmonic components:

$$\begin{aligned}\varphi(x,z,t) = &\sum_{i=1}^{\infty} \frac{gA_{I_i}}{\omega_i} \frac{\cosh\left[k_i(h+z)\right]}{\cosh k_i h} \sin\left(k_i x - \omega_i t + \epsilon_{I_i}\right) + \\ &\sum_{i=1}^{\infty} \frac{gA_{R_i}}{\omega_i} \frac{\cosh\left[k_i(h+z)\right]}{\cosh k_i h} \sin\left(k_i x + \omega_i t + \epsilon_{R_i}\right).\end{aligned} \tag{E.1}$$

g is the acceleration of gravity, ω_i and k_i are the frequency and wave number of the i^{th} wave component, A_{I_i} and ϵ_{I_i} are the amplitude and phase angle of the i^{th} incident wave component and A_{R_i} and ϵ_{R_i} are the amplitude and phase angle of the i^{th} reflected wave component.

The wave elevation follows from the linear dynamic free-surface condition,

$$\zeta(x,t) = -\frac{1}{g}\frac{\partial\varphi}{\partial t}\bigg|_{z=0} = \sum_{i=1}^{\infty} \left[A_{I_i}\cos(\phi_{I_i} - \omega_i t) + A_{R_i}\cos(\phi_{R_i} + \omega_i t)\right], \tag{E.2}$$

where

$$\begin{aligned}\phi_{I_i} &= k_i x + \epsilon_{I_i}, \\ \phi_{R_i} &= k_i x + \epsilon_{R_i}.\end{aligned} \tag{E.3}$$

The fluid velocity is given by the gradient of the velocity potential, $(u,w) = \nabla\varphi$, and can be written as

$$\begin{aligned}u(x,z,t) &= \sum_{i=1}^{\infty} \left[A_{I_i} Z_i \cos(\phi_{I_i} - \omega_i t) + A_{R_i} Z_i \cos(\phi_{R_i} + \omega_i t)\right], \\ w(x,z,t) &= \sum_{i=1}^{\infty} \left[A_{I_i} Y_i \sin(\phi_{I_i} - \omega_i t) + A_{R_i} Y_i \sin(\phi_{R_i} + \omega_i t)\right].\end{aligned} \tag{E.4}$$

Z_i and Y_i are velocity transfer functions defined as

$$\begin{aligned}Z_i &= \frac{gk_i}{\omega_i}\frac{\cosh\left[k_i(h+z)\right]}{\cosh k_i h}, \\ Y_i &= \frac{gk_i}{\omega_i}\frac{\sinh\left[k_i(h+z)\right]}{\cosh k_i h}.\end{aligned} \tag{E.5}$$

The expressions for the wave elevation and the horizontal velocity component can be rearranged in the form of Fourier series as

$$\begin{aligned}\zeta(x,t) &= \sum_{i=1}^{\infty} \left[P_i\cos(\omega_i t) + Q_i\sin(\omega_i t)\right], \\ u(x,z,t) &= \sum_{i=1}^{\infty} \left[C_i\cos(\omega_i t) + D_i\sin(\omega_i t)\right],\end{aligned} \tag{E.6}$$

where the Fourier coefficients are given as

$$\begin{aligned}
\frac{C_i}{Z_i} &= A_{I_i}\cos(\phi_{I_i}) - A_{R_i}\cos(\phi_{R_i}),\\
\frac{D_i}{Z_i} &= A_{I_i}\sin(\phi_{I_i}) + A_{R_i}\sin(\phi_{R_i}),\\
P_i &= A_{I_i}\cos(\phi_{I_i}) + A_{R_i}\cos(\phi_{R_i}),\\
Q_i &= A_{I_i}\sin(\phi_{I_i}) - A_{R_i}\sin(\phi_{R_i}).
\end{aligned} \tag{E.7}$$

The coefficients P_i, Q_i, C_i and D_i in (E.6) are obtained by performing Fourier analysis of the recorded wave elevation and fluid velocity in the probes in Figure E.1. The velocity transfer functions in (E.5) are calculated by taking k_i as the wave number given by the linear dispersion relation for the i^{th} component. Having obtained these, the amplitudes and phases of the propagating and reflected wave components can be obtained:

$$\begin{aligned}
A_{I_i} &= \frac{1}{2}\sqrt{(P_i + \frac{C_i}{Z_i})^2 + (Q_i + \frac{D_i}{Z_i})^2},\\
A_{R_i} &= \frac{1}{2}\sqrt{(P_i - \frac{C_i}{Z_i})^2 + (Q_i - \frac{D_i}{Z_i})^2},\\
\phi_{I_i} &= \tan^{-1}(\frac{Q_i + D_i/Z_i}{P_i + C_i/Z_i}),\\
\phi_{R_i} &= \tan^{-1}(\frac{-Q_i + D_i/Z_i}{P_i - C_i/Z_i}).
\end{aligned} \tag{E.8}$$

By inserting (E.8) into (E.2), the wave elevation is separated into propagating and reflected waves. In practice, the number of wave components i taken into consideration in (E.1) and following expressions must be truncated to a finite number. In the present work we use 100 components with evenly spaced frequencies covering the range of expected wave frequencies.

E.2 Numerical Examples

The performance of the reconstruction is illustrated in Figure E.2 for two values of the wave steepness kA_I, where A_I is the specified incident wave amplitude. The wave probe is located between approximately a distance λ from the moving wavemaker, and the velocity probe is located approximately 0.23λ below the still free surface. For both values of kA_I, the wave is generated as a single regular wave. However, the performance of the method has been confirmed to be similar for irregular waves generated by superimposing multiple regular wave components. The figure shows that the sum of the wave elevation of the reconstructed propagating and reflected wave is in good agreement with the wave elevation measured in the probe except for in the last part of the time series. Minor differences can be observed at the crest and troughs, which is likely due to the fact that the method assumes linear wave theory whereas the simulated waves are non-linear.

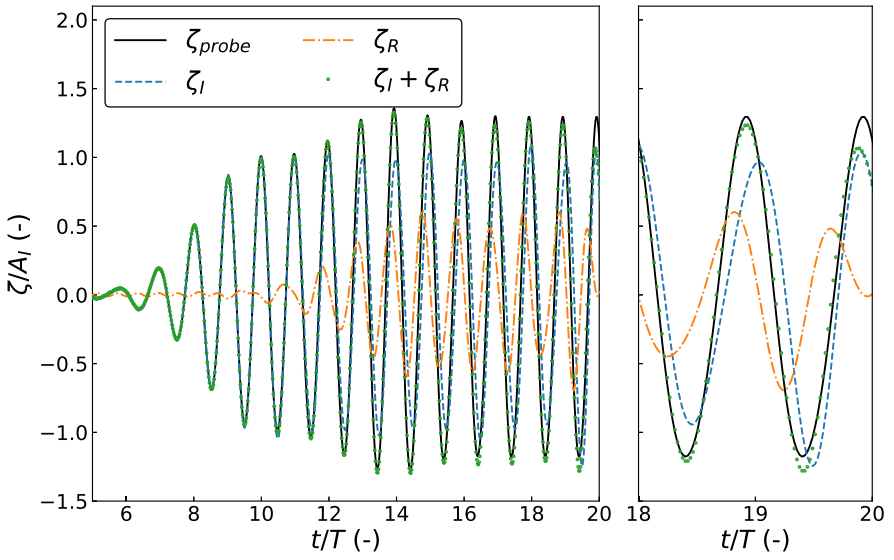

(a) $kA_I = 0.035$

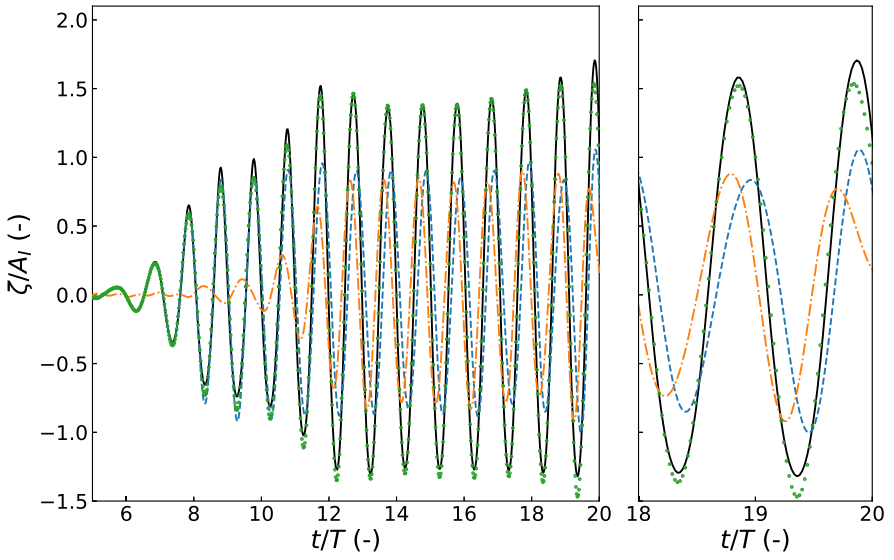

(b) $kA_I = 0.280$

Figure E.2: Elevation of measured wave in wave probe ζ_{probe}, reconstructed propagating wave ζ_I, reconstructed reflected wave ζ_R and total reconstructed wave $\zeta_I + \zeta_R$ for two values of kA_I. The axes are normalized against the specified incident wave period T and amplitude A_I.

The initial intention for implementing the reconstruction method was to identify the reflected wave in real time so that this could be damped out by the damping zone next to the wavemaker. The main idea is that the amplitudes and phases in (E.8) can be calculated during the simulation in the x coordinate of the wave and velocity probes. Using (E.1) - (E.2), the velocity potential and elevation of incident and reflected waves can be predicted at the position of the numerical beach to ensure that only the reflected part of the wave is damped.

In order to spatially extrapolate the propagating and reflected wave components in real-time from the probe position to the numerical beach, it is imperative that the waves are accurately reconstructed for the last time step of the recorded probe time series. As shown in the enlarged panels in Figure E.2, however, the reconstruction clearly fails to reproduce the measured wave elevation towards the end of the time series[1]. As a consequence, attempts to implement this strategy to damp reflected waves were unsuccessful.

Even though the method was found to be inapplicable to damp reflected waves, it remains a powerful tool to identify propagating and reflected waves in the interior part of a time series for post-processing purposes such as to determine the wave reflection coefficient.

[1]This is likely related to the so-called Gibb's phenomenon, that states that an overshoot occurs at discontinuities of a Fourier series. Indeed, the reconstruction also fails at the beginning of a time series.

Previous PhD theses published at the Department of Marine Technology (earlier: Faculty of Marine Technology) NORWEGIAN UNIVERSITY OF SCIENCE AND TECHNOLOGY

Report No.	Author	Title
	Kavlie, Dag	Optimization of Plane Elastic Grillages, 1967
	Hansen, Hans R.	Man-Machine Communication and Data-Storage Methods in Ship Structural Design, 1971
	Gisvold, Kaare M.	A Method for non-linear mixed -integer programming and its Application to Design Problems, 1971
	Lund, Sverre	Tanker Frame Optimalization by means of SUMT-Transformation and Behaviour Models, 1971
	Vinje, Tor	On Vibration of Spherical Shells Interacting with Fluid, 1972
	Lorentz, Jan D.	Tank Arrangement for Crude Oil Carriers in Accordance with the new Anti-Pollution Regulations, 1975
	Carlsen, Carl A.	Computer-Aided Design of Tanker Structures, 1975
	Larsen, Carl M.	Static and Dynamic Analysis of Offshore Pipelines during Installation, 1976
UR-79-01	Brigt Hatlestad, MK	The finite element method used in a fatigue evaluation of fixed offshore platforms. (Dr.Ing. Thesis)
UR-79-02	Erik Pettersen, MK	Analysis and design of cellular structures. (Dr.Ing. Thesis)
UR-79-03	Sverre Valsgård, MK	Finite difference and finite element methods applied to nonlinear analysis of plated structures. (Dr.Ing. Thesis)
UR-79-04	Nils T. Nordsve, MK	Finite element collapse analysis of structural members considering imperfections and stresses due to fabrication. (Dr.Ing. Thesis)
UR-79-05	Ivar J. Fylling, MK	Analysis of towline forces in ocean towing systems. (Dr.Ing. Thesis)
UR-80-06	Nils Sandsmark, MM	Analysis of Stationary and Transient Heat Conduction by the Use of the Finite Element Method. (Dr.Ing. Thesis)
UR-80-09	Sverre Haver, MK	Analysis of uncertainties related to the stochastic modeling of ocean waves. (Dr.Ing. Thesis)
UR-81-15	Odland, Jonas	On the Strength of welded Ring stiffened cylindrical Shells primarily subjected to axial Compression
UR-82-17	Engesvik, Knut	Analysis of Uncertainties in the fatigue Capacity of

		Welded Joints
UR-82-18	Rye, Henrik	Ocean wave groups
UR-83-30	Eide, Oddvar Inge	On Cumulative Fatigue Damage in Steel Welded Joints
UR-83-33	Mo, Olav	Stochastic Time Domain Analysis of Slender Offshore Structures
UR-83-34	Amdahl, Jørgen	Energy absorption in Ship-platform impacts
UR-84-37	Mørch, Morten	Motions and mooring forces of semi submersibles as determined by full-scale measurements and theoretical analysis
UR-84-38	Soares, C. Guedes	Probabilistic models for load effects in ship structures
UR-84-39	Aarsnes, Jan V.	Current forces on ships
UR-84-40	Czujko, Jerzy	Collapse Analysis of Plates subjected to Biaxial Compression and Lateral Load
UR-85-46	Alf G. Engseth, MK	Finite element collapse analysis of tubular steel offshore structures. (Dr.Ing. Thesis)
UR-86-47	Dengody Sheshappa, MP	A Computer Design Model for Optimizing Fishing Vessel Designs Based on Techno-Economic Analysis. (Dr.Ing. Thesis)
UR-86-48	Vidar Aanesland, MH	A Theoretical and Numerical Study of Ship Wave Resistance. (Dr.Ing. Thesis)
UR-86-49	Heinz-Joachim Wessel, MK	Fracture Mechanics Analysis of Crack Growth in Plate Girders. (Dr.Ing. Thesis)
UR-86-50	Jon Taby, MK	Ultimate and Post-ultimate Strength of Dented Tubular Members. (Dr.Ing. Thesis)
UR-86-51	Walter Lian, MH	A Numerical Study of Two-Dimensional Separated Flow Past Bluff Bodies at Moderate KC-Numbers. (Dr.Ing. Thesis)
UR-86-52	Bjørn Sortland, MH	Force Measurements in Oscillating Flow on Ship Sections and Circular Cylinders in a U-Tube Water Tank. (Dr.Ing. Thesis)
UR-86-53	Kurt Strand, MM	A System Dynamic Approach to One-dimensional Fluid Flow. (Dr.Ing. Thesis)
UR-86-54	Arne Edvin Løken, MH	Three Dimensional Second Order Hydrodynamic Effects on Ocean Structures in Waves. (Dr.Ing. Thesis)
UR-86-55	Sigurd Falch, MH	A Numerical Study of Slamming of Two-Dimensional Bodies. (Dr.Ing. Thesis)
UR-87-56	Arne Braathen, MH	Application of a Vortex Tracking Method to the Prediction of Roll Damping of a Two-Dimension Floating Body. (Dr.Ing. Thesis)

UR-87-57	Bernt Leira, MK	Gaussian Vector Processes for Reliability Analysis involving Wave-Induced Load Effects. (Dr.Ing. Thesis)
UR-87-58	Magnus Småvik, MM	Thermal Load and Process Characteristics in a Two-Stroke Diesel Engine with Thermal Barriers (in Norwegian). (Dr.Ing. Thesis)
MTA-88-59	Bernt Arild Bremdal, MP	An Investigation of Marine Installation Processes – A Knowledge - Based Planning Approach. (Dr.Ing. Thesis)
MTA-88-60	Xu Jun, MK	Non-linear Dynamic Analysis of Space-framed Offshore Structures. (Dr.Ing. Thesis)
MTA-89-61	Gang Miao, MH	Hydrodynamic Forces and Dynamic Responses of Circular Cylinders in Wave Zones. (Dr.Ing. Thesis)
MTA-89-62	Martin Greenhow, MH	Linear and Non-Linear Studies of Waves and Floating Bodies. Part I and Part II. (Dr.Techn. Thesis)
MTA-89-63	Chang Li, MH	Force Coefficients of Spheres and Cubes in Oscillatory Flow with and without Current. (Dr.Ing. Thesis
MTA-89-64	Hu Ying, MP	A Study of Marketing and Design in Development of Marine Transport Systems. (Dr.Ing. Thesis)
MTA-89-65	Arild Jæger, MH	Seakeeping, Dynamic Stability and Performance of a Wedge Shaped Planing Hull. (Dr.Ing. Thesis)
MTA-89-66	Chan Siu Hung, MM	The dynamic characteristics of tilting-pad bearings
MTA-89-67	Kim Wikstrøm, MP	Analysis av projekteringen for ett offshore projekt. (Licenciat-avhandling)
MTA-89-68	Jiao Guoyang, MK	Reliability Analysis of Crack Growth under Random Loading, considering Model Updating. (Dr.Ing. Thesis)
MTA-89-69	Arnt Olufsen, MK	Uncertainty and Reliability Analysis of Fixed Offshore Structures. (Dr.Ing. Thesis)
MTA-89-70	Wu Yu-Lin, MR	System Reliability Analyses of Offshore Structures using improved Truss and Beam Models. (Dr.Ing. Thesis)
MTA-90-71	Jan Roger Hoff, MH	Three-dimensional Green function of a vessel with forward speed in waves. (Dr.Ing. Thesis)
MTA-90-72	Rong Zhao, MH	Slow-Drift Motions of a Moored Two-Dimensional Body in Irregular Waves. (Dr.Ing. Thesis)
MTA-90-73	Atle Minsaas, MP	Economical Risk Analysis. (Dr.Ing. Thesis)
MTA-90-74	Knut-Aril Farnes, MK	Long-term Statistics of Response in Non-linear Marine Structures. (Dr.Ing. Thesis)
MTA-90-75	Torbjørn Sotberg, MK	Application of Reliability Methods for Safety Assessment of Submarine Pipelines. (Dr.Ing.

		Thesis)
MTA-90-76	Zeuthen, Steffen, MP	SEAMAID. A computational model of the design process in a constraint-based logic programming environment. An example from the offshore domain. (Dr.Ing. Thesis)
MTA-91-77	Haagensen, Sven, MM	Fuel Dependant Cyclic Variability in a Spark Ignition Engine - An Optical Approach. (Dr.Ing. Thesis)
MTA-91-78	Løland, Geir, MH	Current forces on and flow through fish farms. (Dr.Ing. Thesis)
MTA-91-79	Hoen, Christopher, MK	System Identification of Structures Excited by Stochastic Load Processes. (Dr.Ing. Thesis)
MTA-91-80	Haugen, Stein, MK	Probabilistic Evaluation of Frequency of Collision between Ships and Offshore Platforms. (Dr.Ing. Thesis)
MTA-91-81	Sødahl, Nils, MK	Methods for Design and Analysis of Flexible Risers. (Dr.Ing. Thesis)
MTA-91-82	Ormberg, Harald, MK	Non-linear Response Analysis of Floating Fish Farm Systems. (Dr.Ing. Thesis)
MTA-91-83	Marley, Mark J., MK	Time Variant Reliability under Fatigue Degradation. (Dr.Ing. Thesis)
MTA-91-84	Krokstad, Jørgen R., MH	Second-order Loads in Multidirectional Seas. (Dr.Ing. Thesis)
MTA-91-85	Molteberg, Gunnar A., MM	The Application of System Identification Techniques to Performance Monitoring of Four Stroke Turbocharged Diesel Engines. (Dr.Ing. Thesis)
MTA-92-86	Mørch, Hans Jørgen Bjelke, MH	Aspects of Hydrofoil Design: with Emphasis on Hydrofoil Interaction in Calm Water. (Dr.Ing. Thesis)
MTA-92-87	Chan Siu Hung, MM	Nonlinear Analysis of Rotordynamic Instabilities in Highspeed Turbomachinery. (Dr.Ing. Thesis)
MTA-92-88	Bessason, Bjarni, MK	Assessment of Earthquake Loading and Response of Seismically Isolated Bridges. (Dr.Ing. Thesis)
MTA-92-89	Langli, Geir, MP	Improving Operational Safety through exploitation of Design Knowledge - an investigation of offshore platform safety. (Dr.Ing. Thesis)
MTA-92-90	Sævik, Svein, MK	On Stresses and Fatigue in Flexible Pipes. (Dr.Ing. Thesis)
MTA-92-91	Ask, Tor Ø., MM	Ignition and Flame Growth in Lean Gas-Air Mixtures. An Experimental Study with a Schlieren System. (Dr.Ing. Thesis)
MTA-86-92	Hessen, Gunnar, MK	Fracture Mechanics Analysis of Stiffened Tubular Members. (Dr.Ing. Thesis)

MTA-93-93	Steinebach, Christian, MM	Knowledge Based Systems for Diagnosis of Rotating Machinery. (Dr.Ing. Thesis)
MTA-93-94	Dalane, Jan Inge, MK	System Reliability in Design and Maintenance of Fixed Offshore Structures. (Dr.Ing. Thesis)
MTA-93-95	Steen, Sverre, MH	Cobblestone Effect on SES. (Dr.Ing. Thesis)
MTA-93-96	Karunakaran, Daniel, MK	Nonlinear Dynamic Response and Reliability Analysis of Drag-dominated Offshore Platforms. (Dr.Ing. Thesis)
MTA-93-97	Hagen, Arnulf, MP	The Framework of a Design Process Language. (Dr.Ing. Thesis)
MTA-93-98	Nordrik, Rune, MM	Investigation of Spark Ignition and Autoignition in Methane and Air Using Computational Fluid Dynamics and Chemical Reaction Kinetics. A Numerical Study of Ignition Processes in Internal Combustion Engines. (Dr.Ing. Thesis)
MTA-94-99	Passano, Elizabeth, MK	Efficient Analysis of Nonlinear Slender Marine Structures. (Dr.Ing. Thesis)
MTA-94-100	Kvålsvold, Jan, MH	Hydroelastic Modelling of Wetdeck Slamming on Multihull Vessels. (Dr.Ing. Thesis)
MTA-94-102	Bech, Sidsel M., MK	Experimental and Numerical Determination of Stiffness and Strength of GRP/PVC Sandwich Structures. (Dr.Ing. Thesis)
MTA-95-103	Paulsen, Hallvard, MM	A Study of Transient Jet and Spray using a Schlieren Method and Digital Image Processing. (Dr.Ing. Thesis)
MTA-95-104	Hovde, Geir Olav, MK	Fatigue and Overload Reliability of Offshore Structural Systems, Considering the Effect of Inspection and Repair. (Dr.Ing. Thesis)
MTA-95-105	Wang, Xiaozhi, MK	Reliability Analysis of Production Ships with Emphasis on Load Combination and Ultimate Strength. (Dr.Ing. Thesis)
MTA-95-106	Ulstein, Tore, MH	Nonlinear Effects of a Flexible Stern Seal Bag on Cobblestone Oscillations of an SES. (Dr.Ing. Thesis)
MTA-95-107	Solaas, Frøydis, MH	Analytical and Numerical Studies of Sloshing in Tanks. (Dr.Ing. Thesis)
MTA-95-108	Hellan, Øyvind, MK	Nonlinear Pushover and Cyclic Analyses in Ultimate Limit State Design and Reassessment of Tubular Steel Offshore Structures. (Dr.Ing. Thesis)
MTA-95-109	Hermundstad, Ole A., MK	Theoretical and Experimental Hydroelastic Analysis of High Speed Vessels. (Dr.Ing. Thesis)
MTA-96-110	Bratland, Anne K., MH	Wave-Current Interaction Effects on Large-Volume Bodies in Water of Finite Depth. (Dr.Ing. Thesis)
MTA-96-111	Herfjord, Kjell, MH	A Study of Two-dimensional Separated Flow by a Combination of the Finite Element Method and

		Navier-Stokes Equations. (Dr.Ing. Thesis)
MTA-96-112	Æsøy, Vilmar, MM	Hot Surface Assisted Compression Ignition in a Direct Injection Natural Gas Engine. (Dr.Ing. Thesis)
MTA-96-113	Eknes, Monika L., MK	Escalation Scenarios Initiated by Gas Explosions on Offshore Installations. (Dr.Ing. Thesis)
MTA-96-114	Erikstad, Stein O., MP	A Decision Support Model for Preliminary Ship Design. (Dr.Ing. Thesis)
MTA-96-115	Pedersen, Egil, MH	A Nautical Study of Towed Marine Seismic Streamer Cable Configurations. (Dr.Ing. Thesis)
MTA-97-116	Moksnes, Paul O., MM	Modelling Two-Phase Thermo-Fluid Systems Using Bond Graphs. (Dr.Ing. Thesis)
MTA-97-117	Halse, Karl H., MK	On Vortex Shedding and Prediction of Vortex-Induced Vibrations of Circular Cylinders. (Dr.Ing. Thesis)
MTA-97-118	Igland, Ragnar T., MK	Reliability Analysis of Pipelines during Laying, considering Ultimate Strength under Combined Loads. (Dr.Ing. Thesis)
MTA-97-119	Pedersen, Hans-P., MP	Levendefiskteknologi for fiskefartøy. (Dr.Ing. Thesis)
MTA-98-120	Vikestad, Kyrre, MK	Multi-Frequency Response of a Cylinder Subjected to Vortex Shedding and Support Motions. (Dr.Ing. Thesis)
MTA-98-121	Azadi, Mohammad R. E., MK	Analysis of Static and Dynamic Pile-Soil-Jacket Behaviour. (Dr.Ing. Thesis)
MTA-98-122	Ulltang, Terje, MP	A Communication Model for Product Information. (Dr.Ing. Thesis)
MTA-98-123	Torbergsen, Erik, MM	Impeller/Diffuser Interaction Forces in Centrifugal Pumps. (Dr.Ing. Thesis)
MTA-98-124	Hansen, Edmond, MH	A Discrete Element Model to Study Marginal Ice Zone Dynamics and the Behaviour of Vessels Moored in Broken Ice. (Dr.Ing. Thesis)
MTA-98-125	Videiro, Paulo M., MK	Reliability Based Design of Marine Structures. (Dr.Ing. Thesis)
MTA-99-126	Mainçon, Philippe, MK	Fatigue Reliability of Long Welds Application to Titanium Risers. (Dr.Ing. Thesis)
MTA-99-127	Haugen, Elin M., MH	Hydroelastic Analysis of Slamming on Stiffened Plates with Application to Catamaran Wetdecks. (Dr.Ing. Thesis)
MTA-99-128	Langhelle, Nina K., MK	Experimental Validation and Calibration of Nonlinear Finite Element Models for Use in Design of Aluminium Structures Exposed to Fire. (Dr.Ing. Thesis)
MTA-99-	Berstad, Are J., MK	Calculation of Fatigue Damage in Ship Structures.

129		(Dr.Ing. Thesis)
MTA-99-130	Andersen, Trond M., MM	Short Term Maintenance Planning. (Dr.Ing. Thesis)
MTA-99-131	Tveiten, Bård Wathne, MK	Fatigue Assessment of Welded Aluminium Ship Details. (Dr.Ing. Thesis)
MTA-99-132	Søreide, Fredrik, MP	Applications of underwater technology in deep water archaeology. Principles and practice. (Dr.Ing. Thesis)
MTA-99-133	Tønnessen, Rune, MH	A Finite Element Method Applied to Unsteady Viscous Flow Around 2D Blunt Bodies With Sharp Corners. (Dr.Ing. Thesis)
MTA-99-134	Elvekrok, Dag R., MP	Engineering Integration in Field Development Projects in the Norwegian Oil and Gas Industry. The Supplier Management of Norne. (Dr.Ing. Thesis)
MTA-99-135	Fagerholt, Kjetil, MP	Optimeringsbaserte Metoder for Ruteplanlegging innen skipsfart. (Dr.Ing. Thesis)
MTA-99-136	Bysveen, Marie, MM	Visualization in Two Directions on a Dynamic Combustion Rig for Studies of Fuel Quality. (Dr.Ing. Thesis)
MTA-2000-137	Storteig, Eskild, MM	Dynamic characteristics and leakage performance of liquid annular seals in centrifugal pumps. (Dr.Ing. Thesis)
MTA-2000-138	Sagli, Gro, MK	Model uncertainty and simplified estimates of long term extremes of hull girder loads in ships. (Dr.Ing. Thesis)
MTA-2000-139	Tronstad, Harald, MK	Nonlinear analysis and design of cable net structures like fishing gear based on the finite element method. (Dr.Ing. Thesis)
MTA-2000-140	Kroneberg, André, MP	Innovation in shipping by using scenarios. (Dr.Ing. Thesis)
MTA-2000-141	Haslum, Herbjørn Alf, MH	Simplified methods applied to nonlinear motion of spar platforms. (Dr.Ing. Thesis)
MTA-2001-142	Samdal, Ole Johan, MM	Modelling of Degradation Mechanisms and Stressor Interaction on Static Mechanical Equipment Residual Lifetime. (Dr.Ing. Thesis)
MTA-2001-143	Baarholm, Rolf Jarle, MH	Theoretical and experimental studies of wave impact underneath decks of offshore platforms. (Dr.Ing. Thesis)
MTA-2001-144	Wang, Lihua, MK	Probabilistic Analysis of Nonlinear Wave-induced Loads on Ships. (Dr.Ing. Thesis)
MTA-2001-145	Kristensen, Odd H. Holt, MK	Ultimate Capacity of Aluminium Plates under Multiple Loads, Considering HAZ Properties. (Dr.Ing. Thesis)
MTA-2001-146	Greco, Marilena, MH	A Two-Dimensional Study of Green-Water

		Loading. (Dr.Ing. Thesis)
MTA-2001-147	Heggelund, Svein E., MK	Calculation of Global Design Loads and Load Effects in Large High Speed Catamarans. (Dr.Ing. Thesis)
MTA-2001-148	Babalola, Olusegun T., MK	Fatigue Strength of Titanium Risers – Defect Sensitivity. (Dr.Ing. Thesis)
MTA-2001-149	Mohammed, Abuu K., MK	Nonlinear Shell Finite Elements for Ultimate Strength and Collapse Analysis of Ship Structures. (Dr.Ing. Thesis)
MTA-2002-150	Holmedal, Lars E., MH	Wave-current interactions in the vicinity of the sea bed. (Dr.Ing. Thesis)
MTA-2002-151	Rognebakke, Olav F., MH	Sloshing in rectangular tanks and interaction with ship motions. (Dr.Ing. Thesis)
MTA-2002-152	Lader, Pål Furset, MH	Geometry and Kinematics of Breaking Waves. (Dr.Ing. Thesis)
MTA-2002-153	Yang, Qinzheng, MH	Wash and wave resistance of ships in finite water depth. (Dr.Ing. Thesis)
MTA-2002-154	Melhus, Øyvin, MM	Utilization of VOC in Diesel Engines. Ignition and combustion of VOC released by crude oil tankers. (Dr.Ing. Thesis)
MTA-2002-155	Ronæss, Marit, MH	Wave Induced Motions of Two Ships Advancing on Parallel Course. (Dr.Ing. Thesis)
MTA-2002-156	Økland, Ole D., MK	Numerical and experimental investigation of whipping in twin hull vessels exposed to severe wet deck slamming. (Dr.Ing. Thesis)
MTA-2002-157	Ge, Chunhua, MK	Global Hydroelastic Response of Catamarans due to Wet Deck Slamming. (Dr.Ing. Thesis)
MTA-2002-158	Byklum, Eirik, MK	Nonlinear Shell Finite Elements for Ultimate Strength and Collapse Analysis of Ship Structures. (Dr.Ing. Thesis)
IMT-2003-1	Chen, Haibo, MK	Probabilistic Evaluation of FPSO-Tanker Collision in Tandem Offloading Operation. (Dr.Ing. Thesis)
IMT-2003-2	Skaugset, Kjetil Bjørn, MK	On the Suppression of Vortex Induced Vibrations of Circular Cylinders by Radial Water Jets. (Dr.Ing. Thesis)
IMT-2003-3	Chezhian, Muthu	Three-Dimensional Analysis of Slamming. (Dr.Ing. Thesis)
IMT-2003-4	Buhaug, Øyvind	Deposit Formation on Cylinder Liner Surfaces in Medium Speed Engines. (Dr.Ing. Thesis)
IMT-2003-5	Tregde, Vidar	Aspects of Ship Design: Optimization of Aft Hull with Inverse Geometry Design. (Dr.Ing. Thesis)
IMT-	Wist, Hanne Therese	Statistical Properties of Successive Ocean Wave

2003-6		Parameters. (Dr.Ing. Thesis)
IMT-2004-7	Ransau, Samuel	Numerical Methods for Flows with Evolving Interfaces. (Dr.Ing. Thesis)
IMT-2004-8	Soma, Torkel	Blue-Chip or Sub-Standard. A data interrogation approach of identity safety characteristics of shipping organization. (Dr.Ing. Thesis)
IMT-2004-9	Ersdal, Svein	An experimental study of hydrodynamic forces on cylinders and cables in near axial flow. (Dr.Ing. Thesis)
IMT-2005-10	Brodtkorb, Per Andreas	The Probability of Occurrence of Dangerous Wave Situations at Sea. (Dr.Ing. Thesis)
IMT-2005-11	Yttervik, Rune	Ocean current variability in relation to offshore engineering. (Dr.Ing. Thesis)
IMT-2005-12	Fredheim, Arne	Current Forces on Net-Structures. (Dr.Ing. Thesis)
IMT-2005-13	Heggernes, Kjetil	Flow around marine structures. (Dr.Ing. Thesis
IMT-2005-14	Fouques, Sebastien	Lagrangian Modelling of Ocean Surface Waves and Synthetic Aperture Radar Wave Measurements. (Dr.Ing. Thesis)
IMT-2006-15	Holm, Håvard	Numerical calculation of viscous free surface flow around marine structures. (Dr.Ing. Thesis)
IMT-2006-16	Bjørheim, Lars G.	Failure Assessment of Long Through Thickness Fatigue Cracks in Ship Hulls. (Dr.Ing. Thesis)
IMT-2006-17	Hansson, Lisbeth	Safety Management for Prevention of Occupational Accidents. (Dr.Ing. Thesis)
IMT-2006-18	Zhu, Xinying	Application of the CIP Method to Strongly Nonlinear Wave-Body Interaction Problems. (Dr.Ing. Thesis)
IMT-2006-19	Reite, Karl Johan	Modelling and Control of Trawl Systems. (Dr.Ing. Thesis)
IMT-2006-20	Smogeli, Øyvind Notland	Control of Marine Propellers. From Normal to Extreme Conditions. (Dr.Ing. Thesis)
IMT-2007-21	Storhaug, Gaute	Experimental Investigation of Wave Induced Vibrations and Their Effect on the Fatigue Loading of Ships. (Dr.Ing. Thesis)
IMT-2007-22	Sun, Hui	A Boundary Element Method Applied to Strongly Nonlinear Wave-Body Interaction Problems. (PhD Thesis, CeSOS)
IMT-2007-23	Rustad, Anne Marthine	Modelling and Control of Top Tensioned Risers. (PhD Thesis, CeSOS)
IMT-2007-24	Johansen, Vegar	Modelling flexible slender system for real-time simulations and control applications
IMT-2007-25	Wroldsen, Anders Sunde	Modelling and control of tensegrity structures.

		(PhD Thesis, CeSOS)
IMT-2007-26	Aronsen, Kristoffer Høye	An experimental investigation of in-line and combined inline and cross flow vortex induced vibrations. (Dr. avhandling, IMT)
IMT-2007-27	Gao, Zhen	Stochastic Response Analysis of Mooring Systems with Emphasis on Frequency-domain Analysis of Fatigue due to Wide-band Response Processes (PhD Thesis, CeSOS)
IMT-2007-28	Thorstensen, Tom Anders	Lifetime Profit Modelling of Ageing Systems Utilizing Information about Technical Condition. (Dr.ing. thesis, IMT)
IMT-2008-29	Refsnes, Jon Erling Gorset	Nonlinear Model-Based Control of Slender Body AUVs (PhD Thesis, IMT)
IMT-2008-30	Berntsen, Per Ivar B.	Structural Reliability Based Position Mooring. (PhD-Thesis, IMT)
IMT-2008-31	Ye, Naiquan	Fatigue Assessment of Aluminium Welded Box-stiffener Joints in Ships (Dr.ing. thesis, IMT)
IMT-2008-32	Radan, Damir	Integrated Control of Marine Electrical Power Systems. (PhD-Thesis, IMT)
IMT-2008-33	Thomassen, Paul	Methods for Dynamic Response Analysis and Fatigue Life Estimation of Floating Fish Cages. (Dr.ing. thesis, IMT)
IMT-2008-34	Pákozdi, Csaba	A Smoothed Particle Hydrodynamics Study of Two-dimensional Nonlinear Sloshing in Rectangular Tanks. (Dr.ing.thesis, IMT/ CeSOS)
IMT-2007-35	Grytøyr, Guttorm	A Higher-Order Boundary Element Method and Applications to Marine Hydrodynamics. (Dr.ing.thesis, IMT)
IMT-2008-36	Drummen, Ingo	Experimental and Numerical Investigation of Nonlinear Wave-Induced Load Effects in Containerships considering Hydroelasticity. (PhD thesis, CeSOS)
IMT-2008-37	Skejic, Renato	Maneuvering and Seakeeping of a Singel Ship and of Two Ships in Interaction. (PhD-Thesis, CeSOS)
IMT-2008-38	Harlem, Alf	An Age-Based Replacement Model for Repairable Systems with Attention to High-Speed Marine Diesel Engines. (PhD-Thesis, IMT)
IMT-2008-39	Alsos, Hagbart S.	Ship Grounding. Analysis of Ductile Fracture, Bottom Damage and Hull Girder Response. (PhD-thesis, IMT)
IMT-2008-40	Graczyk, Mateusz	Experimental Investigation of Sloshing Loading and Load Effects in Membrane LNG Tanks Subjected to Random Excitation. (PhD-thesis, CeSOS)
IMT-2008-41	Taghipour, Reza	Efficient Prediction of Dynamic Response for Flexible amd Multi-body Marine Structures. (PhD-

		thesis, CeSOS)
IMT-2008-42	Ruth, Eivind	Propulsion control and thrust allocation on marine vessels. (PhD thesis, CeSOS)
IMT-2008-43	Nystad, Bent Helge	Technical Condition Indexes and Remaining Useful Life of Aggregated Systems. PhD thesis, IMT
IMT-2008-44	Soni, Prashant Kumar	Hydrodynamic Coefficients for Vortex Induced Vibrations of Flexible Beams, PhD thesis, CeSOS
IMT-2009-45	Amlashi, Hadi K.K.	Ultimate Strength and Reliability-based Design of Ship Hulls with Emphasis on Combined Global and Local Loads. PhD Thesis, IMT
IMT-2009-46	Pedersen, Tom Arne	Bond Graph Modelling of Marine Power Systems. PhD Thesis, IMT
IMT-2009-47	Kristiansen, Trygve	Two-Dimensional Numerical and Experimental Studies of Piston-Mode Resonance. PhD-Thesis, CeSOS
IMT-2009-48	Ong, Muk Chen	Applications of a Standard High Reynolds Number Model and a Stochastic Scour Prediction Model for Marine Structures. PhD-thesis, IMT
IMT-2009-49	Hong, Lin	Simplified Analysis and Design of Ships subjected to Collision and Grounding. PhD-thesis, IMT
IMT-2009-50	Koushan, Kamran	Vortex Induced Vibrations of Free Span Pipelines, PhD thesis, IMT
IMT-2009-51	Korsvik, Jarl Eirik	Heuristic Methods for Ship Routing and Scheduling. PhD-thesis, IMT
IMT-2009-52	Lee, Jihoon	Experimental Investigation and Numerical in Analyzing the Ocean Current Displacement of Longlines. Ph.d.-Thesis, IMT.
IMT-2009-53	Vestbøstad, Tone Gran	A Numerical Study of Wave-in-Deck Impact usin a Two-Dimensional Constrained Interpolation Profile Method, Ph.d.thesis, CeSOS.
IMT-2009-54	Bruun, Kristine	Bond Graph Modelling of Fuel Cells for Marine Power Plants. Ph.d.-thesis, IMT
IMT 2009-55	Holstad, Anders	Numerical Investigation of Turbulence in a Sekwed Three-Dimensional Channel Flow, Ph.d.-thesis, IMT.
IMT 2009-56	Ayala-Uraga, Efren	Reliability-Based Assessment of Deteriorating Ship-shaped Offshore Structures, Ph.d.-thesis, IMT
IMT 2009-57	Kong, Xiangjun	A Numerical Study of a Damaged Ship in Beam Sea Waves. Ph.d.-thesis, IMT/CeSOS.
IMT 2010-58	Kristiansen, David	Wave Induced Effects on Floaters of Aquaculture Plants, Ph.d.-thesis, CeSOS.

IMT 2010-59	Ludvigsen, Martin	An ROV-Toolbox for Optical and Acoustic Scientific Seabed Investigation. Ph.d.-thesis IMT.
IMT 2010-60	Hals, Jørgen	Modelling and Phase Control of Wave-Energy Converters. Ph.d.thesis, CeSOS.
IMT 2010- 61	Shu, Zhi	Uncertainty Assessment of Wave Loads and Ultimate Strength of Tankers and Bulk Carriers in a Reliability Framework. Ph.d. Thesis, IMT/ CeSOS
IMT 2010-62	Shao, Yanlin	Numerical Potential-Flow Studies on Weakly-Nonlinear Wave-Body Interactions with/without Small Forward Speed, Ph.d.thesis,CeSOS.
IMT 2010-63	Califano, Andrea	Dynamic Loads on Marine Propellers due to Intermittent Ventilation. Ph.d.thesis, IMT.
IMT 2010-64	El Khoury, George	Numerical Simulations of Massively Separated Turbulent Flows, Ph.d.-thesis, IMT
IMT 2010-65	Seim, Knut Sponheim	Mixing Process in Dense Overflows with Emphasis on the Faroe Bank Channel Overflow. Ph.d.thesis, IMT
IMT 2010-66	Jia, Huirong	Structural Analysis of Intect and Damaged Ships in a Collission Risk Analysis Perspective. Ph.d.thesis CeSoS.
IMT 2010-67	Jiao, Linlin	Wave-Induced Effects on a Pontoon-type Very Large Floating Structures (VLFS). Ph.D.-thesis, CeSOS.
IMT 2010-68	Abrahamsen, Bjørn Christian	Sloshing Induced Tank Roof with Entrapped Air Pocket. Ph.d.thesis, CeSOS.
IMT 2011-69	Karimirad, Madjid	Stochastic Dynamic Response Analysis of Spar-Type Wind Turbines with Catenary or Taut Mooring Systems. Ph.d.-thesis, CeSOS.
IMT - 2011-70	Erlend Meland	Condition Monitoring of Safety Critical Valves. Ph.d.-thesis, IMT.
IMT – 2011-71	Yang, Limin	Stochastic Dynamic System Analysis of Wave Energy Converter with Hydraulic Power Take-Off, with Particular Reference to Wear Damage Analysis, Ph.d. Thesis, CeSOS.
IMT – 2011-72	Visscher, Jan	Application of Particla Image Velocimetry on Turbulent Marine Flows, Ph.d.Thesis, IMT.
IMT – 2011-73	Su, Biao	Numerical Predictions of Global and Local Ice Loads on Ships. Ph.d.Thesis, CeSOS.
IMT – 2011-74	Liu, Zhenhui	Analytical and Numerical Analysis of Iceberg Collision with Ship Structures. Ph.d.Thesis, IMT.
IMT – 2011-75	Aarsæther, Karl Gunnar	Modeling and Analysis of Ship Traffic by Observation and Numerical Simulation. Ph.d.Thesis, IMT.

Imt – 2011-76	Wu, Jie	Hydrodynamic Force Identification from Stochastic Vortex Induced Vibration Experiments with Slender Beams. Ph.d.Thesis, IMT.
Imt – 2011-77	Amini, Hamid	Azimuth Propulsors in Off-design Conditions. Ph.d.Thesis, IMT.
IMT – 2011-78	Nguyen, Tan-Hoi	Toward a System of Real-Time Prediction and Monitoring of Bottom Damage Conditions During Ship Grounding. Ph.d.thesis, IMT.
IMT- 2011-79	Tavakoli, Mohammad T.	Assessment of Oil Spill in Ship Collision and Grounding, Ph.d.thesis, IMT.
IMT- 2011-80	Guo, Bingjie	Numerical and Experimental Investigation of Added Resistance in Waves. Ph.d.Thesis, IMT.
IMT- 2011-81	Chen, Qiaofeng	Ultimate Strength of Aluminium Panels, considering HAZ Effects, IMT
IMT- 2012-82	Kota, Ravikiran S.	Wave Loads on Decks of Offshore Structures in Random Seas, CeSOS.
IMT- 2012-83	Sten, Ronny	Dynamic Simulation of Deep Water Drilling Risers with Heave Compensating System, IMT.
IMT- 2012-84	Berle, Øyvind	Risk and resilience in global maritime supply chains, IMT.
IMT- 2012-85	Fang, Shaoji	Fault Tolerant Position Mooring Control Based on Structural Reliability, CeSOS.
IMT- 2012-86	You, Jikun	Numerical studies on wave forces and moored ship motions in intermediate and shallow water, CeSOS.
IMT- 2012-87	Xiang ,Xu	Maneuvering of two interacting ships in waves, CeSOS
IMT- 2012-88	Dong, Wenbin	Time-domain fatigue response and reliability analysis of offshore wind turbines with emphasis on welded tubular joints and gear components, CeSOS
IMT- 2012-89	Zhu, Suji	Investigation of Wave-Induced Nonlinear Load Effects in Open Ships considering Hull Girder Vibrations in Bending and Torsion, CeSOS
IMT- 2012-90	Zhou, Li	Numerical and Experimental Investigation of Station-keeping in Level Ice, CeSOS
IMT- 2012-91	Ushakov, Sergey	Particulate matter emission characteristics from diesel enignes operating on conventional and alternative marine fuels, IMT
IMT- 2013-1	Yin, Decao	Experimental and Numerical Analysis of Combined In-line and Cross-flow Vortex Induced Vibrations, CeSOS

IMT-2013-2	Kurniawan, Adi	Modelling and geometry optimisation of wave energy converters, CeSOS
IMT-2013-3	Al Ryati, Nabil	Technical condition indexes doe auxiliary marine diesel engines, IMT
IMT-2013-4	Firoozkoohi, Reza	Experimental, numerical and analytical investigation of the effect of screens on sloshing, CeSOS
IMT-2013-5	Ommani, Babak	Potential-Flow Predictions of a Semi-Displacement Vessel Including Applications to Calm Water Broaching, CeSOS
IMT-2013-6	Xing, Yihan	Modelling and analysis of the gearbox in a floating spar-type wind turbine, CeSOS
IMT-7-2013	Balland, Océane	Optimization models for reducing air emissions from ships, IMT
IMT-8-2013	Yang, Dan	Transitional wake flow behind an inclined flat plate-----Computation and analysis, IMT
IMT-9-2013	Abdillah, Suyuthi	Prediction of Extreme Loads and Fatigue Damage for a Ship Hull due to Ice Action, IMT
IMT-10-2013	Ramìrez, Pedro Agustìn Pèrez	Ageing management and life extension of technical systems- Concepts and methods applied to oil and gas facilities, IMT
IMT-11-2013	Chuang, Zhenju	Experimental and Numerical Investigation of Speed Loss due to Seakeeping and Maneuvering. IMT
IMT-12-2013	Etemaddar, Mahmoud	Load and Response Analysis of Wind Turbines under Atmospheric Icing and Controller System Faults with Emphasis on Spar Type Floating Wind Turbines, IMT
IMT-13-2013	Lindstad, Haakon	Strategies and measures for reducing maritime CO2 emissons, IMT
IMT-14-2013	Haris, Sabril	Damage interaction analysis of ship collisions, IMT
IMT-15-2013	Shainee, Mohamed	Conceptual Design, Numerical and Experimental Investigation of a SPM Cage Concept for Offshore Mariculture, IMT
IMT-16-2013	Gansel, Lars	Flow past porous cylinders and effects of biofouling and fish behavior on the flow in and around Atlantic salmon net cages, IMT
IMT-17-2013	Gaspar, Henrique	Handling Aspects of Complexity in Conceptual Ship Design, IMT
IMT-18-2013	Thys, Maxime	Theoretical and Experimental Investigation of a Free Running Fishing Vessel at Small Frequency of Encounter, CeSOS
IMT-19-2013	Aglen, Ida	VIV in Free Spanning Pipelines, CeSOS

IMT-1-2014	Song, An	Theoretical and experimental studies of wave diffraction and radiation loads on a horizontally submerged perforated plate, CeSOS
IMT-2-2014	Rogne, Øyvind Ygre	Numerical and Experimental Investigation of a Hinged 5-body Wave Energy Converter, CeSOS
IMT-3-2014	Dai, Lijuan	Safe and efficient operation and maintenance of offshore wind farms ,IMT
IMT-4-2014	Bachynski, Erin Elizabeth	Design and Dynamic Analysis of Tension Leg Platform Wind Turbines, CeSOS
IMT-5-2014	Wang, Jingbo	Water Entry of Freefall Wedged – Wedge motions and Cavity Dynamics, CeSOS
IMT-6-2014	Kim, Ekaterina	Experimental and numerical studies related to the coupled behavior of ice mass and steel structures during accidental collisions, IMT
IMT-7-2014	Tan, Xiang	Numerical investigation of ship's continuous- mode icebreaking in leverl ice, CeSOS
IMT-8-2014	Muliawan, Made Jaya	Design and Analysis of Combined Floating Wave and Wind Power Facilities, with Emphasis on Extreme Load Effects of the Mooring System, CeSOS
IMT-9-2014	Jiang, Zhiyu	Long-term response analysis of wind turbines with an emphasis on fault and shutdown conditions, IMT
IMT-10-2014	Dukan, Fredrik	ROV Motion Control Systems, IMT
IMT-11-2014	Grimsmo, Nils I.	Dynamic simulations of hydraulic cylinder for heave compensation of deep water drilling risers, IMT
IMT-12-2014	Kvittem, Marit I.	Modelling and response analysis for fatigue design of a semisubmersible wind turbine, CeSOS
IMT-13-2014	Akhtar, Juned	The Effects of Human Fatigue on Risk at Sea, IMT
IMT-14-2014	Syahroni, Nur	Fatigue Assessment of Welded Joints Taking into Account Effects of Residual Stress, IMT
IMT-1-2015	Bøckmann, Eirik	Wave Propulsion of ships, IMT
IMT-2-2015	Wang, Kai	Modelling and dynamic analysis of a semi-submersible floating vertical axis wind turbine, CeSOS
IMT-3-2015	Fredriksen, Arnt Gunvald	A numerical and experimental study of a two-dimensional body with moonpool in waves and current, CeSOS
IMT-4-2015	Jose Patricio Gallardo Canabes	Numerical studies of viscous flow around bluff bodies, IMT

IMT-5-2015	Vegard Longva	Formulation and application of finite element techniques for slender marine structures subjected to contact interactions, IMT
IMT-6-2015	Jacobus De Vaal	Aerodynamic modelling of floating wind turbines, CeSOS
IMT-7-2015	Fachri Nasution	Fatigue Performance of Copper Power Conductors, IMT
IMT-8-2015	Oleh I Karpa	Development of bivariate extreme value distributions for applications in marine technology,CeSOS
IMT-9-2015	Daniel de Almeida Fernandes	An output feedback motion control system for ROVs, AMOS
IMT-10-2015	Bo Zhao	Particle Filter for Fault Diagnosis: Application to Dynamic Positioning Vessel and Underwater Robotics, CeSOS
IMT-11-2015	Wenting Zhu	Impact of emission allocation in maritime transportation, IMT
IMT-12-2015	Amir Rasekhi Nejad	Dynamic Analysis and Design of Gearboxes in Offshore Wind Turbines in a Structural Reliability Perspective, CeSOS
IMT-13-2015	Arturo Jesùs Ortega Malca	Dynamic Response of Flexibles Risers due to Unsteady Slug Flow, CeSOS
IMT-14-2015	Dagfinn Husjord	Guidance and decision-support system for safe navigation of ships operating in close proximity, IMT
IMT-15-2015	Anirban Bhattacharyya	Ducted Propellers: Behaviour in Waves and Scale Effects, IMT
IMT-16-2015	Qin Zhang	Image Processing for Ice Parameter Identification in Ice Management, IMT
IMT-1-2016	Vincentius Rumawas	Human Factors in Ship Design and Operation: An Experiential Learning, IMT
IMT-2-2016	Martin Storheim	Structural response in ship-platform and ship-ice collisions, IMT
IMT-3-2016	Mia Abrahamsen Prsic	Numerical Simulations of the Flow around single and Tandem Circular Cylinders Close to a Plane Wall, IMT
IMT-4-2016	Tufan Arslan	Large-eddy simulations of cross-flow around ship sections, IMT

IMT-5-2016	Pierre Yves-Henry	Parametrisation of aquatic vegetation in hydraulic and coastal research,IMT
IMT-6-2016	Lin Li	Dynamic Analysis of the Instalation of Monopiles for Offshore Wind Turbines, CeSOS
IMT-7-2016	Øivind Kåre Kjerstad	Dynamic Positioning of Marine Vessels in Ice, IMT
IMT-8-2016	Xiaopeng Wu	Numerical Analysis of Anchor Handling and Fish Trawling Operations in a Safety Perspective, CeSOS
IMT-9-2016	Zhengshun Cheng	Integrated Dynamic Analysis of Floating Vertical Axis Wind Turbines, CeSOS
IMT-10-2016	Ling Wan	Experimental and Numerical Study of a Combined Offshore Wind and Wave Energy Converter Concept
IMT-11-2016	Wei Chai	Stochastic dynamic analysis and reliability evaluation of the roll motion for ships in random seas, CeSOS
IMT-12-2016	Øyvind Selnes Patricksson	Decision support for conceptual ship design with focus on a changing life cycle and future uncertainty, IMT
IMT-13-2016	Mats Jørgen Thorsen	Time domain analysis of vortex-induced vibrations, IMT
IMT-14-2016	Edgar McGuinness	Safety in the Norwegian Fishing Fleet – Analysis and measures for improvement, IMT
IMT-15-2016	Sepideh Jafarzadeh	Energy effiency and emission abatement in the fishing fleet, IMT
IMT-16-2016	Wilson Ivan Guachamin Acero	Assessment of marine operations for offshore wind turbine installation with emphasis on response-based operational limits, IMT
IMT-17-2016	Mauro Candeloro	Tools and Methods for Autonomous Operations on Seabed and Water Coumn using Underwater Vehicles, IMT
IMT-18-2016	Valentin Chabaud	Real-Time Hybrid Model Testing of Floating Wind Tubines, IMT
IMT-1-2017	Mohammad Saud Afzal	Three-dimensional streaming in a sea bed boundary layer
IMT-2-2017	Peng Li	A Theoretical and Experimental Study of Wave-induced Hydroelastic Response of a Circular Floating Collar
IMT-3-2017	Martin Bergström	A simulation-based design method for arctic maritime transport systems

IMT-4-2017	Bhushan Taskar	The effect of waves on marine propellers and propulsion
IMT-5-2017	Mohsen Bardestani	A two-dimensional numerical and experimental study of a floater with net and sinker tube in waves and current
IMT-6-2017	Fatemeh Hoseini Dadmarzi	Direct Numerical Simualtion of turbulent wakes behind different plate configurations
IMT-7-2017	Michel R. Miyazaki	Modeling and control of hybrid marine power plants
IMT-8-2017	Giri Rajasekhar Gunnu	Safety and effiency enhancement of anchor handling operations with particular emphasis on the stability of anchor handling vessels
IMT-9-2017	Kevin Koosup Yum	Transient Performance and Emissions of a Turbocharged Diesel Engine for Marine Power Plants
IMT-10-2017	Zhaolong Yu	Hydrodynamic and structural aspects of ship collisions
IMT-11-2017	Martin Hassel	Risk Analysis and Modelling of Allisions between Passing Vessels and Offshore Installations
IMT-12-2017	Astrid H. Brodtkorb	Hybrid Control of Marine Vessels – Dynamic Positioning in Varying Conditions
IMT-13-2017	Kjersti Bruserud	Simultaneous stochastic model of waves and current for prediction of structural design loads
IMT-14-2017	Finn-Idar Grøtta Giske	Long-Term Extreme Response Analysis of Marine Structures Using Inverse Reliability Methods
IMT-15-2017	Stian Skjong	Modeling and Simulation of Maritime Systems and Operations for Virtual Prototyping using co-Simulations
IMT-1-2018	Yingguang Chu	Virtual Prototyping for Marine Crane Design and Operations
IMT-2-2018	Sergey Gavrilin	Validation of ship manoeuvring simulation models
IMT-3-2018	Jeevith Hegde	Tools and methods to manage risk in autonomous subsea inspection,maintenance and repair operations
IMT-4-2018	Ida M. Strand	Sea Loads on Closed Flexible Fish Cages
IMT-5-2018	Erlend Kvinge Jørgensen	Navigation and Control of Underwater Robotic Vehicles

IMT-6-2018	Bård Stovner	Aided Intertial Navigation of Underwater Vehicles
IMT-7-2018	Erlend Liavåg Grotle	Thermodynamic Response Enhanced by Sloshing in Marine LNG Fuel Tanks
IMT-8-2018	Børge Rokseth	Safety and Verification of Advanced Maritime Vessels
IMT-9-2018	Jan Vidar Ulveseter	Advances in Semi-Empirical Time Domain Modelling of Vortex-Induced Vibrations
IMT-10-2018	Chenyu Luan	Design and analysis for a steel braceless semi-submersible hull for supporting a 5-MW horizontal axis wind turbine
IMT-11-2018	Carl Fredrik Rehn	Ship Design under Uncertainty
IMT-12-2018	Øyvind Ødegård	Towards Autonomous Operations and Systems in Marine Archaeology
IMT-13-2018	Stein Melvær Nornes	Guidance and Control of Marine Robotics for Ocean Mapping and Monitoring
IMT-14-2018	Petter Norgren	Autonomous Underwater Vehicles in Arctic Marine Operations: Arctic marine research and ice monitoring
IMT-15-2018	Minjoo Choi	Modular Adaptable Ship Design for Handling Uncertainty in the Future Operating Context
MT-16-2018	Ole Alexander Eidsvik	Dynamics of Remotely Operated Underwater Vehicle Systems
IMT-17-2018	Mahdi Ghane	Fault Diagnosis of Floating Wind Turbine Drivetrain- Methodologies and Applications
IMT-18-2018	Christoph Alexander Thieme	Risk Analysis and Modelling of Autonomous Marine Systems
IMT-19-2018	Yugao Shen	Operational limits for floating-collar fish farms in waves and current, without and with well-boat presence
IMT-20-2018	Tianjiao Dai	Investigations of Shear Interaction and Stresses in Flexible Pipes and Umbilicals
IMT-21-2018	Sigurd Solheim Pettersen	Resilience by Latent Capabilities in Marine Systems
IMT-22-2018	Thomas Sauder	Fidelity of Cyber-physical Empirical Methods. Application to the Active Truncation of Slender Marine Structures
IMT-23-2018	Jan-Tore Horn	Statistical and Modelling Uncertainties in the Design of Offshore Wind Turbines

IMT-24-2018	Anna Swider	Data Mining Methods for the Analysis of Power Systems of Vessels
IMT-1-2019	Zhao He	Hydrodynamic study of a moored fish farming cage with fish influence
IMT-2-2019	Isar Ghamari	Numerical and Experimental Study on the Ship Parametric Roll Resonance and the Effect of Anti-Roll Tank
IMT-3-2019	Håkon Strandenes	Turbulent Flow Simulations at Higher Reynolds Numbers
IMT-4-2019	Siri Mariane Holen	Safety in Norwegian Fish Farming – Concepts and Methods for Improvement
IMT-5-2019	Ping Fu	Reliability Analysis of Wake-Induced Riser Collision
IMT-6-2019	Vladimir Krivopolianskii	Experimental Investigation of Injection and Combustion Processes in Marine Gas Engines using Constant Volume Rig
IMT-7-2019	Anna Maria Kozlowska	Hydrodynamic Loads on Marine Propellers Subject to Ventilation and out of Water Condition.
IMT-8-2019	Hans-Martin Heyn	Motion Sensing on Vessels Operating in Sea Ice: A Local Ice Monitoring System for Transit and Stationkeeping Operations under the Influence of Sea Ice
IMT-9-2019	Stefan Vilsen	Method for Real-Time Hybrid Model Testing of Ocean Structures – Case on Slender Marine Systems
IMT-10-2019	Finn-Christian W. Hanssen	Non-Linear Wave-Body Interaction in Severe Waves

ISBN 978-82-326-3944-1 (printed version)
ISBN 978-82-326-3945-8 (electronic version)
ISSN 1503-8181

NTNU
Norwegian University of
Science and Technology

Doctoral Thesis
Finn-Christian Wickmann Hanssen

Doctoral theses at NTNU, 2019:173

Finn-Christian Wickmann Hanssen

Non-Linear Wave-Body Interaction in Severe Waves

NTNU
Norwegian University of
Science and Technology
Faculty of Engineering
Department of Marine Technology

NTNU
Norwegian University of
Science and Technology

Doctoral theses at NTNU, 2019:173
NTNU